THE UNIVERSITY *of* EDINBURGH

Experimental and Numerical Investigation of Ratcheting and Low-Cycle Fatigue in Metal Components

Konstantinos Chatziioannou

THE UNIVERSITY
of EDINBURGH

Thesis submitted in fulfilment of
the requirements for the degree of
Doctor of Philosophy
to the
University of Edinburgh — 2020

Abstract

Structures loaded cyclically beyond their elastic limit experience gradual accumulation of plastic deformations or strains which may eventually lead to material deterioration and ductile fracture. Assessing the life expectancy of their structural members requires the development and implementation of appropriate material models into the finite element environment, using robust numerical integration schemes. It is the purpose of the present Thesis to investigate through rigorous numerical analyses and experimental testing the mechanical behaviour of metal components subjected to intense cyclic loading. Advanced numerical tools are developed to simulate multi-axial material ratcheting and cyclic plasticity-damage response in metal structural components. The ultra low-cycle fatigue of high-strength steel welded tubular joints is also investigated through large-scale experiments.

An implicit numerical scheme is proposed in Chapter 2 for simulating the mechanical response of thin-walled structures subjected to inelastic cyclic loading. The constitutive model is formulated explicitly for plane stress conditions, accounts for combined kinematic/isotropic hardening and follows the von-Mises yield criterion. Emphasis is given to kinematic hardening part, which is described with an advanced multiple backstress model suitable for multi-axial material ratcheting simulation. Constitutive relations are integrated implicitly using the Euler-backward integration technique. Two main novelties of the algorithm refer to the incremental update of the internal variables through the solution of a single scalar equation, and the explicit formulation of the consistent

tangent moduli. The numerical scheme is implemented into the finite element software ABAQUS (2016) as a material user-subroutine UMAT and its capabilities are demonstrated through the numerical simulation of large-scale experiments on pipe elbows, a characteristic mechanical component that experiences multi-axial ratcheting response. In the sequence, the proposed numerical scheme is employed to investigate the ratcheting collapse of dented externally pressurised tubular circular members subjected to cyclic axial loading.

The numerical implementation of coupled cyclic plasticity-damage models is presented in Chapter 3, suitable for simulating low-cycle fatigue in metal components. Constitutive relations account for J_2-flow theory with nonlinear kinematic/isotropic hardening, coupled with isotropic continuum damage mechanics. The damage potential is written in a general form, allowing for implementing any isotropic damage model reported in the literature. The constitutive relations are integrated implicitly considering in the most general case the 3D finite element formulation. An additional numerical scheme is proposed explicitly for plane stress conditions by extending the *plane-stress projection* method to the requirements of the model. Both numerical schemes feature computational efficiency as incremental update of internal variables is achieved through the solution of a single scalar equation. The integration algorithms are consistently linearised to ensure numerical robustness in large-scale computations. The proposed numerical schemes are implemented into ABAQUS (2016) software as user material subroutines UMAT and are validated against large-scale tests on pipe elbows that failed from ultra low-cycle fatigue.

In the last part of the Thesis, the ultra low-cycle fatigue performance of welded tubular X-joints is examined, motivated by the need of safeguarding the integrity of offshore platforms under extreme loading conditions. Seven specimens, representing X-brace joints of a bottom-founded offshore tubular jacket with a scaling factor of 1:3 are tested under strong, fully-reversed cyclic in-plane bending. The seven specimens formed a

through-thickness fatigue crack within less than 100 cycles, simulating extreme loading conditions. Rigorous finite element models are also developed, with emphasis on constitutive modelling, to simulate the cyclic loading procedure, providing very good comparisons in terms of load-displacement response and local strain predictions during the initial loading cycles. The experimental data are compared with a large dataset of low-cycle fatigue experiments on welded components, reported in the literature for mild and high-strength steel materials, as well as with existing design provisions.

Acknowledgements

First of all I would like to express my gratitude to my supervisors, Dr. Yuner Huang and Prof. Spyros A. Karamanos, for providing me the opportunity to work on such a challenging topic. Their advises during my journey have been a guiding compass for my development as a researcher and as an individual. The financial support provided by The University of Edinburgh through a PhD scholarship is also acknowledged. At the same time, I would like to thank my brother, Petros Chatziioannou, my close friends Harris Hariskos and Nikolaos Ringas, as well as my childhood friends in Greece for being with me all the way. I am very grateful to my parents, Ioannis Chatziioannou and Sofia Samara for their support all those years and for always being there for me. I would like to close this paragraph by expressing my sincere appreciation to my partner in crime, Ms. Anna Georgiadou, for her endless patience and unlimited support all these years.

List of Publications

K. Chatziioannou, Y. Huang, S. A. Karamanos. Dented Externally-Pressurised Pipes Subjected to Cyclic Axial Loading (2019). Proceedings of the ASME 38^{th} International Conference on Ocean, Offshore and Arctic Engineering, pp. OMAE2019-95814.

K. Chatziioannou, Y. Huang, S. A. Karamanos. Simulation of Piping Ratcheting Experiments using Advanced Plane Stress Cyclic Elastoplasticity Models (2019). Finalist in student competition, ASME 2019 Pressure Vessels and Piping Conference, pp. PVP2019-93507.

K. Chatziioannou, Y. Huang, S. A. Karamanos. Coupled Numerical Simulation of Low-Cycle Fatigue under Plane Stress Conditions (2019). Invited lecturer in COMPLAS 2019, International Conference on Computational Plasticity.

K. Chatziioannou, S. A. Karamanos, Y. Huang. Experimental Investigation on Welded S700 High Strength Steel Tubular X-Joints under Low-Cycle Fatigue Loading. Proceedings of the 17^{th} International Symposium on Tubular Structures, p. 263-267.

K. Chatziioannou, S. A. Karamanos, Y. Huang. Ultra Low-Cycle Fatigue Performance of S420 and S700 Steel Welded Tubular X-joints (2019). International Journal of Fatigue, 129, p. 105221

K. Chatziioannou, S. A. Karamanos, Y. Huang. An Implicit Numerical Scheme for Cyclic Elastoplasticity and Ratcheting under Plane Stress Conditions (2019). Computers and Structures, Minor revision requested.

K. Chatziioannou, Y. Huang, S. A. Karamanos. Simulation of Piping Ratcheting Experiments using Advanced Plane Stress Cyclic Elastoplasticity Models (2019). International Journal of Pressure Vessels and Piping, 143, 021501-1-10 .

K. Chatziioannou, S. A. Karamanos, Y. Huang. A Robust Integration Algorithm for Cyclic Plasticity-Damage Models (2020). Engineering Structures, Minor revision requested.

K. Chatziioannou, S. A. Karamanos, Y. Huang. A CDM Model for Ultra Low-Cycle Fatigue of High Strength Steel Components. Under preparation.

K. Chatziioannou, S. A. Karamanos, Y. Huang. A Robust Integration Algorithm for Cyclic Plasticity-Damage Models under Plane Stress Conditions. Under preparation.

Contents

List of Tables

List of Figures

Chapter 1

Introduction and state of the art

1.1 Introduction

Offshore structures and subsea installations are often exposed to extreme weather conditions. Their main unit consists mainly of circular tubular components and welded tubular connections which are designed to respond elastically under the effect of the applied wind and wave loading. However, the oil and gas sector have repeatedly reported structural failures attributed to strong inelastic loading [Cruz and Krausmann (2008)], which had catastrophic consequences in the global economy and the environment. A major challenge in the design of offshore assemblies lies on safeguarding their structural integrity under severe loading conditions. Most of the time, global collapse initiates from local failure of critical components, subsequently leading to the complete failure of the structure. A common type of local failure is depicted in Fig. 1.1, showing the formation of through-thickness crack in a tubular welded connection of an offshore jacket substructure which has been subjected to intense cyclic loading.

Figure 1.1: Through-thickness crack on high-strength steel welded X-joints subjected to extreme cyclic loading [Chatziioannou et al. (2019c)].

There are a number of possible sources of extreme cyclic loading (e.g. earthquakes, shutdown/startup or storm conditions) in which case structural members are loaded beyond their elastic limit and are plastically deformed. Upon repeated inelastic loading, structural components experience gradual accumulation of plastic deformation or strain, which eventually may lead to low-cycle fatigue failure [Kyriakides and Shaw (1987); Vaze and Corona (1998); Lu (2003); Wei et al. (2004)]. The assessment of the fatigue life of such components requires accurate prediction of inelastic strain and its evolution, also referred to as "ratcheting". Numerous constitutive material modes have been proposed to simulate material ratcheting in metal components. However, accurate prediction of ratcheting, and particularly in circular tubular components, constitutes even today a challenge as it requires the use of dedicated constitutive models, implemented in the finite element environment.

Accumulation of plastic strains due to intense cyclic loading eventually leads to the initiation, growth and coalescence of micro-voids, and subsequently the formation of microcracks. This phenomenon is referred in the literature as "ductile plastic damage" and

has been extensively studied by means of micro-mechanics [Rice and Tracey (1969); Rousselier (1987)]. However, in macro-scale level structural computations, which are of interest for the majority of practical applications, the use of micro-mechanics models is prohibiting due to the size of the structure. In this case, material deterioration and ductile fracture due to cyclic inelastic loading can be numerically predicted based on the principles of Continuum Damage Mechanics (CDM) [Lemaitre (1971)]. CDM provides the foundations for the development of fully-coupled cyclic plasticity-damage material models, which account for the degrading effect of damage in the plastic response. Methodologies for the numerical implementation of such elaborate constitutive models within the finite element environment through implicit and unconditionally stable integration algorithms remain, still, an open research topic.

Dedicated numerical tools for simulating low-cycle fatigue in metals may not always be accessible. In addition, available test data for calibrating the material model can often be quite limited. In such cases, large-scale experimental campaigns are prompted for investigating low-cycle fatigue of offshore structural members, and particularly tubular welded connections. Despite the large number of published work on the high-cycle fatigue of welded tubular joints, the low-cycle fatigue behaviour of such joints has received substantially less attention. Another issue related to the construction of offshore structural systems for wind energy production, which attracts increasing attention is the use of high-strength steel. Until recently, metal alloys of grade up to S355 have been used exclusively in the offshore wind sector. Design methodologies for the fatigue design of regular steel welded joints are well established [Itoga et al. (2003); Yildirim and Marquis (2012)]. On the other hand, less attention has been paid to the fatigue of welded tubular components made of high-strength steel material, especially for their low-cycle fatigue behaviour and design [Health and Safety Executive (2004)].

Motivated by the aforementioned challenging topics which are still open for investigation, the present Thesis examines through experiments and advanced numerical simulations the low-cycle fatigue behaviour of steel structural members. Towards this

purpose, numerical integration algorithms are developed for implementing elaborate constitutive material models into the finite element environment, capable of simulating accurately multi-axial material ratcheting and the cyclic plasticity-damage response of metal components. The main objective is to derive numerical integration methodologies which feature optimum performance and can be used efficiently in demanding simulations. The proposed numerical schemes are implemented within the finite element environment as material user subroutines and are validated by simulating successfully experimental data obtained by the literature. Furthermore, the ultra low-cycle fatigue of high-strength steel welded tubular joints is examined through an experimental program, considering large-scale welded X-joints, obtained from an offshore jacket substructure of a large output wind turbine. The experimental findings are numerically re-produced to some extend and state of the art design standards are evaluated in predicting the number of cycles to failure obtained from testing the high-strength steel welded connections.

The document is structured in the following manner. An extensive literature review is presented in the remaining part of Chapter 1, reporting state of the art developments related to the topics under investigation. In Chapter 2, the numerical integration of an advanced cyclic plasticity model is presented, suitable for simulating multi-axial ratcheting in thin-walled tubular components modelled with shell-type finite elements, which follow the plane stress formulation. The proposed numerical scheme is validated against cyclic bending experiments on pipe elbows. It is then employed to simulate the mechanical response of externally-pressured dented circular tubular components subjected to axial ratcheting. Next, the numerical integration of a robust cyclic plasticity-damage constitutive model is presented in Chapter 3, offering an optimised solution method for simulating plasticity-damage response and implementing any CDM model proposed in the literature under a common computational framework. Two distinctly different integration algorithms are proposed; one for the general case of 3D formulation and another for plane stress conditions. Both numerical schemes are validated against large-scale experiments on pipe elbows that failed under ultra low-cycle fatigue.

Issues related to spurious mesh dependency originating from the strain-softening material response are also addressed using an appropriate simulation methodology. The results of the experimental campaign which was organised and executed within the framework of the PhD are presented in Chapter 4. Finally, the most important conclusions of the present work and its contribution to the current state of the art are summarised in Chapter 5.

1.2 State of the art

An extensive literature review covering the topics elaborated within the Thesis is presented herein. The literature review is split into three main parts related to the main areas of research. The first part discusses the state of the art advancements in predicting the multi-axial ratcheting response of metal circular tubular components, also referred to as "steel piping" in the nuclear and the offshore industries. Particular attention is given to pipe elbows which feature a characteristic example of steel piping that experiences multi-axial ratcheting response due to its geometric configuration. The second part covers the literature on the simulation of cyclic-plasticity damage response and ductile fracture in metal components. The last part of the literature review reports previous experimental studies on welded tubular X-joints with emphasis on high strength steel. Current design approaches for low-cycle fatigue in metal components are also discussed to some extend.

1.2.1 Ratcheting in circular tubular components

Metal circular tubular components (piping) are widely used in industrial applications such as power plants (nuclear or fossil), chemical and petrochemical facilities, or gas and oil terminals. As a result, their structural integrity is crucial for the safe operation of the industrial facility. In the presence of severe external actions, such as earthquakes

or shutdowns/startups, steel piping are imposed to strong cyclic loading conditions and may fail due to low-cycle fatigue [EPRI (1992, 1994)]. The experimental studies of Rider et al. (1995) and Wei et al. (2004) among others have shown that progressive accumulation of plastic strain due to cyclic loading ("ratcheting") may accelerate low-cycle fatigue cracking. Additional experiments on metallic circular tubular components conducted by Shaw and Kyriakides (1985) and Corona and Kyriakides (1988) have shown that failure due to ratcheting may occur in the form of local collapse prior to wall cracking. An extensive investigation of uni-/multi-axial material ratcheting in metal alloys has been reported in the early work of Hassan et al. (1992) and Hassan and Kyriakides (1994a,b).

1.2.1.1 Experimental investigation of ratcheting in pipe elbows

Metal pipe elbows fall within the broad category of piping and are vital components of industrial facilities. Accurate prediction of their low-cycle fatigue behaviour features still a challenge, mainly due to the multi-axial ratcheting response. Yahiaoui et al. (1996a,b) tested in total 16 pairs of carbon/stainless steel pipe elbows under in-/out-of-plane resonance dynamic bending to simulate seismic excitation. Strain measurements were obtained with respect to the hoop and the axial direction to identify the principal direction of ratcheting in each loading condition. Moreton et al. (1996) used the experimental data reported by Yahiaoui et al. (1996a,b) to determine the minimum cyclic bending moment necessary to initiate ratcheting. Additional experimental results on pipe elbows subjected to seismic loading have been reported by Slagis (1998). Using a shaking table, Slagis (1998) tested 32 piping components to quantify the impact of fabrication details on their low-cycle fatigue behaviour. Suzuki et al. (2002) reported initial results of a 6-year experimental campaign aiming at evaluating the cyclic elastoplastic behaviour and fatigue damage of steel piping under severe seismic excitation. More recently, Chen et al. (2005) tested steel pipe elbows under constant internal pressure and cyclic in-plane bending to examine the multi-axial ratcheting

response. The experimental results showed intense ratcheting in the hoop direction, while the ratcheting strain rate grew with the increase of the internal pressure. Pipe wall thinning effects were investigated by Shi et al. (2013); pipe elbows with local wall thinning at extrados and the crown were tested under constant internal pressure and cyclic in-plane bending to quantify the effect of local wall thinning in the ratcheting response.

Vishnuvardhan et al. (2013) investigated ratcheting failure of pressurised straight pipes and elbows under reversed bending. Strain measurements were obtained, showing rapid accumulation of plastic strain ("ratcheting") in both types of specimens. In this experimental study failure was observed as through-wall crack accompanied by simultaneous local ovalization of the pipe cross section. Varelis et al. (2013) reported additional experimental results concerning low-cycle fatigue of pipe elbows. Failure was identified through the development of through-thickness cracking, followed by a pipe cross-section ovalization at the bend. The experimental data were compared with design standards ASME B31.3 (2006) and EN 13480-3 (2002), highlighting the conservativeness of current design tools in predicting the number of cycles to failure.

1.2.1.2 Constitutive models for ratcheting prediction

The accurate numerical prediction of the cyclic inelastic material response is a key issue for assessing the low-cycle fatigue of metal components. An extensive literature review discussing relevant approaches and limitations can be found in the recent paper by Chen et al. (2013). In particular, the choice of the kinematic hardening rule has been pinpointed as the key issue for predicting ratcheting. A large number of constitutive models have been developed with the purpose of predicting accurately plastic strain in steel circular tubular members and particularly its evolution with respect to the loading cycles. In the framework of the so-called *coupled* constitutive models, Prager (1956) proposed a linear kinematic hardening rule (Eq. 1.1) for simulating the cyclic inelastic

response of the material.

$$\dot{\boldsymbol{a}} = C\dot{\boldsymbol{\varepsilon}}^p \tag{1.1}$$

In Eq. (1.1), $\dot{\boldsymbol{a}}$ denotes the rate form of the kinematic hardening tensor $\boldsymbol{a}$, also referred to as backstress tensor. Furthermore, C is the hardening modulus and $\boldsymbol{\varepsilon}^p$ is the plastic strain tensor. Armstrong and Frederick (1966) identified the inability of the Prager (1956) hardening rule to simulate the cyclic-plasticity response of the material and proposed a nonlinear kinematic hardening rule by adding a recovery term in the evolution equation.

$$\dot{\boldsymbol{a}} = C\dot{\boldsymbol{\varepsilon}}^p - \gamma \boldsymbol{a}\dot{\varepsilon}_q \tag{1.2}$$

In Eq. (1.2), ε_q is the equivalent plastic strain and γ is a dimensionless parameter that controls the maximum value and the rate of saturation of the backstress tensor. Chaboche (1986) in his pioneer work revised the kinematic hardening rule proposed by Armstrong and Frederick (1966) by showing that the use of a single backstress tensor leads to ratcheting over-prediction. To alleviate this shortcoming, he proposed the use of four superimposed nonlinear backstresses as shown in Eq. (1.3).

$$\dot{\boldsymbol{a}} = \sum_{i=1}^{4} \left(\dot{\boldsymbol{a}}^i\right) = \sum_{i=1}^{4} \left(C^i\right) \dot{\boldsymbol{\varepsilon}}^p - \sum_{i=1}^{4} \left(\gamma^i \boldsymbol{a}^i\right) \dot{\varepsilon}_q \tag{1.3}$$

In a follow-up paper, Chaboche (1991) revised Eq. (1.3) towards more accurate prediction of ratcheting, and particularly ratcheting shakedown.

$$\dot{\boldsymbol{a}} = \sum_{i=1}^{4} \left(\dot{\boldsymbol{a}}^i\right) = \sum_{i=1}^{4} \left(C^i\right) \dot{\boldsymbol{\varepsilon}}^p - \sum_{i=1}^{4} \left(\gamma^i \boldsymbol{a}^i \chi_i\right) \dot{\varepsilon}_q \tag{1.4}$$

$$\chi_i = \begin{cases} 1, & i = 1,2,3 \\ \left\langle 1 - \dfrac{\overline{a}^4}{\sqrt{\boldsymbol{a}\cdot\boldsymbol{a}}} \right\rangle, & i = 4 \end{cases} \tag{1.5}$$

In Eq. (1.4), $\langle\cdot\rangle$ are the Macaulay brackets and $\overline{a}^4$ is a threshold term which determines whether the recovery term of the fourth backstress tensor is active. Another hardening rule (Eq. 1.6) has been proposed by Ohno and Wang (1994) who modified further the classical kinematic hardening rule of Armstrong and Frederick (1966) in an attempt to predict more accurately the evolution of plastic strains.

$$\dot{\boldsymbol{a}} = \sum_{i=1}^{N} \left(\dot{\boldsymbol{a}}^i\right) = \sum_{i=1}^{N} \left(C^i\right) \dot{\boldsymbol{\varepsilon}}^p - \sum_{i=1}^{N} \left[\gamma^i \boldsymbol{a}^i \left\langle \dot{\boldsymbol{\varepsilon}}^p \cdot \frac{\boldsymbol{a}^i}{f(\boldsymbol{a}^i)} \right\rangle \left(\frac{f(\boldsymbol{a}^i)}{C_i/\gamma_i} \right)^{m_i} \right] \tag{1.6}$$

Modified kinematic hardening rules have also been proposed by Guionnet (1992) and a few years later by Abdel-Karim and Ohno (2000). The kinematic hardening model proposed by Guionnet (1992) requires the definition of numerous material constants which are not well defined. It also obtains a complicated form which makes its implementation within the finite element environment a challenging task. The kinematic hardening model proposed by Abdel-Karim and Ohno (2000) is formulated by superimposing the hardening rules of Armstrong and Frederick (1966) and Ohno and Wang (1993). This hardening rule provides improved ratcheting prediction in comparison to Chaboche (1986, 1991) models but similarly to Chaboche (1986, 1991) hardening rules, it fails to simulate multi-axial ratcheting. The numerical/experimental study of Bari and Hassan (2000, 2001) demonstrated that the multi-linear hardening rule of Mróz (1967) as well as the more advanced nonlinear kinematic hardening models proposed by Chaboche (1986, 1991), Ohno and Wang (1994) and Guionnet (1992) tend to over-predict multi-axial ratcheting evolution. More recently, Bari and Hassan (2002) proposed a new kinematic hardening rule (Eq. 1.7) which leads to more accurate simulation of multi-axial ratcheting in steel components.

$$\dot{\boldsymbol{a}}' = \sum_{i=1}^{N} C_i \dot{\boldsymbol{\varepsilon}}^p - \sum_{i=1}^{N} \left(\gamma_i \left[\boldsymbol{a}'^i \delta_i + (1-\delta_i)(\boldsymbol{a}'^i \cdot \boldsymbol{n})\boldsymbol{n} \right] \chi_i \dot{\varepsilon}_q \right) \tag{1.7}$$

In Eq. (1.7), parameter χ_i is computed as in Eq. (1.4). In addition, δ_i in Eq. (1.7) is a multi-axial ratcheting parameter while $\boldsymbol{n}$ is the unit outward to the yield surface

tensor. Bari and Hassan (2002) and subsequently, Rahman and Hassan (2005); Rahman et al. (2008) showed that the use of this hardening rule may result in more accurate prediction of multi-axial ratcheting in metal components. However, neither Bari and Hassan (2002) nor Rahman et al. (2008) have proposed a robust numerical scheme for implementing this elaborate kinematic hardening rule within the finite element environment.

1.2.1.3 Implementation of constitutive models for ratcheting simulation

The implementation of elaborate constitutive models, which consider advanced hardening rules in the finite element environment, may provide a valuable tool for simulating the mechanical response of structural components undergoing cyclic inelastic loading. In particular, the use of shell-type elements, which employ the plane stress formulation, is favoured in simulating thin-walled structures due to its computational efficiency. Nevertheless, the plane stress condition imposes an additional computational challenge in the development of a robust numerical integration scheme and its consistent jacobian. Towards this purpose, previous attempts have extended existing integration algorithms, originally proposed for 3D formulations, to account for the plane stress condition by (*a*) increasing the number of integration equations to satisfy the out-of-plane zero stress constraints [Aravas (1987)], or (*b*) incorporating nested Newton-Rapson iterative solutions to satisfy the out-of-plane constraints [Dodds (1987)], or finally (*c*) using the *plane-stress projection* plasticity concept involving only in-plane stress/strain components [Jetteur (1986); Simo and Taylor (1986)]. From a computational standpoint, the implementation approach outlined in (*c*) features optimum performance [Millard (1995); de Souza Neto et al. (2008)] and it is prompted for large-scale computations.

The use of advanced constitutive models in large-scale computations necessitates their

efficient implementation within the finite element environment, which may be a challenging task for complex constitutive models. Methods (*a*) and (*b*) have found application in the literature. Using method (*a*), Aravas (1987) proposed an implicit numerical scheme for pressure-dependent metal plasticity; this scheme is capable of describing plane stress conditions as a special case of pressure dependency. Method (*a*) was also employed by Sawyer et al. (2001) who proposed an implicit numerical scheme for J_2 cyclic elastoplasticity considering the classical Chaboche (1986) model. The elastoplastic tangent moduli in [Sawyer et al. (2001)] are computed using an approximate method and this might affect the rate of convergence in large-scale computations. The plane-stress implementation methodology (*a*) was also used by Ohno et al. (2013) for implementing a simplified version of the kinematic hardening rule proposed by Ohno and Wang (1994). Rahman (2006) implemented the kinematic hardening rule proposed by Bari and Hassan (2002) in finite element environment using method (*a*), considering the plane stress algorithm as a special case of the three-dimensional case. However, the proposed integration algorithm could be further optimised whereas the consistent tangent moduli for plane stress conditions are not explicitly defined. It should be noted that the numerical integration schemes proposed in [Sawyer et al. (2001); Ohno et al. (2013); Rahman (2006)] require the simultaneous solution of multiple equations, which has a direct impact on their numerical efficiency. The *plane-stress projection* method has been introduced in implicit integration schemes by Jetteur (1986) considering isotropic hardening solely, and by Simo and Taylor (1986) accounting for isotropic and linear kinematic hardening. The same method was used by Hartmann et al. (1998) for the numerical implementation of the cyclic plasticity model proposed by Haupt et al. (1992). In that numerical scheme [Hartmann et al. (1998)], the integration of the constitutive relations requires the simultaneous solution of three nonlinear equations, while the proposed numerical solution method features only first-order convergence, and may lead to a noticeable increase of the computational cost in large-scale computations. Recently, Cleja-Ţigoiu and Stoicuţa (2014) revised the *plane-stress projection* method in an attempt to simulate more accurately the mechanical response of very thin

plates. The proposed numerical scheme accounts for nonlinear isotropic and linear kinematic hardening and therefore, may not be appropriate for ratcheting simulation.

1.2.1.4 Numerical simulation of multi-axial ratcheting in steel pipe elbows

Despite the existence of test data, as described in Section 1.2.1.1, and the recent advancements in simulating cyclic plasticity response [Section 1.2.1.2], the numerical simulation of material ratcheting in large-scale components is still a challenging topic. Balan and Redektop (2004) examined numerically the effect of bi-directional loading on the fatigue assessment of pressurised pipe elbows with local thinning effects using bi-linear kinematic hardening. Chen et al. (2005) implemented the hardening rules proposed by Ohno and Wang (1993, 1994) and Chen and Jiao (2004) in ANSYS (1995) software to simulate cyclic bending experiments on pipe elbows. The numerical predictions in terms of plastic strain range and accumulation were in good agreement with the experimental data only for relatively low applied loading. Oh et al. (2008) evaluated shakedown limits in pipe elbows subjected to cyclic bending using a simplified simulation methodology which combines the results of a linear elastic analysis, and a nonlinear analysis employing elastic-perfectly plastic material model. Hassan and his research team [Rahman et al. (2008); Hassan and Rahman (2008, 2015); Hassan et al. (2015)] simulated experiments on steel piping under cyclic inelastic loading, using several advanced hardening models, towards ratcheting predictions. The results indicated the strengths and weaknesses of each constitutive model, and demonstrated the capability of the kinematic hardening rule proposed by Bari and Hassan (2002) in simulating multi-axial ratcheting evolution. Shi et al. (2013) employed the modified hardening rule proposed by Chen and Jiao (2004) for the numerical simulation of cyclic bending tests on pipe elbows. The numerical predictions were sufficiently accurate in tests where the ratcheting strain rate was low but failed to predict ratcheting evolution when plastic strains were rapidly accumulated over the load cycles.

More recently, Varelis et al. (2013); Varelis and Karamanos (2015) presented results from numerical simulations on steel pipe elbows under inelastic loading, implementing in the finite element environment the bounding-surface cyclic-plasticity model initially proposed by Tseng and Lee (1983). Moreover, Foroutan et al. (2018) implemented the hardening rule proposed by Ahmadzadeh and Varvani-Farahani (2013) and presented numerical results which were in good agreement with experimental data obtained from pipe elbows. On the other hand, Liu et al. (2019) as well as Rahmatfam et al. (2019) simulated numerically the ratcheting response of pipe elbows subjected to cyclic bending using more traditional kinematic hardening rules such as those proposed by Ohno and Wang (1993) and Chen and Jiao (2004). The main conclusion drawn from the aforementioned studies is that the use of appropriate numerical tools, which employ advanced hardening rules, are required for assessing the structural performance of steel pipe elbows and circular tubular components under severe cyclic loading leading to low-cycle fatigue. Towards that purpose, the reliable prediction of strain ratcheting is shown to be of paramount importance [Labbé et al. (2016); Sollogoub (2017)].

1.2.1.5 Collapse of dented offshore pipelines due to axial ratcheting

Pipeline systems constitute the “arteries” of the oil and gas industry transporting large quantities of hydrocarbons. Their structural safety during installation and operation is vital; any malfunction or damage may lead to economic loses and environmental pollution [Hopkins (1995); Wang et al. (2013)]. Offshore pipelines are currently installed in deep waters, exceeding 2,000 metres of water depth, and operate under significantly high pressure and temperature, which might lead to plastic deformations and buckling [Di Vito (2010)]. During a lifetime of 20 to 30 years, these systems exhibit hundreds of shutdowns/restarts, which in combination with the externally applied pressure may lead to cyclic loading, followed by plastic strain accumulation (“ratcheting”) and low-cycle fatigue failure.

Circular tubular structural components under combined axial loading and pressure

have been the subject of investigation of numerous research articles. Madhaven and Babcock (1987) investigated the effect of axial tensile loading on the critical buckling pressure, whereas Kyriakides and Chang (1992) reported experiments and numerical simulations on the effect of axial tensile loading on the buckling propagation pressure. The interaction between axial tension and external pressure has been also examined by Karamanos and Tassoulas (1995) in X42 steel circular tubular members. More recently, Paquette and Kyriakides (2006) investigated the behaviour of super-duplex stainless steel tubes under axial compression and internal pressure. Jiao and Kyriakides (2009) extended the work of Paquette and Kyriakides (2006) by examining circular tubular components subjected to cyclic axial loading and subsequently to a combination of cyclic axial loading and internal pressure [Jiao and Kyriakides (2011a,b)]. In both cases, it was identified that instability occurred when the net shortening or the average strain on the tube reached a critical value, very close to the value observed under monotonic loading [Paquette and Kyriakides (2006)].

The aforementioned investigations concerned intact (perfect) tubular components, neglecting the effects of accidental interferences. However, numerous oil and gas pipeline failures are attributed to third-party damages such as dents and gouges [Dai et al. (2017)]. Dent interferences have found to be more critical in comparison with gouges and can be categorized to “plain” or “kinked” dents according to the shape of the local distortion [Wang and Smith (1982)]. Azadeh and Taheri (2014) examined experimentally the behaviour of plain dented carbon steel tubes under cyclic axial loading and demonstrated that the number of cycles to collapse can be decreased by up to 75% for a dent (δ) equal to 0.14 times the diameter (δ/D=14%). Zeinoddini et al. (2015a) and Zeinoddini et al. (2015b) performed a series of experiments on un-symmetrically dented tubes in order to investigate the elastoplastic buckling capacity and the ratcheting behaviour of cyclically loaded high strength steel dented tubes. It was shown that semi-analytical equations proposed for conventional steel material are always on the safe side while design codes such as Norsok (2004) and DNV-RP-F111 (2010) provide reasonably accurate results only for small dent magnitudes.

Recently, Naghipour et al. (2018) examined experimentally high strength steel tubes with local gouge and dent defects. The presence of gouges had a minor impact on the performance of the tube while comparisons with analytical solutions demonstrated an over-prediction of the damaged tube capacity. Pournara et al. (2018) investigated numerically/experimentally the performance of dented tubes subjected to internal pressure and cyclic bending pressure. Strain concentration factors on the dent location were obtained, for evaluating the fatigue life of the material.

1.2.1.6 Discussion on multi-axial ratcheting simulation

In summary, it can be identified that numerical prediction of multi-axial ratcheting in steel circular tubular components still remains a challenge, leading unavoidably to conservative design against low-cycle fatigue. The majority of ratcheting constitutive models reported in the literature fail to predict multi-axial ratcheting evolution. It was argued by Chen et al. (2013) in his review paper that the implementation methodology has a direct impact on the quality of the numerical results. Therefore, the development of a robust numerical integration scheme for an advanced ratcheting constitutive model, capable of simulating uni-/multi-axial ratcheting in metal components is investigated in the present Thesis.

1.2.2 Numerical simulation of damage using Continuum Damage Mechanics models

In the event of extreme loading conditions such as earthquakes or storm conditions, metal components experience gradual reduction of their structural capacity due to damage initiation, and may fail within limited number of load cycles. Simulating material degradation and ductile rupture in metals subjected to repeated inelastic loading requires the consideration of damage effects into the material model. Damage can be incorporated into the inelastic constitutive relations based on the principles

of CDM, formulated in an early stage by Kachanov (1958) and later established on a scientific basis by Chaboche (1978); Lemaitre and Chaboche (1978); Murakami (1981). Major contributions on the CDM approach have been presented by Lemaitre (1984) and later by Voyiadjis (1988) who introduced into the constitutive relations of cyclic plasticity an internal scalar variable, expressed by the corresponding kinetic law of damage, to model the progressive deterioration of the material.

1.2.2.1 Continuum Damage Mechanics framework

In the framework of CDM, damage is integrated into the constitutive relations of cyclic elastoplasticity based on the concept of *effective stress* tensor [Kachanov (1958)] and the hypothesis of strain equivalence [Lemaitre (1971)]. The *effective stress* approach dictates that the stress tensor ($\boldsymbol{\sigma}$) of the damaged material is related to the fictitious stress tensor ($\widetilde{\boldsymbol{\sigma}}$) of the corresponding un-damaged material through Eq. (1.8).

$$\widetilde{\boldsymbol{\sigma}} = \frac{\boldsymbol{\sigma}}{1-\boldsymbol{D}} \tag{1.8}$$

where $\boldsymbol{D}$ represents the damage internal variable. In the most general case, voids are oriented in different planes and damage is described with rigorous forth order [Leckie and Onat (1981); Krajcinovic (1985); Kattan and Voyiadjis (2001)] or more elaborate second order tensors [Voyiadjis et al. (2008); Desmorat and Otin (2008); Dunand et al. (2012)]. The consideration of anisotropy in the damage variable increases the complexity of the constitutive model, while the calibration of the resulting CDM model is not very straightforward even with state of the art equipment [Lin et al. (2005)]. On the other hand, isotropic CDM assumes that microvoids are uniformly distributed in the material and thus, damage can be expressed through a scalar variable D [Lemaitre (1985)].

Isotropic damage mechanics provides a powerful tool for modelling ductile damage and fracture in metal alloys, and local constitutive models coupled with isotropic CDM

models are extensively used [Li et al. (2011); Soyarslan et al. (2012); Ma and Yuan (2013); Lian et al. (2014); Masih et al. (2015); Majzoobi et al. (2018); Nam et al. (2018); Fincato and Tsutsumi (2019)]. A wide range of CDM models have been proposed to describe different trends of damage evolution in metals and for more information the reader can refer in [Lemaitre (1985); Bonora (1997); Celentano and Chaboche (2007); Besson (2009b); Voyiadjis et al. (2012); Li et al. (2015); Zhan et al. (2017); Gautam et al. (2018); Zhang et al. (2020)]. From a computational standpoint, complex CDM models impose additional difficulties in the development of an implicit numerical scheme, whereas another challenge in simulating plasticity-damage response is associated with spurious mesh dependency, originating from the strain-softening material response after damage initiation [de Borst et al. (1993)]. For these two reasons, the majority of the aforementioned studies used either uncoupled constitutive models or coupled ones with the consideration of constant element size in their analyses. The uncoupled approach may fail to predict accurately local strains and consequently damage evolution after damage initiation, while the use of constant element size limits the transferability of the results to other applications, where a different mesh strategy should be applied. A recent review article addressing issues related to the numerical simulation of damage and mesh dependency has been presented by Besson (2009a). The most well-know material constitutive equations and computational tools developed within the last 20 years are discussed in Besson (2009a).

1.2.2.2 Numerical implementation of plasticity-damage material models

Towards accurate and efficient simulation of low-cycle fatigue of metal components, a coupled plasticity-damage numerical integration scheme should be implemented within the finite element environment. An implicit numerical scheme for coupled cyclic elastoplasticity, incorporating nonlinear isotropic and kinematic hardening with a single backstress, has been presented in an early form by Benallal et al. (1988) and subsequently by Doghri (1995). In both studies, incremental stress update is achieved

through the solution of a system of four algebraic equations in terms of the internal variables. Furthermore, the integration algorithm and the proposed consistent linearisation methodology account for isotropic damage functions that depend explicitly on the effective stress tensor whereas important modifications are required for the consideration of more elaborate CDM models such as those proposed by Bonora (1997); Voyiadjis et al. (2012); Pirondi et al. (2006); Nam et al. (2018) among others. Additional coupled numerical schemes were reported by Singh and Pandey (1999), de Souza Neto (2002), Saanouni et al. (2001), Lemaitre and Desmorat (2005) and Soyarslan and Tekkaya (2010), which are applicable to limited CDM models while consider less elaborate hardening rules. In the majority of these models, the integration algorithms are computationally costly requiring the simultaneous solution of multiple equations and possibly matrix inversion within the iterative solution procedure. Voyiadjis et al. (2012) also proposed a coupled numerical scheme by extending the methodology presented in [Voyiadjis et al. (2013)] for classical elastoplasticity but update of the internal variables is based on explicit integration of the constitutive relations. Recently, Bonora et al. (2014) presented a modified version of the numerical scheme proposed by Doghri (1995) based on the kinematic hardening rule proposed by Chaboche (1986) and the so-called *partial-coupling*, accounting for the degrading effect of damage on the Young's modulus but neglecting its influence on the plastic flow. This model is formulated similarly to the classical fully-coupled ones and accounts for a generalised isotropic damage potential, but the resulting integration scheme is rather costly, requiring the simultaneous solution of 12 equations [Eqs. 40-51 in Bonora et al. (2014)].

1.2.2.3 Mesh dependency in plasticity-damage simulations

The coupling of plasticity with damage under a local constitutive model introduces numerical convergence difficulties which originate from the strain-softening response of the material. Material softening leads to localisation of inelastic strains in a band

that is only one element across regardless of the element's dimensions. Upon refinement of the mesh, strain accumulate on a band of zero thickness and thus, the finite element results are mesh-biased as mesh refinement leads unavoidably to lower energy dissipation during the process of ductile fracture. Alleviation of mesh dependency may be achieved with the use of *micropolar* [de Borst et al. (1993); Aifantis (1984)], *non-local* [Bazant and Jirasek (2002); Besson (2009a); Nguyen et al. (2015)] or *gradient-enhanced* [de Borst (2001); Papadioti et al. (2019)] constitutive models, which modify the continuum problem by introducing an "internal length" parameter. The use of non-local models poses additional difficulties. Their implementation in finite element packages is not straightforward, requiring the development of an appropriate user-defined finite element. Furthermore, the value of the "internal length" parameter determines the width of the *shear band*, while its calibration still remains an open issue.

On the other hand, simulation of material strain-softening with local constitutive models and negligible mesh dependency is feasible with the use of a proper computational framework. Cervera et al. (2003, 2004) demonstrated that mesh dependency effects in localisation problems are not attributed exclusively on the local nature of the constitutive model rather than to spurious pressure oscillations (Fig. 1.2). To mitigate numerical convergence difficulties, they suggested the use of mixed pressure/displacement finite element formulation (so called "hybrid") to satisfy the isochoric plastic deformations of J_2-flow theory in combination with the so-called "fracture energy regularisation technique" (also referred to as "smeared band approach"), to ensure that dissipated energy during ductile fracture is properly scaled with the element size. Using this computational framework, Cervera et al. (2004); Cervera and Chiumenti (2009) implemented linear/exponential softening functions to simulate the mechanical response of benchmark problems, and the results were free of mesh dependency. In a follow up paper by the same authors [Cervera and Chiumenti (2006)], the isotropic Rankine damage model was also implemented, while more elaborate mixed finite element formulations were presented in [Cervera et al. (2010b,a, 2015)]. It should be noticed that the studies in [Cervera et al. (2003, 2004); Cervera and Chiumenti (2006, 2009); Cervera et al.

(2010b,a, 2015)] focused on monotonic loading conditions, while the numerical results obtained with the proposed simulation methodology were not validated with respect to physical experimental data.

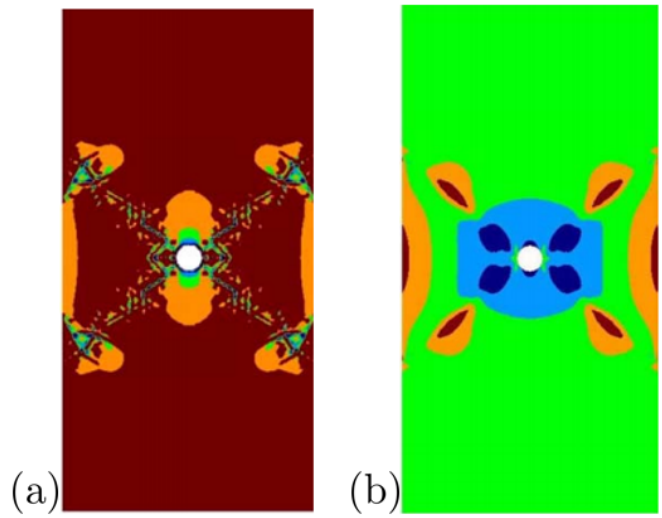

Figure 1.2: Perforated strip specimen subjected to axial loading. Pressure profile observed using (a) standard and (b) mixed ("hybrid") finite elements [Cervera et al. (2004)].

1.2.2.4 Discussion on simulation of cyclic plasticity-damage

Overall, several efforts have been reported on the numerical implementation of coupled cyclic plasticity-damage models in an implicit manner [Doghri (1995); Lemaitre and Desmorat (2005); Bonora et al. (2014)]. However, the corresponding numerical schemes have been limited to specific hardening rules or damage models, while the resulting integration schemes and consistent linearisation methodologies are subject to further optimisation for large-scale computations. Furthermore, the proposed numerical schemes and the corresponding simulation methodologies are validated against small-scale material tests or benchmark problems. This validation approach sets some questions regarding the ability of the proposed numerical schemes to predict low-cycle fatigue failure of large-scale structural components. Therefore, the numerical simulation of low-cycle fatigue on metal components is examined in

the present Thesis, using robust numerical models with emphasis on constitutive modelling.

1.2.3 Low-cycle fatigue of tubular welded X-joints

Welded tubular joints are considered critical structural components of offshore platforms. In particular, their fatigue performance is strongly influenced by the magnitude of the applied cyclic loading. Fatigue failures, which are attributed to repeated loading at relatively low stress amplitude, are described as high-cycle fatigue and are associated with more than 10^4 load cycles [Bai and Jin (2016)]. On the other hand, under extreme cyclic loading, such as severe earthquakes or storm conditions, offshore structural systems and their components are subjected to repeated large inelastic strains. In those extreme cases, failure may occur under a small number of load cycles (less than 100) and is defined as "ultra low-cycle fatigue", referred to as ULCF. It has been shown experimentally that in welded tubular joints, subjected to repeated inelastic loading, crack initiation and propagation is very fast, leading to stiffness and strength degradation after a relatively small number of cycles [Skallerud (1992)]. Despite the large number of published work on the high-cycle fatigue of welded tubular joints, the low-cycle fatigue behaviour of such joints has received substantially less attention. Experimental results concerning ultra low-cycle fatigue tests have been reported in several publications [Nip et al. (2010); Weigand and Berman (2012); Dong et al. (2014)] but those tests concern small-scale specimens which may not be able to represent the multi-axial state of stress in welded tubular joints. On the other hand, low-cycle fatigue tests on welded tubular joints have been quite limited, especially for the ULCF regime. An early experimental study concerning tubular X-joints was reported by Baba et al. (1981). Welded specimens were tested under low-cycle fatigue loading in an attempt to correlate the induced hot-spot stress range with the number of cycles to failure. The impact of welding defects, size effects and residual stresses was also examined. Experimental results on the ultra low-cycle fatigue performance of tubular welded joints were also reported by

Tremblay et al. (2003) and a few years later by Li et al. (2014). Both investigations [Tremblay et al. (2003); Li et al. (2014)] focused on relatively slender bracing connections, and low-cycle failure was attributed to elastoplastic buckling upon repeated loading. Thorough investigations on low-cycle fatigue of steel welded joints have been presented in [Vegte et al. (1989); Health and Safety Executive (2004)], analysing a large set of experimental data. The studies reported that thickness effects are less pronounced in low-cycle fatigue in comparison to high-cycle fatigue, while a lower mean slope is observed in the $logS - logN$ plot. Additional experimental data were published by Skallerud et al. (1995) and Scavuzzo et al. (1998) concerning the low-cycle fatigue performance of tubular welded components. More specifically, Skallerud et al. (1995) examined experimentally large-scale T-joints, fabricated from seamless tubes with yield strength of 360 MPa. Four specimens were tested under intense cyclic axial loading and failure occurred between 7 and 70 load cycles. The ultra low-cycle fatigue endurance was assessed in terms of hot-spot strains and the comparison with the AWS D.1.1-83 (1983) curves highlighted the conservativeness of the code. Scavuzzo et al. (1998) tested 29 carbon steel and 9 stainless steel butt-welded tubes under four-point cyclic bending, leading the specimens to failure within 200 - $2x10^6$ load cycles and providing further information regarding the transition between high-cycle and low-cycle fatigue. A unified design methodology, applicable to high-cycle fatigue and low-cycle fatigue, was recently proposed by Pei and Dong (2019) and Pei et al. (2019), suggesting the use of an equivalent structural strain parameter (ΔE) in combination with a master $\Delta E - N$ curve for assessing the fatigue life of a structural component. Alternatively, an energy-based approach has also been proposed for low-cycle fatigue, that relates the dissipated energy per load cycle to the number of cycles to failure [Fekete (2015); Shi et al. (2018)].

Design methodologies for high-cycle and low-cycle fatigue of regular steel welded joints have been established over the years [Itoga et al. (2003); Yildirim and Marquis (2012)]. On the other hand, less attention has been paid to the fatigue performance of welded tubular components made of high-strength steel material, especially for their

low-cycle fatigue behaviour and design [Health and Safety Executive (2004)]. Valuable experimental data concerning the low-cycle fatigue performance of high-strength steel tubular welded connections were reported in a series of publications by Waalen and Berge (2005), Boge et al. (2007) and Hochman et al. (2010). T-joints, fabricated from seamless tubes with yield strength of 500 MPa and chord diameter and thickness of 323.8 mm and 15.9 mm were tested under cyclic in-plane bending, out-of plane bending and axial loading, resulting in low-cycle fatigue failure between 3,000 and 200,000 loading cycles. The experimental results obtained from the three studies were compared with a large data-set and design provisions, and new $S-N$ curves were proposed for the low-cycle fatigue range corresponding to less than 10^5 load cycles. More recently, experimental data concerning welded tubular X-joints, with yield strength higher than 700 MPa, under strong cyclic loading, were presented by Varelis et al. (2016, 2020). The comparison of the experimental results with existing design provisions highlighted the conservative predictions of available design equations for the fatigue life of welded joints made of high-strength steel material within the low-cycle fatigue regime.

Drawing from the limited experimental data on the low-cycle fatigue performance of high-strength steel, an experimental campaign is conducted considering large-scale tubular X-joints. This work aims in providing additional data for establishing a design methodology for high-strength steel welded tubular joints exhibiting ultra low-cycle fatigue.

1.2.4 Summary

The topics discussed in Sections 1.2.1 - 1.2.3 are investigated in the Thesis with the purpose of contributing to the state of the art. The accurate simulation of multi-axial ratcheting in circular tubular components is examined in Chapter 2. A new numerical integration scheme is developed and it is validated against large-scale tests in tubular components. Next, the simulation of cyclic plasticity-damage response in metal alloys

is investigated in Section 3 using advanced numerical simulations with emphasis on constitutive modelling. Following, the experimental data reported from testing large-scale tubular welded connections and the supporting numerical simulation results are presented Chapter 4. The Thesis closes with the most important conclusions and recommendations for future work, discussed in Chapter 5.

Chapter 2

Numerical simulation of ratcheting in piping components

2.1 Introduction

The numerical simulation of multi-axial material ratcheting in steel circular tubular components subjected to cyclic inelastic loading is examined in the present Chapter. Material deterioration due to cyclic loading is neglected at this stage and emphasis is given to accurate prediction of plastic strain and its evolution using cyclic elastoplastic material models. The investigation is numerical, supported with corresponding experimental data wherever available.

A numerical scheme is developed for the implementation of an advanced cyclic plasticity model, suitable for simulating the mechanical response of thin-walled structures subjected to inelastic cyclic loading. The proposed numerical scheme is implemented

within the commercial finite element software ABAQUS (2016) as a material user subroutine and its efficiency and capabilities are demonstrated through the numerical analysis of large-scale cyclic bending experiments on steel pipe elbows. Following, the proposed numerical scheme is employed to investigate ratcheting collapse of high-strength stainless steel dented offshore pipelines subjected to cyclic axial loading.

2.2 Numerical implementation of an advanced ratcheting constitutive model

The development of an implicit numerical scheme for simulating multi-axial material ratcheting in metal components using advanced hardening rules is presented. In this way, a robust numerical tool is developed for analysing metal tubular components, as well as thin-walled structural components (with hollow or open section) under severe cyclic loading, associated with repeated inelastic response. The model is formulated specifically for plane stress conditions which are prompted for simulating tubular components while feature computational efficiency in comparison to 3D formulations.

The constitutive relations of the material model are formulated on the basis of J_2 *plane-stress projection* cyclic elastoplasticity model [Simo and Taylor (1986)] with mixed (isotropic and kinematic) nonlinear hardening. In particular, kinematic hardening is considered in a general form extending the one proposed by Bari and Hassan (2002) and allowing for integrating a wide range of cyclic-plasticity models reported in the literature. Constitutive relations are integrated implicitly, and incremental update of the internal variables is achieved through the solution of a single scalar equation, which is solved using a robust numerical solution method. Consistent linearisation of the integration algorithm is also provided in explicit form and the numerical integration methodology presented herein is more robust in comparison to the one reported by Rahman (2006). Furthermore, the accuracy of the proposed integration algorithm is examined by means of iso-error maps.

2.2.1 Constitutive relations

The constitutive relations are formulated explicitly for plane stress conditions using a *plane-stress projection* J_2 cyclic-plasticity model, considering nonlinear isotropic hardening and an advanced nonlinear kinematic hardening rule written in a general form, capable of representing a wide class of kinematic hardening models reported in the literature. Throughout the Chapter, tensors are denoted with boldface symbols, while the following relations apply between second-order tensors ($\boldsymbol{a}$, $\boldsymbol{b}$), fourth-order tensors ($\boldsymbol{M}$) and their Cartesian components a_{ij}, b_{ij}, M_{ijkl}.

$$\boldsymbol{a}\cdot\boldsymbol{b} = a_{ij}\, b_{ij}$$
$$\boldsymbol{M}\boldsymbol{a} = M_{ijkl}\, a_{kl}$$
$$\boldsymbol{a}\boldsymbol{M}\boldsymbol{b} = \boldsymbol{a}\cdot(\boldsymbol{M}\boldsymbol{b})$$

The strain tensor $\boldsymbol{\varepsilon}$ is additively decomposed to its elastic part $\boldsymbol{\varepsilon}^e$ and plastic part $\boldsymbol{\varepsilon}^p$ as

$$\boldsymbol{\varepsilon} = \boldsymbol{\varepsilon}^e + \boldsymbol{\varepsilon}^p \tag{2.1}$$

which are written in terms of their in-plane components as follows

$$\boldsymbol{\varepsilon} = \begin{bmatrix} \varepsilon_{11} & \varepsilon_{22} & 2\varepsilon_{12} \end{bmatrix}^t \quad \boldsymbol{\varepsilon}^p = \begin{bmatrix} \varepsilon^p_{11} & \varepsilon^p_{22} & 2\varepsilon^p_{12} \end{bmatrix}^t \tag{2.2}$$

It is underlined that the out-of-plane normal strain components ε_{33}, ε^e_{33} and ε^p_{33} are not necessarily zero but they are not explicitly considered in the formulation. These are treated as dependent variables, and are computed based on the plane stress constraints and the isochoric plastic flow conditions which, for an isotropic material, are defined as

$$\varepsilon^e_{33} = -\nu\,(\varepsilon^e_{11} + \varepsilon^e_{22})\,, \qquad \varepsilon^p_{33} = -\varepsilon^p_{11} - \varepsilon^p_{22} \tag{2.3}$$

where v is the Poisson's ratio. The constitutive model is formulated on the basis of hyper-elasticity. Starting from a free energy potential similar to those presented by Simo and Taylor (1986); Doghri (1993), the stress strain response is expressed through the isotropic elastic moduli as follows:

$$\boldsymbol{\sigma} = \boldsymbol{M}\boldsymbol{\varepsilon}^{e} = \boldsymbol{D}\left(\boldsymbol{\varepsilon} - \boldsymbol{\varepsilon}^{p}\right) \tag{2.4}$$

where $\boldsymbol{M}$ is the fourth-order elastic rigidity tensor, formulated for plane stress conditions and defined with two material constants for isotropic materials; the Poisson's ratio (v) and the Young's modulus (E). Limiting ourselves to small strain theory, the hyper-elastic and the hypo-elastic version of the model lead to identical numerical integration scheme.

Plane stress constraints require the out of plane components of the stress and the back-stress tensors to be equal to zero (i.e. $\sigma_{13} = \sigma_{23} = \sigma_{33} = 0$, $\alpha_{13} = \alpha_{23} = \alpha_{33} = 0$). Therefore, the Voigt notation of the stress and the backstress total tensors is defined as

$$\boldsymbol{\sigma} = \begin{bmatrix} \sigma_{11} & \sigma_{22} & \sigma_{12} \end{bmatrix}^{t} \tag{2.5}$$

$$\boldsymbol{\alpha} = \begin{bmatrix} \alpha_{11} & \alpha_{22} & \alpha_{12} \end{bmatrix}^{t} \tag{2.6}$$

whereas, considering Eq. (2.2), the projection matrix $\boldsymbol{P}$ is expressed as

$$\boldsymbol{P} = \frac{1}{3}\begin{bmatrix} 2 & -1 & 0 \\ -1 & 2 & 0 \\ 0 & 0 & 6 \end{bmatrix} \tag{2.7}$$

$\boldsymbol{s}, \boldsymbol{a'}$ are the deviatoric components of the stress and the backstress tensor, respectively. Components s_{33}, and a'_{33} are not necessarily zero but they are not explicitly considered. The kinematic hardening rule $\boldsymbol{\alpha}$ is written in terms of N backstress equations as

follows:

$$\boldsymbol{\alpha} = \sum_{i=1}^{N} \left(\boldsymbol{\alpha}^i\right) \quad \text{or,} \quad \boldsymbol{a}' = \sum_{i=1}^{N} \left(\boldsymbol{a}'^i\right) \tag{2.8}$$

Defining the second-order tensor $\boldsymbol{\xi}$ as

$$\boldsymbol{\xi} = \boldsymbol{\sigma} - \boldsymbol{\alpha} \tag{2.9}$$

the von-Mises yield criterion is expressed as follows [Simo and Taylor (1986)].

$$F(\boldsymbol{\sigma}, \boldsymbol{\alpha}, \varepsilon_q) = \frac{1}{2}\boldsymbol{\xi}\boldsymbol{P}\boldsymbol{\xi} - \frac{1}{3}k^2(\varepsilon_q) = 0 \tag{2.10}$$

or

$$F(\boldsymbol{\sigma}, \boldsymbol{\alpha}, \varepsilon_q) = \sqrt{\boldsymbol{\xi}\boldsymbol{P}\boldsymbol{\xi}} - \sqrt{\frac{2}{3}}k(\varepsilon_q) = 0 \tag{2.11}$$

where the equivalent plastic strain ε_q will be defined in the sequence. Using associative plasticity, the evolution of plastic strain is in the direction normal to the yield surface, so that

$$\dot{\boldsymbol{\varepsilon}}^p = \dot{\lambda}\frac{\partial F}{\partial \boldsymbol{\sigma}} \tag{2.12}$$

where $\dot{\lambda}$ is the plastic multiplier. Differentiating Eq. (2.10) one obtains

$$\dot{\boldsymbol{\varepsilon}}^p = \dot{\lambda}\boldsymbol{P}\boldsymbol{\xi} \tag{2.13}$$

Accordingly, the equivalent plastic strain rate, defined as follows,

$$\dot{\varepsilon}_q = \sqrt{\frac{2}{3}\dot{\boldsymbol{\varepsilon}}^p \cdot \dot{\boldsymbol{\varepsilon}}^p} \tag{2.14}$$

is equal to

$$\dot{\varepsilon}_q = \dot{\lambda}\sqrt{\frac{2}{3}}\bar{\Phi} \tag{2.15}$$

where scalar $\bar{\Phi}$ is readily computed as

$$\bar{\Phi} = \sqrt{\boldsymbol{\xi} \boldsymbol{P} \boldsymbol{\xi}} \tag{2.16}$$

The governing equation of the backstress tensor $\boldsymbol{\alpha}$ is presented in rate form in Eq. (2.17) and is obtained by modifying the kinematic hardening rule proposed by Bari and Hassan (2002).

$$\dot{\boldsymbol{a}}' = \sum_{i=1}^{N} C_i \dot{\boldsymbol{\varepsilon}}^p - \sum_{i=1}^{N} \left(\gamma_i \left[\boldsymbol{a}'^i \delta_i + (1-\delta_i)(\boldsymbol{a}'^i \cdot \boldsymbol{n}) \boldsymbol{n} \right] \chi_i \dot{\varepsilon}_q \right) \tag{2.17}$$

where in the present study, the second-order tensor $\boldsymbol{n}$ and the scalar χ_i are defined as

$$\boldsymbol{n} = \frac{\boldsymbol{P}\boldsymbol{\xi}}{\bar{\Phi}} \tag{2.18}$$

$$\chi_i = \left\langle 1 - \frac{\overline{a}^i}{\sqrt{\boldsymbol{\alpha}^i \boldsymbol{P} \boldsymbol{\alpha}^i}} \right\rangle \tag{2.19}$$

In Eq. (2.17), C_i and γ_i are the cyclic hardening parameters of the (i) backstress, δ_i is the mutli-axial ratcheting parameter of each backstress tensor, $\langle \cdot \rangle$ are the Macaulay brackets, and $\overline{a}_i$ is the so-called threshold term, which controls whether the recovery term of the (i) backstress is active. Eq. (2.17) is a generalisation of the hardening rule proposed by Bari and Hassan (2002), allowing intentionally for the consideration of multiple multi-axial ratcheting parameters (δ_i), and different $\overline{a}_i$ values for each backstress tensor. This modification is motivated by the work of Rahman et al. (2008), who argued that the use of different δ_i values for each backstress tensor may lead to more accurate simulation of multi-axial ratcheting. Furthermore, Table 2.1 shows that with the appropriate selection of C_i, γ_i, N, δ_i, $\overline{a}_i$, a wide range of hardening rules can be readily described.

Table 2.1: Available kinematic hardening rules.

Hardening rule	Required material parameters
Generic form	N, δ_i, $\overline{a}^i$, C_i, γ_i, $i = 1,2,...,N$
Armstrong and Frederick (1966)	$N = 1$, $\delta_1 = 1$, $\overline{a}^1 = 0$, C_1, γ_1
Bari and Hassan (2002)	$N = 4$, $\delta_i = \delta'$, $\overline{a}^{1-3} = 0$, $\overline{a}^4$, C_{1-4}, γ_{1-4}
Chaboche (1986)	N, $\delta_i = 1$, $\overline{a}^i = 0$, C_i, γ_i
Chaboche (1991)	$N = 4$, $\delta_i = 1$, $\overline{a}^{1-3} = 0$, $\overline{a}^4$, C_{1-4}, γ_{1-4}
Burlet and Cailletaud (1986)	$N = 1$, $\delta_1 = 0$, $\overline{a}^1 = 0$

Using Eqs. (2.13, 2.16-2.18), the backstress tensor is expressed in rate form as

$$\dot{\boldsymbol{\alpha}} = \sum_{i=1}^{N}(C_i)\dot{\lambda}\boldsymbol{\xi} - \sqrt{\frac{2}{3}}\dot{\lambda}\bar{\Phi}\sum_{i=1}^{N}(\gamma_i\delta_i\chi_i\boldsymbol{\alpha}_i) - \sqrt{\frac{2}{3}}\dot{\lambda}\left[\sum_{i=1}^{N}\left(\gamma_i(1-\delta_i)\chi_i\boldsymbol{\alpha}^i\right)\cdot\boldsymbol{n}\right]\boldsymbol{\xi} \quad (2.20)$$

where parameters C_i, γ_i, δ_i, $\overline{a}_i$ should be calibrated from appropriate cyclic material tests as proposed in [Bari and Hassan (2002); Rahman et al. (2008)]. The isotropic hardening function k refers to the evolution of the yield surface size and k is assumed to be a function of the equivalent plastic strain, $k \equiv k(\varepsilon_q)$.

Enforcing the consistency condition on the yield surface, one obtains

$$\dot{F}(\boldsymbol{\sigma},\boldsymbol{\alpha},\varepsilon_q) = \frac{\partial F}{\partial \boldsymbol{\sigma}}\dot{\boldsymbol{\sigma}} + \frac{\partial F}{\partial \boldsymbol{\alpha}}\dot{\boldsymbol{\alpha}} + \frac{\partial F}{\partial \varepsilon_q}\dot{\varepsilon}_q = 0 \quad (2.21)$$

Elaborating Eq. (2.21) and using the rate form of Eq. (2.4), the plastic multiplier $\dot{\lambda}$ can be expressed as

$$\dot{\lambda} = \frac{1}{h}\boldsymbol{\xi}\boldsymbol{P}\boldsymbol{M}\dot{\boldsymbol{\varepsilon}} \quad (2.22)$$

In Eq. (2.22), modulus h is a scalar quantity which is defined as

$$h = \boldsymbol{\xi}\boldsymbol{P}\boldsymbol{M}\boldsymbol{P}\boldsymbol{\xi} + \left[\sum_{i=1}^{N}(C_i) + \frac{2}{3}k'(\varepsilon_q) - \sqrt{\frac{2}{3}}\sum_{i=1}^{N}\left(\gamma_i(1-\delta_i)\chi_i\boldsymbol{\alpha}^i\right)\cdot\boldsymbol{n}\right]\bar{\Phi}^2 - \sqrt{\frac{2}{3}}\bar{\Phi}\boldsymbol{\xi}\boldsymbol{P}\sum_{i=1}^{N}\left(\gamma_i\delta_i\chi_i\boldsymbol{\alpha}^i\right) \tag{2.23}$$

In Eq. (2.23), the prime $(\cdot)'$ denotes differentiation of $(\cdot)$ with respect to ε_q. As shown in [Simo and Taylor (1986)], in an isotropic material matrices $\boldsymbol{P}$ and $\boldsymbol{M}$ have the same eigenvectors, which implies that these matrices commute, and therefore, it can be readily shown that $\boldsymbol{P}\boldsymbol{M} = \boldsymbol{M}\boldsymbol{P}$. Substituting Eq. (2.22) into the rate form of Eq. (2.4) one obtains

$$\dot{\boldsymbol{\sigma}} = \left(\boldsymbol{M} - \frac{1}{h}\boldsymbol{P}\boldsymbol{M}\boldsymbol{\xi}\otimes\boldsymbol{P}\boldsymbol{M}\boldsymbol{\xi}\right)\dot{\boldsymbol{\varepsilon}} \tag{2.24}$$

Hence,

$$\boldsymbol{M}_{ep} = \boldsymbol{M} - \frac{1}{h}\boldsymbol{P}\boldsymbol{M}\boldsymbol{\xi}\otimes\boldsymbol{P}\boldsymbol{M}\boldsymbol{\xi} \tag{2.25}$$

$\boldsymbol{M}_{ep}$ is a fourth-order symmetric tensor, expressing the continuum elastoplastic tangent operator moduli.

2.2.2 Implicit integration of the constitutive model

An implicit numerical integration scheme of the above constitutive model is developed, based on the Euler-backward integration technique. The methodologies presented in [Jetteur (1986); Simo and Taylor (1986)] for classical elastoplasticity are extended to the requirements of the present study. Starting with the internal variables ($\boldsymbol{\sigma}_n$, $\boldsymbol{\alpha}_n$, $\boldsymbol{\varepsilon}^p_n$, $\varepsilon_{q,n}$) at the beginning of the current step t_n, the trial stresses $\boldsymbol{\sigma}^e$ are anticipated at

increment t_{n+1} considering a purely elastic behaviour.

$$\boldsymbol{\sigma}^e = \boldsymbol{M}\,(\boldsymbol{\varepsilon}_{n+1} - \boldsymbol{\varepsilon}_n^p) \tag{2.26}$$

If the elastic prediction violates the yield condition,

$$F(\boldsymbol{\sigma}^e, \boldsymbol{\alpha}_n, \varepsilon_{q,n}) = \frac{1}{2}\,(\boldsymbol{\sigma}^e - \boldsymbol{\alpha}_n)\,\boldsymbol{P}\,(\boldsymbol{\sigma}^e - \boldsymbol{\alpha}_n) - \frac{1}{3}k^2(\varepsilon_{q,n}) > 0 \tag{2.27}$$

an elastoplastic corrector should be considered. Starting from Eq. (2.4), the stress-strain relation at the end of the increment can be evaluated using the Euler-backward integration scheme as follows:

$$\boldsymbol{\sigma}_{n+1} = \boldsymbol{M}\,(\boldsymbol{\varepsilon}_n^e + \Delta\boldsymbol{\varepsilon} - \Delta\boldsymbol{\varepsilon}^p) \tag{2.28}$$

The remaining internal variables are integrated over the step $[t_n;\, t_{n+1}]$ as shown in the following set of equations.

$$\boldsymbol{\xi}_{n+1} = \boldsymbol{\sigma}_{n+1} - \sum_{i=1}^{N} \left(\boldsymbol{\alpha}_{n+1}^i\right) \tag{2.29}$$

$$\bar{\Phi}_{n+1} = \sqrt{\boldsymbol{\xi}_{n+1}\boldsymbol{P}\boldsymbol{\xi}_{n+1}} \tag{2.30}$$

$$\boldsymbol{\varepsilon}_{n+1}^p = \boldsymbol{\varepsilon}_n^p + \Delta\lambda\boldsymbol{P}\boldsymbol{\xi}_{n+1} \tag{2.31}$$

$$\varepsilon_{q,n+1} = \varepsilon_{q,n} + \sqrt{\frac{2}{3}}\Delta\lambda\bar{\Phi}_{n+1} \tag{2.32}$$

Combining Eqs. (2.26, 2.28 2.31), the stress tensor $\boldsymbol{\sigma}_{n+1}$ can be redefined as

$$\boldsymbol{\sigma}_{n+1} = \boldsymbol{\sigma}^e - \Delta\lambda\boldsymbol{P}\boldsymbol{M}\boldsymbol{\xi}_{n+1} \tag{2.33}$$

The integration of the backstress tensor $\boldsymbol{\alpha}$ over the incremental step $[t_n;\ t_{n+1}]$ is achieved by integrating Eq. (2.17) for each backstress tensor separately. Denoting

$$\mu_i = 1 + \gamma_i \delta_i \chi_i \Delta\lambda \sqrt{\frac{2}{3}} \bar{\Phi}_{n+1} \tag{2.34}$$

$$\nu_i = 1 + \gamma_i \chi_i \Delta\lambda \sqrt{\frac{2}{3}} \bar{\Phi}_{n+1} \tag{2.35}$$

the evolution equation for each backstress tensor $\boldsymbol{\alpha}^i_{n+1}$ is computed as

$$\mu_i \boldsymbol{\alpha}^i_{n+1} = \boldsymbol{\alpha}^i_n + C_i \Delta\lambda \boldsymbol{\xi}_{n+1} - \gamma_i (1-\delta_i) \chi_i (\boldsymbol{\alpha}^i_{n+1} \cdot \boldsymbol{n}_{n+1}) \Delta\lambda \sqrt{\frac{2}{3}} \boldsymbol{\xi}_{n+1} \tag{2.36}$$

Eq. (2.36) in its current form indicates that a closed form expression for tensor $\boldsymbol{\alpha}^i_{n+1}$ cannot be obtained due to the presence of the dot product $\boldsymbol{\alpha}^i_{n+1} \cdot \boldsymbol{n}_{n+1}$. To proceed further, both ends of Eq. (2.36) are multiplied by $\boldsymbol{n}_{n+1}$, and the scalar quantity (dot product) $\boldsymbol{\alpha}^i_{n+1} \cdot \boldsymbol{n}_{n+1}$ is computed as follows:

$$\boldsymbol{\alpha}^i_{n+1} \cdot \boldsymbol{n}_{n+1} = \frac{1}{\bar{\Phi}_{n+1}} \frac{\boldsymbol{\alpha}^i_n}{\nu_i} \boldsymbol{P} \boldsymbol{\xi}_{n+1} + \frac{C_i}{\nu_i} \Delta\lambda \bar{\Phi}_{n+1} \tag{2.37}$$

Using Eq. (2.37), the backstress tensor $\boldsymbol{\alpha}^i_{n+1}$ can be written in a straightforward manner. Extending Eqs. (2.34-2.37) to multiple backstresses, the total backstress tensor $\boldsymbol{\alpha}_{n+1}$ at step t_{n+1} is defined in Eq. (2.38) below.

$$\begin{aligned} \boldsymbol{\alpha}_{n+1} = & \sum_{i=1}^{N} \left(\frac{\boldsymbol{\alpha}^i_n}{\mu_i} \right) - \sqrt{\frac{2}{3}} \frac{\Delta\lambda}{\bar{\Phi}_{n+1}} \left[\sum_{i=1}^{N} \left(\frac{\gamma_i (1-\delta_i) \chi_i}{\mu_i \nu_i} \boldsymbol{\alpha}^i_n \right) \boldsymbol{P} \boldsymbol{\xi}_{n+1} \right] \boldsymbol{\xi}_{n+1} \\ & + \left[\sum_{i=1}^{N} \left(\frac{C_i}{\mu_i} \right) - \sqrt{\frac{2}{3}} \Delta\lambda \bar{\Phi}_{n+1} \sum_{i=1}^{N} \left(\frac{C_i \gamma_i (1-\delta_i) \chi_i}{\mu_i \nu_i} \right) \right] \Delta\lambda \boldsymbol{\xi}_{n+1} \end{aligned} \tag{2.38}$$

All terms in Eq. (2.38), including term χ_i, are integrated implicitly. Combining Eqs. (2.29, 2.33, 2.38), the second-order tensor $\boldsymbol{\xi}_{n+1}$ is expressed as

$$\begin{aligned}\boldsymbol{\xi}_{n+1} = \boldsymbol{\sigma}^e - \Delta\lambda \boldsymbol{P}\boldsymbol{M}\boldsymbol{\xi}_{n+1} - \sum_{i=1}^{N}\left(\frac{\boldsymbol{\alpha}_n^i}{\mu_i}\right) \\ - \sqrt{\frac{2}{3}}\frac{\Delta\lambda}{\bar{\Phi}_{n+1}}\left[\sum_{i=1}^{N}\left(\frac{\gamma_i(1-\delta_i)\chi_i}{\mu_i v_i}\boldsymbol{\alpha}_n^i\right)\boldsymbol{P}\boldsymbol{\xi}_{n+1}\right]\boldsymbol{\xi}_{n+1} \\ - \left[\sum_{i=1}^{N}\left(\frac{C_i}{\mu_i}\right) + \sqrt{\frac{2}{3}}\Delta\lambda\bar{\Phi}_{n+1}\sum_{i=1}^{N}\left(\frac{C_i\gamma_i(1-\delta_i)\chi_i}{\mu_i v_i}\right)\right]\Delta\lambda\boldsymbol{\xi}_{n+1}\end{aligned} \tag{2.39}$$

With a few extra mathematical manipulations in Eq. (2.39), $\boldsymbol{\xi}_{n+1}$ is computed as

$$\boldsymbol{\xi}_{n+1} = \frac{1}{1+\Delta\lambda\rho_1}\boldsymbol{\Xi}\boldsymbol{M}^{-1}\left[\boldsymbol{\sigma}^e - \sum_{i=1}^{N}\left(\frac{\boldsymbol{\alpha}_n^i}{\mu_i}\right)\right] \tag{2.40}$$

where the scalar quantity ρ_1 and the fourth-order tensor $\boldsymbol{\Xi}$ are defined as follows:

$$\boldsymbol{\Xi} = \left[\boldsymbol{M}^{-1} + \frac{\Delta\lambda}{1+\Delta\lambda\rho_1}\boldsymbol{P}\right]^{-1} \tag{2.41}$$

$$\begin{aligned}\rho_1 = \sum_{i=1}^{N}\left(\frac{C_i}{\mu_i}\right) + \sqrt{\frac{2}{3}}\frac{1}{\bar{\Phi}_{n+1}}\sum_{i=1}^{N}\left(\frac{\gamma_i(1-\delta_i)\chi_i}{\mu_i v_i}\boldsymbol{\alpha}_n^i\right)\boldsymbol{P}\boldsymbol{\xi}_{n+1} \\ + \sqrt{\frac{2}{3}}\Delta\lambda\bar{\Phi}_{n+1}\sum_{i=1}^{N}\left(\frac{C_i\gamma_i(1-\delta_i)\chi_i}{\mu_i v_i}\right)\end{aligned} \tag{2.42}$$

Finally, enforcing the von-Mises criterion at the end of the increment $t = t_{n+1}$ (consistency condition), it is required that the following equation is satisfied:

$$F(\boldsymbol{\sigma}_{n+1}, \boldsymbol{\alpha}_{n+1}, \varepsilon_{q,n+1}) = 0 \tag{2.43}$$

Equivalently

$$F_{n+1}(\Delta\lambda) \equiv \frac{1}{2}\boldsymbol{\xi}_{n+1}\boldsymbol{P}\boldsymbol{\xi}_{n+1} - \frac{1}{3}k^2(\varepsilon_{q,n+1}) = 0 \tag{2.44}$$

or

$$F_{n+1}(\Delta\lambda) \equiv \sqrt{\boldsymbol{\xi}_{n+1}\boldsymbol{P}\boldsymbol{\xi}_{n+1}} - \sqrt{\frac{2}{3}}k(\varepsilon_{q,n+1}) = 0 \tag{2.45}$$

Substituting Eq. (2.40) in Eqs. (2.44 or 2.45), a single scalar equation with respect to the plastic multiplier $\Delta\lambda$ is formed. Eq. (2.40) in its current form indicates that solving Eqs. (2.44 or 2.45) in terms of $\Delta\lambda$ requires extensive calculations and matrix inversion within the Newton's method. However, regardless of the complexity of the constitutive model employed herein, Eq. (2.45) can be simplified significantly and readily solved with an iterative Newton's method by extending the method proposed in [Simo and Taylor (1986)] for classical elastoplasticity to more elaborate models considered in the present study. This methodology is presented in detail in Section 2.2.3. The main feature of the present integration algorithm is that allows the implementation of a wide range of advanced hardening rules not yet available in leading commercial finite element software. Furthermore, in comparison to other numerical schemes proposed in the literature for plasticity models of similar fidelity [Aravas (1987); Hartmann et al. (1998); Ohno et al. (2013)], the return-mapping stage of the constitutive integration algorithm is reduced to the solution of a single scalar equation, increasing significantly its computational efficiency.

2.2.3 Newton's scheme of the integration algorithm

2.2.3.1 Evaluation of the consistency condition

The main challenge in implementing the proposed integration algorithm within the finite element environment concerns the efficient solution of the consistency condition (Eqs. 2.44 or 2.45). As mentioned in section 2.2.1, for an isotropic material the stress rigidity tensor $\boldsymbol{M}$ and the projection matrix $\boldsymbol{P}$ commute because they have the same

eigenvectors. In mathematical terms:

$$\boldsymbol{P} = \boldsymbol{Q}\boldsymbol{\Lambda}_P\boldsymbol{Q}^t \qquad \text{and} \qquad \boldsymbol{M} = \boldsymbol{Q}\boldsymbol{\Lambda}_D\boldsymbol{Q}^t \tag{2.46}$$

where $\boldsymbol{\Lambda}_P$, $\boldsymbol{\Lambda}_D$ and $\boldsymbol{Q}$ derive from the spectral decomposition of matrices $\boldsymbol{M}$ and $\boldsymbol{P}$, and represent the eigenvalues of each array and the normalised eigenvectors, respectively.

$$\boldsymbol{Q} = \frac{1}{\sqrt{2}}\begin{bmatrix} 1 & -1 & 0 \\ 1 & 1 & 0 \\ 0 & 0 & \sqrt{2} \end{bmatrix} \quad \boldsymbol{\Lambda}_P = \begin{bmatrix} \frac{1}{3} & 0 & 0 \\ 0 & 1 & 0 \\ 0 & 0 & 2 \end{bmatrix} \quad \boldsymbol{\Lambda}_D = \begin{bmatrix} \frac{E}{1-v} & 0 & 0 \\ 0 & 2G & 0 \\ 0 & 0 & G \end{bmatrix} \tag{2.47}$$

In Eq. (2.47), G is the only undefined material parameter and corresponds to the shear modulus of the isotropic material. A new second-order tensor $\boldsymbol{\eta}$ is introduced, which is defined as

$$\boldsymbol{\eta} = \boldsymbol{Q}^t\boldsymbol{\xi}, \quad \boldsymbol{\eta}_{n+1} = \frac{1}{\sqrt{2}}\begin{bmatrix} \xi^{11}_{n+1} + \xi^{22}_{n+1} \\ -\xi^{11}_{n+1} + \xi^{22}_{n+1} \\ \sqrt{2}\xi^{12}_{n+1} \end{bmatrix} \tag{2.48}$$

By multiplying both parts of Eq. (2.40) by $\boldsymbol{Q}^t$, the internal variables at state t_{n+1} can be expressed with respect to the trial anticipated values as

$$\boldsymbol{\eta}_{n+1} = \left[(1+\Delta\lambda\rho_1)\boldsymbol{I} + \Delta\lambda\boldsymbol{\Lambda}_P\boldsymbol{\Lambda}_D\right]^{-1}\boldsymbol{\eta}^e = \boldsymbol{\Gamma}\boldsymbol{\eta}^e \tag{2.49}$$

where $\boldsymbol{I}$ is the 3×3 identity matrix and the scalar ρ_1 has been presented in Eq. (2.42). Eq. (2.49) shows that $\boldsymbol{\Gamma}$ represents an invertible 3×3 diagonal matrix which can be readily computed as

$$\boldsymbol{\Gamma} = Diag\left[\frac{1}{1+\Delta\lambda\left(\rho_1 + \frac{E}{3(1-v)}\right)}, \frac{1}{1+\Delta\lambda\left(\rho_1+2G\right)}, \frac{1}{1+\Delta\lambda\left(\rho_1+2G\right)}\right] \tag{2.50}$$

Furthermore, the tensor $\boldsymbol{\eta}^e = \begin{bmatrix} \eta^e_{11} & \eta^e_{22} & \eta^e_{12} \end{bmatrix}$ is expressed with respect to the trial stress tensor $\boldsymbol{\sigma}^e$ and the backstress tensor $\boldsymbol{\alpha}_n$ as

$$\begin{aligned}
\eta^e_{11} &= \frac{1}{\sqrt{2}}\left[\sigma^e_{11} + \sigma^e_{22} - \sum_{i=1}^{N}\left(\frac{\alpha^i_{n,11} + \alpha^i_{n,22}}{\mu_i}\right)\right] \\
\eta^e_{22} &= \frac{1}{\sqrt{2}}\left[\sigma^e_{22} - \sigma^e_{11} - \sum_{i=1}^{N}\left(\frac{\alpha^i_{n,22} - \alpha^i_{n,11}}{\mu_i}\right)\right] \\
\eta^e_{12} &= \sigma^e_{12} - \sum_{i=1}^{N}\left(\frac{\alpha^i_{n,12}}{\mu_i}\right)
\end{aligned} \tag{2.51}$$

where the scalar μ_i has been introduced in Eq. (2.34). With the aid of Eqs. (2.49-2.51), the term $\bar{\Phi}_{n+1}$ can be computed as

$$\bar{\Phi}_{n+1} = \sqrt{\boldsymbol{\xi}_{n+1}\boldsymbol{P}\boldsymbol{\xi}_{n+1}} = \sqrt{\boldsymbol{\eta}_{n+1}\boldsymbol{\Lambda}_P\boldsymbol{\eta}_{n+1}} = \sqrt{\frac{1}{3}(\eta^{11}_{n+1})^2 + (\eta^{22}_{n+1})^2 + 2(\eta^{12}_{n+1})^2} \tag{2.52}$$

and the consistency condition presented in Eq. (2.45) takes the following simple form.

$$\begin{aligned}
F_{n+1}(\Delta\lambda) = &\sqrt{\frac{\left(\eta^e_{11}\right)^2}{3\left[1 + \Delta\lambda\left(\rho_1 + \frac{E}{3(1-\nu)}\right)\right]^2} + \frac{\left(\eta^e_{22}\right)^2 + 2\left(\eta^e_{12}\right)^2}{\left[1 + \Delta\lambda\left(\rho_1 + 2G\right)\right]^2}} \\
&- \sqrt{\frac{2}{3}}k\left(\varepsilon_{q,n} + \Delta\lambda\sqrt{\frac{2}{3}}\bar{\Phi}_{n+1}\right)
\end{aligned} \tag{2.53}$$

It can be shown that Eq. (2.53) decreases monotonically for $\Delta\lambda \in [0, \infty]$ and thus, it is ideally suited for a local iterative solution procedure employing Newton's solution method. The Newton's method requires the evaluation of the derivative $\dfrac{\partial F_{n+1}(\Delta\lambda)}{\partial\Delta\lambda}$, the computation of which may not be very straightforward due to complexity of the constitutive model at hand. The methodology for the evaluation of the derivative $\dfrac{\partial F_{n+1}(\Delta\lambda)}{\partial\Delta\lambda}$ is presented next.

2.2.3.2 Differentiation of the consistency condition

The derivative $\dfrac{\partial F_{n+1}(\Delta\lambda)}{\partial\Delta\lambda}$ is evaluated in the present section. Differentiating the consistency condition expressed in Eq. (2.45), the derivative of $F_{n+1}(\Delta\lambda)$ with respect to $\Delta\lambda$ is computed as

$$\frac{\partial F_{n+1}(\Delta\lambda)}{\partial\Delta\lambda} = \frac{1}{2\bar{\Phi}_{n+1}} d\eta - \frac{2}{3} k'_{n+1} \left(\bar{\Phi}_{n+1} + \frac{\Delta\lambda}{2\bar{\Phi}_{n+1}} d\eta \right) \tag{2.54}$$

where

$$d\eta = \frac{2}{3}\eta^{11}_{n+1}\eta^{11'}_{n+1} + 2\eta^{22}_{n+1}\eta^{22'}_{n+1} + 4\eta^{12}_{n+1}\eta^{12'}_{n+1} \tag{2.55}$$

and the prime $(\cdot)'$ indicates differentiation of $(\cdot)$ with respect to $\Delta\lambda$. The derivatives $\eta^{ij\,'}_{n+1}$ can be obtained by differentiating Eq. (2.49).

$$\begin{aligned}
\eta^{11'}_{n+1} &= \Gamma'_{11}\eta^{e}_{11} + \Gamma_{11}\eta^{e'}_{11} \\
\eta^{22'}_{n+1} &= \Gamma'_{22}\eta^{e}_{22} + \Gamma_{22}\eta^{e'}_{22} \\
\eta^{12'}_{n+1} &= \Gamma'_{22}\eta^{e}_{12} + \Gamma_{22}\eta^{e'}_{12} \quad (\Gamma_{22} \equiv \Gamma_{33})
\end{aligned} \tag{2.56}$$

where terms $\Gamma_{i,j}$ are the diagonal components of the fourth-order tensor $\mathbf{\Gamma}$, expressed in Eq. (2.50). The derivatives Γ'_{ij} are evaluated as

$$\begin{aligned}
\Gamma'_{11} &= -\Gamma^2_{11}\left[\rho_1 + \frac{E}{3(1-\nu)} + \Delta\lambda\rho'_1\right] \\
\Gamma'_{22} &= -\Gamma^2_{22}\left[\rho_1 + 2G + \Delta\lambda\rho'_1\right]
\end{aligned} \tag{2.57}$$

whereas the derivative ρ_1' can be obtained as follows by differentiating Eq. (2.42) with respect to $\Delta\lambda$:

$$\begin{aligned}\rho_1' = \frac{\partial}{\partial\Delta\lambda}\left\{\sum_{i=1}^{N}\left(\frac{C_i}{\mu_i}\right)\right\} + \sqrt{\frac{2}{3}}\frac{\partial}{\partial\Delta\lambda}\left\{\Delta\lambda\bar{\Phi}_{n+1}\sum_{i=1}^{N}\left(\frac{C_i\gamma_i(1-\delta_i)\chi_i}{\mu_i v_i}\right)\right\} \\ + \sqrt{\frac{2}{3}}\frac{\partial}{\partial\Delta\lambda}\left\{\frac{1}{\bar{\Phi}_{n+1}}\sum_{i=1}^{N}\left(\frac{\gamma_i(1-\delta_i)\chi_i}{\mu_i v_i}\boldsymbol{\alpha}_n^i\right)\boldsymbol{Q}\boldsymbol{\Lambda}_D\boldsymbol{\eta}_{n+1}\right\}\end{aligned} \tag{2.58}$$

Collecting the terms in Eq. (2.58), one may write

$$\rho_1' = A_1 + B_1 d\eta + \boldsymbol{R}\cdot\boldsymbol{\eta}_{n+1}' \tag{2.59}$$

where

$$\begin{aligned}A_1 &= \sqrt{\frac{2}{3}}\bar{\Phi}_{n+1}\left[\sum_{i=1}^{N}\left(\frac{C_i\gamma_i(1-\delta_i)\chi_i}{\mu_i v_i}\right) - \Delta\lambda\sum_{i=1}^{N}\left(\frac{C_i\gamma_i\delta_i\chi_i'}{\mu_i^2}\right) - \sum_{i=1}^{N}\left(\frac{C_i\gamma_i\delta_i\chi_i}{\mu_i^2}\right)\right] \\ &+ \sqrt{\frac{2}{3}}\Delta\lambda\bar{\Phi}_{n+1}\left(\frac{C_i\gamma_i(1-\delta_i)\chi_i'}{\mu_i v_i}\right) - \frac{2}{3}\Delta\lambda^2\bar{\Phi}_{n+1}^2\sum_{i=1}^{N}\left(\frac{C_i\gamma_i^2(1-\delta_i^2)\chi_i\chi_i'}{(\mu_i v_i)^2}\right) \\ &- \frac{2}{3}\Delta\lambda\bar{\Phi}_{n+1}^2\sum_{i=1}^{N}\left(\frac{C_i\gamma_i^2(1-\delta_i^2)\chi_i^2}{(\mu_i v_i)^2}\right) + \sqrt{\frac{2}{3}}\bar{\Phi}_{n+1}^{-1}\sum_{i=1}^{N}\left(\frac{\gamma_i(1-\delta_i)\chi_i'}{(\mu_i v_i)^2}\boldsymbol{\alpha}_n^i\right)\boldsymbol{Q}\boldsymbol{\Lambda}_D\boldsymbol{\eta}_{n+1} \\ &- \sqrt{\frac{32}{27}}\Delta\lambda^2\bar{\Phi}_{n+1}^3\left[\Delta\lambda\sum_{i=1}^{N}\left(\frac{C_i\gamma_i^3\delta_i(1-\delta_i)\chi_i^2\chi_i'}{(\mu_i v_i)^2}\right) + \sum_{i=1}^{N}\left(\frac{C_i\gamma_i^3\delta_i(1-\delta_i)\chi_i^3}{(\mu_i v_i)^2}\right)\right] \\ &- \frac{2}{3}\left[\Delta\lambda\sum_{i=1}^{N}\left(\frac{\gamma_i^2(1-\delta_i^2)\chi_i\chi_i'}{(\mu_i v_i)^2}\boldsymbol{\alpha}_n^i\right) + \sum_{i=1}^{N}\left(\frac{\gamma_i^2(1-\delta_i^2)\chi_i^2}{(\mu_i v_i)^2}\boldsymbol{\alpha}_n^i\right)\right]\boldsymbol{Q}\boldsymbol{\Lambda}_D\boldsymbol{\eta}_{n+1} \\ &- \sqrt{\frac{32}{27}}\Delta\lambda\bar{\Phi}_{n+1}\left[\Delta\lambda\sum_{i=1}^{N}\left(\frac{\gamma_i^3\delta_i(1-\delta_i)\chi_i^2\chi_i'}{(\mu_i v_i)^2}\boldsymbol{\alpha}_n^i\right)\right. \\ &\qquad\left. + \sum_{i=1}^{N}\left(\frac{\gamma_i^3\delta_i(1-\delta_i)\chi_i^3\chi_i'}{(\mu_i v_i)^2}\boldsymbol{\alpha}_n^i\right)\right]\boldsymbol{Q}\boldsymbol{\Lambda}_D\boldsymbol{\eta}_{n+1}\end{aligned} \tag{2.60}$$

$$
\begin{aligned}
B_1 = &-\sqrt{\frac{2}{3}}\frac{\Delta\lambda}{2\bar{\Phi}_{n+1}}\left[\sum_{i=1}^{N}\left(\frac{C_i\gamma_i\delta_i\chi_i}{\mu_i^2}\right)-\sum_{i=1}^{N}\left(\frac{C_i\gamma_i(1-\delta_i)\chi_i}{\mu_i v_i}\right)\right] \\
&-\frac{1}{3}\Delta\lambda^2\sum_{i=1}^{N}\left(\frac{C_i\gamma_i^2(1-\delta_i^2)\chi_i^2}{(\mu_i v_i)^2}\right)-\sqrt{\frac{8}{27}}\Delta\lambda^3\bar{\Phi}_{n+1}\sum_{i=1}^{N}\left(\frac{C_i\gamma_i^3\delta_i(1-\delta_i)\chi_i^3}{(\mu_i v_i)^2}\right) \\
&-\left[\sqrt{\frac{2}{3}}\frac{1}{2\bar{\Phi}_{n+1}^3}\sum_{i=1}^{N}\left(\frac{\gamma_i(1-\delta_i)\chi_i}{\mu_i v_i}\boldsymbol{\alpha}_n^i\right)+\frac{1}{3}\frac{\Delta\lambda}{\bar{\Phi}_{n+1}^2}\sum_{i=1}^{N}\left(\frac{\gamma_i^2(1-\delta_i^2)\chi_i^2}{(\mu_i v_i)^2}\boldsymbol{\alpha}_n^i\right)\right. \\
&\qquad\left.+\sqrt{\frac{8}{27}}\frac{\Delta\lambda^2}{\bar{\Phi}_{n+1}}\sum_{i=1}^{N}\left(\frac{\gamma_i^3\delta_i(1-\delta_i)\chi_i^3}{(\mu_i v_i)^2}\boldsymbol{\alpha}_n^i\right)\right]\boldsymbol{Q}\boldsymbol{\Lambda}_D\boldsymbol{\eta}_{n+1}
\end{aligned}
\tag{2.61}
$$

$$
\boldsymbol{R}=\sqrt{\frac{2}{3}}\frac{1}{\bar{\Phi}_{n+1}}\sum_{i=1}^{N}\left(\frac{\gamma_i(1-\delta_i)\chi_i}{\mu_i v_i}\boldsymbol{\alpha}_n^i\right)\boldsymbol{Q}\boldsymbol{\Lambda}_D \tag{2.62}
$$

In Eq. (2.60), the derivative χ_i' is computed as follows

$$
\chi_i'=\begin{cases}\dfrac{\overline{a}_i}{(\boldsymbol{\alpha}_{n+1}^i\boldsymbol{P}\boldsymbol{\alpha}_{n+1}^i)^{3/2}}\boldsymbol{\alpha}_{n+1}^i\boldsymbol{P}\boldsymbol{\alpha}'^i_{n+1}, & \text{if } \chi_i\neq 0\\ 0, & \text{if } \chi_i=0\end{cases} \tag{2.63}
$$

where $\boldsymbol{\alpha}'^i_{n+1}$ is the derivative of the backstress tensor with respect to $\Delta\lambda$. The derivative $\boldsymbol{\alpha}'^i_{n+1}$ may be computed analytically by differentiating Eq. (2.38) or numerically as shown in Eq. (2.64).

$$
\boldsymbol{\alpha}'^i_{n+1}=\frac{\boldsymbol{\alpha}_{n+1}^{i\,(k)}-\boldsymbol{\alpha}_{n+1}^{i\,(k-1)}}{\Delta\lambda^{(k)}-\Delta\lambda^{(k-1)}} \tag{2.64}
$$

where (k) denotes the current iteration within the Newton's scheme. Both methods for evaluating $\boldsymbol{\alpha}'^i_{n+1}$ are equally efficient. Furthermore, the derivatives $\eta_{ij}^{e'}$ are computed

as

$$
\begin{aligned}
\eta_{11}^{e'} =& \eta_{11}^{r} + \eta_{11}^{d} d\eta \\
\eta_{11}^{r} =& \sqrt{\frac{1}{3}}\bar{\Phi}_{n+1}\left[\sum_{i=1}^{N}\left(\frac{\gamma_i\delta_i\chi_i}{\mu_i^2}(\alpha_{n,11}^{i}+\alpha_{n,22}^{i})\right)\right. \\
&\left. + \Delta\lambda\sum_{i=1}^{N}\left(\frac{\gamma_i\delta_i\chi_i'}{\mu_i^2}(\alpha_{n,11}^{i}+\alpha_{n,22}^{i})\right)\right] \\
\eta_{11}^{d} =& \sqrt{\frac{1}{3}}\sum_{i=1}^{N}\left(\frac{\gamma_i\delta_i\chi_i}{\mu_i^2}(\alpha_{n,11}^{i}+\alpha_{n,22}^{i})\right)\frac{\Delta\lambda}{2\bar{\Phi}_{n+1}} \\
\eta_{22}^{e'} =& \eta_{22}^{r} + \eta_{22}^{d} d\eta \\
\eta_{22}^{r} =& \sqrt{\frac{1}{3}}\bar{\Phi}_{n+1}\left[\sum_{i=1}^{N}\left(\frac{\gamma_i\delta_i\chi_i}{\mu_i^2}(\alpha_{n,22}^{i}-\alpha_{n,11}^{i})\right)\right. \\
&\left. + \Delta\lambda\sum_{i=1}^{N}\left(\frac{\gamma_i\delta_i\chi_i'}{\mu_i^2}(\alpha_{n,22}^{i}-\alpha_{n,11}^{i})\right)\right] \\
\eta_{22}^{d} =& \sqrt{\frac{1}{3}}\sum_{i=1}^{N}\left(\frac{\gamma_i\delta_i\chi_i}{\mu_i^2}(\alpha_{n,22}^{i}-\alpha_{n,11}^{i})\right)\frac{\Delta\lambda}{2\bar{\Phi}_{n+1}} \\
\eta_{12}^{e'} =& \eta_{12}^{r} + \eta_{12}^{d} d\eta \\
\eta_{12}^{r} =& \sqrt{\frac{2}{3}}\bar{\Phi}_{n+1}\left[\sum_{i=1}^{N}\left(\frac{\gamma_i\delta_i\chi_i}{\mu_i^2}\alpha_{n,12}^{i}\right) + \Delta\lambda\sum_{i=1}^{N}\left(\frac{\gamma_i\delta_i\chi_i'}{\mu_i^2}\alpha_{n,12}^{i}\right)\right] \\
\eta_{12}^{d} =& \sqrt{\frac{2}{3}}\sum_{i=1}^{N}\left(\frac{\gamma_i\delta_i\chi_i}{\mu_i^2}\alpha_{n,12}^{i}\right)\frac{\Delta\lambda}{2\bar{\Phi}_{n+1}}
\end{aligned}
\tag{2.65}
$$

Substituting Eqs. (2.57-2.65) into Eq. (2.56), and after some mathematical manipulations, the terms $\boldsymbol{\eta}'_{n+1}$ can be expressed with respect to $d\eta$ as follows:

$$
\begin{aligned}
\eta_{n+1}^{11'} &= D_{11}^{r} + D_{11}^{d} d\eta + D_{11}^{\eta}(R_{22}\eta_{n+1}^{22'} + R_{12}\eta_{n+1}^{12'}) \\
\eta_{n+1}^{22'} &= D_{22}^{r} + D_{22}^{d} d\eta + D_{22}^{\eta}\eta_{n+1}^{12'} \\
\eta_{n+1}^{12'} &= D_{12}^{r} + D_{12}^{d} d\eta
\end{aligned}
\tag{2.66}
$$

with

$$
\begin{aligned}
D^r_{11} &= \frac{\Gamma_{11}\eta^r_{11} - \Gamma^2_{11}\eta^e_{11}\left(\rho_1 + \frac{E}{3(1-\nu)} + \Delta\lambda A_1\right)}{1+\Gamma^2_{11}\eta^e_{11}\Delta\lambda R_{11}} \\
D^d_{11} &= \frac{\Gamma_{11}\eta^d_{11} - \Gamma^2_{11}\eta^e_{11}\Delta\lambda B_1}{1+\Gamma^2_{11}\eta^e_{11}\Delta\lambda R_{11}} \\
D^\eta_{11} &= \frac{-\Gamma^2_{11}\eta^e_{11}\Delta\lambda}{1+\Gamma^2_{11}\eta^e_{11}\Delta\lambda R_{11}}
\end{aligned}
\tag{2.67}
$$

$$
\begin{aligned}
D^r_{22} &= \frac{\Gamma_{22}\eta^r_{22} - \Gamma^2_{22}\eta^e_{22}\left(\rho_1 + 2G + \Delta\lambda A_1 + \Delta\lambda R_{11}D^r_{11}\right)}{1+\Gamma^2_{22}\eta^e_{22}\Delta\lambda R_{22}\left(R_{11}D^\eta_{11}+1\right)} \\
D^d_{22} &= \frac{\Gamma_{22}\eta^d_{22} - \Gamma^2_{22}\eta^e_{22}\Delta\lambda\left(B_1 + R_{11}D^d_{11}\right)}{1+\Gamma^2_{22}\eta^e_{22}\Delta\lambda R_{22}\left(R_{11}D^\eta_{11}+1\right)} \\
D^\eta_{22} &= -\frac{\Gamma^2_{22}\eta^e_{22}\Delta\lambda R_{12}\left(R_{11}D^\eta_{11}+1\right)}{1+\Gamma^2_{22}\eta^e_{22}\Delta\lambda R_{22}\left(R_{11}D^\eta_{11}+1\right)}
\end{aligned}
\tag{2.68}
$$

$$
\begin{aligned}
D^r_{12} &= \frac{\Gamma_{22}\eta^r_{12} - \Gamma^2_{22}\eta^e_{12}\left[\rho_1 + 2G + \Delta\lambda\left(A_1 + R_{11}D^r_{11} + R_{22}(R_{11}D^\eta_{11}+1)D^r_{22}\right)\right]}{1+\Gamma^2_{22}\eta^e_{12}\Delta\lambda\left(R_{11}D^\eta_{11}+1\right)\left(R_{22}D^\eta_{22}+R12\right)} \\
D^d_{12} &= \frac{\Gamma_{22}\eta^d_{12} - \Gamma^2_{22}\eta^e_{12}\Delta\lambda\left[B_1 + R_{11}D^d_{11} + R_{22}(R_{11}D^\eta_{11}+1)D^d_{22}\right]}{1+\Gamma^2_{22}\eta^e_{12}\Delta\lambda\left(R_{11}D^\eta_{11}+1\right)\left(R_{22}D^\eta_{22}+R12\right)}
\end{aligned}
\tag{2.69}
$$

Setting

$$
\begin{aligned}
H^r_{22} &= D^r_{22} + D^\eta_{22}D^r_{12} \\
H^d_{22} &= D^d_{22} + D^\eta_{22}D^d_{12} \\
H^r_{11} &= D^r_{11} + D^\eta_{11}R_{22}H^r_{22} + D^\eta_{11}R_{12}D^r_{12} \\
H^d_{11} &= D^d_{11} + D^\eta_{11}R_{22}H^d_{22} + D^\eta_{11}R_{12}D^d_{12}
\end{aligned}
\tag{2.70}
$$

the second-order tensor $\boldsymbol{\eta}'_{n+1}$ is expressed in terms of a single unknown, $d\eta$, as follows:

$$\begin{aligned}
\eta^{11'}_{n+1} &= H^r_{11} + H^d_{11} d\eta \\
\eta^{22'}_{n+1} &= H^r_{22} + H^d_{22} d\eta \\
\eta^{12'}_{n+1} &= D^r_{12} + D^d_{12} d\eta
\end{aligned} \tag{2.71}$$

Substituting Eq. (2.71) in Eq. (2.55), $d\eta$ can be computed as

$$d\eta = \frac{\frac{2}{3}H^r_{11}\eta^{11}_{n+1} + 2H^r_{22}\eta^{22}_{n+1} + 4D^r_{12}\eta^{12}_{n+1}}{1 - \frac{2}{3}H^d_{11}\eta^{11}_{n+1} - 2H^d_{22}\eta^{22}_{n+1} - 4D^d_{12}\eta^{12}_{n+1}} \tag{2.72}$$

Once the value of $d\eta$ has been obtained, the derivative $\dfrac{\partial F_{n+1}(\Delta\lambda)}{\partial\Delta\lambda}$ can be readily evaluated using Eq. (2.54), and this is employed for the solution of $F_{n+1}(\Delta\lambda) = 0$. It should be clarified that within Newton's scheme, the scalar quantities ρ_1, μ_i and v_i are computed using the values of the internal variables obtained from the previous iterative step of the Newton's method. This is dictated by the complexity of the constitutive model. Nevertheless, this mathematical approach does not influence the performance of the algorithm, as convergence is achieved within limited iterations.

2.2.4 Accuracy assessment

The accuracy of the proposed numerical integration scheme is examined with the development of iso-error maps [Simo and Taylor (1986); Ohno et al. (2013); Krieg and Krieg (1977); Schreyer et al. (1979); Ortiz and Popov (1985); Hartmann and Haupt (1993)]. Towards this purpose, three points are considered on the initial yield surface. These points are shown in Fig. 2.1, labeled as "A", "B" and "C" and correspond to "uniaxial tension", "biaxial tension" and "pure shear" states of stress. Then, a sequence of strain increments is applied at each of these stress points using a strain tensor of the general form of $\boldsymbol{\Delta\varepsilon} = \begin{bmatrix} \Delta\varepsilon & \Delta\varepsilon & \Delta\gamma \end{bmatrix}$, and the integration algorithm presented in Sections 2.2.2 and 2.2.3 is employed to calculate the corresponding states of stress.

The accuracy of the calculation is assessed by computing the relative error e, expressed in Eq. (2.73):

$$e = \sqrt{\frac{(\boldsymbol{s}-\bar{\boldsymbol{s}})\cdot(\boldsymbol{s}-\bar{\boldsymbol{s}})}{\bar{\boldsymbol{s}}\cdot\bar{\boldsymbol{s}}}}\cdot 100\% \tag{2.73}$$

In Eq. (2.73), $\boldsymbol{s}$ is the deviatoric component of the stress tensor computed based on the prescribed $\boldsymbol{\Delta\varepsilon}$ with the use of a single integration step and $\bar{\boldsymbol{s}}$ is the stress component obtained after a sufficient number of steps, corresponding to the "exact" solution.

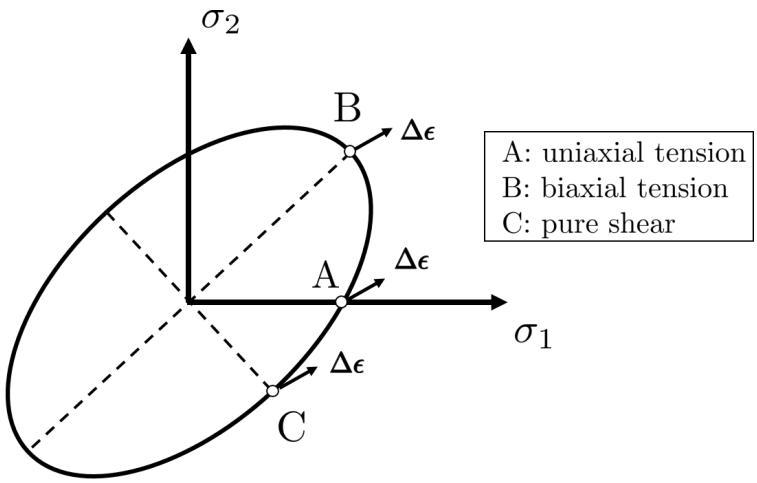

Figure 2.1: Points "A", "B", "C" in the yield surface, which are used for the development of the iso-error maps.

Iso-error maps are drawn using the hardening models proposed by Chaboche (1986) and Bari and Hassan (2002), referred to in the following as "*CH*" and "*BH*", respectively. The iso-error maps have also considered the material parameters presented in Table 2.4. These have been selected according to material tests on steel grade P355N, to be presented in detail in Section 2.3.3. In the iso-error analysis nonlinear isotropic hardening is considered and four backstress tensors are employed to simulate kinematic hardening [Chaboche (1991); Bari and Hassan (2002)].

The iso-error maps developed for points "A", "B" and "C" with the use of hardening models *CH* and *BH* are presented in Figs. (2.2-2.4). The values on the x and the y axes of Figs. (2.2-2.4) correspond to the normalised normal and shear strain increments,

and the normalisation parameters are $\varepsilon_y = \sigma_y/E$ and $\gamma_y = \sigma_y/(\sqrt{3}G)$.

The percentage error values reported with the use of both models show that for relatively small strain increments, the integration error increases proportionally with the applied strain amplitude, whereas for significantly large strain increments, the corresponding error decreases gradually. This behaviour is partly attributed to the fact that the stress tensor may not be parallel to the back-stress tensor. Clearly, for large strain amplitudes, the kinematic hardening is saturated, leading to lower numerical integration error.

The comparison of the results obtained through models *CH* and *BH* indicates that the integration error is within the same order of magnitude. More specifically, the percentage error values reported in Figs. (2.2-2.4) range between 0%-13%, and these error values are satisfactory in comparison to error values reported in other numerical integration schemes in the literature [e.g. Hartmann and Haupt (1993); Chaboche and Cailletaud (1996)].

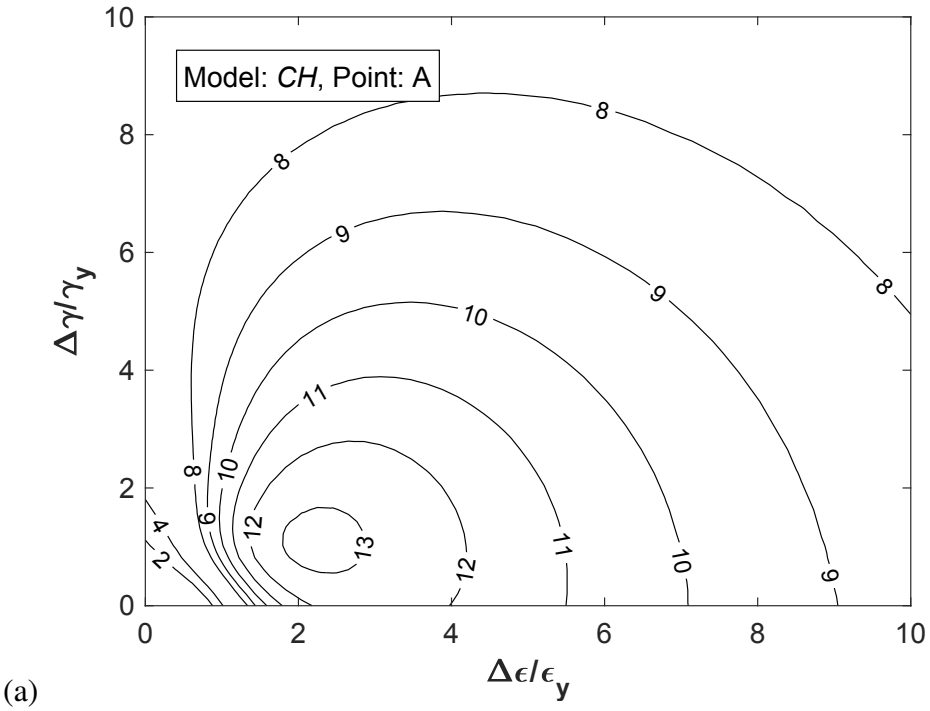

(a)

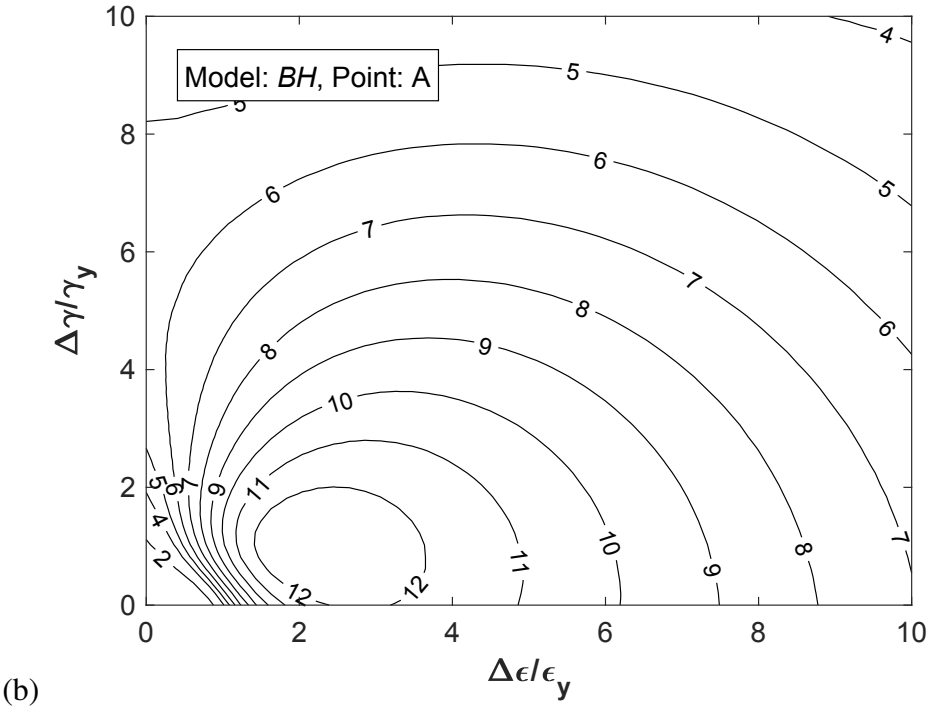

(b)

Figure 2.2: Iso-error maps developed for *CH* and *BH* hardening models, starting from point A on the yield surface (uniaxial tension).

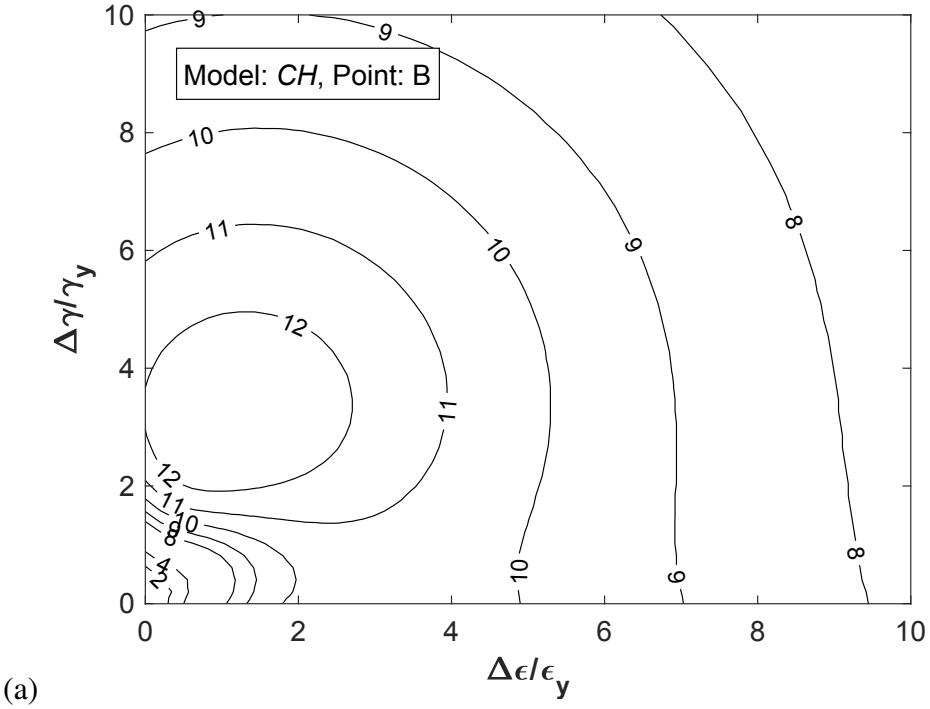

(a)

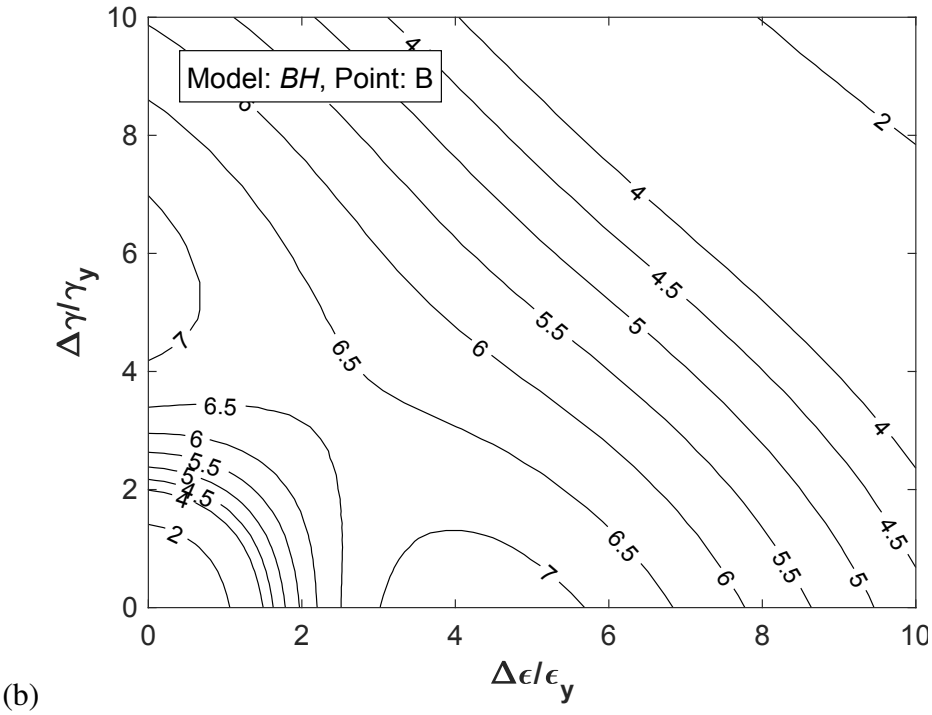

(b)

Figure 2.3: Iso-error maps developed for *CH* and *BH* hardening models, starting from point B on the yield surface (biaxial tension).

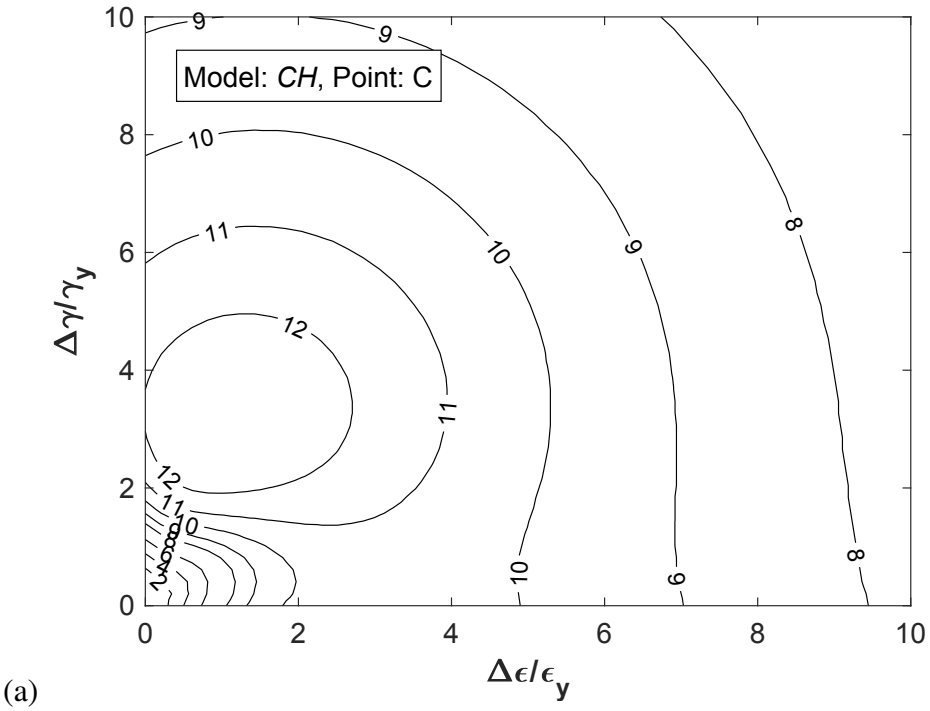

(a)

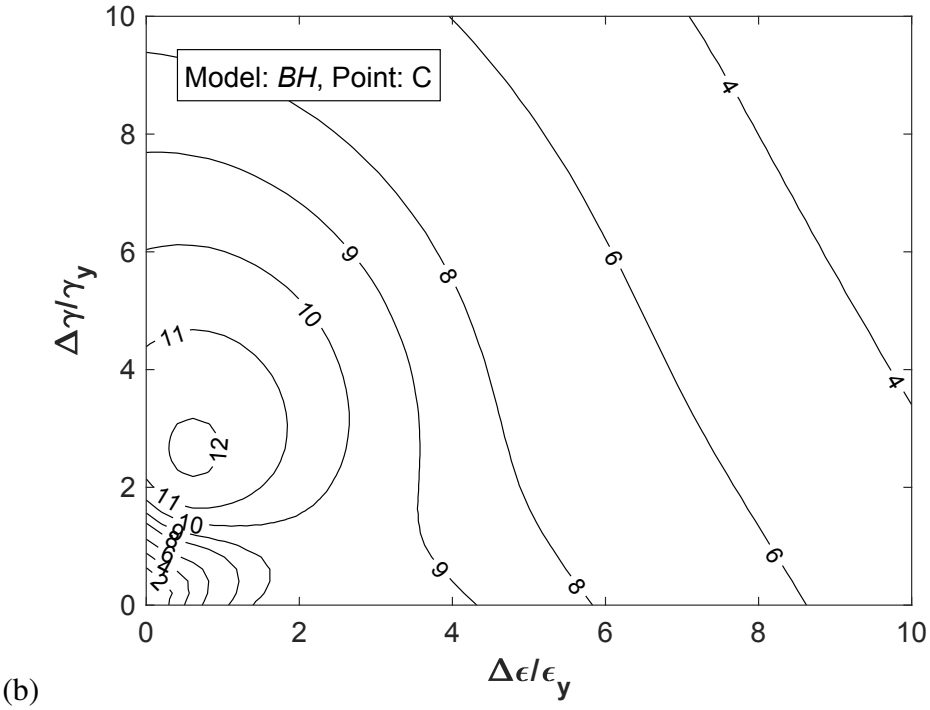

(b)

Figure 2.4: Iso-error maps developed for *CH* and *BH* hardening models, starting from point C on the yield surface (pure shear).

2.2.5 Consistent jacobian

An analytical derivation of the consistent tangent operator moduli is presented in this section, contributing to the robustness of the proposed numerical scheme used in the finite element environment. The methodology is thoroughly presented considering the generalised form of the kinematic hardening rule in Eq. (2.38). The proposed consistent moduli can be used for a wide range of kinematic hardening rules presented in Table 2.1 by adjusting properly the value of parameters N, C_i, γ_i, δ_i and χ_i. Differentiating Eq. (2.28) with respect to $\Delta\boldsymbol{\varepsilon}$ one obtains

$$\frac{\partial \boldsymbol{\sigma}_{n+1}}{\partial \Delta\boldsymbol{\varepsilon}} = \boldsymbol{M} - \boldsymbol{M}\frac{\partial \Delta\boldsymbol{\varepsilon}^{p}}{\partial \Delta\boldsymbol{\varepsilon}} \tag{2.74}$$

Differentiating Eqs. (2.29)-(2.32) with respect to $\Delta\boldsymbol{\varepsilon}$ the following derivatives are derived.

$$\frac{\partial \boldsymbol{\xi}_{n+1}}{\partial \Delta\boldsymbol{\varepsilon}} = \frac{\partial \boldsymbol{\sigma}_{n+1}}{\partial \Delta\boldsymbol{\varepsilon}} - \frac{\partial}{\partial \Delta\boldsymbol{\varepsilon}}\left\{\sum_{i=1}^{N}\boldsymbol{\alpha}^{i}_{n+1}\right\} \tag{2.75}$$

$$\frac{\partial \bar{\Phi}_{n+1}}{\partial \Delta\boldsymbol{\varepsilon}} = \frac{1}{\bar{\Phi}_{n+1}}\boldsymbol{\xi}_{n+1}\boldsymbol{P}\frac{\partial \boldsymbol{\xi}_{n+1}}{\partial \Delta\boldsymbol{\varepsilon}} \tag{2.76}$$

$$\frac{\partial \boldsymbol{\varepsilon}^{p}_{n+1}}{\partial \Delta\boldsymbol{\varepsilon}} = \boldsymbol{P}\boldsymbol{\xi}_{n+1} \otimes \frac{\partial \Delta\lambda}{\partial \Delta\boldsymbol{\varepsilon}} + \Delta\lambda\boldsymbol{P}\frac{\partial \boldsymbol{\xi}_{n+1}}{\partial \Delta\boldsymbol{\varepsilon}} \tag{2.77}$$

$$\frac{\partial \varepsilon_{q,n+1}}{\partial \Delta\boldsymbol{\varepsilon}} = \sqrt{\frac{2}{3}}\left(\bar{\Phi}_{n+1}\frac{\partial \Delta\lambda}{\partial \Delta\boldsymbol{\varepsilon}} + \Delta\lambda\frac{\partial \bar{\Phi}_{n+1}}{\partial \Delta\boldsymbol{\varepsilon}}\right) \tag{2.78}$$

In addition, the derivative $\dfrac{\partial \chi_i}{\partial \Delta\boldsymbol{\varepsilon}}$ is obtained as

$$\frac{\partial \chi_i}{\partial \Delta\boldsymbol{\varepsilon}} = \begin{cases} \dfrac{\overline{a}_i}{(\boldsymbol{\alpha}^{i}_{n+1}\boldsymbol{P}\boldsymbol{\alpha}^{i}_{n+1})^{3/2}}\boldsymbol{\alpha}^{i}_{n+1}\boldsymbol{P}\dfrac{\partial \boldsymbol{\alpha}^{i}_{n+1}}{\partial \Delta\boldsymbol{\varepsilon}}, & \text{if } \chi_i \neq 0 \\ \boldsymbol{0}, & \text{if } \chi_i = 0 \end{cases} \tag{2.79}$$

Consequently, Eq. (2.74) can be reformulated to

$$\frac{\partial \boldsymbol{\sigma}_{n+1}}{\partial \Delta \boldsymbol{\varepsilon}} = \boldsymbol{M} - \boldsymbol{P}\boldsymbol{M}\boldsymbol{\xi}_{n+1} \otimes \frac{\partial \Delta\lambda}{\partial \Delta \boldsymbol{\varepsilon}} - \Delta\lambda \boldsymbol{P}\boldsymbol{M} \frac{\partial \boldsymbol{\xi}_{n+1}}{\partial \Delta \boldsymbol{\varepsilon}} \tag{2.80}$$

Starting from Eq. (2.38), the derivate of backstress tensor $\boldsymbol{\alpha}_{n+1}$ at stage t_{n+1} with respect to $\Delta\boldsymbol{\varepsilon}$ is evaluated as

$$\begin{aligned}\frac{\partial \boldsymbol{\alpha}_{n+1}}{\partial \Delta \boldsymbol{\varepsilon}} =& \frac{\partial}{\partial \Delta \boldsymbol{\varepsilon}} \left\{ \sum_{i=1}^{N} \left(\frac{\boldsymbol{\alpha}_n^i}{\mu_i} \right) \right\} + \frac{\partial}{\partial \Delta \boldsymbol{\varepsilon}} \left\{ \sum_{i=1}^{N} \left(\frac{C_i}{\mu_i} \right) \Delta\lambda \boldsymbol{\xi}_{n+1} \right\} \\ & - \frac{\partial}{\partial \Delta \boldsymbol{\varepsilon}} \left\{ \sqrt{\frac{2}{3}} \frac{\Delta\lambda}{\bar{\Phi}_{n+1}} \left[\sum_{i=1}^{N} \left(\frac{\gamma_i (1 = \delta_i) \chi_i}{\mu_i v_i} \boldsymbol{\alpha}_n \right) \right] \boldsymbol{P}\boldsymbol{\xi}_{n+1} \right\} \\ & - \frac{\partial}{\partial \Delta \boldsymbol{\varepsilon}} \left\{ \sqrt{\frac{2}{3}} \Delta\lambda^2 \bar{\Phi}_{n+1} \sum_{i=1}^{N} \left(\frac{C_i \gamma_i (1-\delta_i) \chi_i}{\mu_i v_i} \right) \boldsymbol{\xi}_{n+1} \right\}\end{aligned} \tag{2.81}$$

Elaborating the terms in Eq. (2.81) and using Eqs. (2.75)-(2.79), the derivative $\dfrac{\partial \boldsymbol{\alpha}_{n+1}}{\partial \Delta \boldsymbol{\varepsilon}}$ can be written as

$$\begin{aligned}\frac{\partial \boldsymbol{\alpha}_{n+1}}{\partial \Delta \boldsymbol{\varepsilon}} =& \left[\sum_{i=1}^{N} \left(\frac{A_i^{\xi}}{A_i^{\star}} \right) \boldsymbol{\xi}_{n+1} + A^{a1} \sum_{i=1}^{N} \left(\frac{\gamma_i \delta_i \chi_i}{A_i^{\star} \mu_i^2} \boldsymbol{\alpha}_n^i \right) \right] \otimes \frac{\partial \Delta\lambda}{\partial \Delta \boldsymbol{\varepsilon}} + \sum_{i=1}^{N} \left(\frac{A_i^{d\xi}}{A_i^{\star}} \right) \frac{\partial \boldsymbol{\sigma}_{n+1}}{\partial \Delta \boldsymbol{\varepsilon}} \\ & + \left[A^{a2} \sum_{i=1}^{N} \left(\frac{\gamma_i^2 (1-\delta_i^2) \chi_i^2}{A_i^{\star} (\mu_i v_i)^2} \boldsymbol{\alpha}_n^i \right) + A^{a3} \sum_{i=1}^{N} \left(\frac{\gamma_i^3 \delta_i (1-\delta_i) \chi_i^3}{A_i^{\star} (\mu_i v_i)^2} \boldsymbol{\alpha}_n^i \right) \right] \otimes \frac{\partial \Delta\lambda}{\partial \Delta \boldsymbol{\varepsilon}}\end{aligned} \tag{2.82}$$

where $A_i^{\xi}, A^{a1}, A^{a2}, A^{a3}, A_i^{d\xi}$ and $A_i^{\star}$ are scalar quantities, expressed as

$$\begin{aligned}A_i^{\xi} =& \frac{C_i}{\mu_i} + \frac{2}{3} \Delta\lambda^2 \bar{\Phi}_{n+1}^2 \frac{C_i \gamma_i^2 (1-\delta_i^2) \chi_i^2}{(\mu_i v_i)^2} - \sqrt{\frac{2}{3}} \frac{1}{\bar{\Phi}_{n+1}} \left(\frac{\gamma_i (1-\delta_i) \chi_i}{\mu_i v_i} \boldsymbol{\alpha}_n^i \right) \boldsymbol{P}\boldsymbol{\xi}_{n+1} \\ & - \sqrt{\frac{2}{3}} \Delta\lambda \bar{\Phi}_{n+1} \left[\frac{C_i \gamma_i \delta_i \chi_i}{\mu_i^2} + 2 \frac{C_i \gamma_i (1-\delta_i) \chi_i}{\mu_i v_i} \right] + \sqrt{\frac{32}{27}} \Delta\lambda^3 \bar{\Phi}_{n+1}^3 \frac{C_i \gamma_i^3 \delta_i (1-\delta_i) \chi_i^3}{(\mu_i v_i)^2}\end{aligned} \tag{2.83}$$

$$A^{a1} = -\sqrt{\frac{2}{3}}\bar{\Phi}_{n+1} \tag{2.84}$$

$$A^{a2} = \frac{2}{3}\Delta\lambda\bar{\Phi}^2_{n+1} \tag{2.85}$$

$$A^{a3} = \sqrt{\frac{32}{27}}\Delta\lambda^2\bar{\Phi}^3_{n+1} \tag{2.86}$$

$$A^{\star}_i = 1 + A^{d\xi}_i + A^{d\alpha}_i \tag{2.87}$$

$$\begin{aligned} A^{d\alpha}_i =& \sqrt{\frac{2}{3}}\Delta\lambda\bar{\Phi}_{n+1}\overline{a}_i\frac{\boldsymbol{\alpha}^i_n\boldsymbol{P}\boldsymbol{\alpha}^i_{n+1}}{(\boldsymbol{\alpha}^i_{n+1}\boldsymbol{P}\boldsymbol{\alpha}^i_{n+1})^{3/2}}\left[\frac{\gamma_i\delta_i}{\mu_i^2} + \frac{\gamma_i(1-\delta_i)}{\mu_i v_i}\right. \\ & \left. - \sqrt{\frac{2}{3}}\Delta\lambda\bar{\Phi}_{n+1}\frac{\gamma_i^2(1-\delta_i^2)\chi_i}{(\mu_i v_i)^2} - \frac{4}{3}\Delta\lambda^2\bar{\Phi}^2_{n+1}\frac{\gamma_i^3\delta_i(1-\delta_i)\chi_i^2}{(\mu_i v_i)^2}\right] \\ & + \sqrt{\frac{2}{3}}\Delta\lambda^2\bar{\Phi}_{n+1}\overline{a}_i\frac{\boldsymbol{\xi}^i_{n+1}\boldsymbol{P}\boldsymbol{\alpha}^i_{n+1}}{(\boldsymbol{\alpha}^i_{n+1}\boldsymbol{P}\boldsymbol{\alpha}^i_{n+1})^{3/2}}\left[\frac{C_i\gamma_i\delta_i}{\mu_i^2} + \frac{C_i\gamma_i(1-\delta_i)}{\mu_i v_i}\right. \\ & \left. - \sqrt{\frac{2}{3}}\Delta\lambda\bar{\Phi}_{n+1}\frac{C_i\gamma_i^2(1-\delta_i^2)\chi_i}{(\mu_i v_i)^2} - \frac{4}{3}\Delta\lambda\bar{\Phi}^2_{n+1}\frac{C_i\gamma_i^3\delta_i(1-\delta_i)\chi_i^2}{(\mu_i v_i)^2}\right] \end{aligned} \tag{2.88}$$

$$\begin{aligned} A^{d\xi}_i =& \left[\frac{2}{3}\Delta\lambda^2\frac{\gamma_i^2(1-\delta_i^2)\chi_i^2}{(\mu_i v_i)^2}\boldsymbol{\alpha}^i_n - \sqrt{\frac{2}{3}}\frac{\Delta\lambda}{\bar{\Phi}_{n+1}}\frac{\gamma_i\delta_i\chi_i}{\mu_i^2}\boldsymbol{\alpha}^i_n\right]\boldsymbol{P}\boldsymbol{\xi}_{n+1} \\ & + \left[\sqrt{\frac{32}{27}}\Delta\lambda^3\bar{\Phi}_{n+1}\frac{\gamma_i^3\delta_i(1-\delta_i)\chi_i^3}{(\mu_i v_i)^2}\boldsymbol{\alpha}^i_n - \sqrt{\frac{2}{3}}\frac{\Delta\lambda}{\bar{\Phi}_{n+1}}\frac{\gamma_i(1-\delta_i)\chi_i}{\mu_i v_i}\boldsymbol{\alpha}^i_n\right]\boldsymbol{P}\boldsymbol{\xi}_{n+1} \\ & - \sqrt{\frac{8}{3}}\Delta\lambda^2\bar{\Phi}_{n+1}\frac{C_i\gamma_i(1-\delta_i)\chi_i}{\mu_i v_i} + \frac{2}{3}\Delta\lambda^3\bar{\Phi}^2_{n+1}\frac{C_i\gamma_i^2(1-\delta_i^2)\chi_i^2}{(\mu_i v_i)^2} \\ & + \sqrt{\frac{32}{27}}\Delta\lambda^4\bar{\Phi}^3_{n+1}\frac{C_i\gamma_i^3\delta_i(1-\delta_i)\chi_i^3}{(\mu_i v_i)^2} + \Delta\lambda\left[\frac{C_i}{\mu_i} - \sqrt{\frac{2}{3}}\Delta\lambda\bar{\Phi}_{n+1}\frac{C_i\gamma_i\delta_i\chi_i}{\mu_i^2}\right] \end{aligned} \tag{2.89}$$

Inserting Eq. (2.82) into Eq. (2.80), the derivative $\dfrac{\partial\boldsymbol{\sigma}_{n+1}}{\partial\Delta\boldsymbol{\varepsilon}}$ can be expressed with respect to a single unknown, $\dfrac{\partial\Delta\lambda}{\partial\Delta\boldsymbol{\varepsilon}}$.

$$\begin{aligned} \frac{\partial\boldsymbol{\sigma}_{n+1}}{\partial\Delta\boldsymbol{\varepsilon}} =& \boldsymbol{X} + \boldsymbol{X}\left[\left(\Delta\lambda\sum_i^N\left(\frac{A^{\xi}_i}{A^{\star}_i}\right) - 1\right)\boldsymbol{P}\boldsymbol{\xi}_{n1} + \Delta\lambda A^{a1}\boldsymbol{P}\sum_{i=1}^N\left(\frac{\gamma_i\delta_i\chi_i}{A^{\star}_i\mu_i^2}\boldsymbol{\alpha}^i_n\right)\right. \\ & \left.\Delta\lambda A^{a2}\boldsymbol{P}\sum_{i=1}^N\left(\frac{\gamma_i^2(1-\delta_i^2)\chi_i^2}{A^{\star}_i(\mu_i v_i)^2}\boldsymbol{\alpha}^i_n\right) + \Delta\lambda A^{a3}\boldsymbol{P}\sum_{i=1}^N\left(\frac{\gamma_i^3\delta_i(1-\delta_i)\chi_i^3}{A^{\star}_i(\mu_i v_i)^2}\boldsymbol{\alpha}^i_n\right)\right]\otimes\frac{\partial\Delta\lambda}{\partial\Delta\boldsymbol{\varepsilon}} \end{aligned} \tag{2.90}$$

where $\boldsymbol{X}$ is a fourth-order tensor, computed as

$$\mathbf{X} = \left[\boldsymbol{D}^{-1} + \Delta\lambda \left(1 - \sum_{i}^{N} \left(\frac{A_i^{d\xi}}{A_i^{\star}} \right) \right) \boldsymbol{P} \right]^{-1} \tag{2.91}$$

Substituting Eq. (2.82) and Eq. (2.90) into Eq. (2.75), the derivative $\frac{\partial \boldsymbol{\xi}_{n+1}}{\partial \Delta \boldsymbol{\varepsilon}}$ is redefined in terms of a single unknown, $\frac{\partial \Delta\lambda}{\partial \Delta \boldsymbol{\varepsilon}}$ as

$$\begin{aligned} \frac{\partial \boldsymbol{\xi}_{n+1}}{\partial \Delta \boldsymbol{\varepsilon}} = & \left[1 - \sum_{i=1}^{N} \left(\frac{A_i^{d\xi}}{A_i^{\star}} \right) \right] \frac{\partial \boldsymbol{\sigma}_{n+1}}{\partial \Delta \boldsymbol{\varepsilon}} - \left[\sum_{i=1}^{N} \left(\frac{A_i^{\xi}}{A_i^{\star}} \right) \boldsymbol{\xi}_{n+1} + A^{a1} \sum_{i=1}^{N} \left(\frac{\gamma_i \delta_i \chi_i}{A_i^{\star} \mu_i^2} \boldsymbol{\alpha}_n^i \right) \right. \\ & \left. + A^{a2} \sum_{i=1}^{N} \left(\frac{\gamma_i^2 (1-\delta_i^2) \chi_i^2}{A_i^{\star} (\mu_i v_i)^2} \boldsymbol{\alpha}_n^i \right) + A^{a3} \sum_{i=1}^{N} \left(\frac{\gamma_i^3 \delta_i (1-\delta_i) \chi_i^3}{A_i^{\star} (\mu_i v_i)^2} \boldsymbol{\alpha}_n^i \right) \right] \otimes \frac{\partial \Delta\lambda}{\partial \Delta \boldsymbol{\varepsilon}} \end{aligned} \tag{2.92}$$

Next, the derivative $\frac{\partial \Delta\lambda}{\partial \Delta \boldsymbol{\varepsilon}}$ is evaluated by differentiating the consistency condition. Differentiating Eq. (2.44) with respect to $\Delta\boldsymbol{\varepsilon}$ gives

$$\frac{\partial F_{n+1}}{\partial \Delta \boldsymbol{\varepsilon}} = \frac{\partial \bar{\Phi}_{n+1}}{\partial \Delta \boldsymbol{\varepsilon}} - \frac{2}{3} k' \left(\varepsilon_{q,n+1} \right) \left(\frac{\partial \Delta\lambda}{\partial \Delta \boldsymbol{\varepsilon}} \bar{\Phi}_{n+1} + \Delta\lambda \frac{\partial \bar{\Phi}_{n+1}}{\partial \Delta \boldsymbol{\varepsilon}} \right) = 0 \tag{2.93}$$

which can be simplified to the following expression.

$$\boldsymbol{\xi}_{n+1} \boldsymbol{P} \frac{\partial \boldsymbol{\xi}_{n+1}}{\partial \Delta \boldsymbol{\varepsilon}} = \frac{2}{3\theta} k' \left(\varepsilon_{q,n+1} \right) \bar{\Phi}_{n+1}^2 \frac{\partial \Delta\lambda}{\partial \Delta \boldsymbol{\varepsilon}} \tag{2.94}$$

by denoting

$$\theta = 1 - \frac{2}{3} k' \left(\varepsilon_{q,n+1} \right) \Delta\lambda \tag{2.95}$$

Substituting Eq. (2.92) in Eq. (2.94) and equilibrating the two ends, $\frac{\partial \Delta\lambda}{\partial \Delta \boldsymbol{\varepsilon}}$ is evaluated as follows.

$$\frac{\partial \Delta\lambda}{\partial \Delta \boldsymbol{\varepsilon}} = \frac{1 - \sum_{i}^{N} \left(\frac{A_i^{d\xi}}{A_i^{\star}} \right)}{H} \boldsymbol{\xi}_{n+1} \boldsymbol{P} \boldsymbol{X} \tag{2.96}$$

where modulus H is a scalar quantity expressed as

$$\begin{aligned} H = & \left[\sum_i^N \left(\frac{A_i^{d\xi}}{A_i^\star}\right) - 1\right]\left[\left(\delta\lambda \sum_i^N \left(\frac{A_i^{\xi}}{A_i^\star}\right) - 1\right)\boldsymbol{\xi}_{n+1}\boldsymbol{PXP}\boldsymbol{\xi}_{n+1}\right. \\ & + \Delta\lambda A^{a1}\boldsymbol{\xi}_{n+1}\boldsymbol{PXP}\sum_{i=1}^N \left(\frac{\gamma_i\delta_i\chi_i}{A_i^\star\mu_i^2}\boldsymbol{\alpha}_n^i\right) + \Delta\lambda A^{a2}\boldsymbol{\xi}_{n+1}\boldsymbol{PXP}\sum_{i=1}^N \left(\frac{\gamma_i^2(1-\delta_i^2)\chi_i^2}{A_i^\star(\mu_i v_i)^2}\boldsymbol{\alpha}_n^i\right) \\ & \left. + \Delta\lambda A^{a3}\boldsymbol{\xi}_{n+1}\boldsymbol{PXP}\sum_{i=1}^N \left(\frac{\gamma_i^3\delta_i(1-\delta_i)\chi_i^3}{A_i^\star(\mu_i v_i)^2}\boldsymbol{\alpha}_n^i\right)\right] + \sum_i^N \left(\frac{A_i^{\xi}}{A_i^\star}\right)\bar{\Phi}_{n+1}^2 \\ & + A^{a1}\boldsymbol{\xi}_{n+1}\boldsymbol{P}\sum_{i=1}^N \left(\frac{\gamma_i\delta_i\chi_i}{A_i^\star\mu_i^2}\boldsymbol{\alpha}_n^i\right) + A^{a2}\boldsymbol{\xi}_{n+1}\boldsymbol{P}\sum_{i=1}^N \left(\frac{\gamma_i^2(1-\delta_i^2)\chi_i^2}{A_i^\star(\mu_i v_i)^2}\boldsymbol{\alpha}_n^i\right) \\ & + A^{a3}\boldsymbol{\xi}_{n+1}\boldsymbol{P}\sum_{i=1}^N \left(\frac{\gamma_i^3\delta_i(1-\delta_i)\chi_i^3}{A_i^\star(\mu_i v_i)^2}\boldsymbol{\alpha}_n^i\right) + \frac{2}{3\theta}k'\left(\varepsilon_{q,n+1}\right)\bar{\Phi}_{n+1}^2 \end{aligned} \tag{2.97}$$

It can be readily shown that for $\Delta\lambda \to 0$, modulus H is identical to modulus h presented in Eq. (2.23). Finally, inserting Eq. (2.96) into Eq. (2.90), the consistent tangent moduli takes the following form.

$$\begin{aligned} \boldsymbol{M}_{ep}^L = & \boldsymbol{X} + \phi\boldsymbol{PX}\boldsymbol{\xi}_{n+1}\otimes\boldsymbol{PX}\boldsymbol{\xi}_{n+1} + \zeta\boldsymbol{PX}\sum_{i=1}^N \left(\frac{\gamma_i\delta_i\chi_i}{A_i^\star\mu_i^2}\boldsymbol{\alpha}_n^i\right)\otimes\boldsymbol{PX}\boldsymbol{\xi}_{n+1} \\ & + \psi\boldsymbol{PX}\sum_{i=1}^N \left(\frac{\gamma_i^2(1-\delta_i^2)\chi_i^2}{A_i^\star(\mu_i v_i)^2}\boldsymbol{\alpha}_n^i\right)\otimes\boldsymbol{PX}\boldsymbol{\xi}_{n+1} \\ & + \omega\boldsymbol{PX}\sum_{i=1}^N \left(\frac{\gamma_i^3\delta_i(1-\delta_i)\chi_i^3}{A_i^\star(\mu_i v_i)^2}\boldsymbol{\alpha}_n^i\right)\otimes\boldsymbol{PX}\boldsymbol{\xi}_{n+1} \end{aligned} \tag{2.98}$$

where

$$\phi = \frac{1-\sum_i^N \left(\frac{A_i^{d\xi}}{A_i^\star}\right)}{H}\left[\Delta\lambda\sum_i^N \left(\frac{A_i^{\xi}}{A_i^\star}\right) - 1\right] \tag{2.99}$$

$$\zeta = \Delta\lambda A^{a1}\frac{1-\sum_i^N \left(\frac{A_i^{d\xi}}{A_i^\star}\right)}{H} \tag{2.100}$$

$$\psi = \Delta\lambda A^{a2} \frac{1 - \sum_{i}^{N} \left(\frac{A_i^{d\xi}}{A_i^{\star}} \right)}{H} \tag{2.101}$$

$$\omega = \Delta\lambda A^{a3} \frac{1 - \sum_{i}^{N} \left(\frac{A_i^{d\xi}}{A_i^{\star}} \right)}{H} \tag{2.102}$$

In comparison with the continuum operator moduli $\boldsymbol{M}_{ep}$ in Eq. (2.25), the consistent tangent moduli $\boldsymbol{M}_{ep}^{L}$ are non-symmetric. It can be verified that Eq. (2.98) is consistent with the corresponding integration algorithm as for $\Delta\lambda \to 0$, the algorithmic moduli of Eq. (2.98) become equal to the tangent moduli presented in Eq. (2.25). Summarising the integration scheme and the consistent moduli presented in Sections 2.2.2, 2.2.3 and 2.2.5, the methodology for the solution of the incremental problem is presented in Table 2.2.

Table 2.2: Summary of the incremental solution procedure.

Elastic predictor	$\boldsymbol{\sigma}^e = \boldsymbol{D}\left(\boldsymbol{\varepsilon}_{n+1} - \boldsymbol{\varepsilon}_n^p\right)$
Check for yielding	$F(\boldsymbol{\sigma}^e, \boldsymbol{\alpha}_n, \varepsilon_{q,n})$
If $F \leqslant 0$ then set	$\boldsymbol{\sigma}_{n+1} = \boldsymbol{\sigma}^e$, $\boldsymbol{\alpha}_{n+1} = \boldsymbol{\alpha}_n$, $\boldsymbol{\varepsilon}_{n+1}^p = \boldsymbol{\varepsilon}_n^p$, $\varepsilon_{q,n+1} = \varepsilon_{q,n}$
If $F > 0$ elasto-plastic correction is necessary	
†Newton's scheme, set $\Delta\lambda = \Delta\lambda^0$ (initial guess, typically equal to 0.0)	
Compute μ_i, v_i	$\mu_i = 1 + \gamma_i\delta_i\chi_i\Delta\lambda\sqrt{\frac{2}{3}}\bar{\Phi}_{n+1}, \quad v_i = 1 + \gamma_i\chi_i\Delta\lambda\sqrt{\frac{2}{3}}\bar{\Phi}_{n+1}$
Compute ρ_1	$\rho_1 = \sum_{i=1}^N\left(\frac{C_i}{\mu_i}\right) + \sqrt{\frac{2}{3}}\frac{1}{\bar{\Phi}_{n+1}}\sum_{i=1}^N\left(\frac{\gamma_i(1-\delta_i)\chi_i}{\mu_i v_i}\boldsymbol{\alpha}_n^i\right)\boldsymbol{P}\boldsymbol{\xi}_{n+1}$ $+\sqrt{\frac{2}{3}}\Delta\lambda\bar{\Phi}_{n+1}\sum_{i=1}^N\left(\frac{C_i\gamma_i(1-\delta_i)\chi_i}{\mu_i v_i}\right)$
Compute $\boldsymbol{\Gamma}$	$\boldsymbol{\Gamma}$=Diag $\left[\frac{1}{1+\Delta\lambda\left(\rho_1+\frac{E}{3(1-\nu)}\right)}, \frac{1}{1+\Delta\lambda(\rho_1+2G)}, \frac{1}{1+\Delta\lambda(\rho_1+2G)}\right]$
Compute $\boldsymbol{\eta}^e$	$\boldsymbol{\eta}^e = \boldsymbol{Q}^t\left[\boldsymbol{\sigma}^e - \sum_{i=1}^N\left(\frac{\boldsymbol{\alpha}_n^i}{\mu_i}\right)\right]$
Compute $\boldsymbol{\eta}_{n+1}$	$\boldsymbol{\eta}_{n+1} = \boldsymbol{\Gamma}\boldsymbol{\eta}^e$
Compute $\bar{\Phi}_{n+1}$	$\bar{\Phi}_{n+1} = \sqrt{\boldsymbol{\xi}_{n+1}\boldsymbol{P}\boldsymbol{\xi}_{n+1}} = \sqrt{\boldsymbol{\eta}_{n+1}\boldsymbol{\Lambda}_P\boldsymbol{\eta}_{n+1}}$
Check equilibrium	$F_{n+1}(\Delta\lambda) = \bar{\Phi}_{n+1} - \sqrt{\frac{2}{3}}k\left(\varepsilon_n + \Delta\lambda\sqrt{\frac{2}{3}}\bar{\Phi}_{n+1}\right)$
Compute $F'(\Delta\lambda)$	$F'(\Delta\lambda) = \frac{\partial F(\Delta\lambda)}{\partial\Delta\lambda}$
Compute $d\Delta\lambda$	$d\Delta\lambda = \frac{F(\Delta\lambda)}{F'(\Delta\lambda)}$
Update $\Delta\lambda$	$\Delta\lambda = \Delta\lambda + d\Delta\lambda$
Check	$min\left\{\left\lvert\frac{d\Delta\lambda}{\Delta\lambda}\right\rvert, \lvert F(\Delta\lambda)\rvert\right\}$ <tolerance (e.g. 10^{-4}), if not satisfied, repeat
Update internal variables and evaluate $\boldsymbol{M}_{ep}^L$	
Update $\boldsymbol{\xi}_{n+1}$	$\boldsymbol{\xi}_{n+1} = \boldsymbol{Q}\boldsymbol{\eta}_{n+1}$
Update $\boldsymbol{\alpha}_{n+1}$	$\boldsymbol{\alpha}_{n+1} = \sum_{i=1}^N\left(\frac{\boldsymbol{\alpha}_n^i}{\mu_i}\right) - \sqrt{\frac{2}{3}}\frac{\Delta\lambda}{\bar{\Phi}_{n+1}}\left[\sum_{i=1}^N\left(\frac{\gamma_i(1-\delta_i)\chi_i}{\mu_i v_i}\boldsymbol{\alpha}_n^i\right)\boldsymbol{P}\boldsymbol{\xi}_{n+1}\right]\boldsymbol{\xi}_{n+1}$ $+\left[\sum_{i=1}^N\left(\frac{C_i}{\mu_i}\right) - \sqrt{\frac{2}{3}}\Delta\lambda\bar{\Phi}_{n+1}\sum_{i=1}^N\left(\frac{C_i\gamma_i(1-\delta_i)\chi_i}{\mu_i v_i}\right)\right]\Delta\lambda\boldsymbol{\xi}_{n+1}$
Update $\boldsymbol{\sigma}_{n+1}$	$\boldsymbol{\sigma}_{n+1} = \boldsymbol{\xi}_{n+1} + \boldsymbol{\alpha}_{n+1}$
Update $\boldsymbol{M}_{ep}^L$	$\boldsymbol{M}_{ep}^L = \boldsymbol{X} + \phi\boldsymbol{P}\boldsymbol{X}\boldsymbol{\xi}_{n+1}\otimes\boldsymbol{P}\boldsymbol{X}\boldsymbol{\xi}_{n+1} + \zeta\boldsymbol{P}\boldsymbol{X}\sum_{i=1}^N\left(\frac{\gamma_i\delta_i\chi_i}{A_i^\star\mu_i^2}\boldsymbol{\alpha}_n^i\right)\otimes\boldsymbol{P}\boldsymbol{X}\boldsymbol{\xi}_{n+1}$ $+\psi\boldsymbol{P}\boldsymbol{X}\sum_{i=1}^N\left(\frac{\gamma_i^2(1-\delta_i^2)\chi_i^2}{A_i^\star(\mu_i v_i)^2}\boldsymbol{\alpha}_n^i\right)\otimes\boldsymbol{P}\boldsymbol{X}\boldsymbol{\xi}_{n+1}$ $+\omega\boldsymbol{P}\boldsymbol{X}\sum_{i=1}^N\left(\frac{\gamma_i^3\delta_i(1-\delta_i)\chi_i^3}{A_i^\star(\mu_i v_i)^2}\boldsymbol{\alpha}_n^i\right)\otimes\boldsymbol{P}\boldsymbol{X}\boldsymbol{\xi}_{n+1}$

† Quantities μ_i, v_i, ρ_1 and χ_i are evaluated using the values of the internal variables obtained in the previous step of the Newton's scheme.

2.3 Validation of proposed numerical scheme against ratcheting experiments on pipe elbows

The numerical scheme presented in Section 2.2 is implemented within the finite element software ABAQUS (2016) as a material user subroutine. Following, it is employed to examine the capabilities of three advanced kinematic hardening rules in predicting the multi-axial ratcheting response measured in physical experiments. The kinematic hardening rules under consideration are calibrated based on the available cyclic material tests, and a set of large-scale experiments on steel pipe elbows subjected to strong cyclic loading [Pappa et al. (2012)] are simulated numerically. The efficiency of the hardening rules in predicting the mechanical behaviour of the pipe elbows is examined in terms of force-displacement response, local strain range and accumulation, and the corresponding cross-sectional ovalization.

2.3.1 Experimental program

The experiments under consideration have been conducted at Delft University of Technology in the course of a large European research project INDUSE [Pappa et al. (2012); Varelis et al. (2013); Varelis and Karamanos (2015)] on pipe elbows (also referred to as "bends"), a common mechanical component in industrial facilities that exhibits multi-axial ratcheting response under cyclic inelastic loading. The specimens consist of 8-inch diameter SCH40 long-radius induction bends with bend ratio of R/D = 1.5, where R is the radius of bend (328.65 mm), and D is the pipe diameter (219.1 mm). The pipe bends are welded to two straight pipes of length equal to five times the diameter (L = 1100 mm). The nominal outer diameter and thickness are equal to 219.1 mm and 8.18 mm, while the base material of the specimen is steel P355N according to BS EN 10216-1 (2013). Thickness measurements were conducted in each specimen prior to testing, indicating variations on the pipe bend thickness, which could be up to

25% higher than the nominal value, especially at the intrados area. A photograph of the experimental set-up is presented in Fig. 2.5. The ends of the straight pipes are capped with steel plates, welded on the specimen. The specimen is loaded through a horizontal hydraulic actuator connected to one end of the specimen with a hinge, while the other end is pin-supported to facilitate the displacement-control testing conditions. The pipe elbow specimens feature a characteristic example of multi-axial ratcheting response. Although tested under displacement-controlled conditions, they exhibit accumulation of plastic strain in both hoop and axial direction, attributed to the significant ovalization of the pipe bend cross-section.

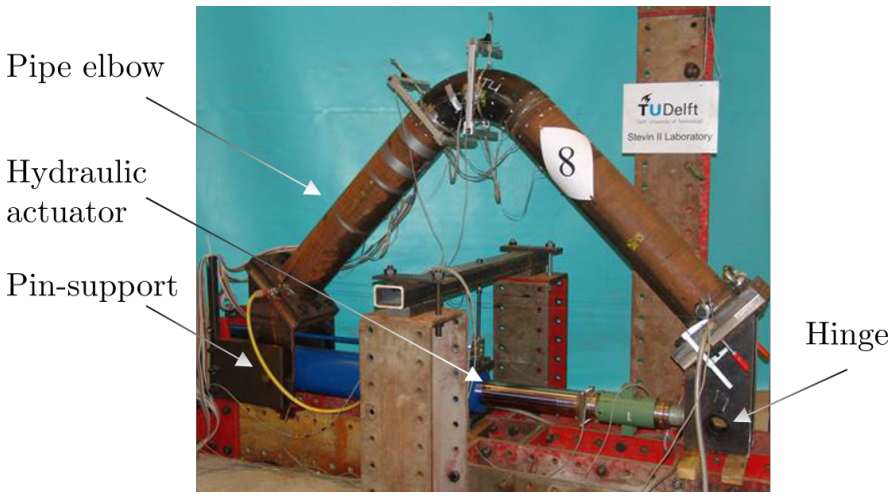

Figure 2.5: Experimental set-up of the elbow specimen [source: Pappa et al. (2012)].

The specimens are instrumented to record the cross-sectional ovalization at the bend and strains in the hoop and the axial direction. Axial strain measurements are examined at extrados and intrados locations where maximum values are expected. On the other hand, hoop strain is maximised at the elbow flank location where five strain gauges were attached as shown in Fig. 2.6. Strain gauge 5 is located exactly at the flank, while the distance between adjacent strain gauges is equal to 3 mm and 6 mm with respect to the axial and the hoop direction. The experimental campaign [Pappa et al. (2012)] consists of seven tests and the test conditions of each specimen are summarised in Table 2.3.

Table 2.3: Testing conditions.

Test	$E2$	$E3$	$E4$	$E5$	$E6$	$E7$	$E8$
Displacement amplitude (mm)	$\pm$ 70	$\pm$ 100	$\pm$ 150	$\pm$ 200	$\pm$ 250	$\pm$ 300	Increasing amplitude

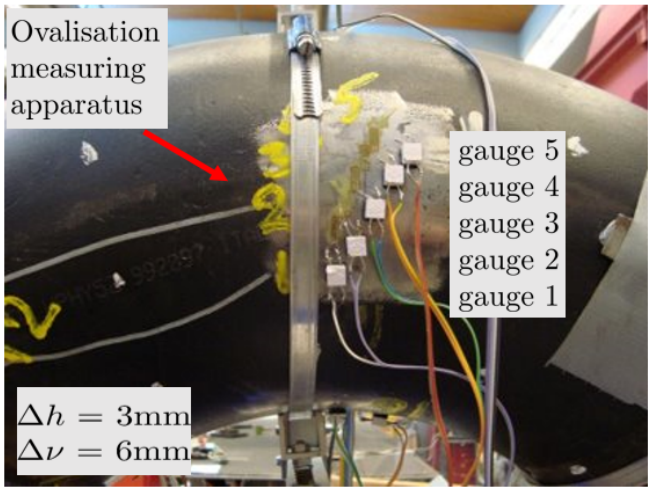

Figure 2.6: Location of strain gauges at elbow flank [source: Pappa et al. (2012)].

2.3.2 Finite element model

A finite element model, which employs the proposed numerical scheme through an appropriate material user-subroutine (UMAT) is developed in the finite element package ABAQUS (2016) to simulate the experimental procedure. The experimental set-up, presented in Fig. 2.5, is doubly symmetric and allows for modelling only 1/4 of the specimen with the use of the appropriate boundary conditions. Therefore, the finite element model employed (Fig. 2.7) consists of a straight tube connected through tie constraints with the half bend. It should be clarified that the weld geometry is not modelled as it would require the use of 3D elements and multiple coupling constraints. A preliminary numerical analysis showed that modelling of the weld geometry has a minimum impact on the results. The thickness measurements conducted on the specimens prior to testing indicated that the elbow is thicker than the straight pipe. This is taken into account in the finite element model by considering a thickness of

9.1 mm for the bend. In addition, a reference point, RP-1, is kinematically coupled with the edge nodes of the straight tube to simulate the roller support and the capping conditions applied during testing. Point RP-1 is free to rotate around the z axis, while the displacement with respect to x axis is prescribed and corresponds to the horizontal displacement applied during testing.

A preliminary sensitivity analysis has been conducted to identify an optimised mesh. The use of linear as well as high-order finite elements was examined, showing that both simulation methods do not suffer from locking phenomena. The results of the sensitivity study showed that 10 mm×10 mm linear 4-node finite elements (S4) with five integration points through the shell thickness are adequate for meshing the elbow bend. Furthermore, the straight pipe is meshed using a single bias meshing technique, and the element size varies from 10 mm×10 mm near the bend to 10 mm×30 mm at the capped end.

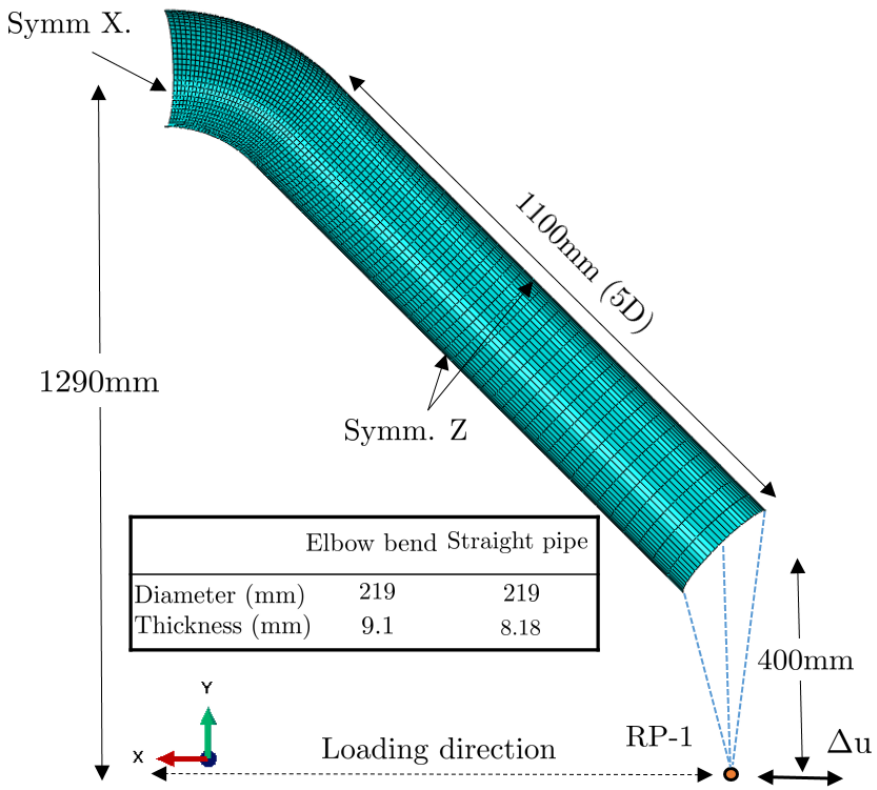

Figure 2.7: Meshed finite element model of the test specimen using plane stress (shell-type) elements.

2.3.3 Calibration of the constitutive models

The accuracy of the numerical predictions depends strongly on the proper calibration of the constitutive models. For this purpose, strip specimens (coupons) have been extracted from the longitudinal and the transverse direction of similar pipe bends (of the same heat) to examine the cyclic properties of the steel material P355N in the inelastic range. The strip specimens were tested under strain-controlled and stress-controlled conditions to investigate the cyclic hardening and the uni-axial ratcheting response of the steel material [Pappa et al. (2012)]. The experiments on strip specimens showed very similar stress-strain response for the coupons extracted from the longitudinal and the transverse direction, indicating an isotropic material.

In the present investigation, the capabilities of three advanced kinematic hardening rules are evaluated. The hardening parameters of the employed constitutive model are selected in accordance with Table 2.1 to describe the hardening rules proposed by Chaboche (1986), Chaboche (1991) and Bari and Hassan (2002). For simplicity the corresponding hardening rules are denoted as "*CH*", "*Mod. CH*" and "*BH*". Hardening models *CH* and *BH* have already been presented in Section 2.2.4 for the needs of the iso-error analysis. It is expected that the proposed constitutive model in its generic form (Table 2.1) may provide more accurate ratcheting predictions, but its calibration requires biaxial material test data which are not available herein. Therefore, we limit our investigation in these three hardening rules.

A sensitivity analysis has been performed with the purpose of identifying the best set of material parameters to fit the experimental data. In the *BH* model, multi-axial ratcheting experiments should be preferably used to calibrate the multi-axial ratcheting parameters δ_i [Bari and Hassan (2002); Rahman et al. (2008)], but such tests are not available in the present experimental program. In the present study, models *CH*, *Mod. CH* and *BH* are calibrated considering (a) the hysteresis response recorded from strain-controlled material tests at 2.2% strain amplitude, and (b) the

ratcheting response obtained from uni-axial ratcheting tests (stress-controlled tests) at a load ratio $R = -0.8$ associated with severe plastic reversal. Kinematic hardening is simulated using four backstress tensors as proposed in [Chaboche (1991); Bari and Hassan (2002)] and isotropic hardening is described with an exponential function with saturation $k(\varepsilon_q) = Q_\infty \left(1 - e^{-b\varepsilon_q}\right)$, where Q_∞ and b are the isotropic hardening parameters, defined from appropriate material tests. The selected material parameters are presented in Table 2.4.

The resulting stress-strain plots and the ratcheting results obtained from material tests and numerical simulations are presented in Figs. (2.8-2.9). In the strain-controlled response, shown in Fig. 2.8, all three hardening rules provide similar results and hence, a single line plot is used, denoted as "numerical" in Fig. 2.8. All three models are also capable of predicting quite accurately the stress-controlled tests within the first 100 load cycles as shown in Fig. 2.9. It should be noted that the ratcheting predictions of *Mod. CH* and *BH* models are almost identical because the effect of multi-axial ratcheting parameter δ is less evident under uni-axial loading conditions [Bari and Hassan (2002)].

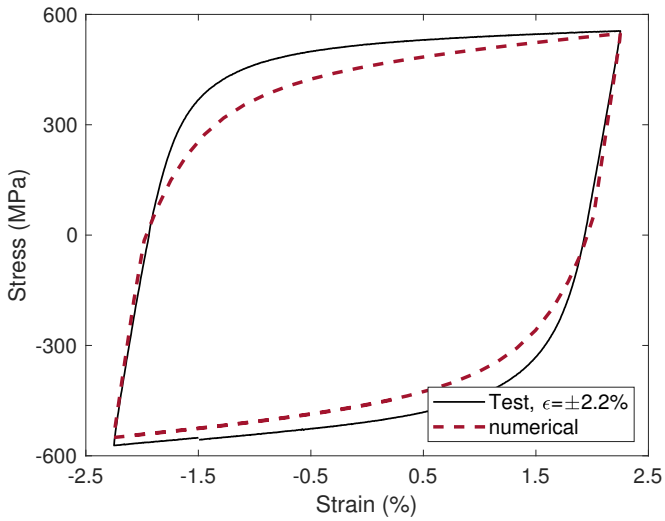

Figure 2.8: Stress-strain response obtained from strain-controlled material tests [strip specimens from 8-inch P355N, SCH40 bends Pappa et al. (2012)] and numerical simulations.

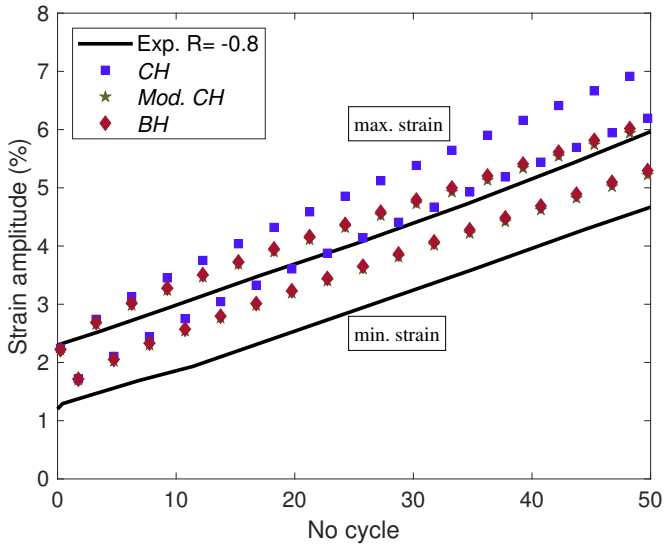

Figure 2.9: Maximum/minimum strain observed in stress-controlled material tests [strip specimens from 8-inch P355N, SCH40 bends Pappa et al. (2012)] at stress ratio R=-0.8 and numerical simulations.

Table 2.4: Material properties of constitutive model.

Model	E (MPa)	v	σ_y (MPa)	Q_∞ (MPa)	b	C_{1-4} (MPa)	γ_{1-4}	δ_i	$\overline{\alpha}^4$ (MPa)
CH	2×10^5	0.3	315	-50	80	45,000 11,500 6,000 2,700	650 200 190 15	1.0	0.0
Mod. CH	2×10^5	0.3	315	-50	80	45,000 11,500 6,000 2,700	650 200 190 15	1.0	10.0
BH	2×10^5	0.3	315	-50	80	45,000 11,500 6,000 2,700	650 200 190 15	0.85	15.0

2.3.4 Numerical simulation results

The experimental data obtained from the seven specimens ($E2$ - $E8$) are numerically simulated with the use of the finite element model presented in Section 2.3.2, equipped with the proposed numerical scheme, which is implemented as a material subroutine UMAT. The purpose of the simulations is to highlight the numerical efficiency of the proposed numerical scheme and demonstrate that elaborate hardening rules are required for simulating accurately multi-axial ratcheting in structural components subjected to cyclic inelastic loading. The accuracy of the numerical analyses is assessed with respect to experimental data in terms of force-displacement response, local strain amplitude and accumulation with respect to the loading cycles and local ovalization values at the elbow flank. The numerical analyses are limited to the first 50 cycles of the experiments, where experimental measurements are available. It is noted that after a substantial number of load cycles, subject to testing conditions, material degradation initiates and influences the mechanical response, leading to low-cycle fatigue. In this case, cyclic elastoplasticity constitutive models coupled with damage are required to simulate the response of the pipe elbow specimens, but such a formulation lays outside the scope of the present study.

From a computational standpoint, all numerical simulations were completed within less than two hours using a standard four-node Xeon Processor at 2.4Gh with 2GB Ram per node. Furthermore, additional analyses were conducted using ABAQUS (2016) built-in Chaboche (1986) cyclic plasticity model, and in all four cases (i.e. *CH*, *Mod. CH*, *BH* and ABAQUS) global convergence is achieved in 3 iterations per increment. The performance of the proposed algorithm has also been examined in terms of local convergence by computing the maximum number of local iterations required in each integration point of the model at every increment. The maximum number of local iterations within Newton's scheme, observed by scanning the entire model was less than 15, demonstrating the robustness of the proposed integration algorithm. Therefore, in addition to fast global convergence, local convergence is

also achieved in limited number of iterations. Comparison with the ABAQUS built-in model in terms of local convergence may not be available as such information is not provided to the user.

2.3.4.1 Force-displacement response

The accuracy of the numerical scheme equipped with the aforementioned advanced kinematic hardening rules is examined in terms of force-displacement response. The hysteresis response of experiments $E2$ - $E7$ and the force amplitude obtained from specimen $E8$, tested under increasing displacement amplitude, are presented in Figs, (2.10, 2.11). In terms of force-displacement response, the three hardening models provide negligible differences in their predictions and thus, a common plot is considered denoted as "numerical". It should be underlined that the additional features incorporated in the *Mod. CH* and *BH* hardening models may not affect significantly the global structural response, especially during the initial loading cycles where plastic strains are relatively low. The good comparison between experimental data and numerical predictions shows that the present numerical scheme is capable of simulating quite accurately the inelastic response of the pipe elbow specimens under large amplitude inelastic cyclic loading.

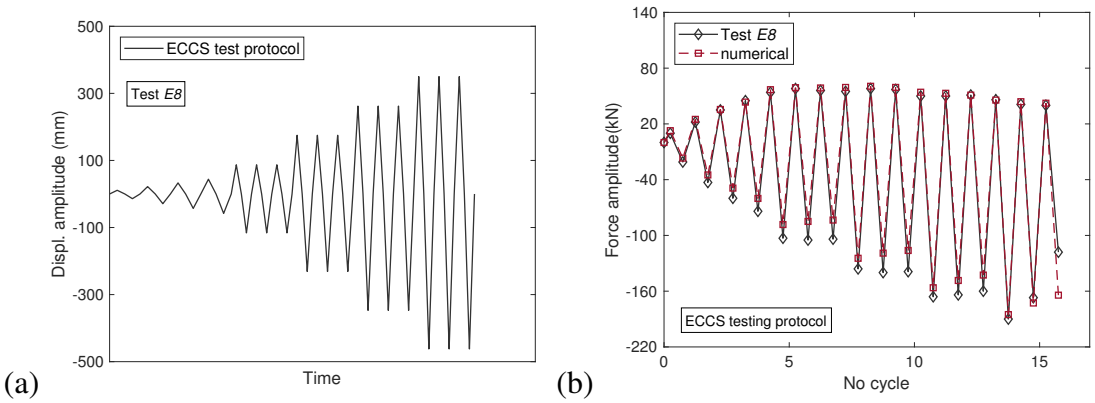

Figure 2.10: Experimentally and numerically obtained force amplitude of specimen $E8$.

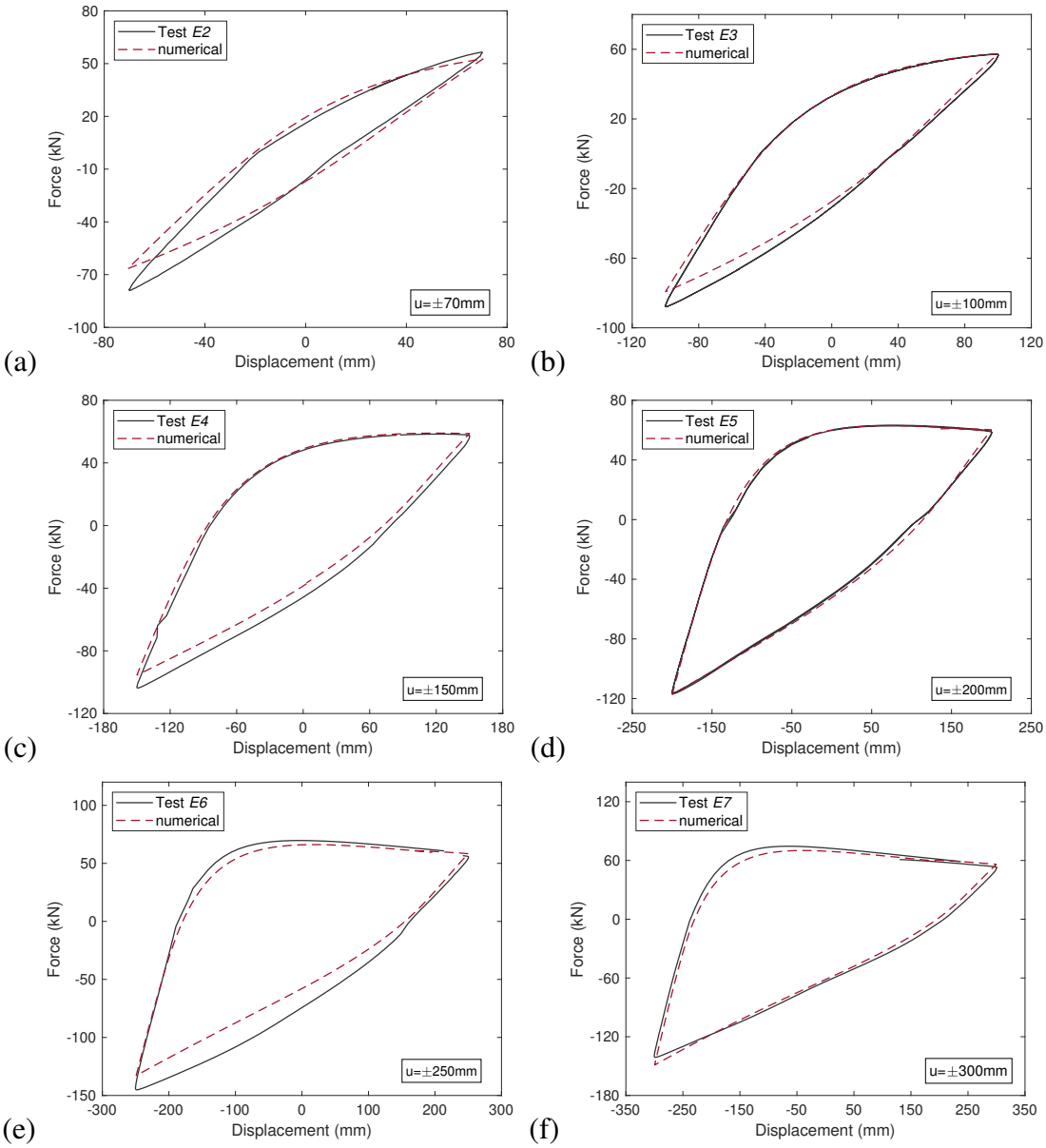

Figure 2.11: Experimentally and numerically obtained force-displacement response of specimens $E2$ - $E7$.

2.3.4.2 Local strains

The accurate prediction of local strains at the critical locations is essential for the design of piping components under low-cycle fatigue. Pipe elbows subjected to strong in-plane cyclic bending experience intense yielding around the elbow flank area and ratchet significantly in the hoop direction of the pipe [Yahiaoui et al. (1996a,b)]. Therefore, comparisons between experimental and numerical results are provided in terms of hoop strains at the elbow flank area. Wherever available, longitudinal strain measurements at extrados and intrados are also examined. The accuracy of the numerical model is examined by comparing the experimental results with numerical predictions in terms of maximum and minimum strain values for a significant number of cycles.

In specimen $E2$, subjected to displacement amplitude of ± 70 mm, hoop strain measurements obtained at gauge 3 and gauge 5 (Fig. 2.6) are examined. Fig. 2.12 shows that hardening model *CH* over-predicts material ratcheting. Larger differences are observed at the flank location (Fig. 2.12a), which become less significant when focusing on gauge 3 and the corresponding predictions (Fig. 2.12b). Hardening models *Mod. CH* and *BH* provide more accurate predictions. In particular the *BH* model provides the most accurate predictions in comparison with the experimental measurements. With respect to measurements of longitudinal strain obtained at the intrados and the extrados of the pipe elbow (Fig. 2.13), the measured strains are rather low and exhibit negligible ratcheting, so that the three models appear to provide satisfactory results.

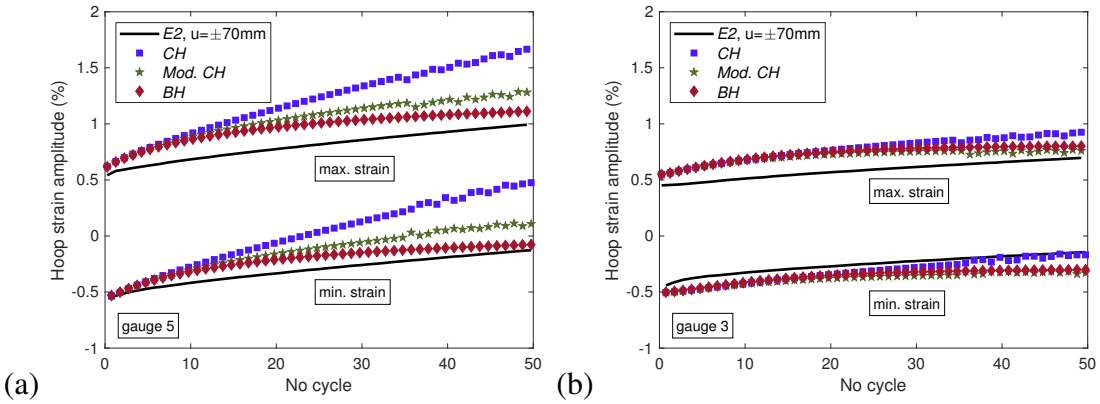

Figure 2.12: Hoop strain evolution observed at the elbow flank of specimen $E2$.

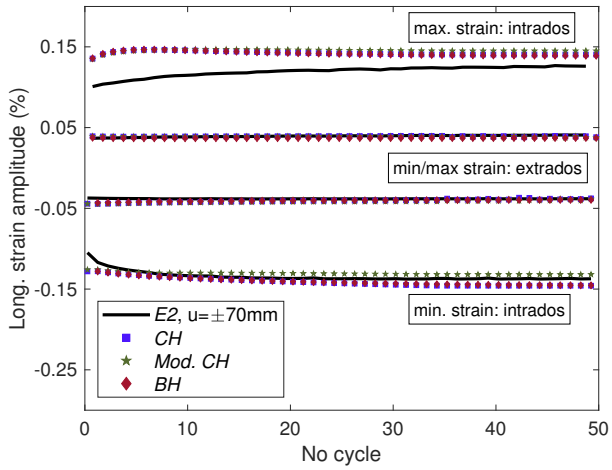

Figure 2.13: Longitudinal strain evolution observed at the intrados and extrados of specimen $E2$.

The analysis of specimen $E3$ (Fig. 2.14) subjected to displacement amplitude of ± 100 mm shows that the differences in the results obtained with the three hardening models follow the same trends observed in specimen $E2$. However, in this case, the differences between *Mod. CH* and *BH* become more pronounced. In addition, the *BH* model provides the most accurate predictions with respect to experimental data.

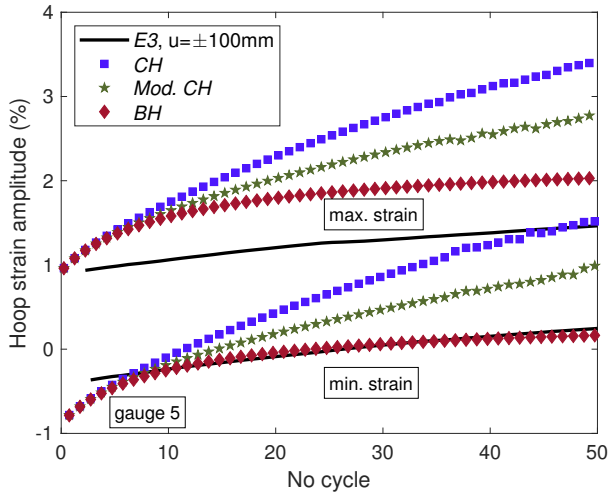

Figure 2.14: Hoop strain range evolution observed at the elbow flank of specimens $E3$.

Specimen $E4$ has been subjected to displacement amplitude of ± 150 mm, and hoop strain measurements have been interrupted in less than 20 load cycles due to large values of strain and failure of the strain gauge. Furthermore, longitudinal strain measurements at extrados are provided for the first 50 cycles, but no measurements have been obtained at elbow intrados due to strain gauge detachment at early stage of testing. The strain gauge 5, located exactly at the crown location, detached quite early, at the 7^{th} load cycle (Fig. 2.15a), whereas gauge 4 failed after 18 cycles. In both cases, the superiority of the advanced hardening models *Mod. CH* and *BH* over the more conventional model *CH* is obvious, even within the above limited number of load cycles. Model *CH* predicts fairly well the minimum strain in every load cycle but over-predicts the value of the strain range. On the other hand, the results obtained with model *BH* compare very well with the experimental data. This is also illustrated in Fig. 2.15(c) which presents the evolution of the hoop strain at the elbow flank during the test and the numerical simulation. Similar conclusions are drawn from Fig. 2.16, which shows the evolution of the longitudinal strains at the extrados location. The results obtained with the use of *Mod. CH* and *BH* models are close to the experimental measurements, while model *CH* over-predicts significantly the maximum strain. Furthermore, the strain ratcheting and the gradual reduction of ratcheting rate predicted by the *BH* model is in good agreement with the corresponding experimental data, as shown in Figs. (2.15-2.16).

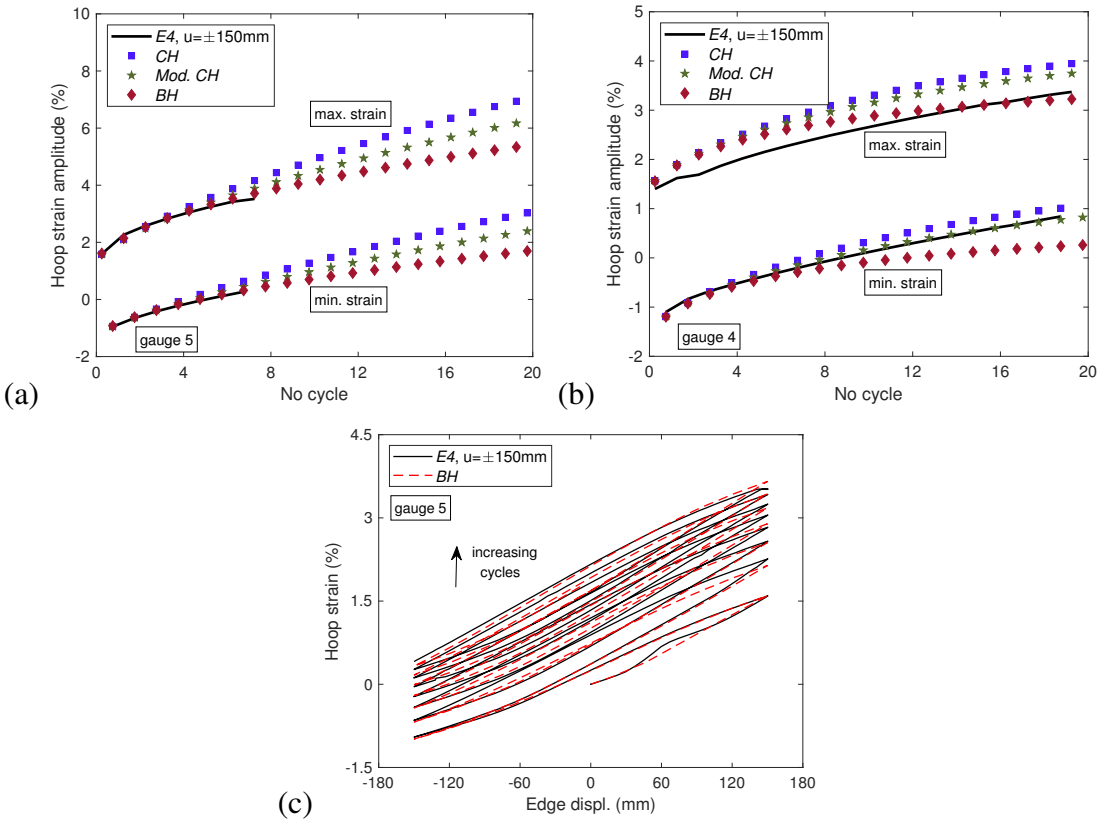

Figure 2.15: Hoop strain evolution observed at the elbow flank of specimen $E4$.

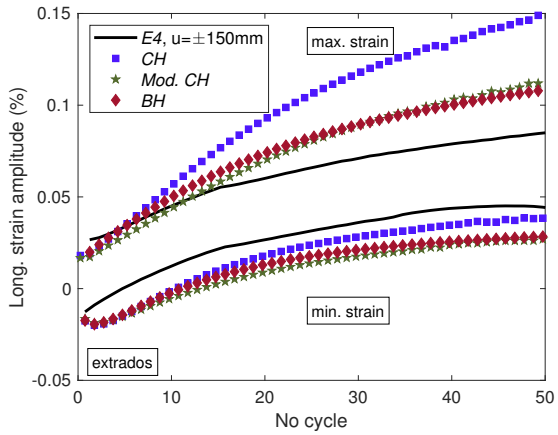

Figure 2.16: Longitudinal strain evolution observed at the extrados of specimens $E4$.

Strain measurements in specimen $E5$ are not available exactly at the crown location due to early failure of the corresponding strain gauge, and comparisons of the numerical predictions with strain readings from gauge 3 are shown in Fig. 2.17. As expected, ratcheting is less severe at this location and the corresponding strain amplitudes are limited to $\pm 2.5\%$ regardless of the large induced displacements. The results obtained from the three hardening models have similar accuracy with respect to the experimental results, whereas model *BH* provides better accuracy on the value of the maximum induced hoop strain in every load cycle. Contour plots illustrating the distribution of hoop strains on the inner and the outer surface of specimen $E5$ are presented in Fig. 2.18, corresponding to the first load cycle at maximum closing and opening displacement, obtained with the *BH* model. The location of maximum hoop strain at the inner and the outer surface of the elbow is observed. In addition, Fig. 2.19 shows the evolution of the equivalent plastic strain (denoted as SDV7 in UMAT) at the outer surface of the pipe bend, during the first 28 load cycles.

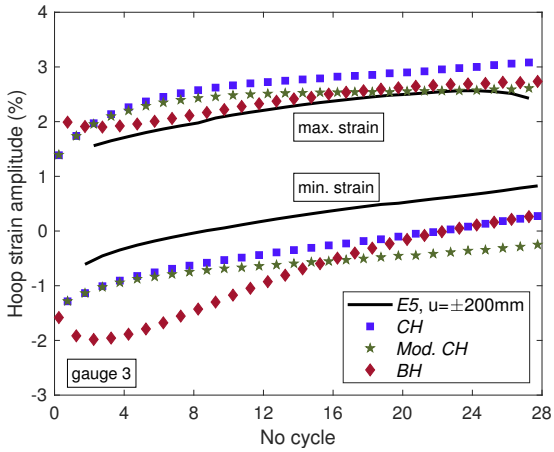

Figure 2.17: Hoop strain evolution observed near the elbow flank of specimens $E5$.

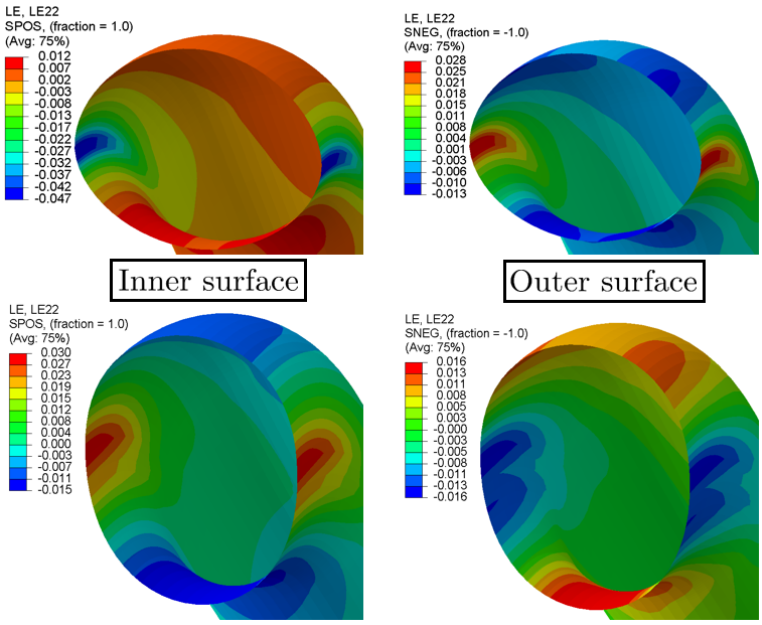

Figure 2.18: Distribution of hoop strain at inner and outer surface at the maximum closing/opening displacement of specimen $E5$ at the first loading cycle (hardening model *BH*).

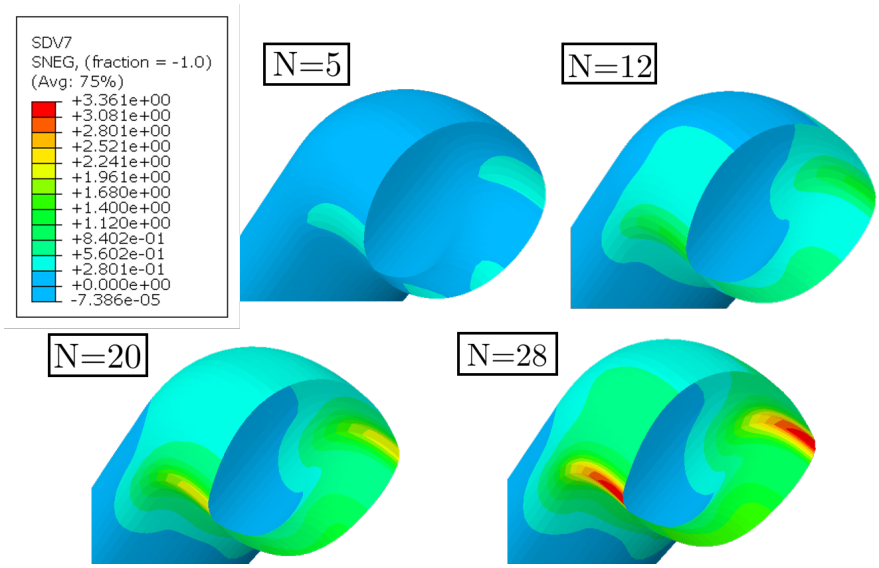

Figure 2.19: Evolution of plastic hoop strain in specimen $E5$ over the load cycles, obtained with the use of *BH* hardening model.

Hoop strain accumulation at the elbow flank area of specimens $E6$ - $E8$ has also been obtained, and is presented in Fig. (2.20-2.22). In these experiments, applied

displacement amplitude is significantly high and the specimens failed under low-cycle fatigue by forming a through-thickness crack in less than 16 load cycles. The available experimental data for local strain are very limited, because the majority of the strain gauges reached their capacity or detached from the pipe quite early during testing of those specimens. Fig. 2.20 and Fig. 2.21 show that the numerical models simulate the maximum strain in specimens $E6$ and $E7$ accurately, but fail to predict accurately the evolution of the minimum strain over the load cycles. This discrepancy is attributed to the gradual detachment of the strain gauges from the pipe elbow surface. Numerical results obtained from specimen $E8$, subjected to an increasing amplitude loading protocol [European Convention for Constructional Steelwork (1968)], are also provided in Fig. 2.22. The numerical results compare very well with the experimental measurements, demonstrating the accuracy and the efficiency of the numerical scheme.

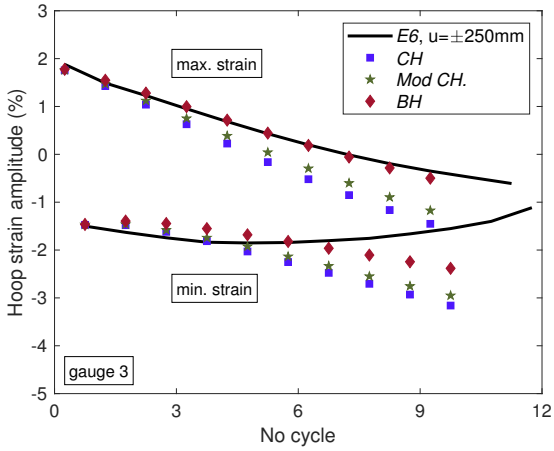

Figure 2.20: Hoop strain evolution observed near the elbow flank of specimens $E6$.

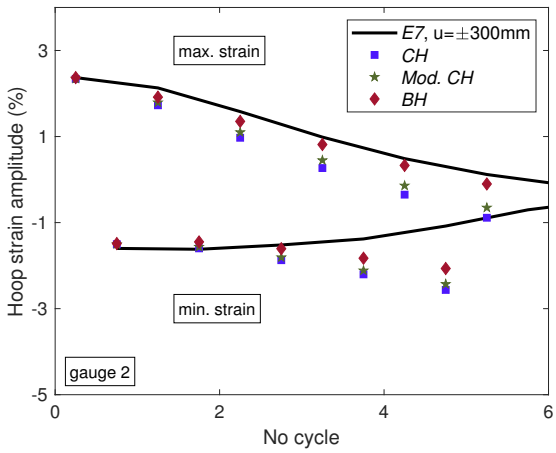

Figure 2.21: Hoop strain evolution observed near the elbow flank of specimens $E7$.

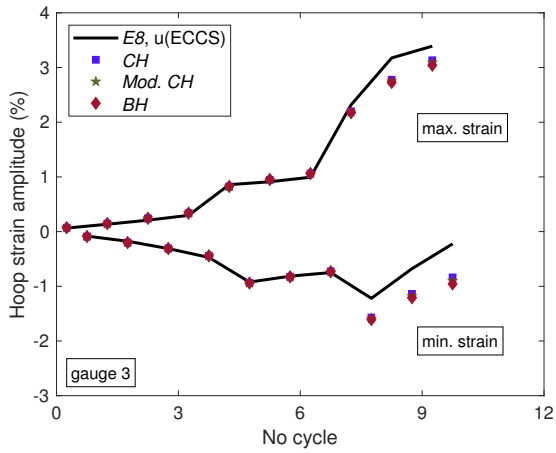

Figure 2.22: Hoop strain evolution observed near the elbow flank of specimens $E8$.

2.3.4.3 Cross-section ovalization at bend

In addition to strains, numerical predictions in terms of cross-sectional ovalization are presented. A special apparatus, shown in Fig. 2.6, has been used to measure the change of diameter in the vertical direction at the crown location (Dv_c) during the experiments [Pappa et al. (2012)]. Fig. 2.23 shows the normalized flattening values ("ovalization") obtained both experimentally and numerically through the simulation of tests $E2$-$E7$. The ovalization values are expressed by the following dimensionless ovalization parameter:

$$Ov_c = \frac{D - Dv_c}{D} \tag{2.103}$$

where D is the nominal diameter and Dv_c is the distance between pipe elbow intrados and extrados at the stage of maximum opening/closing displacement. Fig. 2.23 shows that the increase of applied displacement amplitude leads to higher ovalization. Furthermore, the ovalization values increase only slightly with respect to the loading cycles, an observation verified by both the experimental data and the numerical results, obtained from all three hardening models. Therefore, the corresponding ovalization values are plotted in the bar-chart of Fig. 2.23 in one bar, denoted as "numerical". The chart shows that ovalization of specimens $E2$-$E7$ depends on the loading amplitude and

ranges between 3% and 15% for the cases examined in the present work. Furthermore, minor differences are observed between the maximum closing and opening ovalization values in both cases. The good comparison between the numerical results and the experimental data shows that the numerical scheme equipped with the three hardening rules under consideration is capable of providing quite satisfactory predictions of pipe elbow ovalization.

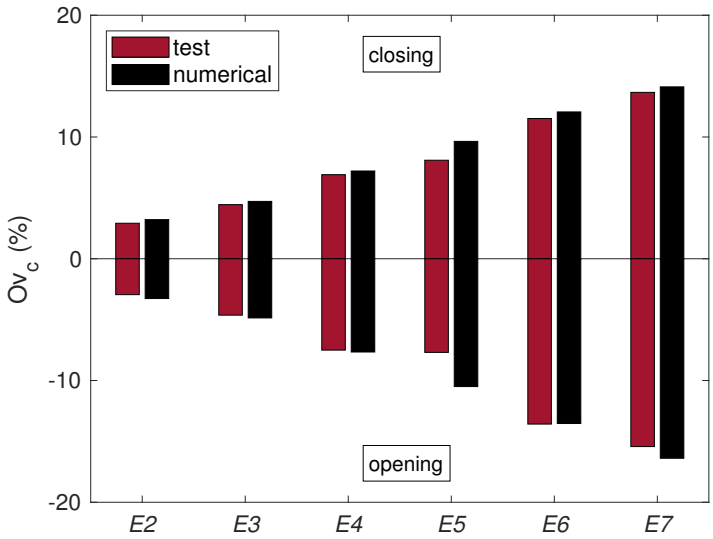

Figure 2.23: Experimentally and numerically obtained ovalization values of specimens $E2$-$E7$.

2.4 Locally-dented offshore pipelines subjected to cyclic axial loading

The mechanical response of externally-pressurized dented pipes, subjected to cyclic axial loading, is examined with the use of finite element models. The work is undertaken as a first part of a large-scale project, which involves the cooperation of The University of Edinburgh with Tianjin University, on the structural integrity of deep offshore pipelines. The research work is motivated by the mechanical response of offshore pipelines, which are often subjected to cyclic loading during installation or operation and may collapse because of accumulation of plastic deformations at the dent area. In this study, pipe segments are subjected to cyclic axial loading, in the presence of constant external pressure. Prior to the application of external pressure and axial loading, the pipes are locally dented, in the form of a "smooth dent" or "local ovalization", so that collapse initiates at the dent area. The investigation concerns thick pipes of outer diameter D = 51 mm and thickness t = 2 mm made of high-strength stainless steel. The dimensions are chosen based on the pipe specimen sizes to be tested in the laboratory of Tianjin University.

At this stage the work is numerical, while an extensive experimental campaign is expected to initiate in the near future. A finite element model is developed in the finite element package ABAQUS (2016) and the numerical scheme presented in Section 2.2 is employed to simulate the mechanical response of externally-pressurized dented pipes. The material parameters of the constitutive model under consideration are calibrated by matching the limited experimental data that are available at this point with stress-strain curves reported in the literature.

The interaction between tensile/compressive loading and external pressure on intact and dented pipes with $D/t = 25.5$ is examined. Two pipes with different dent magnitude are selected and analysed under cyclic axial loading in the presence of external

pressure. The numerical results are aimed at identifying the inter-relation between the magnitude of the applied loading and the number of loading cycles to failure.

2.4.1 Finite element model

Material properties and geometric characteristics of the finite element model employed in the present analyses are obtained based on the physical specimens at University of Tianjin. The D/t ratio of the specimens is similar to those examined by Jiao and Kyriakides (2009, 2011b) and equal to $D/t = 25.5$. The total length (L) considered is equal to 44 times the diameter ($L = 44D$), ensuring the elimination of end-restraint interferences. The analysis is divided in three steps. In the first step, two symmetric dents are formed on the pipe surface by pressing two rigid cylindrical intenders of diameter D_1 ($D_1/D = 0.75$) in the radial direction. In the following, external pressure is gradually applied based on the prescribed value, amplifying further the dent magnitude. In the last stage of the analysis, the pipe is loaded under monotonic or cyclic tensile/compressive axial loading, in the presence of constant external pressure.

The numerical model is presented in Fig. 2.24. One end of the pipe is structurally coupled with the reference point RP-1 for load application purposes, whereas the other end is pin-supported. The denting tools are also shown in Fig. 2.24. These are responsible for the formation of two "smooth" symmetrically placed dents, on the upper and the bottom side of the pipe, and are modelled in ABAQUS (2016) as 3D discrete rigid bodies. Two additional reference points (RP-2, RP-3) are used to control the movement of the rigid denting tools. The set-up is symmetric, allowing modelling 1/8 of the total structure for computational efficiency, while symmetry conditions are imposed with respect to "x", "y" and "z" axes. Using those symmetry conditions, global buckling phenomena are excluded and not considered.

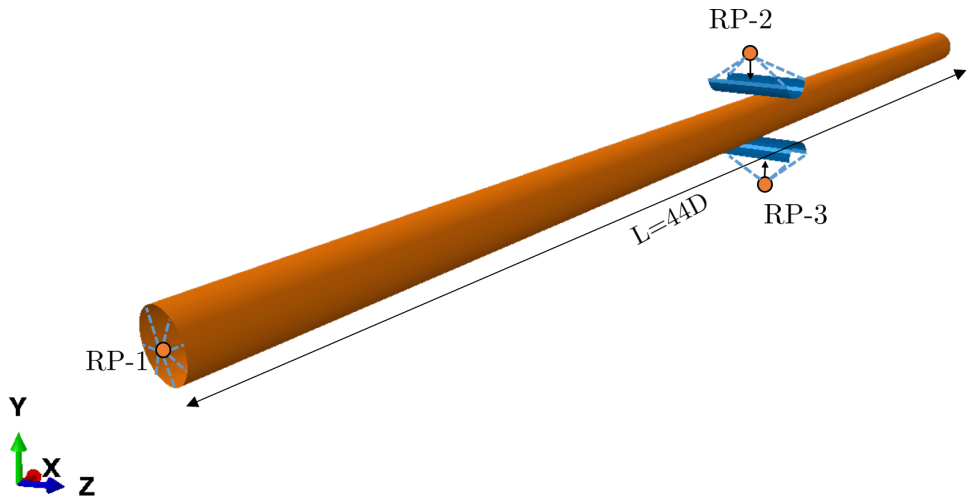

Figure 2.24: Finite element model of the pipe segment.

2.4.2 Calibration of the constitutive model

Accurate simulation of ratcheting depends strongly on the choice of the material model. Coupon specimens have been extracted from the testing pipes for the purpose of calibrating the constitutive model. Although the specimens are very thin, efforts were made to test those coupon specimens under cyclic inelastic loading, but even with the use of an anti-buckling device the specimens buckled in the first load reversal. In the present study the available experimental data are limited to monotonic stress-strain curve. In the absence of dedicated material testing, kinematic hardening is simulated with the nonlinear hardening rule with multiple backstresses as proposed by Chaboche (1986). The cyclic hardening parameters are calibrated by matching the yield stress and the monotonic hardening response of the stainless steel material to the cyclic material curves reported by Jiao and Kyriakides (2011b), obtained from testing stainless steel material of grade SS304. The selected material parameters are presented in Table 2.5. The resulting stress-strain curve obtained numerically and the corresponding experimental data from tensile monotonic tests are presented in Fig. 2.25.

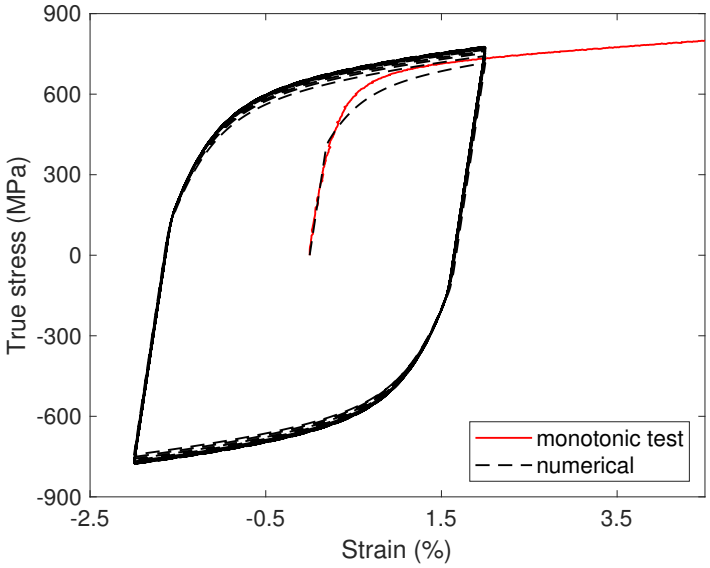

Figure 2.25: Experimental results from monotonic material tests and cyclic strain-stress curve for 2% strain amplitude.

Table 2.5: Material properties of constitutive model.

Model	E (MPa)	v	σ_y (MPa)	Q_∞ (MPa)	b	C_{1-4} (MPa)	γ_{1-4})
Chaboche (1986)	2×10^5	0.3	400	50	5	45,000	450
						20,000	200
						4,000	30
						1,200	5

2.4.3 Simulation of denting procedure

In the first step of the numerical simulation, the denting tools which are modelled as rigid rods are statically translated in the radial direction of the pipe to introduce two symmetric smooth dents. In this step, the pipe is rigidly supported at the two ends, while a vertical displacement is applied on the denting device. The relation between the denting amplitude (δ) and the pressing force (F) is depicted in Fig. 2.26, where the denting displacement (δ) is normalized based on the diameter of the pipe (δ/D). The denting force is normalized according to the "plastic denting load" F_V, employed by

Reid and Bell (1982) and by Karamanos and Eleftheriadis (2004) and defined as

$$F_V = \sigma_y^* t^2 \frac{b}{R} \tag{2.104}$$

where, σ_y^* is the yield stress under plain strain conditions ($1.15\sigma_y$), t and R are the pipe thickness and radius and b is a characteristic width, taken equal to the diameter of the indenter (D_1). Two pipes with dents of 7.3% and 12.3% are examined and will be referred to as "Pipe-1" and "Pipe-2", respectively. Fig. 2.26 indicates that dents of magnitude equal to 7.3% or 12.3% may be formed on the pipe subjected to pressing force values (accidental damage) that may be found in practice. It should be also mentioned that external pressure may noticeably amplify initial dents. The numerical analyses showed that the application of external pressure levels beyond 50% of the collapse pressure could lead to the increase of dent size up to 25%. Furthermore, the "wavy" pattern of the load-displacement curves is due to contact algorithm and has been noticed in previous publications [Karamanos and Eleftheriadis (2004)].

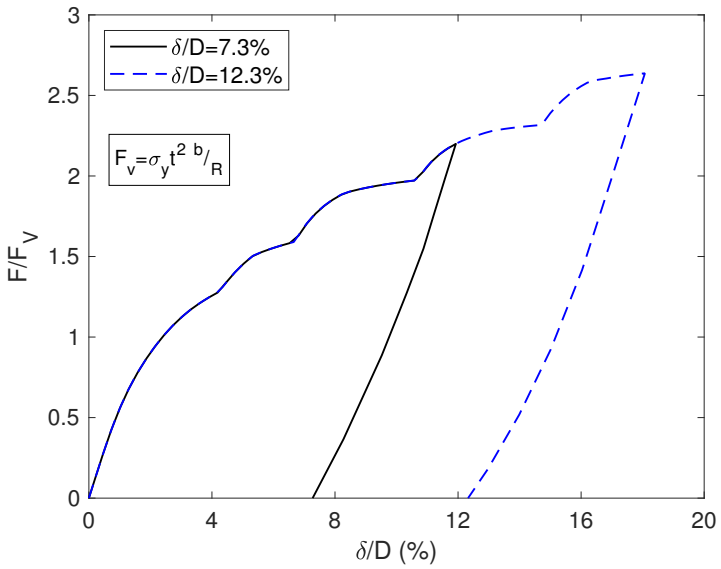

Figure 2.26: Numerical simulation of denting procedure.

2.4.4 Force-pressure interaction

The mechanical response of Pipe-1 and Pipe-2 is examined under monotonic axial loading in order to evaluate the axial capacity of the pipes in the presence of external pressure and draw the corresponding interaction diagrams. The investigation is conducted for tensile and compressive loading at several pressure levels, ranging from significantly low values up to the critical buckling pressure (p_{crit}). External pressure is applied on the pipe first, and subsequently, keeping the external pressure constant, axial load (tensile or compressive) is increased until the pipe collapses. The results are presented graphically in Fig. 2.27 through the appropriate interaction curve. In Fig. 2.27, axial force is presented normalized according to the yield strength of the member ($F_y = \sigma_y A$) while the pressure values are normalized with respect to the nominal yield pressure of the pipe p_y; $p_y = 2\sigma_y t/D$ with t being the thickness of the pipe. For comparison purposes, the results from the analysis of a non-dented (intact) pipe with δ/D = 0% are also presented to quantify the influence of the dent magnitude on the structural capacity of the pipes. In the non-dented pipe, a negligible dent has been considered to enable the computation of the critical buckling pressure.

Fig. 2.27 shows that the existence of a dent reduces considerably the critical buckling pressure of the member; for Pipe-1 and Pipe-2 the buckling pressure is 23% and 36% lower than that of the intact pipe (δ/D = 0%). Furthermore, the shape of the force-pressure interaction curve is asymmetric for compressive and tensile loading, as shown in Fig. 2.27. The squash load of the pipe is higher than the corresponding tensile capacity under the same external pressure. This difference is attributed to the elasto-plastic material response and the von Mises yield criterion, as shown schematically in Fig. 2.28. The combination of tension (F_t) and external pressure leads to yielding under lower axial loading in comparison to the corresponding case under compressive loading.

Fig. 2.29 depicts the collapsed configuration of Pipe-1 and Pipe-2 under external pressure and axial loading. In Fig. 2.29, symmetry with respect to the longitudinal axis is not used for clarity reasons. In the case of tensile loading (Fig. 2.29a), both axial force and pressure elongate the pipe, which fails under collapse of its entire length due to buckling propagation. On the other hand, axial compression results in a local deformation pattern around the dent area.

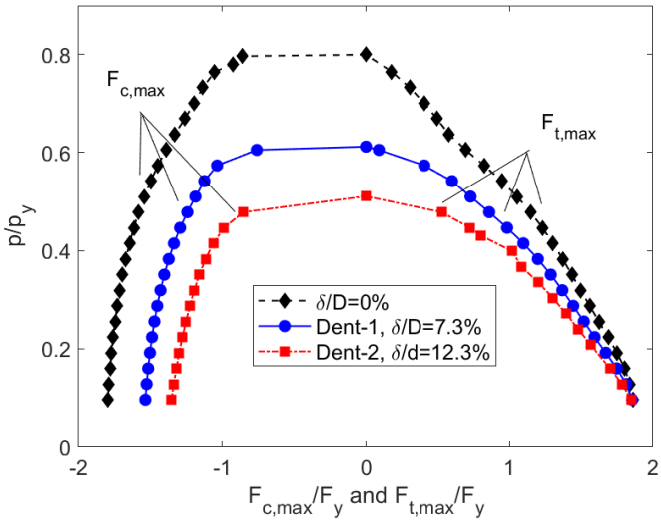

Figure 2.27: Force-external pressure interaction diagram for normalised dents of δ/D=0%, 7.23% and 12.3%.

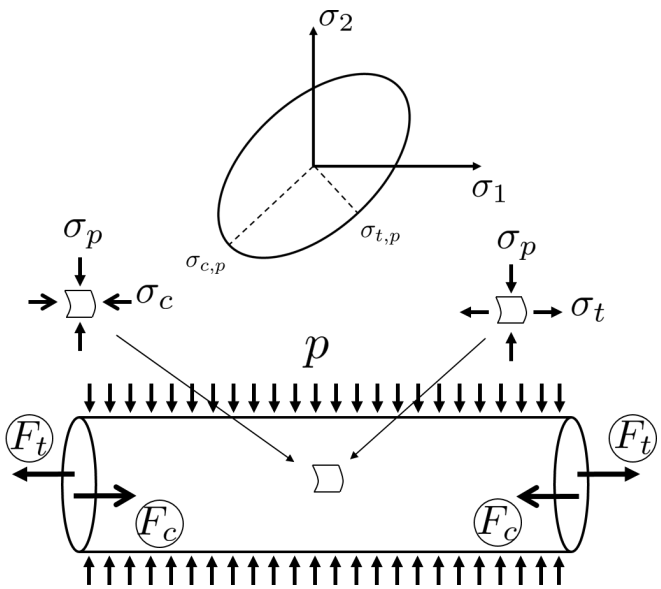

Figure 2.28: Material yielding under external pressure/compression and external pressure/tension.

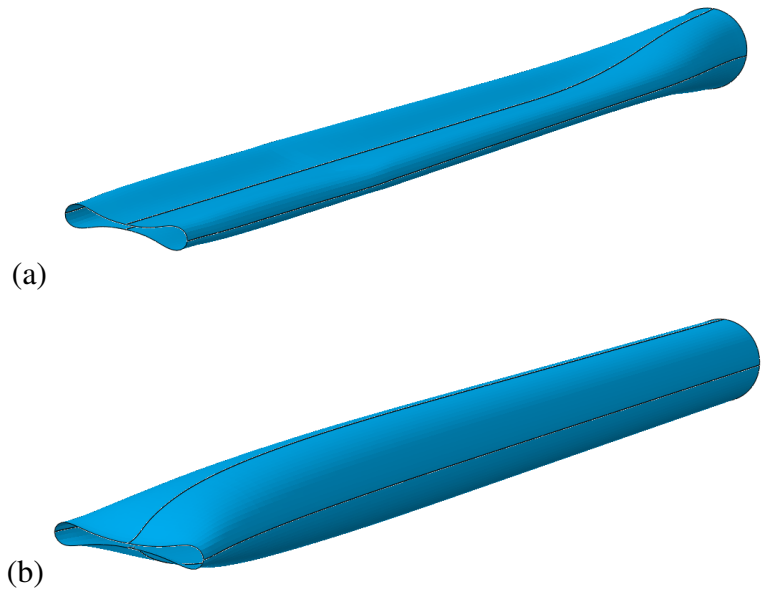

Figure 2.29: Collapse configuration under (a) tensile, (b) compressive loading and external pressure.

2.4.5 Cyclic load analysis

The performance of Pipe-1 and Pipe-2 is examined under cyclic inelastic axial loading in the presence of constant external pressure, towards investigation of ratcheting leading to structural collapse. Two pressure levels are chosen for each pipe based on the pressure levels to be considered in the forthcoming experimental study. Pipe-1 is examined under constant normalized external pressure of p/p_y = 0.13 and p/p_y = 0.37 while Pipe-2 is subjected to pressure levels of p/p_y = 0.13 and p/p_y = 0.30. Regarding the applied cyclic axial load, tensile loading amplitude has been chosen so that it is dominant and both pipes ratchet in the tensile direction. Compressive loading amplitude is considered the same in all cases, with a magnitude equal to 97% of the yield load. On the other hand, normalized tensile loading amplitude (F_t/F_y) ranges from 0.97 up to 1.54. The aim of the investigation is to identify a possible link between collapse under monotonic and cyclic loading conditions based on the prescribed pressure levels.

The mechanical response of Pipe-1 and Pipe-2 is examined in terms of averaged axial

deformation or net pipe elongation, ovalization measurements at the dent location with respect to the vertical direction (ΔD_V) and averaged equivalent plastic strain at the dent location. The latter is computed as the average value of the equivalent plastic strain obtained at the dent "valley" (Fig. 2.30).

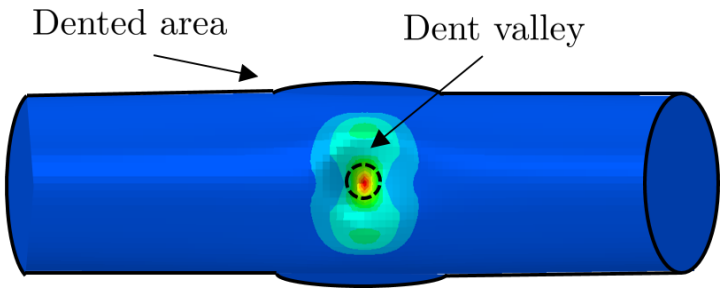

Figure 2.30: Definition of dented area and dent "valley".

2.4.5.1 Analysis of Pipe-1

The results from the analysis of Pipe-1 (δ/D = 7.3%) under p/p_y = 0.13 and p/p_y = 0.37 are presented in Fig. 2.31. From Fig. 2.27, the normalized monotonic tensile capacity of Pipe-1 under these pressure levels are $F_{t,max}/F_y$ = 1.78 and $F_{t,max}/F_y$ = 1.22, respectively. Normalized values of axial tensile load amplitude F_t/F_y range between 1.14 and 1.54 for p/p_y = 0.13 and 1.02 to 1.06 for p/p_y = 0.37. High external pressure corresponds to smaller allowed force range, as collapse is controlled by the presence of external pressure.

Fig. 2.31 presents the evolution of the measured quantities throughout the loading cycles for different loading amplitudes and two pressure levels. Results from the corresponding monotonic investigation under tensile loading and the same pressure levels are also depicted for comparison purposes. Fig. 2.31 indicates that under normalized pressure of p/p_y = 0.13, strain ratcheting is influenced by the magnitude of the applied tensile loading. For low tensile loading, Pipe-1 shortens with an initial rate which is somewhat decreased after the first 5-10 load cycles depending on the tensile loading amplitude. For higher load amplitude, net pipe elongation accumulates under a constant rate throughout the load history. A similar pattern is identified when

examining the evolution of the averaged equivalent plastic strain. For tensile load amplitude lower than 1.38, material initially ratchets slowly, but a sudden increase on the ratcheting rate is observed as the pipe approaches failure (collapse). For higher tensile load amplitude, ratcheting manifests rapidly from the initial load cycles. The accumulation rate of ovalization tends to increase over the loading cycles while maximum ovalization values can reach up to 50% prior to collapse.

Different behaviour is observed for Pipe-1 under normalized pressure level of p/p_y = 0.37 and relatively low tensile load amplitudes as shown in 2.27. This relatively high pressure level has a direct impact on the ratcheting response and the structural stability of the pipe. Failure occurs in less than 5 cycles in all cases examined regardless of the amplitude of tensile loading. Comparing the strain values with the corresponding strain obtained from the monotonic scenario, collapse occurs at a value of averaged equivalent plastic strain close to the one obtained from the monotonic tensile analysis.

It is worth noting that Corona and Kyriakides (1991) correlated collapse due to cyclic bending with the value of local ovalization during monotonic loading. Furthermore, the investigation of Jiao and Kyriakides (2009, 2011a,b) on internally pressurized pipes under cyclic axial loading showed that buckling failure under cyclic loading occurs when the averaged accumulated strain or net-shortening of the tube reaches a level that corresponds to the average strain obtained at the maximum load under monotonic loading conditions.

The results presented in Fig. 2.31 show that local ovalization or net pipe elongation may not be appropriate parameters for inter-relating collapse between monotonic and cyclic cases. On the other hand, Figs. 2.31(d, e) show a good correlation between the averaged equivalent plastic strain at the dent at the stage of collapse under monotonic and cyclic loading conditions. At both pressure levels, the pipe ratchets in the tensile direction and collapse occurs when the averaged equivalent plastic strain is close to the average equivalent plastic strain of the pressurized pipe at collapse under monotonic tensile analysis.

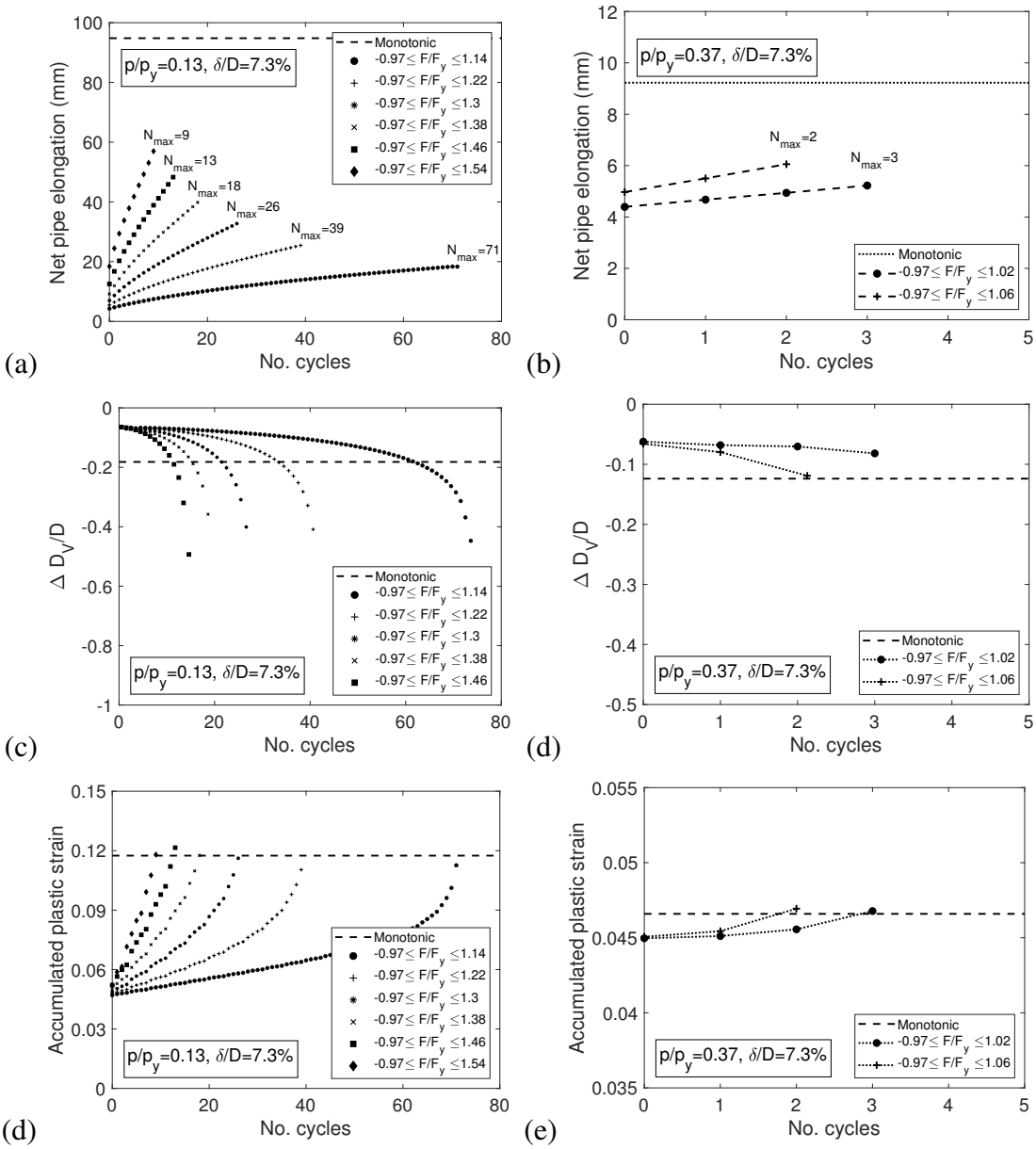

Figure 2.31: Ratcheting response of Pipe-1 under $p/p_y = 0.13$ (a, c, d) and $p/p_y = 0.37$ (b, c, e) pressure in terms of net-shortening, local ovalization and averaged equivalent plastic strain at the dent location.

The collapse configuration of Pipe-1 (Fig. 2.32) shows that under cyclic axial loading and external pressure, Pipe-1 is locally deformed around the dent area and the collapse configuration is analogous to the corresponding shape obtained under monotonic loading conditions (Fig. 2.29b).

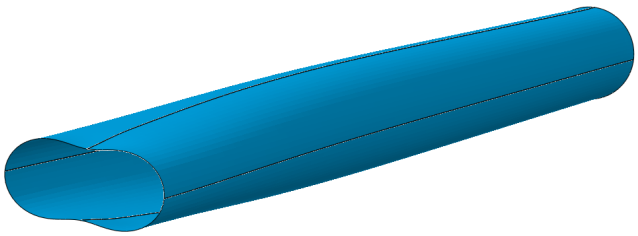

Figure 2.32: Collapse configuration of Pipe-1 under cyclic loading and external pressure.

2.4.5.2 Analysis of Pipe-2

Pipe-2 (δ/D = 12.3%) is examined under normalized external pressure levels of p/p_y = 0.13 and p/p_y = 0.30 and the results in terms of net pipe elongation, ovalization measurements and averaged equivalent plastic strain are presented in Fig. 2.33. The normalized value of tensile load amplitude (F_t/F_y) ranges between 1.14 to 1.54 and 1.02 to 1.06 for the cases of p/p_y = 0.13 and p/p_y = 0.30, respectively. Fig. 2.33(a, c, e) depicts the accumulation of axial deformations (net pipe elongation), ovalization measurements at the dent and the material ratcheting response of Pipe-2 under a relatively low level of external pressure (p/p_y = 0.13). In terms of net pipe elongation evolution, two stages can be identified for relatively low loading while for higher tensile loading, axial deformations are accumulated in a constant rate throughout the loading history. Under external pressure p/p_y = 0.13, the axial capacity of Pipe-2 is almost equal to the axial capacity of Pipe-1. However, the comparison of Fig. 2.33(a) with Fig. 2.31(a) shows that collapse in Pipe-2 occurs at 38% fewer loading cycles with respect to Pipe-1. Furthermore, the net pipe elongation values at collapse under monotonic loading is significantly higher than the corresponding values observed under cyclic conditions. In terms of equivalent plastic strain, collapse under cyclic conditions occurs in slightly higher values of averaged equivalent plastic strain in comparison to monotonic loading. Nevertheless, the average difference in terms of equivalent plastic strain between cyclic and monotonic loading scenarios is roughly 10%. Hence, the value of the averaged equivalent plastic strain obtained from a monotonic analysis can

provide a fair estimate of the maximum averaged equivalent plastic strain expected close to the collapse under cyclic conditions. The ovalization accumulation shows that both Pipe-1 and Pipe-2 present similar ovalization values prior to the occurrence of instability under $p/p_y = 0.13$ but those values may not be correlated with the ovalization from the corresponding monotonic cases.

Pipe-2 is also analysed under normalized external pressure of $p/p_y = 0.30$ and the results are included in Fig. 2.33(b, d, f). The combination of this high pressure with the large dent magnitude narrows down the analysis cases to only two, whereas failure occurred within the first couple of cycles. Fig. 2.33 shows that the accumulation rates observed in the measured quantities are proportional to the applied load. Comparing the values of the examined quantities at the instance of collapse, critical net pipe elongation obtained from the monotonic scenario is excessively higher than those obtained from cyclic investigations. On the other hand, the average equivalent plastic strain obtained under cyclic conditions is less than 9% higher in comparison to the monotonic scenario, which is an observation compatible with the results obtained from Pipe-1.

Overall, the results from Pipe-1 under $p/p_y = 0.37$ and Pipe-2 under $p/p_y = 0.30$ indicate that the collapse of both systems is severely influenced by the level of external pressure in combination with the dent magnitude. Large dent values are associated with initial local ovalization, leading to severe local plasticity effects, resulting in early collapse of the pipe.

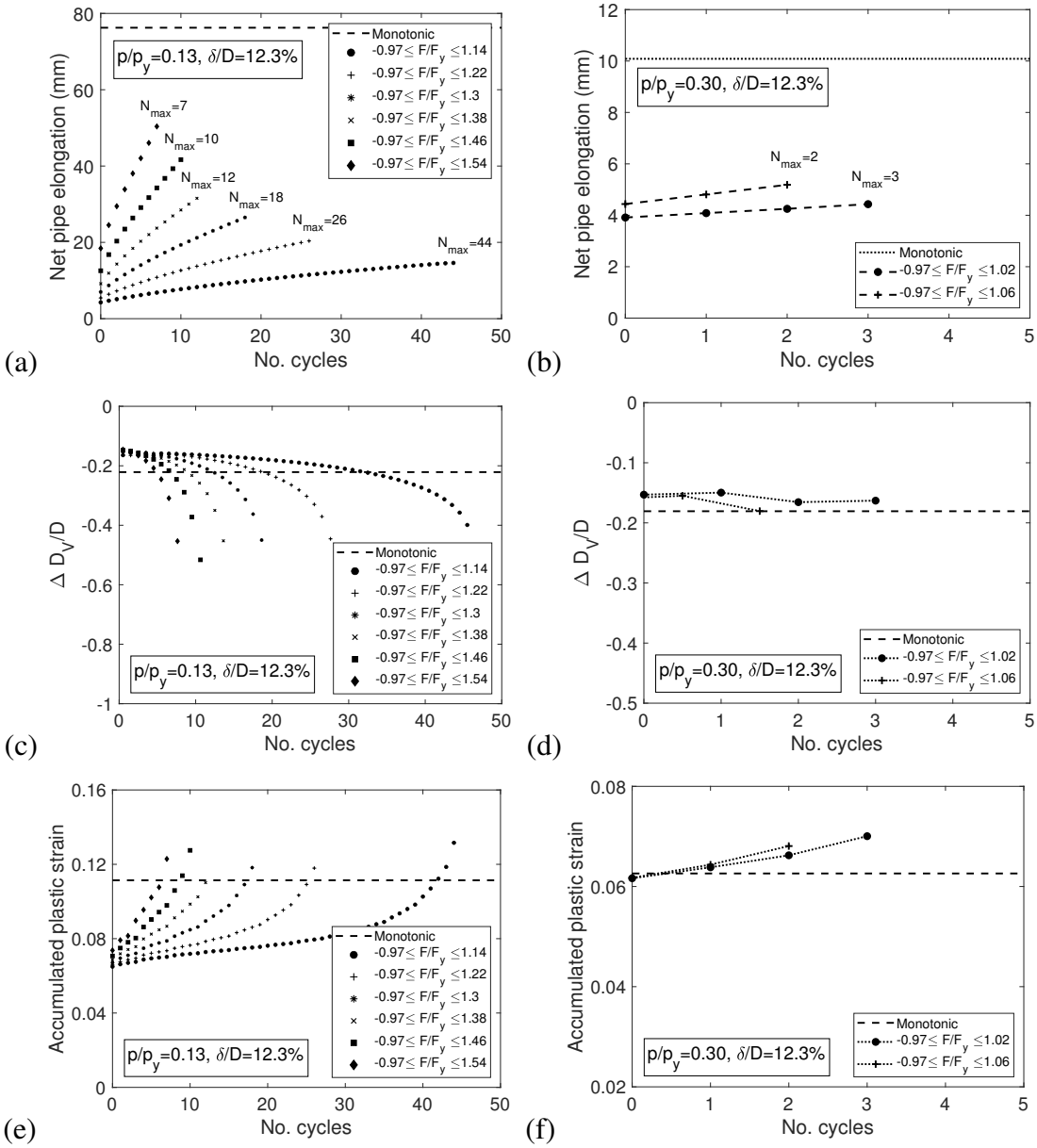

Figure 2.33: Ratcheting response of Pipe-2 under $p/p_y = 0.13$ (a, c, d) and $p/p_y = 0.30$ (b, c, e) pressure in terms of net-shortening, local ovalization and averaged equivalent plastic strain at the dent location.

2.5 Summary

The multi-axial ratcheting response of steel circular tubular components subjected to cyclic inelastic loading is investigated using rigorous numerical tools, with emphasis on constitutive modelling. A robust numerical implementation scheme is presented in Section 2.2 for simulating multi-axial ratcheting in metal components, offering advanced capabilities which are not yet available even in leading commercial finite element software. The proposed numerical integration scheme features computational efficiency and ensures stability and quadratic convergence in large-scale computations by providing the consistent tangent moduli in explicit form.

The numerical scheme proposed in Section 2.2 is implemented in Section 2.3 within the finite element software ABAQUS (2016) as a material user subroutine UMAT and its efficiency is demonstrated through the numerical simulation of large-scale cyclic bending tests on pipe elbows. Three advanced kinematic hardening rules are employed using the proposed framework to simulate the mechanical behaviour of the elbow specimens, highlighting that elaborate kinematic hardening models are required to predict accurately multi-axial ratcheting evolution.

In Section 2.4, the ratcheting collapse of externally pressurised dented stainless steel pipes is numerically simulated. The influence of dent magnitude and external pressure on the structural performance of the pipe is quantified for monotonic and cyclic loading conditions. The mechanical response of two pipes with different dent magnitude is thoroughly examined and it is shown that methodologies proposed for intact pipes fail to inter-relate collapse under monotonic and cyclic loading. It is demonstrated that in dented pipes, collapse under cyclic and monotonic axial loading can be correlated through the averaged accumulated plastic strain at the dent valley.

Chapter 3

Simulation of cyclic plasticity-damage in metal structural components

3.1 Introduction

Metal structural components are often exposed to severe cyclic loading (e.g. earthquakes or storm conditions in offshore structures) and failure may occur in the form of ductile rupture. To simulate numerically the elastoplastic response and account for material softening due to the formation of microvoids and microcracks, and to predict the life expectancy of the metallic component, the implementation of cyclic plasticity constitutive models coupled with damage is required. In such models, damage is simulated with a macroscopic variable which describes material softening initiating upon strong reversed cyclic loading. Another quantity, defined as critical damage state is used to determine local rupture of the material point.

Two implementation methods are developed, one for plane stress conditions and another for the more general case of 3D formulation. Each numerical scheme is formulated in a different manner to allow the development of optimised integration algorithms and consistent linearisation methodologies. In comparison to Chapter 2, kinematic hardening is simulated using more traditional nonlinear models as less attention is given to multi-axial ratcheting simulation. In theory, advanced kinematic hardening rules could be coupled with cyclic plasticity-damage constitutive models but such task is not be attempted herein. To free the solution from spurious mesh dependency originating from the strain-softening material response, an appropriate simulation methodology is adopted using "built-in" tools in commercial finite element packages. Both numerical schemes are implemented within the commercial finite element software ABAQUS (2016) as material user subroutines UMAT and their capabilities are demonstrated by simulating successfully the elastoplastic-damage response and ductile rupture in large-scale physical experiments.

3.2 Numerical scheme for cyclic-plasticity damage: 3D formulation

This section presents the development, implementation and validation of the proposed numerical integration scheme, developed for 3D formulation. Constitutive relations are based on J_2-flow theory coupled with damage. Mixed hardening is assumed with nonlinear isotropic hardening and the kinematic hardening rule proposed by Chaboche (1986) with multiple backstresses. The isotropic damage potential employed is a scalar function of the damage state, the equivalent plastic strain and the stress tensor, allowing for the implementation of any isotropic CDM model reported in the literature. An implicit integration scheme is developed, extending and enhancing existing methodologies proposed elsewhere for classical elastoplasticity. A main feature of the present algorithm is that incremental update of the internal variables

requires the solution of a single scalar equation with respect to the equivalent plastic strain increment, improving the efficiency of the numerical integration procedure. This offers an optimised numerical scheme for coupled plasticity-damage implementation in comparison with previous studies [Doghri (1995); Lemaitre and Desmorat (2005); Bonora et al. (2014)]. The integration algorithm is consistently linearised by enhancing the methodology proposed by Simo and Taylor (1984) for classical elastoplasticity to the requirements of the present model, leading to a robust numerical scheme. It is shown that the single-equation integration algorithm obtains a rather simple form and allows for the explicit formulation of the consistent jacobian, thus minimising the computational cost. The proposed numerical scheme is implemented in ABAQUS (2016) software as material user-subroutine UMAT and is validated successfully against large-scale laboratory experiments.

3.2.1 Constitutive relations

The theoretical formulation of the presented numerical scheme is based on von-Mises cyclic plasticity with nonlinear kinematic and isotropic hardening. Damage is introduced in the constitutive equations through an isotropic damage function in terms of the effective stress [Kachanov (1958)] and the hypothesis of strain equivalence [Lemaitre (1971)]. For convenience, tensors are denoted with boldface symbols while the following relations apply between second-order tensors ($\boldsymbol{a}$, $\boldsymbol{b}$) and fourth-order tensors ($\boldsymbol{M}$), and their Cartesian components:

$$\boldsymbol{a}\cdot\boldsymbol{b} = a_{ij}\, b_{ij}$$

$$\boldsymbol{M}\boldsymbol{a} = M_{ijkl}\, a_{kl}$$

The strain tensor $\boldsymbol{\varepsilon}$ is additively decomposed to the elastic part $\boldsymbol{\varepsilon}^e$ and the plastic part $\boldsymbol{\varepsilon}^p$.

$$\boldsymbol{\varepsilon} = \boldsymbol{\varepsilon}^e + \boldsymbol{\varepsilon}^p \tag{3.1}$$

Starting from a free energy potential, such as those presented in [Simo and Ju (1989); Doghri (1995)], the elastic stress strain response of the damaged material is derived based on a hyper-elastic constitutive formulation as:

$$\boldsymbol{\sigma} = (1-D)\boldsymbol{M}\,\boldsymbol{\varepsilon}^{e} \tag{3.2}$$

where, $\boldsymbol{\sigma}$ is the stress tensor, $\boldsymbol{M}$ is the fourth-order elastic rigidity tensor and D denotes the isotropic damage state. The von-Mises yield criterion, including damage, is expressed as follows [Lemaitre (1984)]:

$$F(\boldsymbol{s},\boldsymbol{a},\varepsilon_q,D) = \sqrt{\left(\frac{1}{1-D}\boldsymbol{s}-\boldsymbol{a}\right)\cdot\left(\frac{1}{1-D}\boldsymbol{s}-\boldsymbol{a}\right)} - \sqrt{\frac{2}{3}}k(\varepsilon_q) = 0 \tag{3.3}$$

where $\boldsymbol{a}$ is the deviatoric part of the backstress tensor $\boldsymbol{\alpha}$ and ε_q is the equivalent plastic strain, to be defined in the sequel. Using associated plasticity, the evolution of plastic strain is in the direction normal to the yield surface, so that

$$\dot{\boldsymbol{\varepsilon}}^{p} = \dot{\lambda}\frac{\partial F}{\partial \boldsymbol{s}} \tag{3.4}$$

where $\dot{\lambda}$ is the plastic multiplier. Differentiating Eq. (3.3) one obtains

$$\dot{\boldsymbol{\varepsilon}}^{p} = \frac{\dot{\lambda}}{1-D}\frac{1}{\left\|\frac{1}{1-D}\boldsymbol{s}-\boldsymbol{a}\right\|}\left(\frac{1}{1-D}\boldsymbol{s}-\boldsymbol{a}\right) = \frac{\dot{\lambda}}{1-D}\boldsymbol{n} \tag{3.5}$$

where $\boldsymbol{n}$ is the unit-value outward normal tensor to the yield surface ($\boldsymbol{n}\cdot\boldsymbol{n}=1$) and $\|\cdot\|$ is the Eucledian norm of a tensor. Accordingly, the equivalent plastic strain rate

$$\dot{\varepsilon}_q = \sqrt{\frac{2}{3}\dot{\boldsymbol{\varepsilon}}^{p}\cdot\dot{\boldsymbol{\varepsilon}}^{p}} \tag{3.6}$$

is equal to

$$\dot{\varepsilon}_q = \sqrt{\frac{2}{3}}\frac{\dot{\lambda}}{1-D} \tag{3.7}$$

and from Eq. (3.7), $\dot{\lambda}$ can be expressed with respect to $\dot{\varepsilon}_q$ as:

$$\dot{\lambda} = \sqrt{\frac{3}{2}}\dot{\varepsilon}_q(1-D) \tag{3.8}$$

while from Eq. (3.5) and Eq. (3.8) the relation between $\dot{\varepsilon}_q$ and $\dot{\boldsymbol{\varepsilon}}^p$ can be written as:

$$\dot{\boldsymbol{\varepsilon}}^p = \sqrt{\frac{3}{2}}\dot{\varepsilon}_q \boldsymbol{n} \tag{3.9}$$

The damage scalar (D), already introduced in Eqs. (3.2-3.8), is written in a general manner to allow the implementation of any isotropic CDM model reported in the literature [e.g. Lemaitre (1985); Bonora (1997); Tai, Hua and Yang (1986); Tai (1990); Voyiadjis et al. (2012)]. The kinetic law of damage ($\dot{D}$) is defined as the derivative of the damage potential (F_D) with respect to the associated variable (Y). For the purpose of the present study, the damage potential is assumed a scalar function of the damage state (D), the equivalent plastic strain (ε_q) and the stress tensor ($\boldsymbol{\sigma}$). Therefore the $\dot{D}$ product is defined as

$$\dot{D} = \frac{\partial F_D\left(\boldsymbol{\sigma}, D, \varepsilon_q\right)}{\partial Y}\dot{\varepsilon}_q = F'_D\dot{\varepsilon}_q \tag{3.10}$$

where F'_D is set for shortness. The kinematic hardening tensor $\boldsymbol{a}$ consists of multiple nonlinear backstresses as proposed by Chaboche (1986). In rate form,

$$\dot{\boldsymbol{a}} = \sum_{i=1}^{N}\left(\dot{\boldsymbol{a}}^i\right) = \sum_{i=1}^{N}\left(C_i\right)\dot{\boldsymbol{\varepsilon}}^p - \sum_{i=1}^{N}\left(\gamma_i \boldsymbol{a}^i\right)\dot{\varepsilon}_q \tag{3.11}$$

which is written as follows, using Eq. (3.9):

$$\dot{\boldsymbol{a}} = \dot{\varepsilon}_q\left[\sqrt{\frac{3}{2}}\sum_{i=1}^{N}\left(C_i\right)\boldsymbol{n} - \sum_{i=1}^{N}\left(\gamma_i \boldsymbol{a}^i\right)\right] \tag{3.12}$$

In the above equation, coefficients C_i, γ_i are hardening parameters of the i backstress tensor which are calibrated from appropriate cyclic material tests. The isotropic

hardening function $k(\varepsilon_q)$ refers to the evolution of the yield surface size and is assumed to be a function of the equivalent plastic strain. Enforcing the consistency condition on the yield surface one obtains

$$\dot{F}(\boldsymbol{s},\boldsymbol{a},\varepsilon_q,D) = \frac{\partial F}{\partial \boldsymbol{s}}\dot{\boldsymbol{s}} + \frac{\partial F}{\partial \boldsymbol{a}}\dot{\boldsymbol{a}} + \frac{\partial F}{\partial D}\dot{D} + \frac{\partial F}{\partial \varepsilon_q}\dot{\varepsilon}_q = 0 \tag{3.13}$$

The undefined partial derivatives of Eq. (3.13) are computed by differentiating the yield potential.

$$\frac{\partial F}{\partial \boldsymbol{a}} = -\boldsymbol{n}, \qquad \frac{\partial F}{\partial D} = \frac{\boldsymbol{s}\cdot\boldsymbol{n}}{(1-D)^2}, \qquad \frac{\partial F}{\partial \varepsilon_q} = -\sqrt{\frac{2}{3}}\frac{\partial k(\varepsilon_q)}{\partial \varepsilon_q} \tag{3.14}$$

The rate form of the deviatoric stress tensor ($\dot{\boldsymbol{s}}$) is evaluated from Eq. (3.2) as

$$\dot{\boldsymbol{s}} = (1-D)2G\dot{\boldsymbol{e}} - (1-D)2G\sqrt{\frac{3}{2}}\dot{\varepsilon}_q\boldsymbol{n} - F'_D\dot{\varepsilon}_q\frac{\boldsymbol{s}}{1-D} \tag{3.15}$$

with G being the shear modulus of an isotropic material. Elaborating Eq. (3.13) and with the aid of Eqs. (3.14, 3.15), the equivalent plastic strain rate can be expressed as

$$\dot{\varepsilon}_q = \frac{2G}{h}\boldsymbol{n}\cdot\dot{\boldsymbol{e}} \tag{3.16}$$

where modulus h is defined by:

$$h = \sqrt{\frac{3}{2}}\left[2G + \sum_{i=1}^{N}(C_i)\right] - \sum_{i=1}^{N}\left(\gamma_i\boldsymbol{a}^i\right)\cdot\boldsymbol{n} + \sqrt{\frac{2}{3}}k'(\varepsilon_q) \tag{3.17}$$

and prime $(\cdot)'$ denotes differentiation with respect to ε_q. Substituting Eq. (3.16) into Eq. (3.15) and taking into account the hydrostatic part of the stress tensor, one obtains:

$$\dot{\boldsymbol{\sigma}} = \left[(1-D)\boldsymbol{M} - \frac{4G^2}{h}\sqrt{\frac{3}{2}}(1-D)\boldsymbol{n}\otimes\boldsymbol{n} - \frac{2GF'_D}{h(1-D)}\boldsymbol{\sigma}\otimes\boldsymbol{n}\right]\dot{\boldsymbol{\varepsilon}} \tag{3.18}$$

where,

$$\boldsymbol{M}_{ep} = (1-D)\boldsymbol{M} - \frac{4G^2}{h}\sqrt{\frac{3}{2}}(1-D)\boldsymbol{n}\otimes\boldsymbol{n} - \frac{2GF'_D}{h(1-D)}\boldsymbol{\sigma}\otimes\boldsymbol{n} \tag{3.19}$$

is a fourth-order non-symmetric tensor, expressing the continuum elastoplastic tangent operator moduli, and $\otimes$ denotes the tensor product of two second-order tensors. The non-symmetric term in Eq. (3.19) originates from Eq. (3.15) and is attributed to coupling of plasticity with damage.

At this point, it is worth noting that cyclic plasticity-damage material models offered by some commercial finite element software such as ABAQUS (2016) are derived on the principles of hypo-elasticity. In comparison to classical elastoplasticity, in coupled plasticity-damage constitutive models, the hypo-elastic and the hyper-elastic formulations present noticeable differences even under small strain theory. The hypo-elastic formulation is based on a degraded stress-strain relation rather than a scaled energy function, neglecting the effect of damage variation on the constitutive relations. In more detail, using hypo-elasticity the last term in Eq. (3.15) is omitted and the continuum tangent operator becomes symmetrical. Consequently, the hypo-elastic formulation leads to a different integration algorithm and corresponding consistent linearisation moduli.

3.2.2 Implicit integration of constitutive equations

An integration scheme of the above constitutive model based on an unconditionally stable Euler-backward scheme is developed. This scheme has been introduced in [Hartmann and Haupt (1993); Simo and Taylor (1984)] for classical elastoplasticity and is modified herein to account for the nonlinear kinematic hardening rule proposed by Chaboche (1986) and the plasticity-damage coupling.

At the beginning of current step t_n, the trial stresses $\boldsymbol{\sigma}^e$ are anticipated for the increment

t_{n+1} considering a purely elastic behaviour under the current state of damage.

$$\boldsymbol{\sigma}^e = (1-D_n)\boldsymbol{M}\,(\boldsymbol{\varepsilon}_n^e + \Delta\boldsymbol{\varepsilon}) \tag{3.20}$$

If the elastic prediction violates the yield condition,

$$F(\boldsymbol{s}^e, \boldsymbol{a}_n, \varepsilon_{q,n}, D_n) = \sqrt{\left(\frac{1}{1-D_n}\boldsymbol{s}^e - \boldsymbol{a}_n\right)\cdot\left(\frac{1}{1-D_n}\boldsymbol{s}^e - \boldsymbol{a}_n\right)} - \sqrt{\frac{2}{3}}k(\varepsilon_{q,n}) > 0 \tag{3.21}$$

an elastoplastic-damage corrector should be considered. In this case, starting from Eq. (3.2), the stress-strain relation at the end of the increment can be evaluated using the Euler-backward integration scheme as follows:

$$\boldsymbol{\sigma}_{n+1} = (1-D_{n+1})\boldsymbol{M}\,(\boldsymbol{\varepsilon}_n^e + \Delta\boldsymbol{\varepsilon}) - 2G(1-D_{n+1})\sqrt{\frac{3}{2}}\Delta\varepsilon_q\boldsymbol{n}_{n+1} \tag{3.22}$$

or using Eq. (3.20),

$$\boldsymbol{\sigma}_{n+1} = \frac{1-D_{n+1}}{1-D_n}\boldsymbol{\sigma}^e - 2G(1-D_{n+1})\sqrt{\frac{3}{2}}\Delta\varepsilon_q\boldsymbol{n}_{n+1} \tag{3.23}$$

where the damage value is integrated as:

$$D_{n+1} = D_n + F'_{D,n+1}\Delta\varepsilon_q \tag{3.24}$$

and $F'_{D,n+1}$ is the value of the damage function, evaluated at step t_{n+1}. From Eq. (3.23), the deviatoric part of the stress tensor is defined as

$$\boldsymbol{s}_{n+1} = \frac{1-D_{n+1}}{1-D_n}\boldsymbol{s}^e - 2G(1-D_{n+1})\sqrt{\frac{3}{2}}\Delta\boldsymbol{\varepsilon}_q\boldsymbol{n}_{n+1} \tag{3.25}$$

Each backstress tensor is integrated individually over the step and the total backstress tensor is evaluated as:

$$\boldsymbol{a}_{n+1} = \sum_{i=1}^{N} \left(\boldsymbol{a}_{n+1}^{i}\right) = \sum_{i=1}^{N} \left(\mu_i \boldsymbol{a}_n^i\right) + \sqrt{\frac{3}{2}} \sum_{i=1}^{N} \left(C_i \mu_i\right) \Delta\varepsilon_q \boldsymbol{n}_{n+1} \tag{3.26}$$

with

$$\mu_i = \left(1 + \gamma_i \Delta\varepsilon_q\right)^{-1} \tag{3.27}$$

Enforcing the von-Mises criterion at the end of the increment (consistency condition),

$$F_{n+1} = \left\| \frac{1}{1-D_{n+1}} \boldsymbol{s}_{n+1} - \boldsymbol{a}_{n+1} \right\| - \sqrt{\frac{2}{3}} k(\varepsilon_{q,n} + \Delta\varepsilon_q) = 0 \tag{3.28}$$

Combining Eq. (3.25) with Eq. (3.26) one derives that

$$\frac{\boldsymbol{s}_{n+1}}{1-D_{n+1}} - \boldsymbol{a}_{n+1} = \frac{\boldsymbol{s}^e}{1-D_n} - \sum_{i=1}^{N} \left(\mu_i \boldsymbol{a}_n\right) - \sqrt{\frac{3}{2}} \Delta\varepsilon_q \left[2G + \sum_{i=1}^{N} \left(\mu_i C_i\right)\right] \boldsymbol{n}_{n+1} \tag{3.29}$$

Subsequently, multiplying all terms of Eq. (3.28) with $\boldsymbol{n}_{n+1}$, one obtains:

$$\frac{1}{1-D_{n+1}} \boldsymbol{s}_{n+1} - \boldsymbol{a}_{n+1} = \sqrt{\frac{2}{3}} k(\varepsilon_{q,n} + \Delta\varepsilon_q) \boldsymbol{n}_{n+1} \tag{3.30}$$

Defining scalar quantity δ_1 and the second order tensor $\boldsymbol{\Xi}^D$ as follows

$$\delta_1 = \sqrt{\frac{3}{2}} \Delta\varepsilon_q \left[2G + \sum_{i=1}^{N} \left(\mu_i C_i\right)\right] \tag{3.31}$$

$$\boldsymbol{\Xi}^D = \frac{1}{1-D_n} \boldsymbol{s}^e - \sum_{i=1}^{N} \left(\mu_i \boldsymbol{a}_n\right) \tag{3.32}$$

Eq. (3.30) can be written in the following form:

$$\boldsymbol{\Xi}^D = \left[\delta_1 + \sqrt{\frac{2}{3}} k(\varepsilon_{q,n} + \Delta\varepsilon_q)\right] \boldsymbol{n}_{n+1} \tag{3.33}$$

Eq. (3.33) shows that $\boldsymbol{\Xi}^D$ is parallel to $\boldsymbol{n}_{n+1}$, therefore the outward unit normal $\boldsymbol{n}_{n+1}$ to the yield surface at the end of the increment can be computed from $\boldsymbol{\Xi}^D$ as

$$\boldsymbol{n}_{n+1} = \frac{1}{\|\boldsymbol{\Xi}^D\|}\boldsymbol{\Xi}^D \tag{3.34}$$

Multiplying both sides of Eq. (3.33) by $\boldsymbol{n}_{n+1}$ and with the aid of Eq. (3.34), the following equation with respect to a single unknown ($\Delta\varepsilon_q$) is formed.

$$G\left(\Delta\varepsilon_q\right) \equiv \|\boldsymbol{\Xi}^D\| - \delta_1 - \sqrt{\frac{2}{3}}k(\varepsilon_{q,n} + \Delta\varepsilon_q) = 0 \tag{3.35}$$

In comparison to other integration algorithms proposed in the literature [e.g. Doghri (1995); Bonora et al. (2014)], the present algorithm couples plasticity with damage using a generalized damage function which depends on the stress tensor, the damage state and the equivalent plastic strain and updates the internal variables through the solution of a single scalar equation (Eq. 3.35). Note that $G(\Delta\varepsilon_q)$ is a monotonically decreasing function of $\Delta\varepsilon_q$ and it can be further shown that

$$\lim_{\Delta\varepsilon_q\to\infty} G(\Delta\varepsilon_q) = -\infty \tag{3.36}$$

Therefore, for positive values of $\Delta\varepsilon_q$, Eq. (3.35) rapidly converges to a unique solution and hence, it can be readily solved using a local iterative solution procedure that employs Newton's method without requiring the predefinition of initial values. The numerical solution of Eq. (3.35) using Newton's method is rather straightforward and therefore it will not be presented in detail.

3.2.3 Consistent elastoplastic operator

An analytical derivation of the consistent tangent operator of the above numerical integration scheme is presented in this section. The corresponding moduli $\boldsymbol{M}_{ep}^{L}$ are

defined as the following derivative.

$$\boldsymbol{M}_{ep}^{L} = \frac{\partial \boldsymbol{\sigma}_{n+1}}{\partial \Delta \boldsymbol{\varepsilon}} \tag{3.37}$$

Therefore, from Eq. (3.22)

$$\boldsymbol{M}_{ep}^{L} = \frac{\partial}{\partial \Delta \boldsymbol{\varepsilon}} \left\{ \frac{1-D_{n+1}}{1-D_n} \boldsymbol{\sigma}^e - (1-D_{n+1}) 2G \sqrt{\frac{3}{2}} \Delta \varepsilon_q \boldsymbol{n}_{n+1} \right\} \tag{3.38}$$

Differentiation of the two terms in the brackets of Eq. (3.38) requires additional analytical work and the calculation of $\frac{\partial \Delta \varepsilon_q}{\partial \Delta \boldsymbol{\varepsilon}}$. More specifically, differentiation of the first term yields

$$\frac{\partial}{\partial \Delta \boldsymbol{\varepsilon}} \left\{ \frac{1-D_{n+1}}{1-D_n} \boldsymbol{\sigma}^e \right\} = \frac{\boldsymbol{\sigma}^e}{1-D_n} \otimes \frac{\partial (1-D_{n+1})}{\partial \Delta \boldsymbol{\varepsilon}} + (1-D_{n+1}) \frac{\partial}{\partial \Delta \boldsymbol{\varepsilon}} \left\{ \frac{\boldsymbol{\sigma}^e}{1-D_n} \right\} \tag{3.39}$$

and differentiation of the second term gives

$$\begin{aligned} \frac{\partial}{\partial \Delta \boldsymbol{\varepsilon}} \left\{ -\sqrt{\frac{3}{2}} 2G(1-D_{n+1}) \Delta \varepsilon_q \boldsymbol{n}_{n+1} \right\} = -2G \sqrt{\frac{3}{2}} \Bigg[& \Delta \varepsilon_q \boldsymbol{n}_{n+1} \otimes \frac{\partial (1-D_{n+1})}{\partial \Delta \boldsymbol{\varepsilon}} \\ & + (1-D_{n+1}) \boldsymbol{n}_{n+1} \otimes \frac{\partial \Delta \varepsilon_q}{\partial \Delta \boldsymbol{\varepsilon}} + (1-D_{n+1}) \Delta \varepsilon_q \frac{\partial \boldsymbol{n}_{n+1}}{\partial \Delta \boldsymbol{\varepsilon}} \Bigg] \end{aligned} \tag{3.40}$$

From Eq. (3.24), the derivative $\frac{\partial D_{n+1}}{\partial \Delta \boldsymbol{\varepsilon}}$ can be expressed as follows by using the chain rule property.

$$\frac{\partial D_{n+1}}{\partial \Delta \boldsymbol{\varepsilon}} = F'_{D,n+1} \frac{\partial \Delta \varepsilon_q}{\partial \Delta \boldsymbol{\varepsilon}} + \Delta \varepsilon_q \left[\frac{\partial F'_{D,n+1}}{\partial \Delta \varepsilon_q} \frac{\partial \Delta \varepsilon_q}{\partial \Delta \boldsymbol{\varepsilon}} + \frac{\partial F'_{D,n+1}}{\partial \boldsymbol{\sigma}_{n+1}} \frac{\partial \boldsymbol{\sigma}_{n+1}}{\partial \Delta \boldsymbol{\varepsilon}} + \frac{\partial F'_{D,n+1}}{\partial D_{n+1}} \frac{\partial D_{n+1}}{\partial \Delta \boldsymbol{\varepsilon}} \right] \tag{3.41}$$

Rearranging the terms in Eq. (3.41), the derivative $\frac{\partial D_{n+1}}{\partial \Delta \boldsymbol{\varepsilon}}$ can be explicitly computed as:

$$\frac{\partial D_{n+1}}{\partial \Delta \boldsymbol{\varepsilon}} = \beta_1 \frac{\partial \Delta \varepsilon_q}{\partial \Delta \boldsymbol{\varepsilon}} + \boldsymbol{v}_1 \frac{\partial \boldsymbol{\sigma}_{n+1}}{\partial \Delta \boldsymbol{\varepsilon}} \tag{3.42}$$

where,

$$\beta_1 = \frac{F'_{D,n+1} + \Delta\varepsilon_q \dfrac{\partial F'_{D,n+1}}{\partial \Delta\varepsilon_q}}{1 - \Delta\varepsilon_q \dfrac{\partial F'_{D,n+1}}{\partial D_{n+1}}} \quad \text{and} \quad \boldsymbol{v}_1 = \frac{\Delta\varepsilon_q}{1 - \Delta\varepsilon_q \dfrac{\partial F'_{D,n+1}}{\partial D_{n+1}}} \frac{\partial F'_{D,n+1}}{\partial \boldsymbol{\sigma}_{n+1}} \tag{3.43}$$

The partial derivatives included in Eq. (3.43) are computed by differentiating the damage function under consideration with respect to the corresponding arguments. Using Eqs. (3.39, 3.40, 3.42), and substituting in Eq. (3.38), the derivative $\dfrac{\partial \boldsymbol{\sigma}_{n+1}}{\partial \Delta\boldsymbol{\varepsilon}}$ can be expressed as:

$$\begin{aligned} \frac{\partial \boldsymbol{\sigma}_{n+1}}{\partial \Delta\boldsymbol{\varepsilon}} = \boldsymbol{X} \Bigg[& (1 - D_{n+1})\boldsymbol{M} - \frac{\beta_1}{1 - D_n} \boldsymbol{\sigma}^e \otimes \frac{\partial \Delta\varepsilon_q}{\partial \Delta\boldsymbol{\varepsilon}} \\ & + 2G\sqrt{\frac{3}{2}} \left(\Delta\varepsilon_q \beta_1 - 1 + D_{n+1} \right) \boldsymbol{n}_{n+1} \otimes \frac{\partial \Delta\varepsilon_q}{\partial \Delta\boldsymbol{\varepsilon}} - 2G\sqrt{\frac{3}{2}} (1 - D_{n+1}) \Delta\varepsilon_q \frac{\partial \boldsymbol{n}_{n+1}}{\Delta\boldsymbol{\varepsilon}} \Bigg] \end{aligned} \tag{3.44}$$

with $\boldsymbol{X}$ being a fourth-order tensor expressed as:

$$\boldsymbol{X} = \left[\boldsymbol{I} + \frac{\boldsymbol{\sigma}^e}{1 - D_n} \otimes \boldsymbol{v}_1 - 2G\sqrt{\frac{3}{2}} \Delta\varepsilon_q \boldsymbol{n}_{n+1} \otimes \boldsymbol{v}_1 \right]^{-1} \tag{3.45}$$

and $\boldsymbol{I}$ is the fourth-order identity tensor. Eq. (3.45) requires matrix inversion which is attributed to the consideration of the stress tensor in the damage potential. Nevertheless, this matrix inversion is computed once in each step and does not influence noticeably the numerical efficiency of the numerical scheme.

Next, the derivative $\dfrac{\partial \Delta\varepsilon_q}{\partial \Delta\boldsymbol{\varepsilon}}$ can be obtained by differentiating the consistency condition, expressed in Eq. (3.35), with respect to $\Delta\boldsymbol{\varepsilon}$. The derivative of Eq. (3.35) with respect to $\Delta\boldsymbol{\varepsilon}$ is written in the following form:

$$\frac{\partial G\left(\Delta\varepsilon_q\right)}{\partial \Delta\boldsymbol{\varepsilon}} \equiv \frac{\partial \|\boldsymbol{\Xi}^D\|}{\partial \Delta\boldsymbol{\varepsilon}} - \frac{\partial \delta_1}{\partial \Delta\boldsymbol{\varepsilon}} - \sqrt{\frac{2}{3}} \frac{\partial k(\varepsilon_{q,n} + \Delta\varepsilon_q)}{\partial \Delta\boldsymbol{\varepsilon}} = 0 \tag{3.46}$$

After some mathematical manipulations, the derivatives of the three terms of Eq. (3.46) are computed as

$$\frac{\partial \|\boldsymbol{\Xi}^D\|}{\partial \Delta\boldsymbol{\varepsilon}} = 2G\boldsymbol{n}_{n+1} + \sum_{i=1}^{N} \left(\gamma_i \mu_i^2 \boldsymbol{a}_n^i\right) \cdot \boldsymbol{n}_{n+1} \frac{\partial \Delta\varepsilon_q}{\Delta\boldsymbol{\varepsilon}} \tag{3.47}$$

$$\sqrt{\frac{2}{3}} \frac{\partial k(\varepsilon_{q,n} + \Delta\varepsilon_q)}{\partial \Delta\boldsymbol{\varepsilon}} = \sqrt{\frac{2}{3}} k'(\varepsilon_{q,n} + \Delta\varepsilon_q) \frac{\partial \Delta\varepsilon_q}{\partial \Delta\boldsymbol{\varepsilon}} \tag{3.48}$$

$$\frac{\partial \delta_1}{\partial \Delta\boldsymbol{\varepsilon}} = \sqrt{\frac{3}{2}} \frac{\partial \Delta\varepsilon_q}{\partial \Delta\boldsymbol{\varepsilon}} \left[2G + \sum_{i=1}^{N} (C_i \mu_i) - \Delta\varepsilon_q \sum_{i=1}^{N} \left(C_i \gamma_i \mu_i^2\right)\right] \tag{3.49}$$

where prime $(\cdot)'$ denotes differentiation with respect to the increment of the equivalent plastic strain ($\Delta\varepsilon_q$). Substituting the right-hand parts of Eqs. (3.47-3.49) in Eq. (3.46), the derivative $\dfrac{\partial \Delta\varepsilon_q}{\partial \Delta\boldsymbol{\varepsilon}}$ is computed as follows:

$$\frac{\partial \Delta\varepsilon_q}{\partial \Delta\boldsymbol{\varepsilon}} = \frac{2G}{H} \boldsymbol{n}_{n+1} \tag{3.50}$$

where modulus H is expressed as,

$$\begin{aligned} H = \sqrt{\frac{3}{2}} \left[2G + \sum_{i=1}^{N} (C_i \mu_i) - \Delta\varepsilon_q \sum_{i=1}^{N} \left(C_i \gamma_i \mu_i^2\right)\right] + \sqrt{\frac{2}{3}} k'(\varepsilon_{q,n} + \Delta\varepsilon_q) \\ - \sum_{i=1}^{N} \left(\gamma_i \mu_i^2 \boldsymbol{a}_n^i\right) \cdot \boldsymbol{n}_{n+1} \end{aligned} \tag{3.51}$$

It can be readily shown that for $\Delta\varepsilon_q \to 0$ modulus H in Eq. (3.51) becomes identical to modulus h obtained from Eq. (3.17). Finally, the derivative $\dfrac{\partial \boldsymbol{n}_{n+1}}{\partial \Delta\boldsymbol{\varepsilon}}$ is computed by considering the following differentiation, using the chain rule

$$\frac{\partial \boldsymbol{n}_{n+1}}{\partial \Delta\boldsymbol{\varepsilon}} = \frac{\partial \boldsymbol{n}_{n+1}}{\partial \boldsymbol{\Xi}^D} \frac{\partial \boldsymbol{\Xi}^D}{\partial \Delta\boldsymbol{\varepsilon}} \tag{3.52}$$

After some mathematical manipulations one obtains

$$\frac{\partial \boldsymbol{n}_{n+1}}{\partial \Delta \boldsymbol{\varepsilon}} = \frac{2G}{\|\boldsymbol{\Xi}^D\|}\left(\boldsymbol{I} - \frac{1}{3}\mathbf{1}\otimes\mathbf{1}\right) + \frac{2G}{H\|\boldsymbol{\Xi}^D\|}\sum_{i=1}^{N}\left(\gamma_i \mu_i^2 \boldsymbol{a}_n^i\right)\otimes \boldsymbol{n}_{n+1} - \frac{2G}{\|\boldsymbol{\Xi}^D\|}\left[1 + \frac{1}{H}\sum_{i=1}^{N}\left(\gamma_i \mu_i^2 \boldsymbol{a}_n^i\right)\cdot \boldsymbol{n}_{n+1}\right]\boldsymbol{n}_{n+1}\otimes \boldsymbol{n}_{n+1} \tag{3.53}$$

Taking into consideration Eqs. (3.50, 3.53), and with the aid of Eq. (3.44), the consistent tangent moduli can be obtained as follows:

$$\boldsymbol{M}_{ep}^{L} = \boldsymbol{X}\left[\phi\boldsymbol{\sigma}^e\otimes\boldsymbol{n}_{n+1} + (1-D_{n+1})\boldsymbol{M} + \chi\boldsymbol{n}_{n+1}\otimes\boldsymbol{n}_{n+1} + \psi\left(\boldsymbol{I} - \frac{1}{3}\mathbf{1}\otimes\mathbf{1}\right) + \frac{\psi}{H}\sum_{i=1}^{N}\left(\gamma_i\mu_i^2\boldsymbol{a}_n^i\right)\otimes\boldsymbol{n}_{n+1}\right] \tag{3.54}$$

where, the scalar coefficients ϕ, χ and ψ are given by the following expressions:

$$\phi = -\frac{2G\beta_1}{H(1-D_n)} \tag{3.55}$$

$$\chi = 4G^2\sqrt{\frac{3}{2}}\left[\frac{\Delta\varepsilon_q\beta_1 - 1 + D_{n+1}}{H} + \frac{\Delta\varepsilon_q(1-D_{n+1})}{\|\boldsymbol{\Xi}^D\|} + \frac{\Delta\varepsilon_q(1-D_{n+1})}{H\|\boldsymbol{\Xi}^D\|}\sum_{=1}^{N}\left(\gamma_i\mu_i^2\boldsymbol{a}_n^i\right)\cdot\boldsymbol{n}_{n+1}\right] \tag{3.56}$$

$$\psi = -\frac{4G^2}{\|\boldsymbol{\Xi}^D\|}\sqrt{\frac{3}{2}}(1-D_{n+1})\Delta\varepsilon_q \tag{3.57}$$

Eqs. (3.38-3.54) indicate that regardless of the strong coupling between plasticity and damage, the consistent moduli are computed in a straightforward manner without requiring excessive analytical work or the solution of a complicated system of equations, as in numerical schemes presented in the past. This feature is attributed to the single-equation integration algorithm developed in Section 3.2.2. It can be verified that Eq. (3.54) is consistent with the present integration algorithm; considering $\Delta\varepsilon_q \to 0$ one can readily show that the algorithmic moduli of Eq. (3.54) become equal to the tangent moduli reported in Eq. (3.19). The derived consistent moduli provide quadratic

converge of the solution method and are different from those presented in [Doghri (1995); Bonora et al. (2014)] due to the consideration of different coupling conditions [Bonora et al. (2014)] and different treatment of the integration algorithm [Doghri (1995); Bonora et al. (2014)]. The solution algorithm of the incremental problem is summarised in Table 3.1.

Table 3.1: Summary of the incremental solution procedure.

Elastic predictor	$\boldsymbol{\sigma}^e = (1-D_n)\boldsymbol{M}\,(\boldsymbol{\varepsilon}_n^e + \Delta\boldsymbol{\varepsilon})$
Check for yielding	$F(\boldsymbol{s}^e, \boldsymbol{a}_n, \varepsilon_{q,n}, D_n)$
If $F \leqslant 0$ then set	$\boldsymbol{s}_{n+1} = \boldsymbol{s}^e$, $\boldsymbol{\sigma}_{n+1} = \boldsymbol{\sigma}^e$, $\boldsymbol{a}_{n+1} = \boldsymbol{a}_n$, $\varepsilon_{q,n+1} = \varepsilon_{q,n}$, $D_{n+1} = D_n$
If $F > 0$ plastic-damage correction is necessary	
Set $\Delta\varepsilon_q = \Delta\varepsilon_q^0$ (arbitrarily initial guess)	
Compute δ_1	$\delta_1 = \sqrt{\frac{3}{2}}\Delta\varepsilon_q \left[2G + \sum_{i=1}^{N}(\mu_i C_i)\right]$
Compute $\boldsymbol{\Xi}^D$	$\boldsymbol{\Xi}^D = \dfrac{1}{1-D_n}\boldsymbol{s}^e - \sum_{i=1}^{N}(\mu_i \boldsymbol{a}_n)$
Check equilibrium	$G(\Delta\varepsilon_q) \equiv \|\boldsymbol{\Xi}^D\| - \delta_1 - \sqrt{\frac{2}{3}}k(\varepsilon_{q,n} + \Delta\varepsilon_q) = 0$
Compute $G'(\Delta\varepsilon_q)$	$G'(\Delta\varepsilon_q) = \dfrac{\partial G(\Delta\varepsilon_q)}{\partial \Delta\varepsilon_q}$
Compute $d\Delta\varepsilon_q$	$d\Delta\varepsilon_q = -\dfrac{G(\Delta\varepsilon_q)}{G'(\Delta\varepsilon_q)}$
Update $\Delta\varepsilon_q$	$\Delta\varepsilon_q = \Delta\varepsilon_q + d\Delta\varepsilon_q$
Check	$\left\|\dfrac{d\Delta\varepsilon_q}{\Delta\varepsilon_q}\right\| < tol$ and $\|G(\Delta\varepsilon_q)\| < tol$, if not repeat
Update internal variables and evaluate $\boldsymbol{M}_{ep}^L$	
Update D_{n+1}	$D_{n+1} = D_n + F'_{D,n+1}\Delta\varepsilon_q$
Compute μ_i	$\mu_i = \left(1 + \gamma_i \Delta\varepsilon_q\right)^{-1}$
Update $\boldsymbol{a}_{n+1}$	$\boldsymbol{a}_{n+1} = \sum_{i=1}^{N}\left(\mu_i \boldsymbol{a}_n^i\right) + \sqrt{\frac{3}{2}}\sum_{i=1}^{N}(C_i\mu_i)\,\Delta\varepsilon_q \boldsymbol{n}_{n+1}$
Update $\boldsymbol{\sigma}_{n+1}$	$\boldsymbol{\sigma}_{n+1} = \dfrac{1-D_{n+1}}{1-D_n}\boldsymbol{\sigma}^e - 2G(1-D_{n+1})\sqrt{\frac{3}{2}}\Delta\varepsilon_q \boldsymbol{n}_{n+1}$
Update $\boldsymbol{M}_{ep}^L$	$\boldsymbol{M}_{ep}^L = \boldsymbol{X}\Big[\phi\boldsymbol{\sigma}^e \otimes \boldsymbol{n}_{n+1} + (1-D_{n+1})\boldsymbol{M} + \chi \boldsymbol{n}_{n+1}\otimes\boldsymbol{n}_{n+1} + \frac{\psi}{H}\sum_{i=1}^{N}\left(\gamma_i \mu_i^2 \boldsymbol{a}_n^i\right)\otimes\boldsymbol{n}_{n+1} + \psi\left(\boldsymbol{I} - \frac{1}{3}\mathbf{1}\otimes\mathbf{1}\right)\Big]$

3.2.4 Algorithmic implementation and simulation of damage

To mitigate mesh dependency and abrupt pressure oscillations, the findings of Cervera et al. (2003, 2004); Cervera and Chiumenti (2006, 2009), discussed in Section 1.2.2.3, are incorporated in the numerical simulation with proper adjustments. With respect to the finite element modelling part, enhanced finite elements incorporating pressure/displacement formulation are employed. This type of finite element formulation is available in the majority of commercial finite element software such as ABAQUS (2016), it can be used for plasticity-damage simulation, and does not increase the computational cost significantly in comparison to standard formulations [ABAQUS (2016)]. Regarding the isotropic damage function, various CDM models can be implemented under the proposed numerical scheme, but to eliminate mesh dependency effects the softening modulus must be properly regularised according to the element size [e.g. Rankine model as shown by Cervera and Chiumenti (2006)]. For the scope of the present study, the modified version of Hillerborg et al. (1976) CDM model is employed, as proposed by Bazant and Oh (1983) on the basis of the smeared band approach. The governing equation of the damage function employed herein is presented in Eq. (3.58).

$$F_D' = \frac{S_{y0}}{2G_f} l_{ch} \tag{3.58}$$

In Eq. (3.58) S_{y0} denotes the radius of the equivalent yield surface at the instant of damage initiation, G_f is the fracture energy release rate per unit crack growth, and l_{ch} is the element's characteristic length. In the present work, linear solid ("brick") finite elements are employed and l_{ch} is taken equal to $\sqrt[3]{(12/\sqrt{2})V_{el}}$ as proposed by Oliver (1989), where V_{el} is the element's volume. In ABAQUS (2016) software, the consideration of V_{el} within the user-material subroutine UMAT requires the development of two supplementary user-subroutines, namely UVARM and UEXTERNALDB. Subroutine UVARM is called in every integration point to compute V_{el} as this information is not

included as input in the user-material subroutine UMAT whereas subroutine UEXTERNALDB is used to transfer this information from UVARM into UMAT.

The major advantage of this "simple" CDM model is that its application requires the definition of a single material parameter, G_f. The material parameter G_f, originally proposed by Hillerborg et al. (1976), is measured from appropriate material tests. More recently, Bai and Wierzbicki (2008) used the CDM model presented in Eq. (3.58) to simulate ductile fracture in metal components under monotonic loading and proposed the calibration of G_f using a combine experimental-numerical calibration approach, which seemingly leads to more accurate results. A similar calibration approach was employed by Novokshanov et al. (2015) who recently modified the CDM model proposed by Bai and Wierzbicki (2008) to account for temperature and strain-rate effects into the damage function.

3.2.5 Simulation of large-scale experiments

3.2.5.1 Experimental program

Very recent experimental studies [Jeon et al. (2017); Pereira et al. (2017); Jiang et al. (2019)] have argued that accurate simulation of the elastoplastic-damage response of steel circular tubular components with computationally efficient numerical tools is a topic that attracts a lot of attention. In light of these studies, the proposed numerical scheme is validated using the experimental data presented in Section 2.3.1 [Pappa et al. (2012)]. Herein, two tests of the experimental campaign are considered. The two specimens ($E6$ and $E7$) have been subjected to severe cyclic loading with amplitude of $\pm$250 mm ($E6$) and $\pm$300 mm ($E7$), which resulted in failure of the specimens under ultra low-cycle fatigue after 15 and 11 cycles, respectively.

3.2.5.2 Finite element model: 3D formulation

The proposed numerical scheme is implemented through an appropriate material user-subroutine UMAT in the commercial finite element package ABAQUS (2016) to simulate the mechanical response of specimen $E6$ and $E7$. The experimental set-up shown in Fig. 2.5 is double-symmetric, allowing for modelling of 1/4 of the specimen with the use of appropriate symmetry conditions. In addition, thickness variation, observed through thickness measurements prior to testing are taken into account in the finite element model. The finite element model presented in Fig. 3.1 consists of a straight pipe, a welding component and a bend (elbow). Continuity conditions among these parts are satisfied through appropriate kinematic coupling of connecting surfaces, while support conditions are utilised with the use of a reference point (RP-1) and kinematic coupling restrains. Reference point RP-1 is kinematically coupled with the end nodes of the straight part, in order to simulate the roller support of the testing set-up, and the fact that the specimens are capped. The horizontal displacement of point RP-1 along the x axis is prescribed and corresponds to the one applied in the experiments. The translational degrees of freedom with respect to y and z axes are fully restrained, together with the rotation about the x and y axes.

To demonstrate that the numerical results are free from spurious mesh dependency, four different meshes of the present finite element model, denoted as "M1", "M2", "M3" and "M4", are used in all simulations. In all cases, linear "brick" elements [C3D8I in ABAQUS (2016)] are used in a non-uniform mesh for increased computational efficiency; denser discretisation is applied at the elbow area, and in particular in the critical location ("flank"), whereas a rather coarse mesh is used for the straight parts where strains are significantly lower. Meshes M1-M4 are illustrated in Fig. 3.2 showing in detail the flank location, while information on the element dimensions and volume at the flank location are summarised in Table 3.2.

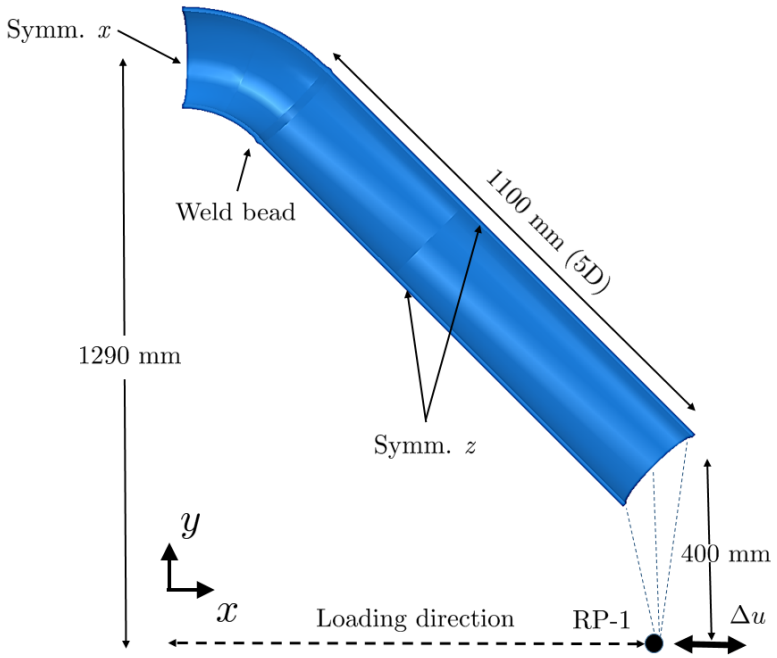

Figure 3.1: Numerical model (solid model) of the test specimen.

Table 3.2: Mesh size information at the elbow flank.

Mesh	M1	M2	M3	M4
Element dim. (mm)	$10 \times 10 \times 2$	$8 \times 8 \times 1.6$	$6.5 \times 6.5 \times 1.33$	$5 \times 5 \times 1.14$
Element vol. (mm^3)	200	102.4	56.2	28.5
l_{ch} (mm)	11.12	8.85	7.62	5.78

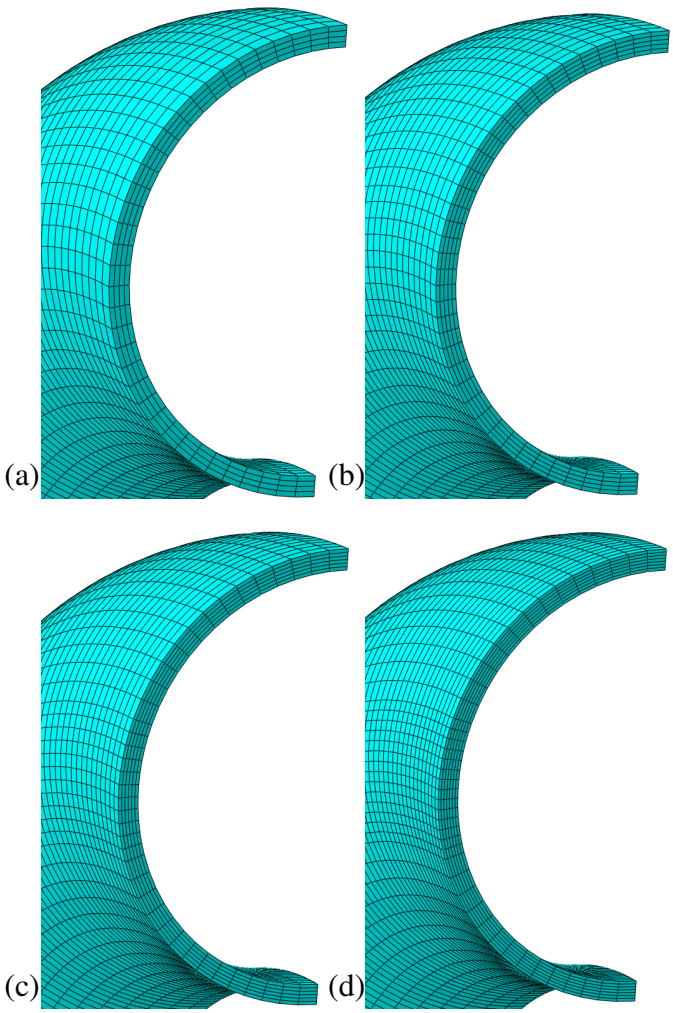

Figure 3.2: Finite element discretization of the elbow area: (a) mesh "M1", (b) mesh "M2", (c) mesh "M3", (d) mesh "M4".

3.2.5.3 Calibration of cyclic plasticity-damage model

The isotropic and kinematic hardening parameters of the constitutive model are chosen so that the strain-control small-scale tests on strip specimens, shown in Fig. 3.3, are accurately represented. The stress-control tests used for calibrating the ratcheting material model [Section 2.3.3] are not considered herein as the numerical simulations are limited to less than 20 load cycles and ratcheting phenomena are not of main concern. Isotropic hardening is simulated with an exponential function with saturation (see Section 2.3.3) and four superimposed backstress tensors are employed to simulate

kinematic hardening [Chaboche (1991); Bari and Hassan (2002)]. The selected material parameters of the constitutive model are presented in Table 3.3. Using those parameters, the stress-strain curves for 1.5% and 2.2% strain amplitude obtained experimentally from material extracted from the elbows are accurately simulated, as shown in Fig. 3.3. On the other hand, no information was available for calibrating the damage parameters. Therefore, in the absence of dedicated material testing and for the purposes of the present simulations, the damage parameters are selected so that the finite element model with mesh M1 can predict accurately the number of cycles to failure of specimen $E7$. To quantify mesh dependency effects, these parameters are kept constant in all analyses.

The damage initiation equivalent plastic strain ε_f is taken equal to 1.0, the critical damage state D_{crit} is considered as 0.20 and the value of G_f, determining the damage evolution rate, is selected equal to 7000 J/mm. Parameter ε_f defines the value of the equivalent plastic strain to initiate damage accumulation and D_{crit} controls the maximum damage value the material can sustain prior to failure. For metals, its was proposed by Lemaitre and Desmorat (2005) that the value of D_{crit} may vary between $0.2 \leq D_{crit} \leq 1.0$, whereas significantly lower D_{crit} values reported by Bonora (1997). Furthermore, in the numerical simulations, once the damage variable in the material point becomes larger than the value of D_{crit}, the integration point is considered as fully damaged and its contribution is disregarded. When damage variable becomes larger than the D_{crit} value in all integration points of the element, then the element is deleted from the mesh. This technique allows modelling the development of through-thickness crack in a consistent manner. Bonora et al. (2004) and Bai and Wierzbicki (2008) have shown that negligible damage is accumulated when the pressure stress in the material is positive (compression) and lower than a specific value. Therefore, the CDM model employed is slightly modified to accommodate cyclic loading conditions; it is selected that damage is accumulated at the material point only under negative pressure stress state.

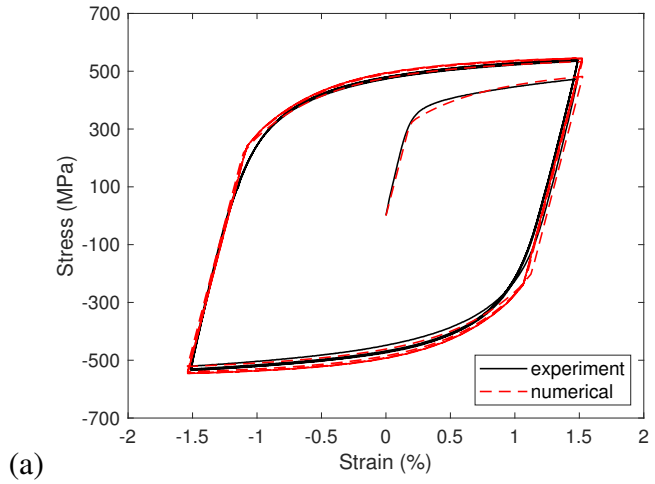

(a)

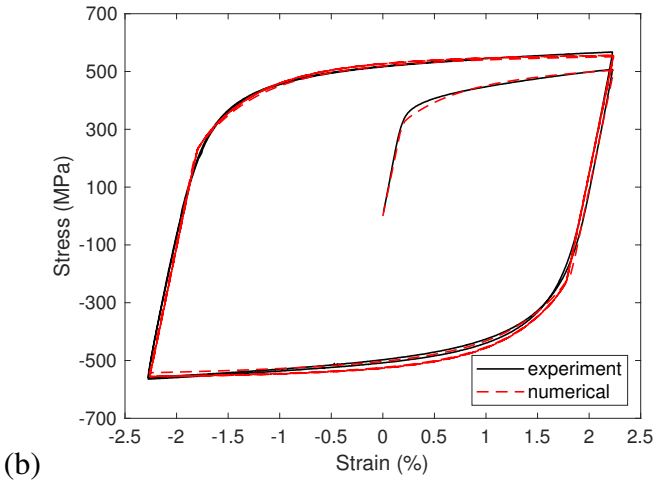

(b)

Figure 3.3: Inelastic material behaviour at strain amplitude (a) 1.5% and (b) 2.0%; material strip tests and numerical fit.

Table 3.3: Material properties of constitutive model.

Model	E (MPa)	v	σ_y (MPa)	Q_∞ (MPa)	b	C_{1-4} (MPa)	γ_{1-4}	ε_f	G_f (J/mm)	D_{crit}
Chaboche (1986)	2×10^5	0.3	315	75	30	16,607 3,000 1,190 380	300 116 100 40	1.0	7000	0.2

3.2.5.4 Numerical simulation results

Numerical results obtained from the finite element model equipped with the proposed numerical scheme implemented as material user subroutine UMAT are presented in Figs. 3.4-3.10 and are compared with the corresponding experimental data reported by Pappa et al. (2012). In Fig. 3.4 the force-displacement relations obtained from the first loading cycle are shown for both specimens. In this figure, the numerical results are denoted as "M1-M4", corresponding to the four finite element meshes. Fig. 3.4 indicates minor differences among the numerical results, while the comparison with experimental data shows the ability of the model to simulate quite accurately the inelastic load-displacement response of the pipe elbow under severe imposed deformations.

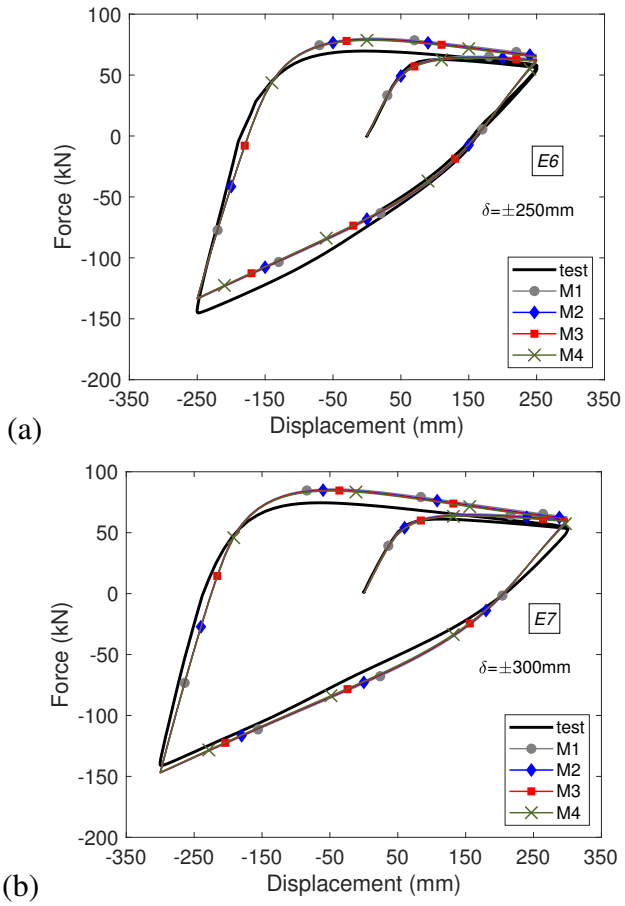

Figure 3.4: First loading cycle for (a) test $E6$ ($\delta = \pm 250$mm) and (b), test $E7$ ($\delta = \pm 300$mm).

Results from the simulation of elbow experiment $E7$ ($\delta = \pm 300$ mm) are presented in Fig. 3.5 and compared with the corresponding experimental data. Fig. 3.5(a, c) presents the force-displacement response obtained from the finer mesh (M4) and from experiment $E7$. In addition, the force amplitude recorded in each load cycle up to the point of through-thickness cracking is presented in Fig. 3.5(b) for meshes M1-M4, while Fig. 3.5(d) shows the corresponding experimental data. The force envelope predicted with mesh M4 is also included in Fig. 3.5(d) for comparison. It is remarkable that although the element size changes significantly between meshes M1 to M4, the results in terms of force amplitude show negligible differences with each other throughout the history of loading, indicating minimal mesh-dependency effects.

The gradual development of through-thickness crack is simulated with element deletion and occurs within 11 load cycles for meshes M1-M4. In meshed models M3 and M4 the through-thickness crack, defined as failure, occurs almost at the same analysis increment, indicating that the numerical results have achieved convergence and may not alter with further refinement of the mesh. Similar behaviour is observed in the work of Cervera and Chiumenti (2006). The number of cycles to failure obtained in all finite element models is very close to the corresponding number of cycles observed in the laboratory experiment (11 cycles).

The numerical predictions are also satisfactory for test $E6$, subjected to $\delta = \pm 250$ mm. Fig. 3.6 shows that the results from all numerical models are consistent and very close to the experimental data. In the numerical simulations, material (and strength) degradation initiated at the 5^{th} load cycle, while minor differences are observed between the four finite element meshes (M1, M2, M3, M4) throughout the load history, supporting further the outcomes derived from the examination of specimen $E7$. The number of cycles to failure obtained with all meshes is again very close to the corresponding number of cycles observed in the laboratory experiment (15 cycles), whereas the numerical results converge upon refinement of the mesh. Regardless of the complexity of these analyses, convergence of the incremental solution throughout the

analysis process is achieved within 2-5 global iterations.

Overall, Figs. (3.5-3.6) demonstrate that the simulation method employed is capable of predicting quite accurately the experimental results throughout the history of loading, despite some small over-prediction of elbow strength degradation in specimen $E6$. This small difference between numerical and experimental results may be attributed to the selection of the damage parameters. Bai and Wierzbicki (2008) suggested that the values of ε_f and D_{crit} should not be considered constant as these depend on the stress state of the material. Notwithstanding, the proper calibration of damage models for cyclic inelastic material response is still an open issue. Additional work is undertaken presently by the researcher to calibrate a CDM model for "ultra low-cycle fatigue" conditions, towards simulating the mechanical response of large-scale tubular welded connections [Chatziioannou (2020)].

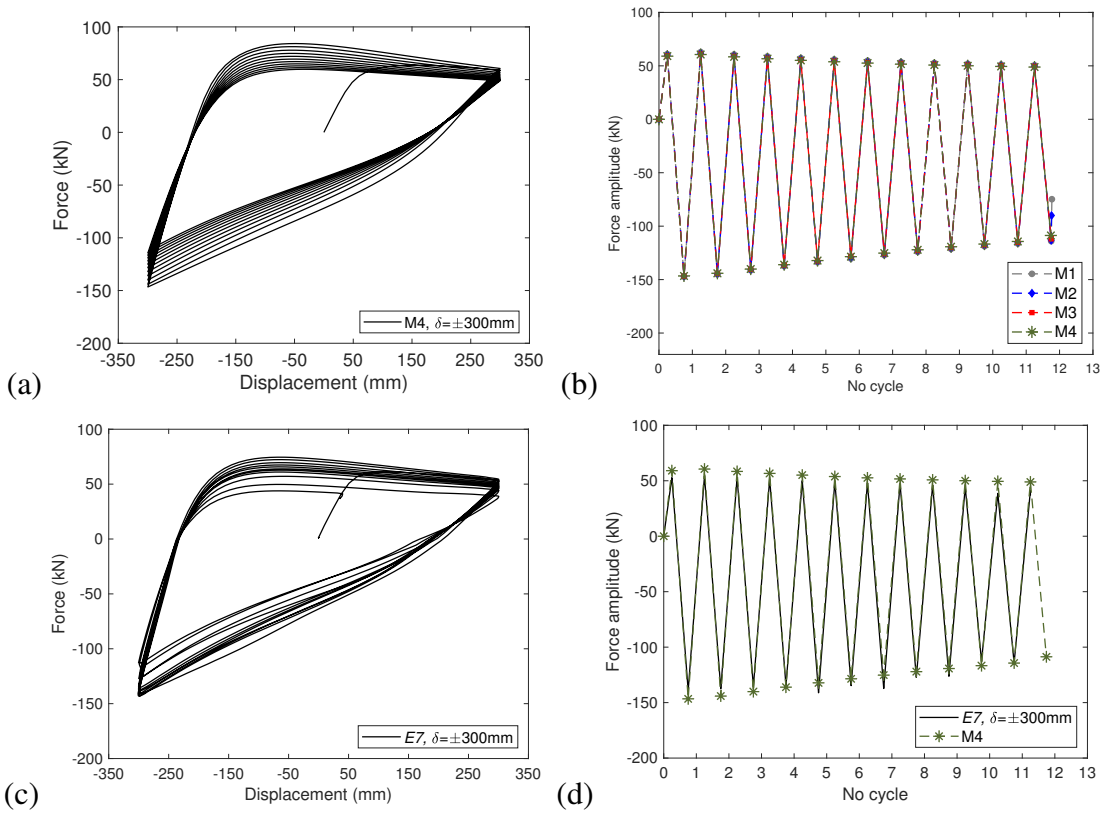

Figure 3.5: Numerical and experimental results for test $E7$ ($\delta = \pm 300$mm) in terms of force-displacement diagrams (a, c) and resistance reduction over the loading cycles (b, d).

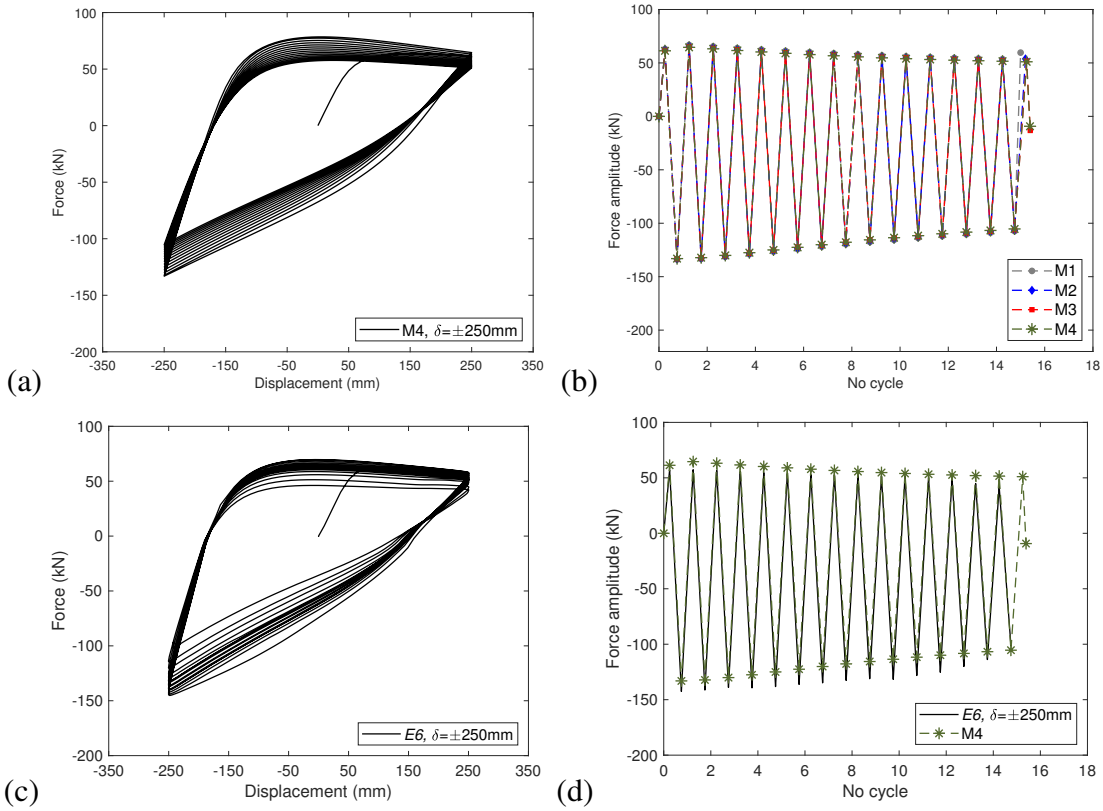

Figure 3.6: Numerical and experimental results for test $E6$ ($\delta = \pm 250$mm) in terms of force-displacement diagrams (a, c) and resistance reduction over the loading cycles.

In the above results, the efficiency of the finite element model equipped with the material user subroutine in simulating the mechanical response of the elbow specimens has been shown in terms of the force-displacement curves, the resistance reduction over the loading cycles and the number of cycles to through-thickness cracking.

Local strain predictions are of particular importance in assessing the integrity of steel structural members against low-cycle fatigue. The strain history at critical locations (elbow "flank") was measured during the experimental study using strain gauges. The majority of the strain gauges were detached due to the large value of the induced strains, and did not record an adequate number of strain cycles. The available data are limited to hoop strain measurements obtained 6 mm and 9 mm from the "flank" location (gauge 3 and gauge 2 in Fig. 2.6). The accuracy of the numerical scheme is also examined by comparing the numerically obtained maximum/minimum strain at the location of the

strain gauge with those recorded during testing. The experimental results of specimens $E6$ and $E7$ are presented in Fig. 3.7, considering also the results obtained from the four finite element meshes (M1, M2, M3 and M4).

Comparisons with experimental measurements are limited to 6 and 4 load cycles for specimens $E6$ and $E7$ due to strain gauge detachment. Fig. 3.7 indicates small differences between the results of meshes M1 to M4. It has to be considered that pipe elbows exhibit large variation of induced strain range near the elbow flank while upon mesh refinement strain measurements are not obtained at the exact same location. All models predict the experimental data satisfactorily during the initial load cycles, but fail to predict ratcheting evolution. In addition, the recorded compressive strains are significantly low and this is attributed on the gradual detachment of the strain gauges as discussed in Section 2.3.4.3. Recent studies [Khutia et al. (2015); Hassan et al. (2015); Foroutan et al. (2018); Chatziioannou et al. (2019b,a)] have shown that accurate simulation of ratcheting in pipe elbow components subjected to cyclic loading requires the use of constitutive models with advanced kinematic hardening rules. Overall, the differences between the results obtained from the four examined meshes remain almost constant throughout the loading history, indicating negligible mesh dependency.

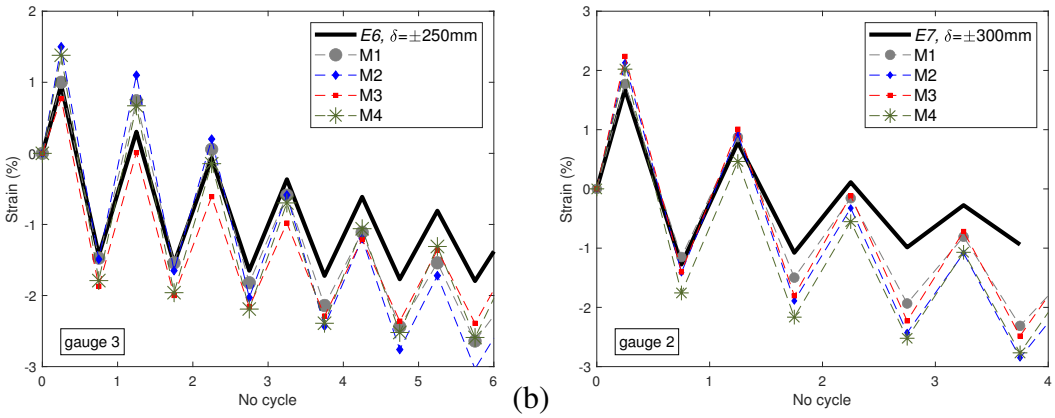

Figure 3.7: Variation of strain at the "flank" location of the two elbows: (a) specimen $E6$ and (b), specimen $E7$; comparisons between numerical results and experimental measurements.

Finally, the numerical simulations indicate the accumulation of damage at the "flank" of the bend due to excessive hoop strain, leading to low-cycle fatigue and pipe wall rupture which is absolutely consistent with the experimental observations. Figs. 3.8, 3.9 depict the local damage accumulation (SDV14) and the development of the through-thickness crack obtained numerically from the simulation of test $E7$ using meshed model M4. As shown in Fig. 3.9, damage initiated from the inner surface of the elbow. Subsequently it also occurred at the outer surface and propagated from both surfaces towards the mid-thickness, forming a through-thickness crack. Figs. 3.8, 3.9 verify that the damage pattern observed in the failure stage of the numerical model is very similar in size and configuration to the crack observed experimentally. Identical crack formations are observed in the other finite element models but are not presented for brevity.

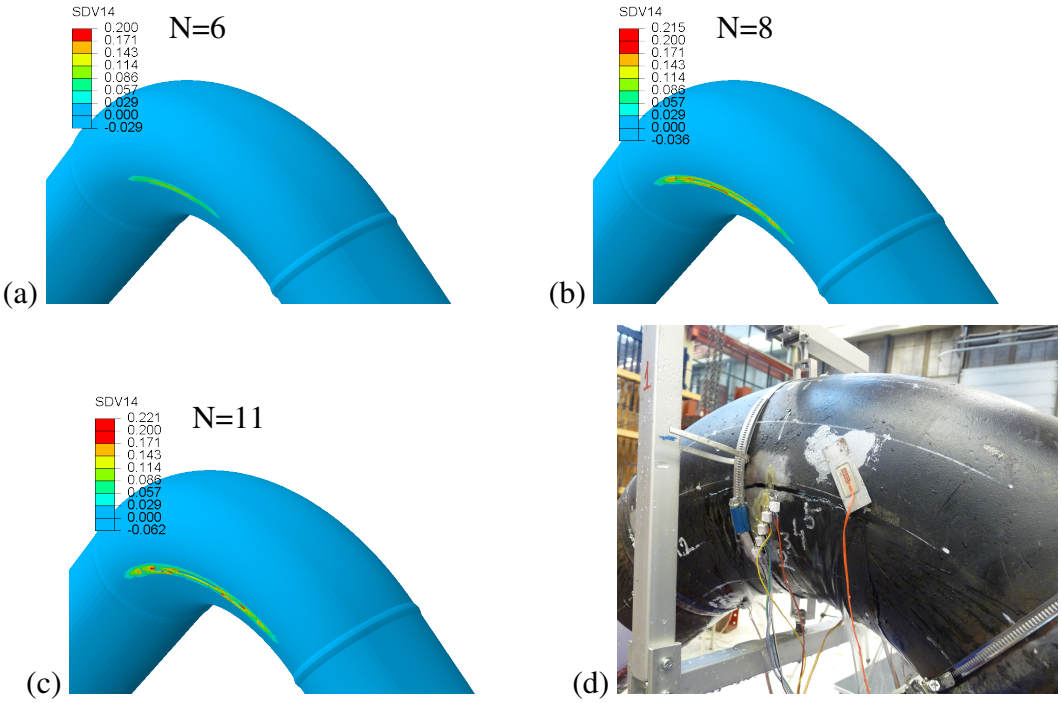

Figure 3.8: Damage distribution obtained from mesh M4 during the (a) 6^{th} load cycle, (b) 8^{th} load cycle and (c), 11 th load cycle; (d) experimental shape of crack specimen $E7$.

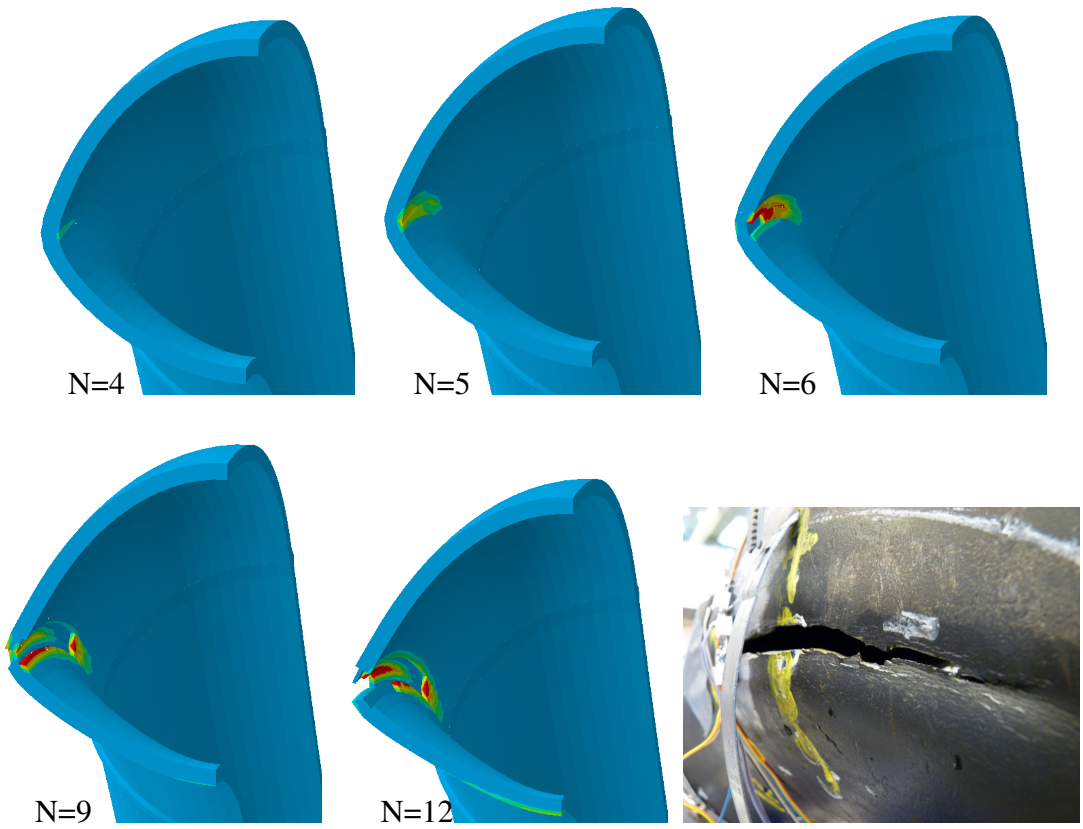

Figure 3.9: Through-thickness crack evolution with respect to loading cycles obtained for specimen $E7$ with mesh M4; Detail of crack configuration of specimen $E7$.

The contribution of mixed pressure/displacement finite element formulation on the quality of the results is also examined by conducting an additional analysis for experiment $E7$ using model M4, this time meshed with standard finite elements (C3D8 in ABAQUS). For shortness, the investigation is limited to the distribution of pressure stress before and after damage initiation. Prior to damage initiation the response is purely elastoplastic and both formulations retrieve identical pressure distribution. Hence, a single contour plot is provided in Fig. 3.10(a), showing the pressure distribution at the end of the 2^{th} load cycle. Two additional contour plots are included in Fig. 3.10(b, c) showing the distribution of pressure stress at the end of 8^{th} load cycle, obtained with standard and mixed finite elements. The comparison of Fig. 3.10(a-c) indicates that the use of standard finite elements in plasticity-damage simulations

leads to spurious pressure oscillation, accompanied with localisation of pressure stress, influencing the quality of the numerical results. On the the hand, the distribution of pressure stress obtained with mixed pressure/displacement formulation, shown in Fig. 3.10(c), is not influenced by the strain-softening material response, and the results are consistent with respect to the pressure distribution shown in Fig. 3.10(a).

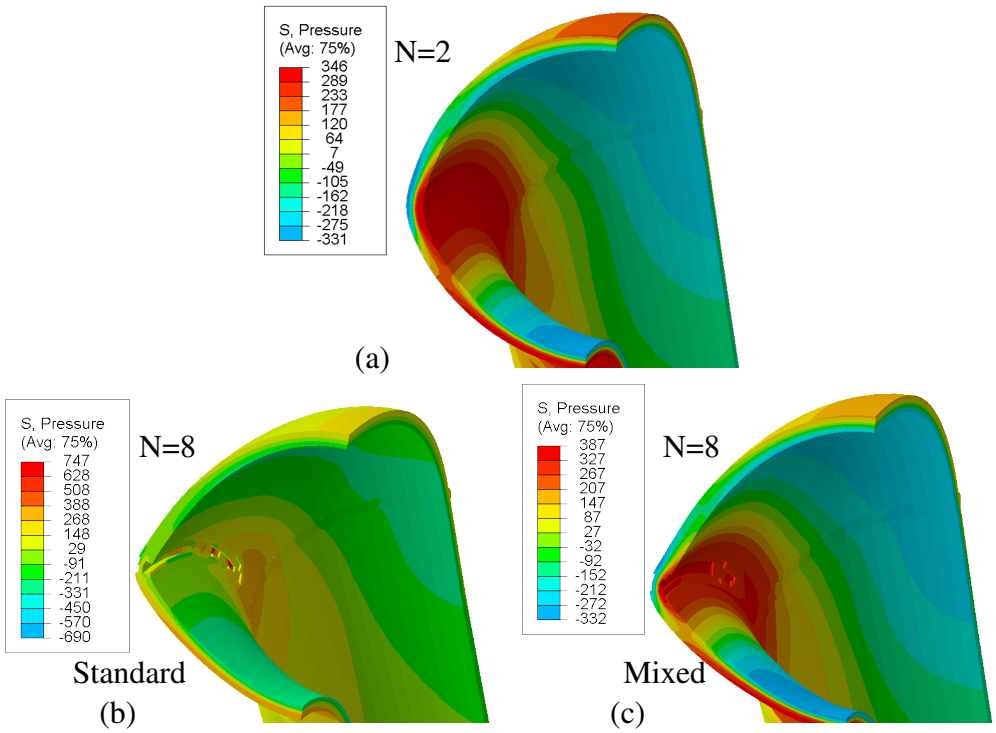

Figure 3.10: Pressure distribution observed in meshed model M4 (a) prior to damage initiation; (b) after damage initiation using standard and (c) mixed pressure/displacement finite element formulation.

3.3 Numerical scheme for cyclic-plasticity damage: Plane stress conditions

The development of an unconditionally-stable numerical integration scheme is presented, suitable for simulating cyclic plasticity-damage response and ductile rupture in thin-walled structural components. The constitutive relations account for J_2-flow theory, combined with nonlinear isotropic hardening and kinematic hardening. In the present investigation, kinematic hardening is limited to the hardening rule proposed by Chaboche (1986) as coupling of advanced hardening rules such as "BH" with damage under plane stress conditions increases the complexity of the solution significantly and the development of a robust integration scheme may not be possible. For convenience, the isotropic damage potential employed is considered a scalar function of the damage state, the plastic multiplier, which is an equivalent expression of the accumulated plastic strain and the stress tensor, allowing for the implementation of a wide range of isotropic CDM models reported in the literature. Constitutive relations are integrated implicitly by extending the *plane-stress projection* model proposed by Simo and Taylor (1986) to the requirements of the present study. In comparison to similar integration algorithms proposed in the past [e.g. Doghri (1995)], in the present numerical scheme incremental update is achieved through the solution of a single scalar equation, which is solved using an efficient solution method. The integration algorithm is consistently linearised to ensure the quadratic convergence of the Newton's solution. The proposed numerical scheme is implemented in finite element software ABAQUS (2016) as material user subroutine UMAT and is validated against large-scale laboratory experiments.

3.3.1 Constitutive relations

The constitutive relations are formulated explicitly for plane stress conditions by developing a coupled *plane-stress projection* model that considers nonlinear isotropic

hardening and the kinematic hardening rule proposed by Chaboche (1986). Throughout Sections 3.3.1-3.3.4, tensors are denoted with boldface symbols, while the following relations apply between second-order tensors ($\boldsymbol{a}$, $\boldsymbol{b}$), fourth-order tensors ($\boldsymbol{M}$) and their Cartesian components a_{ij}, b_{ij}, M_{ijkl}.

$$\boldsymbol{a} \cdot \boldsymbol{b} = a_{ij}\, b_{ij}$$

$$\boldsymbol{M}\boldsymbol{a} = M_{ijkl}\, a_{kl}$$

$$\boldsymbol{a}\boldsymbol{M}\boldsymbol{b} = \boldsymbol{a} \cdot (\boldsymbol{M}\boldsymbol{b})$$

The strain tensor $\boldsymbol{\varepsilon}$ is additively decomposed to its elastic part $\boldsymbol{\varepsilon}^e$ and plastic part $\boldsymbol{\varepsilon}^p$ as

$$\boldsymbol{\varepsilon} = \boldsymbol{\varepsilon}^e + \boldsymbol{\varepsilon}^p \tag{3.59}$$

which are written in terms of their in-plane components as shown in Section 2.2.1. Revising the free energy potential presented by Simo and Taylor (1986) for classical elastoplasticity by adding the damage related terms as per Doghri (1993), the stress strain response of the hyper-elastic damaged material is expressed through the isotropic elastic moduli as follows:

$$\boldsymbol{\sigma} = (1-D)\boldsymbol{M}\boldsymbol{\varepsilon}^e = (1-D)\boldsymbol{M}\,(\boldsymbol{\varepsilon} - \boldsymbol{\varepsilon}^p) \tag{3.60}$$

where D is the value of the isotropic damage variable and $\boldsymbol{M}$ is the fourth-order elastic rigidity tensor, formulated for plane stress conditions and defined with two material constants for isotropic materials; the Poisson's ratio (v) and the Young's modulus (E). It has already been shown in Section 2.2.1 that the *plane-stress projection* method considers only in-plane stress and backtress components in the formulation, allowing the development of robust numerical implementation schemes.

The kinematic hardening rule $\boldsymbol{\alpha}$ is written in terms of N backstress equations as follows:

$$\boldsymbol{\alpha} = \sum_{i=1}^{N} \left(\boldsymbol{\alpha}^i\right) \quad \text{or,} \quad \boldsymbol{a}' = \sum_{i=1}^{N} \left(\boldsymbol{a}'^i\right) \tag{3.61}$$

Defining the second-order tensor $\boldsymbol{\xi}$ as

$$\boldsymbol{\xi} = \frac{\boldsymbol{\sigma}}{1-D} - \boldsymbol{\alpha} \tag{3.62}$$

the von-Mises yield criterion is expressed by extending the formula proposed by Simo and Taylor (1986).

$$F(\boldsymbol{\sigma}, \boldsymbol{\alpha}, \varepsilon_q) = \frac{1}{2}\boldsymbol{\xi}\boldsymbol{P}\boldsymbol{\xi} - \frac{1}{3}k^2(\varepsilon_q) = 0 \tag{3.63}$$

or

$$F(\boldsymbol{\sigma}, \boldsymbol{\alpha}, \varepsilon_q) = \sqrt{\boldsymbol{\xi}\boldsymbol{P}\boldsymbol{\xi}} - \sqrt{\frac{2}{3}}k(\varepsilon_q) = 0 \tag{3.64}$$

Using associative plasticity, the evolution of plastic strain is in the direction normal to the yield surface, so that

$$\dot{\boldsymbol{\varepsilon}}^p = \dot{\lambda}\frac{\partial F}{\partial \boldsymbol{\sigma}} \tag{3.65}$$

where $\dot{\lambda}$ is the plastic multiplier. Differentiating Eq. (3.63) one obtains

$$\dot{\boldsymbol{\varepsilon}}^p = \frac{\dot{\lambda}}{1-D}\boldsymbol{P}\boldsymbol{\xi} \tag{3.66}$$

Accordingly, the equivalent plastic strain rate, defined as follows,

$$\dot{\varepsilon}_q = \sqrt{\frac{2}{3}\dot{\boldsymbol{\varepsilon}}^p \cdot \dot{\boldsymbol{\varepsilon}}^p} \tag{3.67}$$

is equal to

$$\dot{\varepsilon}_q = \frac{\dot{\lambda}}{1-D}\sqrt{\frac{2}{3}}\bar{\Phi} \tag{3.68}$$

where scalar $\bar{\Phi}$ is readily computed as

$$\bar{\Phi} = \sqrt{\boldsymbol{\xi}\boldsymbol{P}\boldsymbol{\xi}} \tag{3.69}$$

The evolution equation of the damage scalar (D) is formulated in the basis of Continuum Damage Mechanics. The kinetic law of damage $(\dot{D})$ is defined as the derivative of the damage potential (F_D) with respect to the associated variable (Y). For the purpose of the present research work, the damage potential is assumed a scalar function of the damage state (D), the plastic multiplier $(\dot{\lambda})$ and the stress tensor $(\boldsymbol{\sigma})$, allowing the implementation of a wide range of CDM models reported in the literature. Therefore, the $\dot{D}$ product is defined as

$$\dot{D} = \frac{\partial F_D\left(\boldsymbol{\sigma}, D, \dot{\lambda}\right)}{\partial Y}\dot{\lambda} = F'_D\dot{\lambda} \tag{3.70}$$

where F'_D is set for shortness. Eq. (3.70) is somewhat different from Eq. (3.10) as $\dot{D}$ is related to variable $\dot{\lambda}$ instead of $\dot{\varepsilon}_q$ as in the 3D formulation. It should be clarified that both expressions are equivalent in the sense that $\dot{\lambda}$ can be expressed in terms of $\dot{\varepsilon}_q$ and vice versa. In the integration algorithm developed for 3D formulation, $\dot{\varepsilon}_q$ is used in Eq. (3.10) as the solution of the integration equation is build around this internal variable. On the other hand, the integration algorithm of the coupled cyclic *plane-stress projection* model presented herein is formulated around variable $\dot{\lambda}$.

Kinematic hardening $(\boldsymbol{a})$ is simulated based on the multiple nonlinear backstress tensor proposed by Chaboche (1986) to allow simulation of the material response under cyclic inelastic conditions. Each backstress tensor is expressed in rate form as

$$\dot{\boldsymbol{a}}^i = C_i\frac{\dot{\lambda}}{1-D}\boldsymbol{\xi} - \gamma_i\boldsymbol{a}^i\sqrt{\frac{2}{3}}\frac{\dot{\lambda}}{1-D}\bar{\Phi} \tag{3.71}$$

Generalising Eq. (3.71) to N backstresses, the following equation is obtained.

$$\boldsymbol{\alpha} = \sum_{i=1}^{N}\left(\boldsymbol{\alpha}^i\right) = \sum_{i=1}^{N}\left(C_i\right)\frac{\dot{\lambda}}{1-D}\boldsymbol{\xi} - \sum_{i=1}^{N}\left(\gamma_i\boldsymbol{a}^i\right)\sqrt{\frac{2}{3}}\frac{\dot{\lambda}}{1-D}\bar{\Phi} \tag{3.72}$$

In Eq. (3.72), C_i and γ_i are the cyclic hardening parameters of each backstress tensor which are calibrated with the use of appropriate material tests [Chaboche (1986)].

The consistency condition ($\dot{F}$) requires the stress point to remain on the yield surface. Therefore,

$$\dot{F}(\boldsymbol{s},\boldsymbol{a},\varepsilon_q,D) = \frac{\partial F}{\partial \boldsymbol{s}}\dot{\boldsymbol{s}} + \frac{\partial F}{\partial \boldsymbol{a}}\dot{\boldsymbol{a}} + \frac{\partial F}{\partial D}\dot{D} + \frac{\partial F}{\partial \varepsilon_q}\dot{\varepsilon}_q = 0 \tag{3.73}$$

Evaluating the terms in Eq. (3.73) and after some mathematical manipulations, the plastic multiplier $\dot{\lambda}$ can be expressed as

$$\dot{\lambda} = \frac{1-D}{h}\boldsymbol{\xi}\boldsymbol{P}\boldsymbol{M}\dot{\boldsymbol{\varepsilon}} \tag{3.74}$$

where modulus h is a scalar quantity defined as

$$h = \boldsymbol{\xi}\boldsymbol{P}\boldsymbol{M}\boldsymbol{P}\boldsymbol{\xi} + \left[\sum_{i=1}^{N}(C_i) + \frac{2}{3}k'(\varepsilon_q)\right]\bar{\Phi}^2 - \sqrt{\frac{2}{3}}\bar{\Phi}\boldsymbol{\xi}\boldsymbol{P}\sum_{i=1}^{N}\left(\gamma_i\boldsymbol{\alpha}^i\right) \tag{3.75}$$

In Eq. (3.75), the prime $(\cdot)'$ denotes differentiation of $(\cdot)$ with respect to ε_q. Substituting Eq. (3.75) into the rate form of Eq. (3.60) one obtains

$$\dot{\boldsymbol{\sigma}} = (1-D)\boldsymbol{M}\dot{\boldsymbol{\varepsilon}} - \frac{1-D}{h}\boldsymbol{P}\boldsymbol{M}\boldsymbol{\xi}\otimes\boldsymbol{P}\boldsymbol{M}\boldsymbol{\xi}\dot{\boldsymbol{\varepsilon}} - \frac{F'_D}{h}\boldsymbol{P}\boldsymbol{M}\boldsymbol{\xi}\otimes\boldsymbol{\sigma}\dot{\boldsymbol{\varepsilon}} \tag{3.76}$$

Hence,

$$\boldsymbol{M}_{ep} = (1-D)\boldsymbol{M} - \frac{1-D}{h}\boldsymbol{P}\boldsymbol{M}\boldsymbol{\xi}\otimes\boldsymbol{P}\boldsymbol{M}\boldsymbol{\xi} - \frac{F'_D}{h}\boldsymbol{P}\boldsymbol{M}\boldsymbol{\xi}\otimes\boldsymbol{\sigma} \tag{3.77}$$

$\boldsymbol{M}_{ep}$ is a fourth-order non-symmetric tensor, expressing the continuum elastoplastic tangent operator moduli. The non-symmetric term in $\boldsymbol{M}_{ep}$ is attributed to coupling between damage and plasticity.

3.3.2 Implicit integration of constitutive equations

3.3.2.1 Integration algorithm

An implicit numerical integration scheme of the above constitutive model is developed, based on the Euler-backward integration technique. The methodologies proposed by Jetteur (1986); Simo and Taylor (1986) for classical elastoplasticity are extended to the requirements of the coupled cyclic plasticity model. Starting with the internal variables ($\boldsymbol{\sigma}_n$, $\boldsymbol{\alpha}_n$, $\boldsymbol{\varepsilon}^p_n$, $\varepsilon_{q,n}$, D_n) at the beginning of the current step t_n, the trial stresses $\boldsymbol{\sigma}^e$ are anticipated at increment t_{n+1} considering a purely elastic behaviour of the damaged material.

$$\boldsymbol{\sigma}^e = (1-D_n)\boldsymbol{M}\,(\boldsymbol{\varepsilon}_{n+1} - \boldsymbol{\varepsilon}^p_n) \tag{3.78}$$

If the elastic prediction violates the yield condition,

$$F(\boldsymbol{\sigma}^e, \boldsymbol{\alpha}_n, \varepsilon_{q,n}, D_n) = \frac{1}{2}\left(\frac{\boldsymbol{\sigma}^e}{1-D_n} - \boldsymbol{\alpha}_n\right)\boldsymbol{P}\left(\frac{\boldsymbol{\sigma}^e}{1-D_n} - \boldsymbol{\alpha}_n\right) - \frac{1}{3}k^2(\varepsilon_{q,n}) > 0 \tag{3.79}$$

an elastoplastic-damage corrector should be considered. Starting from Eq. (3.60), the stress-strain relation at the end of the increment can be evaluated using the Euler-backward integration scheme as follows:

$$\boldsymbol{\sigma}_{n+1} = (1-D_{n+1})\boldsymbol{M}\,(\boldsymbol{\varepsilon}^e_n + \Delta\boldsymbol{\varepsilon} - \Delta\boldsymbol{\varepsilon}^p) \tag{3.80}$$

The remaining internal variables are integrated over the step $[t_n;\, t_{n+1}]$ as shown in the following set of equations.

$$\boldsymbol{\xi}_{n+1} = \frac{\boldsymbol{\sigma}_{n+1}}{1-D_{n+1}} - \sum_{i=1}^{N}\left(\boldsymbol{\alpha}^i_{n+1}\right) \tag{3.81}$$

$$\bar{\Phi}_{n+1} = \sqrt{\boldsymbol{\xi}_{n+1}\boldsymbol{P}\boldsymbol{\xi}_{n+1}} \tag{3.82}$$

$$\boldsymbol{\varepsilon}^p_{n+1} = \boldsymbol{\varepsilon}^p_n + \frac{\Delta\lambda}{1-D_{n+1}}\boldsymbol{P}\boldsymbol{\xi}_{n+1} \tag{3.83}$$

$$\varepsilon_{q,n+1} = \varepsilon_{q,n} + \sqrt{\frac{2}{3}}\frac{\Delta\lambda}{1-D_{n+1}}\bar{\Phi}_{n+1} \tag{3.84}$$

$$D_{n+1} = D_n + \Delta\lambda F'_{D,n+1} \tag{3.85}$$

Combining Eqs. (3.78, 3.60, 3.83), the stress tensor $\boldsymbol{\sigma}_{n+1}$ can be redefined as

$$\frac{\boldsymbol{\sigma}_{n+1}}{1-D_{n+1}} = \frac{\boldsymbol{\sigma}^e}{1-D_n} - \frac{\Delta\lambda}{1-D_{n+1}}\boldsymbol{P}\boldsymbol{M}\boldsymbol{\xi}_{n+1} \tag{3.86}$$

The integration of the backstress tensor $\boldsymbol{\alpha}$ over the incremental step $[t_n;\, t_{n+1}]$ is achieved by integrating Eq. (3.71) for each backstress tensor separately. Denoting

$$\mu_i = \left[1 + \gamma_i\sqrt{\frac{2}{3}}\frac{\Delta\lambda}{1-D_{n+1}}\bar{\Phi}_{n+1}\right]^{-1} \tag{3.87}$$

the evolution equation for each backstress tensor $\boldsymbol{\alpha}^i_{n+1}$ is computed as

$$\boldsymbol{\alpha}^i_{n+1} = \mu_i\boldsymbol{\alpha}^i_n + C_i\mu_i\frac{\Delta\lambda}{1-D_{n+1}}\boldsymbol{\xi}_{n+1} \tag{3.88}$$

Generalising Eq. (3.88) to multiple (N) backstress tensors one obtains

$$\boldsymbol{\alpha}_{n+1} = \sum_{i=1}^{N}\left(\mu_i\boldsymbol{\alpha}^i_n\right) + \sum_{i=1}^{N}\left(C_i\mu_i\right)\frac{\Delta\lambda}{1-D_{n+1}}\boldsymbol{\xi}_{n+1} \tag{3.89}$$

Combining Eqs. (3.86, 3.89), the second-order tensor $\boldsymbol{\xi}_{n+1}$ is expressed as

$$\begin{aligned}\boldsymbol{\xi}_{n+1} = \frac{\boldsymbol{\sigma}^e}{1-D_n} - \frac{\Delta\lambda}{1-D_{n+1}}\boldsymbol{P}\boldsymbol{M}\boldsymbol{\xi}_{n+1} - \sum_{i=1}^{N}\left(\mu_i\boldsymbol{\alpha}_n^i\right) \\ - \sum_{i=1}^{N}\left(C_i\mu_i\right)\frac{\Delta\lambda}{1-D_{n+1}}\boldsymbol{P}\boldsymbol{M}\boldsymbol{\xi}_{n+1}\end{aligned} \tag{3.90}$$

With a few extra mathematical manipulations in Eq. (3.90), $\boldsymbol{\xi}_{n+1}$ is computed as

$$\boldsymbol{\xi}_{n+1} = \frac{1}{\rho_1}\boldsymbol{\Xi}\boldsymbol{M}^{-1}\left[\frac{\boldsymbol{\sigma}^e}{1-D_n} - \sum_{i=1}^{N}\left(\mu_i\boldsymbol{\alpha}_n^i\right)\right] \tag{3.91}$$

where the scalar quantity ρ_1 and the fourth-order tensor $\boldsymbol{\Xi}$ are defined as follows:

$$\boldsymbol{\Xi} = \left[\boldsymbol{M}^{-1} + \frac{1}{\rho_1}\frac{\Delta\lambda}{1-D_{n+1}}\boldsymbol{P}\right]^{-1} \tag{3.92}$$

$$\rho_1 = 1 + \sum_{i=1}^{N}\left(\frac{C_i}{\mu_i}\right)\frac{\Delta\lambda}{1-D_{n+1}} \tag{3.93}$$

Finally, enforcing the von-Mises criterion at the end of the increment $t = t_{n+1}$ (consistency condition), it is required that the following equation is satisfied:

$$F(\boldsymbol{\sigma}_{n+1}, \boldsymbol{\alpha}_{n+1}, \varepsilon_{q,n+1}, D_{n+1}) = 0 \tag{3.94}$$

Equivalently

$$F_{n+1}(\Delta\lambda) \equiv \frac{1}{2}\boldsymbol{\xi}_{n+1}\boldsymbol{P}\boldsymbol{\xi}_{n+1} - \frac{1}{3}k^2(\varepsilon_{q,n+1}) = 0 \tag{3.95}$$

or

$$F_{n+1}(\Delta\lambda) \equiv \sqrt{\boldsymbol{\xi}_{n+1}\boldsymbol{P}\boldsymbol{\xi}_{n+1}} - \sqrt{\frac{2}{3}}k(\varepsilon_{q,n+1}) = 0 \tag{3.96}$$

Substituting Eq. (3.91) in Eqs. (3.95 or 3.96), a single scalar equation with respect to the plastic multiplier $\Delta\lambda$ is formed. Eq. (3.91) in its current form indicates that

solving Eqs. (3.95 or 3.96) in terms of $\Delta\lambda$ requires extensive calculations and matrix inversion within the Newton's method. However, regardless of the complexity of the constitutive model employed herein, Eq. (3.96) can be simplified significantly and readily solved with an iterative Newton's method by extending the method proposed by Simo and Taylor (1986) for classical elastoplasticity to the coupled cyclic plasticity model considered herein. This methodology is presented in detail in Section 3.3.3. The main feature of the present integration algorithm is that allows the implementation of a wide range of CDM models not yet provided even in leading commercial finite element software. In comparison to the numerical scheme proposed by Doghri (1995) for plane stress coupled cyclic plasticity, where a system of 5 nonlinear equations must be solved, the return-mapping stage of the constitutive integration algorithm is reduced to the solution of a single scalar equation, increasing significantly its performance in large-scale computations.

3.3.3 Modified Newton's method

The efficient implementation of the cyclic plasticity-damage model presented in Section 3.3.2.1 necessitates the development of a robust methodology for the solution of Eq. (3.96). The solution of Eq. (3.96) is addressed by modifying the method presented in Section 2.2.3 for the implementation of cyclic plasticity-ratcheting constitutive models.

3.3.3.1 Evaluation of the consistency condition

The single-integration equation shown in Eq. (3.95) or equivalently in Eq. (3.96) can be simplified significantly. It has been demonstrated in Chapter 2, Section 2.2.3 that the elastic stress rigidity tensor $\boldsymbol{M}$ and the projection matrix $\boldsymbol{P}$ commute; have the same

eigenvectors. In addition, the second order tensor $\boldsymbol{\eta}$, shown in Eq. (3.97), is employed.

$$\boldsymbol{\eta} = \boldsymbol{Q}^t \boldsymbol{\xi}, \quad \boldsymbol{\eta}_{n+1} = \frac{1}{\sqrt{2}} \begin{bmatrix} \xi_{n+1}^{11} + \xi_{n+1}^{22} \\ -\xi_{n+1}^{11} + \xi_{n+1}^{22} \\ \sqrt{2}\xi_{n+1}^{12} \end{bmatrix} \tag{3.97}$$

Multiplying both ends of Eq. (3.96) by $\boldsymbol{Q}^t$, the internal variables at step t_{n+1} can be expressed in terms of trial anticipated values as

$$\boldsymbol{\eta}_{n+1} = \left[\left(1 + \sum_{i=1}^{N} (C_i \mu_i) \frac{\Delta\lambda}{1 - D_{n+1}} \right) \boldsymbol{I} + \frac{\Delta\lambda}{1 - D_{n+1}} \boldsymbol{\Lambda}_P \boldsymbol{\Lambda}_D \right]^{-1} \boldsymbol{\eta}^e = \boldsymbol{\Gamma} \boldsymbol{\eta}^e \tag{3.98}$$

where $\boldsymbol{I}$ is the 3×3 identity matrix. The fourth-order tensor $\boldsymbol{\Gamma}$ in Eq. (3.98) represents an invertible 3×3 diagonal matrix, expressed as

$$\begin{aligned} \boldsymbol{\Gamma} &= \begin{bmatrix} \Gamma_{11} & 0 & 0 \\ 0 & \Gamma_{22} & 0 \\ 0 & 0 & \Gamma_{33} \end{bmatrix} \\ \Gamma_{11} &= \left[1 + \frac{\Delta\lambda}{1 - D_{n+1}} \left(\sum_{i=1}^{N} (C_i \mu_i) + \frac{E}{3(1-\nu)} \right) \right]^{-1} \\ \Gamma_{22} &= \left[1 + \frac{\Delta\lambda}{1 - D_{n+1}} \left(\sum_{i=1}^{N} (C_i \mu_i) + 2G \right) \right]^{-1} \quad (\Gamma_{22} \equiv \Gamma_{33}) \end{aligned} \tag{3.99}$$

Furthermore, the tensor $\boldsymbol{\eta}^e = \begin{bmatrix} \eta_{11}^e & \eta_{22}^e & \eta_{12}^e \end{bmatrix}$ is expressed with respect to the trial stress tensor $\boldsymbol{\sigma}^e$ and the backstress tensor $\boldsymbol{\alpha}_n$ as

$$\begin{aligned} \eta_{11}^e &= \frac{1}{\sqrt{2}} \left[\frac{\sigma_{11}^e + \sigma_{22}^e}{1 - D_n} - \sum_{i=1}^{N} \left[\mu_i \left(\alpha_{n,11}^i + \alpha_{n,22}^i \right) \right] \right] \\ \eta_{22}^e &= \frac{1}{\sqrt{2}} \left[\frac{\sigma_{22}^e - \sigma_{11}^e}{1 - D_n} - \sum_{i=1}^{N} \left[\mu_i \left(\alpha_{n,22}^i - \alpha_{n,11}^i \right) \right] \right] \\ \eta_{12}^e &= \frac{\sigma_{12}^e}{1 - D_n} - \sum_{i=1}^{N} \left(\mu_i \alpha_{n,12}^i \right) \end{aligned} \tag{3.100}$$

where the scalar μ_i has been introduced in Eq. (3.87). With the aid of Eqs. (3.98-3.100), the term $\bar{\Phi}_{n+1}$ can be computed as

$$\bar{\Phi}_{n+1} = \sqrt{\boldsymbol{\xi}_{n+1}\boldsymbol{P}\boldsymbol{\xi}_{n+1}} = \sqrt{\boldsymbol{\eta}_{n+1}\boldsymbol{\Lambda}_P\boldsymbol{\eta}_{n+1}} = \sqrt{\frac{1}{3}(\eta^{11}_{n+1})^2 + (\eta^{22}_{n+1})^2 + 2(\eta^{12}_{n+1})^2} \tag{3.101}$$

and the consistency condition presented in Eq. (3.96) takes the following simple form.

$$\begin{aligned} F_{n+1}(\Delta\lambda) =& \sqrt{\frac{1}{3}\Gamma^2_{11}\left(\eta^e_{11}\right)^2 + \Gamma^2_{22}\left(\eta^e_{22}\right)^2 + 2\Gamma^2_{33}\left(\eta^e_{12}\right)^2} \\ & - \sqrt{\frac{2}{3}}k\left(\varepsilon_{q,n} + \sqrt{\frac{2}{3}}\frac{\Delta\lambda}{1-D_{n+1}}\bar{\Phi}_{n+1}\right) \end{aligned} \tag{3.102}$$

It can be shown that Eq. (3.102) decreases monotonically for $\Delta\lambda \in [0,\infty]$ and thus, it is ideally suited for a local iterative solution procedure employing Newton's solution method. Newton's method necessitates the evaluation of derivative $\dfrac{\partial F_{n+1}(\Delta\lambda)}{\partial\Delta\lambda}$. Due to the complexity of the model, an analytical evaluation of derivative $\dfrac{\partial F_{n+1}(\Delta\lambda)}{\partial\Delta\lambda}$ is presented next.

3.3.3.2 Differentiation of the consistency condition

The derivative $\dfrac{\partial F_{n+1}(\Delta\lambda)}{\partial\Delta\lambda}$ is computed in the present section. Differentiating Eq. (3.101) with respect to $\Delta\lambda$ one obtains

$$\frac{\partial F_{n+1}(\Delta\lambda)}{\partial\Delta\lambda} = \frac{1}{2\bar{\Phi}_{n+1}}d\eta - \frac{2}{3}k'_{n+1}\left(\bar{\Phi}_{n+1} + \frac{\Delta\lambda}{2\bar{\Phi}_{n+1}}d\eta\right) \tag{3.103}$$

where

$$d\eta = \frac{2}{3}\eta^{11}_{n+1}\eta^{11'}_{n+1} + 2\eta^{22}_{n+1}\eta^{22'}_{n+1} + 4\eta^{12}_{n+1}\eta^{12'}_{n+1} \tag{3.104}$$

and the prime $(\cdot)'$ indicates differentiation of $(\cdot)$ with respect to $\Delta\lambda$. The derivatives $\eta_{n+1}^{ij\,\prime}$ can be obtained by differentiating Eq. (3.98).

$$\begin{aligned}
\eta_{n+1}^{11'} &= \Gamma'_{11}\eta_{11}^{e} + \Gamma_{11}\eta_{11}^{e'} \\
\eta_{n+1}^{22'} &= \Gamma'_{22}\eta_{22}^{e} + \Gamma_{22}\eta_{22}^{e'} \\
\eta_{n+1}^{12'} &= \Gamma'_{22}\eta_{12}^{e} + \Gamma_{22}\eta_{12}^{e'} \quad (\Gamma_{22} \equiv \Gamma_{33})
\end{aligned} \tag{3.105}$$

where terms $\Gamma_{i,j}$ are the diagonal components of the fourth-order tensor $\mathbf{\Gamma}$, expressed in Eq. (3.99). The following derivatives are also computed to simplify the derivation process.

$$\frac{\partial D_{n+1}}{\partial \Delta\lambda} = F'_{D,n+1} + \Delta\lambda \frac{\partial F'_{D,n+1}}{\partial \Delta\lambda} \tag{3.106}$$

$$\frac{\partial}{\partial \Delta\lambda}\left\{\frac{\Delta\lambda}{1-D_{n+1}}\right\} = \frac{1-D_{n+1}+\Delta\lambda\,\frac{\partial D_{n+1}}{\partial \Delta\lambda}}{\left(1-D_{n+1}\right)^2} \equiv \beta_2 \tag{3.107}$$

$$\frac{\partial \mu_i}{\partial \Delta\lambda} = -\sqrt{\frac{2}{3}}\gamma_i \mu_i^2 \left[\beta_2 \bar{\Phi}_{n+1} + \frac{\Delta\lambda}{1-D_{n+1}} \frac{1}{2\bar{\Phi}_{n+1}} d\eta\right] \tag{3.108}$$

Using Eqs. (3.106-3.108) the partial derivatives in Eq. (3.105) are computed as

$$\begin{aligned}
\Gamma'_{11} &= \Gamma^{r}_{11} + \Gamma^{d}_{11} d\eta \\
\Gamma'_{22} &= \Gamma^{r}_{22} + \Gamma^{d}_{22} d\eta \quad (\Gamma'_{22} \equiv \Gamma'_{33})
\end{aligned} \tag{3.109}$$

$$\begin{aligned}
\eta_{11}^{e'} &= \eta_{11}^{r} + \eta_{11}^{d} d\eta \\
\eta_{22}^{e'} &= \eta_{22}^{r} + \eta_{22}^{d} d\eta \\
\eta_{12}^{e'} &= \eta_{12}^{r} + \eta_{12}^{d} d\eta
\end{aligned} \tag{3.110}$$

where scalar terms Γ^r_{ii} and Γ^d_{ii} are defined as

$$\Gamma^r_{11} = \Gamma^2_{11}\beta_2\left[\sqrt{\frac{2}{3}}\frac{\Delta\lambda}{1-D_{n+1}}\sum_{i=1}^{N}\left(C_i\gamma_i\mu_i^2\right)\bar{\Phi}_{n+1} - \sum_{i=1}^{N}\left(C_i\mu_i\right) - \frac{E}{3(1-\nu)}\right]$$
$$\Gamma^d_{11} = \sqrt{\frac{2}{3}}\Gamma^2_{11}\frac{\Delta\lambda^2}{(1-D_{n+1})^2}\sum_{i=1}^{N}\left(C_i\gamma_i\mu_i^2\right)\frac{1}{2\bar{\Phi}_{n+1}} \tag{3.111}$$
$$\Gamma^r_{22} = \Gamma^2_{22}\beta_2\left[\sqrt{\frac{2}{3}}\frac{\Delta\lambda}{1-D_{n+1}}\sum_{i=1}^{N}\left(C_i\gamma_i\mu_i^2\right)\bar{\Phi}_{n+1} - \sum_{i=1}^{N}\left(C_i\mu_i\right) - 2G\right]$$
$$\Gamma^d_{22} = \sqrt{\frac{2}{3}}\Gamma^2_{22}\frac{\Delta\lambda^2}{(1-D_{n+1})^2}\sum_{i=1}^{N}\left(C_i\gamma_i\mu_i^2\right)\frac{1}{2\bar{\Phi}_{n+1}} \tag{3.112}$$

whereas the scalar quantities $\eta^r_{i,j}$ and $\eta^d_{i,j}$ are computed as

$$\eta^r_{11} = \frac{1}{\sqrt{3}}\sum_{i=1}^{N}\left[\gamma_i\mu_i^2\left(\alpha^i_{n,11}+\alpha^i_{n,22}\right)\right]\beta_2\bar{\Phi}_{n+1}$$
$$\eta^d_{11} = \frac{1}{\sqrt{3}}\sum_{i=1}^{N}\left[\gamma_i\mu_i^2\left(\alpha^i_{n,11}+\alpha^i_{n,22}\right)\right]\frac{\Delta\lambda}{1-D_{n+1}}\frac{1}{2\bar{\Phi}_{n+1}} \tag{3.113}$$
$$\eta^r_{22} = \frac{1}{\sqrt{3}}\sum_{i=1}^{N}\left[\gamma_i\mu_i^2\left(\alpha^i_{n,22}-\alpha^i_{n,11}\right)\right]\beta_2\bar{\Phi}_{n+1}$$
$$\eta^d_{11} = \frac{1}{\sqrt{3}}\sum_{i=1}^{N}\left[\gamma_i\mu_i^2\left(\alpha^i_{n,22}-\alpha^i_{n,11}\right)\right]\frac{\Delta\lambda}{1-D_{n+1}}\frac{1}{2\bar{\Phi}_{n+1}} \tag{3.114}$$
$$\eta^r_{12} = \sqrt{\frac{2}{3}}\sum_{i=1}^{N}\left[\gamma_i\mu_i^2\alpha^i_{n,12}\right]\beta_2\bar{\Phi}_{n+1}$$
$$\eta^d_{12} = \sqrt{\frac{2}{3}}\sum_{i=1}^{N}\left[\gamma_i\mu_i^2\alpha^i_{n,12}\right]\frac{\Delta\lambda}{1-D_{n+1}}\frac{1}{2\bar{\Phi}_{n+1}} \tag{3.115}$$

Using Eqs. (3.105-3.115) and substituting in Eq. (3.104), $d\eta$ is computed as

$$d\eta = \frac{F^r}{F^d} \tag{3.116}$$

where, F^r and F^d are defined as

$$F^r = \frac{2}{3}\left(\Gamma^r_{11}\eta^e_{11}+\Gamma_{11}\eta^r_{11}\right)\eta^{11}_{n+1} + 2\left(\Gamma^r_{22}\eta^e_{22}+\Gamma_{22}\eta^r_{22}\right)\eta^{22}_{n+1} + 4\left(\Gamma^r_{22}\eta^e_{12}+\Gamma_{22}\eta^r_{12}\right)\eta^{12}_{n+1} \tag{3.117}$$

$$F^d = 1 - \frac{2}{3}\left(\Gamma_{11}^d \eta_{11}^e + \Gamma_{11}\eta_{11}^d\right)\eta_{n+1}^{11} - 2\left(\Gamma_{22}^d \eta_{22}^e + \Gamma_{22}\eta_{22}^d\right)\eta_{n+1}^{22} - 4\left(\Gamma_{22}^d \eta_{12}^e + \Gamma_{22}\eta_{12}^d\right)\eta_{n+1}^{12} \tag{3.118}$$

Having computed the term $d\eta$, the derivative $\dfrac{\partial F_{n+1}(\Delta\lambda)}{\partial\Delta\lambda}$ can be evaluated by substituting the terms in Eq. (3.103). It should be clarified that within the iterative procedure, μ_i is computed based on the value of the internal variables obtained from the previous step of the Newton's method. This is dictated by the complexity of the model and the strong coupling between the internal variables. In addition, in case the damage potential $F'_{D,n+1}$ is not constant during the iterative process, two approaches are provided for its computation. $F'_{D,n+1}$ may be computed using the un-converged values of the internal variables or the values of the internal variables obtained from the previous step of the iterative process. Both methods work equally well but the first option may lead to convergence difficulties for D_n values close to 1.0. Regardless of the modifications implemented in the Newton's scheme, the integration algorithm and the solution methodology are quite robust as convergence is achieved within limited iterations.

3.3.4 Consistent elastoplastic operator

An analytical derivation of the consistent tangent operator moduli is presented, contributing to the robustness of the proposed numerical scheme. Differentiating Eq. (3.86) with respect to $\Delta\boldsymbol{\varepsilon}$ one obtains

$$\frac{\partial\boldsymbol{\sigma}_{n+1}}{\partial\Delta\boldsymbol{\varepsilon}} = \frac{\partial}{\partial\Delta\boldsymbol{\varepsilon}}\left\{\frac{1-D_{n+1}}{1-D_n}\boldsymbol{\sigma}^e - \Delta\lambda\boldsymbol{PM}\boldsymbol{\xi}_{n+1}\right\} \tag{3.119}$$

After some calculations Eq. (3.119) can be written as

$$\frac{\partial\boldsymbol{\sigma}_{n+1}}{\partial\Delta\boldsymbol{\varepsilon}} = -\frac{\boldsymbol{\sigma}^e}{1-D_n}\otimes\frac{\partial D_{n+1}}{\partial\Delta\boldsymbol{\varepsilon}} + (1-D_{n+1})\boldsymbol{M} - \boldsymbol{PM}\boldsymbol{\xi}_{n+1}\otimes\frac{\partial\Delta\lambda}{\Delta\boldsymbol{\varepsilon}} - \Delta\lambda\boldsymbol{PM}\frac{\partial\boldsymbol{\xi}_{n+1}}{\partial\Delta\boldsymbol{\varepsilon}} \tag{3.120}$$

The derivative of the damage function D_{n+1} with respect to $\Delta\boldsymbol{\varepsilon}$ is computed similarly to Eq. (3.41) in Section 3.2.3 to retrieve the following.

$$\frac{\partial D_{n+1}}{\partial \Delta\boldsymbol{\varepsilon}} = F'_{D,n+1}\frac{\partial \Delta\lambda}{\partial \Delta\boldsymbol{\varepsilon}} + \Delta\lambda\left[\frac{\partial F'_{D,n+1}}{\partial \Delta\lambda}\frac{\partial \Delta\lambda}{\partial \Delta\boldsymbol{\varepsilon}} + \frac{\partial F'_{D,n+1}}{\partial \boldsymbol{\sigma}_{n+1}}\frac{\partial \boldsymbol{\sigma}_{n+1}}{\partial \Delta\boldsymbol{\varepsilon}} + \frac{\partial F'_{D,n+1}}{\partial D_{n+1}}\frac{\partial D_{n+1}}{\partial \Delta\boldsymbol{\varepsilon}}\right] \tag{3.121}$$

Rearranging the terms in Eq. (3.121), $\dfrac{\partial D_{n+1}}{\partial \Delta\boldsymbol{\varepsilon}}$ is computed as

$$\frac{\partial D_{n+1}}{\partial \Delta\boldsymbol{\varepsilon}} = \beta\frac{\partial \Delta\lambda}{\partial \Delta\boldsymbol{\varepsilon}} + \boldsymbol{v}\cdot\frac{\partial \boldsymbol{\sigma}_{n+1}}{\partial \Delta\boldsymbol{\varepsilon}} \tag{3.122}$$

where, scalar quantity β and the second-order tensor $\boldsymbol{v}$ are defined as

$$\beta = \frac{F'_{D,n+1} + \Delta\lambda\dfrac{\partial F'_{D,n+1}}{\partial \Delta\lambda}}{1 - \Delta\lambda\dfrac{\partial F'_{D,n+1}}{\partial D_{n+1}}} \tag{3.123}$$

$$\boldsymbol{v} = \frac{\Delta\lambda\dfrac{\partial F'_{D,n+1}}{\partial \boldsymbol{\sigma}_{n+1}}}{1 - \Delta\lambda\dfrac{\partial F'_{D,n+1}}{\partial D_{n+1}}} \tag{3.124}$$

Differentiating Eqs. (3.81,3.82, 3.89) with respect to $\Delta\boldsymbol{\varepsilon}$ the following derivatives are derived.

$$\frac{\partial \boldsymbol{\xi}_{n+1}}{\partial \Delta\boldsymbol{\varepsilon}} = \frac{\partial}{\partial \Delta\boldsymbol{\varepsilon}}\left\{\frac{\boldsymbol{\sigma}_{n+1}}{1 - D_{n+1}}\right\} - \frac{\partial}{\partial \Delta\boldsymbol{\varepsilon}}\left\{\sum_{i=1}^{N}\boldsymbol{\alpha}^i_{n+1}\right\} \tag{3.125}$$

$$\frac{\partial \bar{\Phi}_{n+1}}{\partial \Delta\boldsymbol{\varepsilon}} = \frac{1}{\bar{\Phi}_{n+1}}\boldsymbol{\xi}_{n+1}\boldsymbol{P}\frac{\partial \boldsymbol{\xi}_{n+1}}{\partial \Delta\boldsymbol{\varepsilon}} \tag{3.126}$$

$$\frac{\partial \boldsymbol{\alpha}_{n+1}}{\partial \Delta\boldsymbol{\varepsilon}} = \frac{\partial}{\partial \Delta\boldsymbol{\varepsilon}}\left\{\sum_{i=1}^{N}\left(\mu_i\boldsymbol{\alpha}^i_n\right)\right\} + \frac{\partial}{\partial \Delta\boldsymbol{\varepsilon}}\left\{\sum_{i=1}^{N}\left(C_i\mu_i\right)\frac{\Delta\lambda}{1 - D_{n+1}}\boldsymbol{\xi}_{n+1}\right\} \tag{3.127}$$

Evaluating the terms in Eq. (3.127) and after numerous mathematical manipulations, the derivative $\frac{\partial \boldsymbol{\alpha}_{n+1}}{\partial \Delta \boldsymbol{\varepsilon}}$ can be expressed with respect to $\frac{\partial \boldsymbol{\sigma}_{n+1}}{\partial \Delta \boldsymbol{\varepsilon}}$ and $\frac{\partial \boldsymbol{\Delta\lambda}}{\partial \Delta \boldsymbol{\varepsilon}}$as

$$\begin{aligned}\frac{\partial \boldsymbol{\alpha}_{n+1}}{\partial \Delta \boldsymbol{\varepsilon}}(1+\delta_5) = &\left[\delta_1 \sum_{i=1}^{N}\left(\gamma_i \mu_i^2 \boldsymbol{\alpha}_n\right) + \delta_2 \boldsymbol{\xi}_{n+1} + \frac{\delta_5 \beta}{(1-D_{n+1})^2}\boldsymbol{\sigma}_{n+1}\right] \otimes \frac{\partial \boldsymbol{\Delta\lambda}}{\partial \Delta \boldsymbol{\varepsilon}} \\ &+ \left[\delta_3 \sum_{i=1}^{N}\left(\gamma_i \mu_i^2 \boldsymbol{\alpha}_n\right) + \delta_4 \boldsymbol{\xi}_{n+1}\right] \otimes \boldsymbol{\nu} \cdot \frac{\partial \boldsymbol{\sigma}_{n+1}}{\partial \Delta \boldsymbol{\varepsilon}} \\ &+ \frac{\delta_5}{1-D_{n+1}}\left[\frac{\boldsymbol{\sigma}_{n+1}}{1-D_{n+1}} \otimes \boldsymbol{\nu} + \boldsymbol{I}\right] \cdot \frac{\partial \boldsymbol{\sigma}_{n+1}}{\partial \Delta \boldsymbol{\varepsilon}}\end{aligned} \tag{3.128}$$

where $\boldsymbol{I}$ is the fourth-order identity tensor and the scalar quantities $\delta_1 - \delta_5$ are defined as per below.

$$\delta_1 = -\sqrt{\frac{2}{3}}\bar{\Phi}_{n+1}\left[\frac{1-D_{n+1}+\beta\Delta\lambda}{(1-D_{n+1})^2}\right] \tag{3.129}$$

$$\delta_2 = \left[\frac{1-D_{n+1}+\beta\Delta\lambda}{(1-D_{n+1})^2}\right]\left[\sum_{i=1}^{N}\left(C_i\mu_i\right) - \sqrt{\frac{2}{3}}\sum_{i=1}^{N}\left(C_i\gamma_i\mu_i^2\right)\frac{\Delta\lambda}{1-D_{n+1}}\bar{\Phi}_{n+1}\right] \tag{3.130}$$

$$\delta_3 = -\sqrt{\frac{2}{3}}\bar{\Phi}_{n+1}\frac{\Delta\lambda}{(1-D_{n+1})^2} \tag{3.131}$$

$$\delta_4 = \frac{\Delta\lambda}{(1-D_{n+1})^2}\left[\sum_{i=1}^{N}\left(C_i\mu_i\right) - \sqrt{\frac{2}{3}}\sum_{i=1}^{N}\left(C_i\gamma_i\mu_i^2\right)\frac{\Delta\lambda}{1-D_{n+1}}\bar{\Phi}_{n+1}\right] \tag{3.132}$$

$$\delta_5 = (1-D_{n+1})\delta_4 - \sqrt{\frac{2}{3}}\frac{\Delta\lambda}{(1-D_{n+1})\bar{\Phi}_{n+1}}\boldsymbol{\xi}_{n+1}\boldsymbol{P}\sum_{i=1}^{N}\left(\gamma_i\mu_i^2\boldsymbol{\alpha}_n\right) \tag{3.133}$$

Substituting Eq. (3.128) into Eq. (3.125), $\frac{\partial \boldsymbol{\xi}_{n+1}}{\partial \Delta \boldsymbol{\varepsilon}}$ is expressed with respect to $\frac{\partial \boldsymbol{\sigma}_{n+1}}{\partial \Delta \boldsymbol{\varepsilon}}$ and $\frac{\partial \boldsymbol{\Delta\lambda}}{\partial \Delta \boldsymbol{\varepsilon}}$ as

$$\begin{aligned}&\frac{\partial \boldsymbol{\xi}_{n+1}}{\partial \Delta \boldsymbol{\varepsilon}}(1+\delta_5) = \left[\beta\frac{\boldsymbol{\sigma}_{n+1}}{(1-D_{n+1})^2} - \delta_1\sum_{i=1}^{N}\left(\gamma_i\mu_i^2\boldsymbol{\alpha}_n\right) - \delta_2\boldsymbol{\xi}_{n+1}\right] \otimes \frac{\partial \boldsymbol{\Delta\lambda}}{\partial \Delta \boldsymbol{\varepsilon}} + \\ &\left[\frac{1}{1-D_{n+1}}\left(\frac{\boldsymbol{\sigma}_{n+1}}{1-D_{n+1}} \otimes \boldsymbol{\nu} + \boldsymbol{I}\right) - \delta_3\sum_{i=1}^{N}\left(\gamma_i\mu_i^2\boldsymbol{\alpha}_n\right) \otimes \boldsymbol{\nu} - \delta_4\boldsymbol{\xi}_{n+1} \otimes \boldsymbol{\nu}\right] \cdot \frac{\partial \boldsymbol{\sigma}_{n+1}}{\partial \Delta \boldsymbol{\varepsilon}}\end{aligned} \tag{3.134}$$

Using Eqs. (3.128), (3.134) and substituting in Eq. (3.120), $\frac{\partial \boldsymbol{\sigma}_{n+1}}{\partial \Delta \boldsymbol{\varepsilon}}$ can be expressed with respect to single unknown, $\frac{\partial \boldsymbol{\Delta\lambda}}{\partial \Delta \boldsymbol{\varepsilon}}$, as shown below.

$$\begin{aligned}\frac{\partial \boldsymbol{\sigma}_{n+1}}{\partial \Delta \boldsymbol{\varepsilon}} =&(1-D_{n+1})\boldsymbol{XM}-\boldsymbol{X}\left[\beta\frac{\boldsymbol{\sigma}^{e}}{1-D_{n}}+\frac{\Delta\lambda}{1+\delta_{5}}+\frac{\beta}{(1-D_{n+1})^{2}}\boldsymbol{PM}\boldsymbol{\sigma}_{n+1}\right.\\&\left.-\frac{\delta_{1}\Delta\lambda}{1+\delta_{5}}\boldsymbol{PM}\sum_{i=1}^{N}\left(\gamma_{i}\mu_{i}^{2}\boldsymbol{\alpha}_{n}\right)+\left(1-\frac{\Delta\lambda\,\delta_{2}}{1+\delta_{5}}\boldsymbol{PM}\boldsymbol{\xi}_{n+1}\right)\right]\otimes\frac{\partial\boldsymbol{\Delta\lambda}}{\partial\Delta\boldsymbol{\varepsilon}}\end{aligned} \tag{3.135}$$

where, the fourth-order tensor $\boldsymbol{X}$ takes the following form.

$$\begin{aligned}\boldsymbol{X}=&\left[\boldsymbol{I}+\frac{\boldsymbol{\sigma}^{e}}{1-D_{n}}\otimes\boldsymbol{v}+\frac{\Delta\lambda}{1+\delta_{5}}\frac{1}{1-D_{n+1}}\left(\frac{\boldsymbol{PM}\boldsymbol{\sigma}_{n+1}}{1-D_{n+1}}\otimes\boldsymbol{v}+\boldsymbol{PM}\right)\right.\\&\left.-\frac{\Delta\lambda\,\delta_{3}}{1+\delta_{5}}\boldsymbol{PM}\sum_{i=1}^{N}\left(\gamma_{i}\mu_{i}^{2}\boldsymbol{\alpha}_{n}\right)\otimes\boldsymbol{v}-\frac{\Delta\lambda\,\delta_{4}}{1+\delta_{5}}\boldsymbol{PM}\boldsymbol{\xi}_{n+1}\otimes\boldsymbol{v}\right]^{-1}\end{aligned} \tag{3.136}$$

Following, the derivative $\frac{\partial \Delta\lambda}{\partial \Delta \boldsymbol{\varepsilon}}$ is evaluated by differentiating the consistency condition and equilibrating the two ends. Differentiating Eq. (3.95) with respect to $\Delta\boldsymbol{\varepsilon}$ one obtains

$$\frac{\partial F_{n+1}}{\partial \Delta \boldsymbol{\varepsilon}}=\boldsymbol{\xi}_{n+1}\boldsymbol{P}\frac{\partial \boldsymbol{\xi}_{n+1}}{\partial \Delta \boldsymbol{\varepsilon}}-\frac{2}{3}k\left(\varepsilon_{q,n+1}\right)k'\left(\varepsilon_{q,n+1}\right)\frac{\partial}{\partial \Delta \boldsymbol{\varepsilon}}\left\{\sqrt{\frac{2}{3}}\frac{\Delta\lambda}{1-D_{n+1}}\bar{\Phi}_{n+1}\right\} \tag{3.137}$$

whilst,

$$\frac{\partial F_{n+1}}{\partial \Delta \boldsymbol{\varepsilon}}=0 \tag{3.138}$$

All terms in Eq. (3.137) are known from previous differentiations and thus, $\frac{\partial \Delta\lambda}{\partial \Delta \boldsymbol{\varepsilon}}$ can be computed as

$$\frac{\partial \Delta\lambda}{\partial \Delta \boldsymbol{\varepsilon}}=\frac{1-D_{n+1}}{H}\boldsymbol{V_{c}XM} \tag{3.139}$$

where, modulus H and the second order tensor $\boldsymbol{V_c}$ are defined as

$$\begin{aligned} H =& \frac{\beta}{1-D_n}\boldsymbol{V_c X \sigma}^e + \frac{\Delta\lambda}{1+\delta_5}\frac{\beta}{(1-D_{n+1})^2}\boldsymbol{V_c XPM\sigma}_{n+1} + \theta_3 \\ & - \frac{\Delta\lambda\,\delta_1}{1+\delta_5}\boldsymbol{V_c XPM}\sum_{i=1}^{N}\left(\gamma_i\mu_i^2\boldsymbol{\alpha}_n\right) + \left(1-\frac{\Delta\lambda\,\delta_2}{1+\delta_5}\right)\boldsymbol{V_c XPM\xi}_{n+1} \end{aligned} \tag{3.140}$$

$$\boldsymbol{V_c} = \zeta_3\boldsymbol{v} + \theta_1\zeta_2\boldsymbol{\xi}_{n+1}\boldsymbol{P} \tag{3.141}$$

$$\theta_3 = \theta_2\left(\frac{1-D_{n+1}+\beta}{\Delta}\lambda(1-D_{n+1})^2\right) - \theta_1\rho_1 \tag{3.142}$$

$$\zeta_3 = \theta_1\zeta_1 - \theta_2\frac{\Delta\lambda}{(1-D_{n+1})^2} \tag{3.143}$$

$$\zeta_2 = \frac{1}{1+\delta_5}\frac{1}{1-D_{n+1}} \tag{3.144}$$

$$\zeta_1(1+\delta_5) = \boldsymbol{\xi}_{n+1}\boldsymbol{P}\frac{\boldsymbol{\sigma}_{n+1}}{(1-D_{n+1})^2} - \delta_3\boldsymbol{\xi}_{n+1}\boldsymbol{P}\sum_{i=1}^{N}\left(\gamma_i\mu_i^2\boldsymbol{\alpha}_n\right) - \delta_4\bar{\Phi}_{n+1}^2 \tag{3.145}$$

$$\rho_1(1+\delta_5) = \frac{\beta}{(1-D_{n+1})^2}\boldsymbol{\xi}_{n+1}\boldsymbol{P\sigma}_{n+1} - \delta_1\boldsymbol{\xi}_{n+1}\boldsymbol{P}\sum_{i=1}^{N}\left(\gamma_i\mu_i^2\boldsymbol{\alpha}_n\right) - \delta_2\bar{\Phi}_{n+1}^2 \tag{3.146}$$

$$\theta_2 = \sqrt{\frac{8}{27}}k\left(\varepsilon_{q,n+1}\right)k'\left(\varepsilon_{q,n+1}\right)\bar{\Phi}_{n+1} \tag{3.147}$$

$$\theta_1 = 1 - \sqrt{\frac{8}{27}}k\left(\varepsilon_{q,n+1}\right)k'\left(\varepsilon_{q,n+1}\right)\frac{\Delta\lambda}{1-D_{n+1}}\bar{\Phi}_{n+1}^{-1} \tag{3.148}$$

It can be readily shown that for $\Delta\lambda \to 0$ modulus H in Eq. (3.140) becomes identical to modulus h obtained from Eq. (3.75). Finally, substituting Eq. (3.139) in Eq. (3.135) the consistent tangent moduli obtain the following form.

$$\begin{aligned} \boldsymbol{M}_{ep}^{L} =& (1-D_{n+1})\boldsymbol{XM} - \frac{\beta}{1-D_n}\frac{1-D_{n+1}}{H}\boldsymbol{X\sigma}^e \otimes \boldsymbol{XMV_c} \\ & - \frac{\Delta\lambda}{1+\delta_5}\frac{\beta}{1-D_{n+1}}\frac{1}{H}\boldsymbol{XPM\sigma}_{n+1} \otimes \boldsymbol{XMV_c} \\ & \frac{\Delta\lambda\,\delta_1}{1+\delta_5}\frac{1-D_{n+1}}{H}\boldsymbol{XPM}\sum_{i=1}^{N}\left(\gamma_i\mu_i^2\boldsymbol{\alpha}_n\right) \otimes \boldsymbol{XMV_c} \\ & - \left(1-\frac{\Delta\lambda\,\delta_2}{1+\delta_5}\right)\frac{1-D_{n+1}}{H}\boldsymbol{XPM\xi}_{n+1}\boldsymbol{XMV_c} \end{aligned} \tag{3.149}$$

Eqs. (3.149) shows that regardless of the strong coupling between plasticity and damage and the complexity of the model, the consistent moduli are provided in explicit form. It can be verified that Eq. (3.149) is consistent with the present integration algorithm; considering $\Delta\lambda \rightarrow 0$ one can readily show that the algorithmic moduli of Eq. (3.149) become equal to the tangent moduli reported in Eq. (3.77). The derived consistent moduli provide quadratic converge of the solution method. The solution algorithm of the incremental problem is summarised in Table 3.4.

Table 3.4: Summary of the incremental solution procedure.

Elastic predictor	$\boldsymbol{\sigma}^e = (1-D_n)\boldsymbol{M}\left(\boldsymbol{\varepsilon}_{n+1} - \boldsymbol{\varepsilon}_n^p\right)$
Check for yielding	$F(\boldsymbol{\sigma}^e, \boldsymbol{a}_n, \varepsilon_{q,n}, D_n)$
If $F \leqslant 0$ then set	$\Delta\lambda = 0$, $\boldsymbol{\sigma}_{n+1} = \boldsymbol{\sigma}^e$, $\boldsymbol{a}_{n+1} = \boldsymbol{a}_n$, $\varepsilon_{q,n+1} = \varepsilon_{q,n}$, $D_{n+1} = D_n$
If $F > 0$ plastic-damage correction is necessary	
Newton's scheme, set $\Delta\lambda = \Delta\lambda^0$ (initial guess, typically equal to 0.0)	
†Compute μ_i	$\mu_i = \left[1 + \gamma_i \sqrt{\frac{2}{3}} \frac{\Delta\lambda}{1-D_{n+1}} \bar{\Phi}_{n+1}\right]^{-1}$
⋆Compute D_{n+1}	$D_{n+1} = \Delta\lambda F'_{D,n+1}$
Compute $\boldsymbol{\Gamma}$	$\boldsymbol{\Gamma}$=Diag$[\Gamma_{11}, \quad \Gamma_{22}, \quad \Gamma_{22}]$
Compute $\boldsymbol{\eta}^e$	$\boldsymbol{\eta}^e = \boldsymbol{Q}^t \left[\frac{\boldsymbol{\sigma}^e}{1-D_n} - \sum_{i=1}^{N} \left(\frac{\boldsymbol{\alpha}_n^i}{\mu_i}\right)\right]$
Compute $\boldsymbol{\eta}_{n+1}$	$\boldsymbol{\eta}_{n+1} = \boldsymbol{\Gamma}\boldsymbol{\eta}^e$
Compute $\bar{\Phi}_{n+1}$	$\bar{\Phi}_{n+1} = \sqrt{\boldsymbol{\xi}_{n+1}\boldsymbol{P}\boldsymbol{\xi}_{n+1}} = \sqrt{\boldsymbol{\eta}_{n+1}\boldsymbol{\Lambda}_P\boldsymbol{\eta}_{n+1}}$
Check equilibrium	$F_{n+1}(\Delta\lambda) = \bar{\Phi}_{n+1} - \sqrt{\frac{2}{3}} k \left(\varepsilon_{q,n} + \sqrt{\frac{2}{3}} \frac{\Delta\lambda}{1-D_{n+1}} \bar{\Phi}_{n+1}\right)$
Compute $F'(\Delta\lambda)$	$F'(\Delta\lambda) = \frac{\partial F(\Delta\lambda)}{\partial \Delta\lambda}$
Compute $d\Delta\lambda$	$d\Delta\lambda = \frac{F(\Delta\lambda)}{F'(\Delta\lambda)}$
Update $\Delta\lambda$	$\Delta\lambda = \Delta\lambda + d\Delta\lambda$
Check	$min\left\{\left\lvert\frac{d\Delta\lambda}{\Delta\lambda}\right\rvert, \lvert F(\Delta\lambda)\rvert\right\}$ <tolerance (e.g. 10^{-4}), if not satisfied, repeat
Update internal variables and evaluate $\boldsymbol{M}_{ep}^L$	
Update $\boldsymbol{\xi}_{n+1}$	$\boldsymbol{\xi}_{n+1} = \boldsymbol{Q}\boldsymbol{\eta}_{n+1}$
Update $\boldsymbol{\alpha}_{n+1}$	$\boldsymbol{\alpha}_{n+1} = \sum_{i=1}^{N}\left(\mu_i\boldsymbol{\alpha}_n^i\right) + \sum_{i=1}^{N}\left(C_i\mu_i\right)\frac{\Delta\lambda}{1-D_{n+1}}\boldsymbol{\xi}_{n+1}$
Update $\boldsymbol{\sigma}_{n+1}$	$\boldsymbol{\sigma}_{n+1} = (1-D_{n+1})\left(\boldsymbol{\xi}_{n+1} + \boldsymbol{\alpha}_{n+1}\right)$
Update $\boldsymbol{M}_{ep}^L$	$\boldsymbol{M}_{ep}^L = (1-D_{n+1})\boldsymbol{X}\boldsymbol{M} - \frac{\beta}{1-D_n}\frac{1-D_{n+1}}{H}\boldsymbol{X}\boldsymbol{\sigma}^e \otimes \boldsymbol{X}\boldsymbol{M}\boldsymbol{V_c}$ $-\frac{\Delta\lambda}{1+\delta_5}\frac{\beta}{1-D_{n+1}}\frac{1}{H}\boldsymbol{X}\boldsymbol{P}\boldsymbol{M}\boldsymbol{\sigma}_{n+1} \otimes \boldsymbol{X}\boldsymbol{M}\boldsymbol{V_c}$ $\frac{\Delta\lambda\delta_1}{1+\delta_5}\frac{1-D_{n+1}}{H}\boldsymbol{X}\boldsymbol{P}\boldsymbol{M}\sum_{i=1}^{N}\left(\gamma_i\mu_i^2\boldsymbol{\alpha}_n\right) \otimes \boldsymbol{X}\boldsymbol{M}\boldsymbol{V_c}$ $-\left(1 - \frac{\Delta\lambda\delta_2}{1+\delta_5}\right)\frac{1-D_{n+1}}{H}\boldsymbol{X}\boldsymbol{P}\boldsymbol{M}\boldsymbol{\xi}_{n+1}\boldsymbol{X}\boldsymbol{M}\boldsymbol{V_c}$

† Quantity μ_i is evaluated using the values of the internal variables obtained in the previous step of the Newton's scheme.

⋆ The damage evolution function $F'_{D,n+1}$ can be updated using the internal variables of the previous iterative step or the un-converged values of the internal variables.

3.3.5 Algorithmic implementation and simulation of damage

The strain-softening response originating from material deterioration leads unavoidably to spurious mesh dependency. This is true for both 3D and plane stress formulation. To minimise mesh dependency effects, the simulation strategy employed in Section 3.2.4 is also adopted herein with necessary modifications. More specifically, hybrid finite elements incorporating pressure/displacement formulation are not available in ABAQUS (2016) software for shell-type plane stress formulation. Instead, conventional shell-type elements with displacement only degrees of freedom are used. It should be noted that hybrid finite elements are prompted for plasticity-damage simulations to ensure the isochoric plastic deformations of J_2-flow theory and eliminate spurious pressure oscillations (Fig. 3.10). It is expected that under plane stress formulation pressure localisation will be much less evident in comparison to 3D formulation. Hybrid finite elements for plane stress conditions can be implemented in commercial finite element software as a user defined element [Bathe (1996); De and Bathe (2001)], but such a task lies outside the scope of this work.

The isotropic damage function can be described with a wide range of CDM models incorporated under the proposed numerical scheme, but to eliminate mesh dependency the softening modulus must be properly regularised according to the element size. In the present investigation the modified version of Hillerborg et al. (1976) CDM model is employed, as proposed by Bazant and Oh (1983) on the basis of smeared band approach. This CDM model has been presented in detail in Section 3.2.4 and therefore it will not be discussed further herein. Regarding the regularisation of the damage function, linear shell finite elements (S4) are employed in the present work and l_{ch} is taken equal to $\sqrt[3]{(12/\sqrt{2})V_{el}}$ as proposed by Oliver (1989), where V_{el} is the element's volume. The value of V_{el} is not provided exclusively in the material user subroutine UMAT, and for its computation the utility subroutines UVARM and UEXTERNALDB, presented in Section 3.2.4, are employed.

The choice of this particular CDM model for both sets of analyses (i.e. 3D and plane stress formulation) is attributed to its simplicity and the limited number of calibrated parameters. Additional work is undertaken at the moment for calibrating a CDM model to simulate damage evolution in metal structural components experiencing ultra low-cycle fatigue.

3.3.6 Simulation of large-scale experiments

The numerical scheme presented in Sections 3.3.1 - 3.3.4 is validated in simulating elastoplastic-damage response and ductile fracture in thin-walled metal structural components subjected to intense cyclic loading. For this purpose, two pipe elbow specimens of the experimental campaign presented in Section 2.3.1 are examined. The two specimens, namely $E6$ and $E7$ have been subjected to excessive cyclic loading with amplitude of $\pm$250 mm ($E6$) and $\pm$300 mm ($E7$), which resulted in failure of the specimens under ultra low-cycle fatigue after 15 and 11 cycles, respectively. For additional information regarding the experimental data the reader can refer in Section 2.3.1.

The mechanical behaviour of specimen $E6$ and $E7$ is numerically simulated using the finite element software ABAQUS (2016) enhanced with the proposed numerical scheme, which is implemented as material user subroutine UMAT. The finite element model of the experimental set-up is presented in detail in Section 2.3.2 and it will not be discussed further for brevity. Mesh dependency effects are also examined using four different meshes (M1, M2, M3, M4) of the finite element model. Information regarding the finite element size at the elbow flank are provided in Table 3.5. In all cases, 9 integration points are considered through the thickness.

Table 3.5: Mesh size information at the elbow flank.

Mesh	M1	M2	M3	M4
Element dim. (mm)	10×10	8×8	6×6	4×4
l_{ch} (mm)	17.7	15.2	12.15	9.82

3.3.6.1 Calibration of cyclic plasticity-damage model

The proper calibration of the material model is a key issue towards simulating accurately the mechanical response of the pipe elbow specimens. Isotropic hardening as well as kinematic hardening are considered and the the cyclic hardening parameters of the material model are obtained from Table 3.3.

As already discussed in Section 3.2.5.3, no information is available for calibrating the damage related parameters. In the absence of dedicated material testing and for the purposes of the present simulations, the damage parameters are selected so that the finite element model with mesh M1 can predict accurately the number of cycles to failure of specimen $E7$. To quantify mesh dependency effects, these parameters are kept constant in all analyses.

The damage initiation equivalent plastic strain ε_f and the critical damage state D_{crit} are kept as in the 3D model; that is 1.0 and 0.2, respectively. On the other hand, a different G_f value is selected due to different formulation of the damage evolution function. To accommodate for the order of magnitude difference between $\Delta\varepsilon_q$ and $\Delta\lambda$, G_F is selected equal to 220 J/mm. Furthermore, damage is accumulated only under negative pressure values.

3.3.6.2 Numerical simulation results

Comparisons are provided between experimental data and numerical results in a similar manner with the investigation in Section 3.2.5. The force-displacement response of the first loading cycle is shown in Fig. 3.11 for both specimens. Numerical results are reported for the four finite element meshes, denoted as "M1-M4". Fig. 3.11 shows minor differences between the numerical results, while the comparison with experimental data shows the ability of the model to simulate quite accurately the inelastic load-displacement response of the pipe elbow under severe imposed deformations.

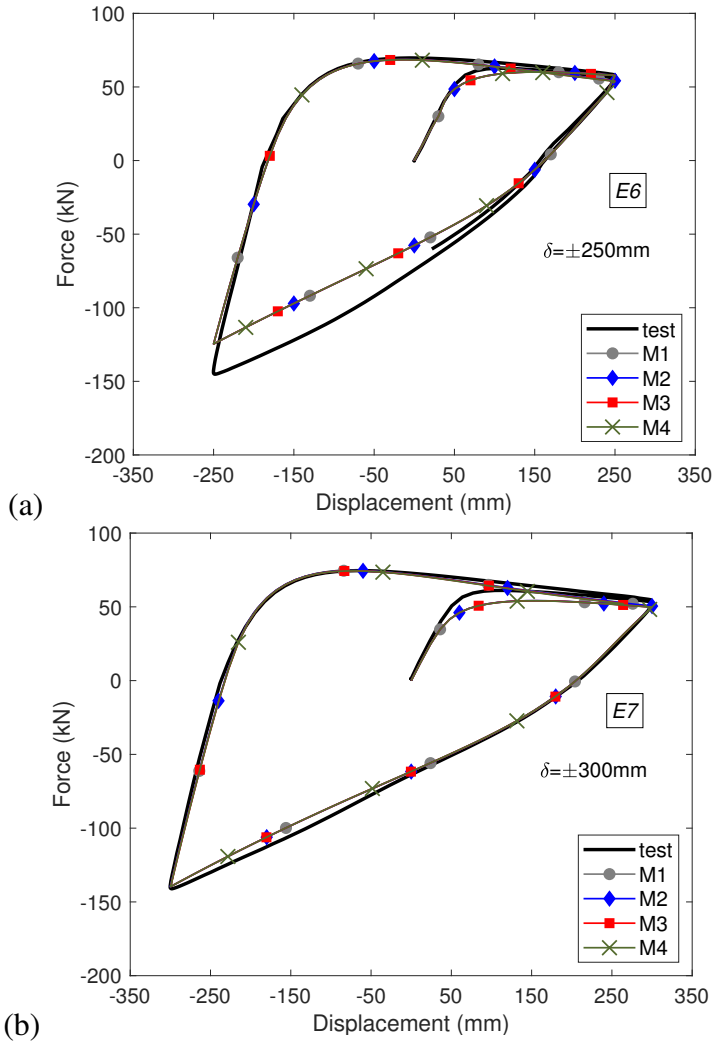

Figure 3.11: First loading cycle for (a) test $E6$ ($\delta = \pm 250$mm) and (b), test $E7$ ($\delta = \pm 300$mm).

The force-displacement response and the force amplitude recorded in each load cycle up to the point of through-thickness cracking are presented in Fig. 3.12 and Fig. 3.13 for specimens $E7$ and $E6$, respectively. The numerical results obtained with the four finite element meshes are presented and can be compared with the corresponding experimental data. Fig. 3.12(b) and Fig. 3.13(b) indicate that the results of the four meshes present negligible differences in terms of force amplitude, demonstrating that mesh dependency effects have minor impact. However, the number of cycles to through-thickness cracking obtained with the four meshes fluctuate more compared to the 3D model. The use of conventional finite elements leads unavoidably to some pressure oscillation and additional strain localisation at the shear band (Fig. 3.16), influencing the number of cycles to failure. In addition, the shell-model considers only a single element through the thickness and the size of this element might affect the development of through-thickness crack.

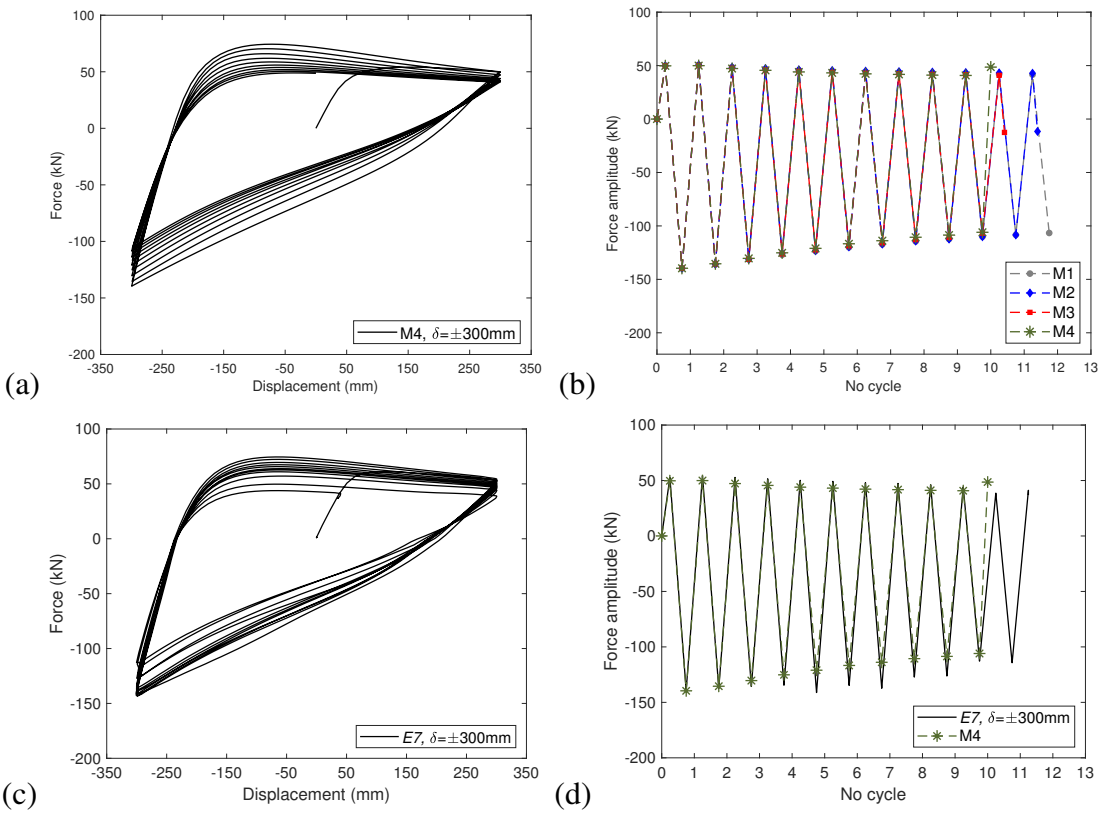

Figure 3.12: Numerical and experimental results for test $E7$ ($\delta = \pm 300$mm) in terms of force-displacement diagrams (a, c) and resistance reduction over the loading cycles (b, d).

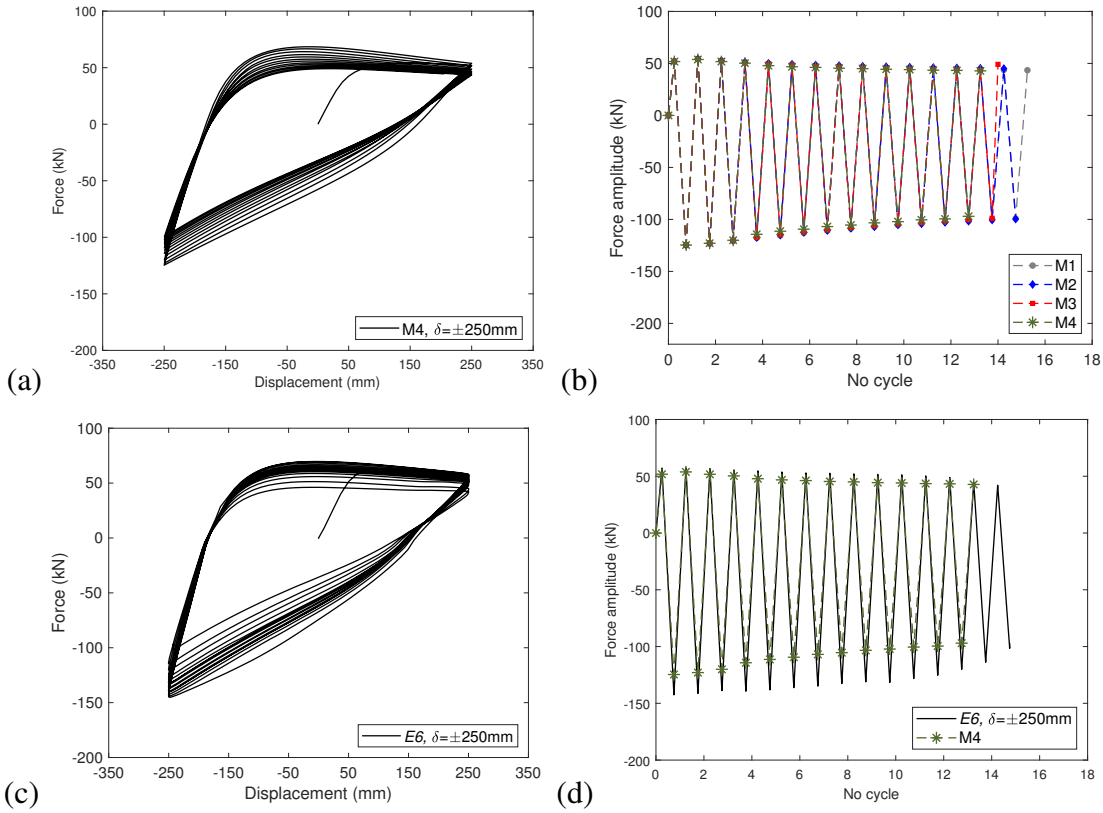

Figure 3.13: Numerical and experimental results for test $E6$ ($\delta = \pm 250$mm) in terms of force-displacement diagrams (a, c) and resistance reduction over the loading cycles (b, d).

In terms of computational efficiency, regardless of the complexity of these analyses, rapid convergence of the incremental solution is observed throughout the analysis (3-4 global iterations). The analysis time of the shell model is approximately 10 times less compared to the 3D model.

The ability of the material model to simulate strain evolution throughout the load cycles is also examined and the results obtained with the four finite element meshes are presented in Fig. 3.14. The strain plots in Fig. 3.14 concern hoop strain measurements obtained 6 mm and 9 mm from the "flank" location (gauge 2 and gauge 3 in Fig. 2.6). The experimental results of specimens $E6$ and $E7$ are presented, considering also the results obtained from the four finite element meshes (M1, M2, M3 and M4).

Comparisons with experimental measurements are limited to 6 and 4 load cycles for specimens $E6$ and $E7$ due to strain gauge detachment. The numerical predictions are in good agreement with the experimental data especially during the initial load cycles. Furthermore, the results of the four meshes present somewhat different trends of strain evolution even from the initial load cycles. This is more evident when examining mesh M4. This behaviour is not evident in the 3D model (Fig. 3.8) because it is attributed to pressure localisation, shown in the contour plots of Fig. 3.16.

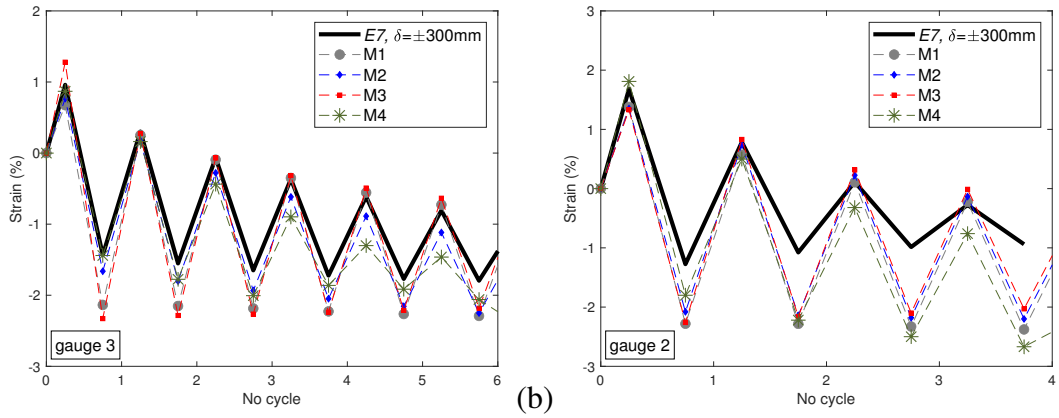

(a) (b)

Figure 3.14: Variation of strain at the "flank" location of the two elbows: (a) specimen $E6$ and (b), specimen $E7$; comparisons between numerical results and experimental measurements.

Finally, the numerical simulations indicate accumulation of damage at the "flank" of the bend due to excessive hoop strain, leading to low-cycle fatigue and pipe wall rupture which is absolutely consistent with the experimental observations. Fig. 3.15 depicts the local damage accumulation (SDV5) and the development of through-thickness crack obtained numerically from the simulation of test $E7$ using meshed model M4. Fig. 3.15 verifies that the damage pattern observed in the failure stage of the numerical model is very similar in size and configuration to the crack observed experimentally. Identical crack formations are observed in the other finite element models but are not presented for brevity.

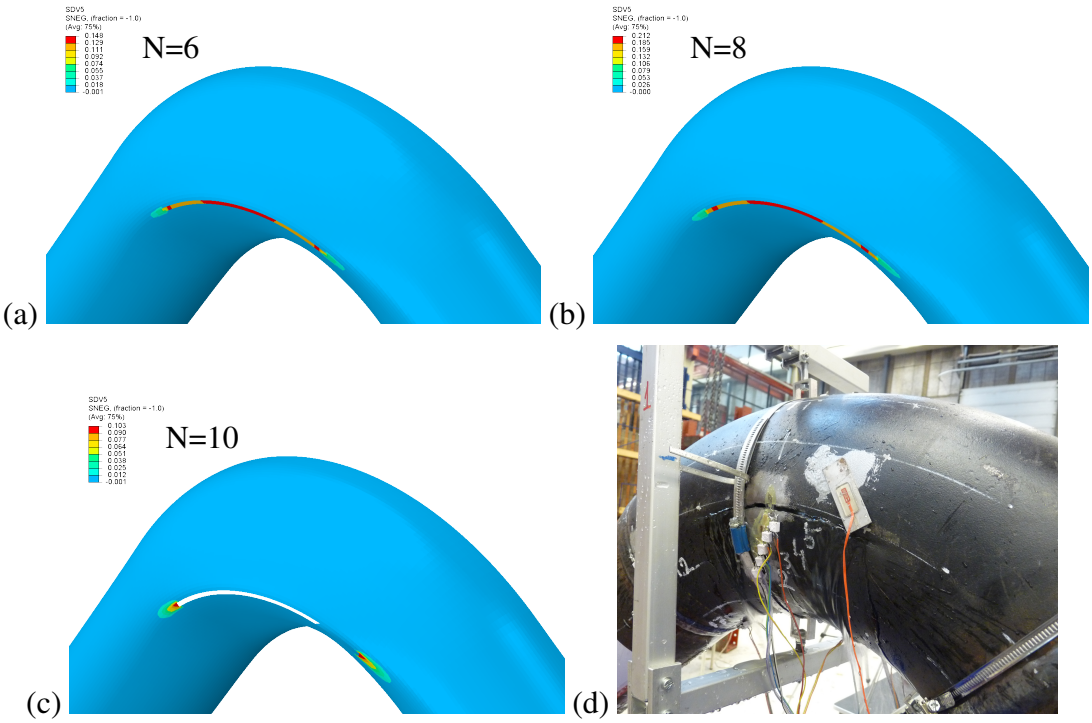

Figure 3.15: Damage distribution obtained from mesh M4 during the (a) 6^{th} load cycle, (b) 8^{th} load cycle and (c), 10^{th} load cycle; (d) shape of crack specimen $E7$.

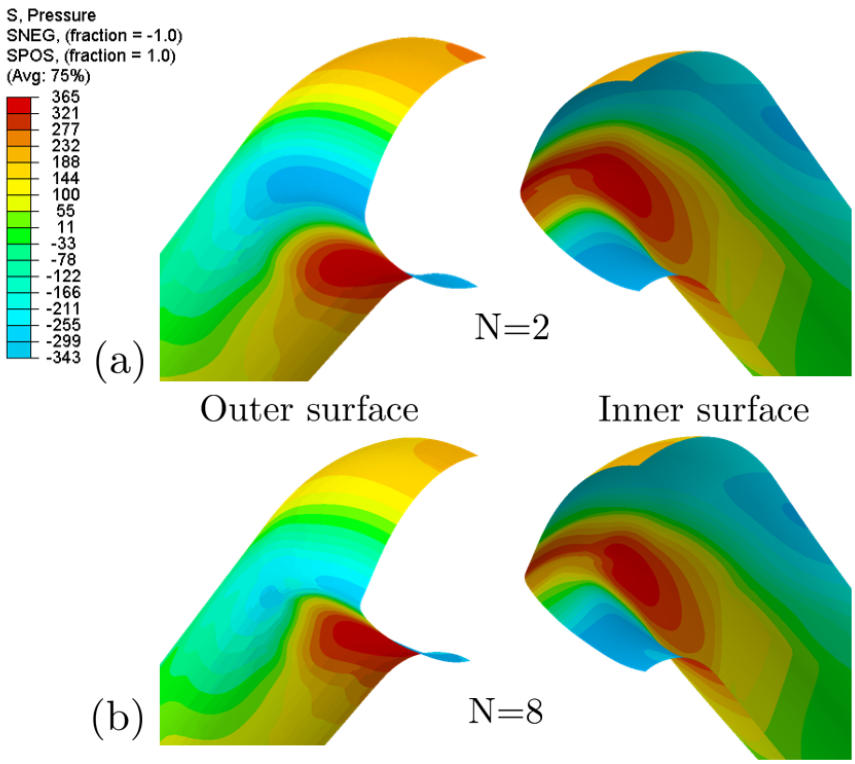

Figure 3.16: Pressure distribution observed in the inner and the outer surface of meshed model M4 (a) prior to damage initiation; (b) after damage initiation.

3.4 Summary

The cyclic plasticity-damage response and ductile fracture of steel metal components is investigated with the use of rigorous numerical tools. Two computational frameworks are presented for implementing cyclic plasticity-damage material models for 3D and plane stress formulation. The ultimate goal is to develop optimised implementation schemes for simulating low-cycle fatigue in metals.

It is demonstrated that the proposed numerical integration schemes feature computational efficiency in comparison to similar numerical methods reported in the literature. Constitutive relations are integrated implicitly through the solution of a single scalar equation and the consistent tangent operator is provided in explicit form to guarantee robustness. Issues related to strain-softening and mesh dependency are discussed and an appropriate simulation strategy is adopted to mitigate these effects.

The capabilities of the proposed numerical schemes for 3D and plane stress formulation are demonstrated by comparing very successfully numerical results with experimental measurements obtained from two large-scale laboratory (physical) tests on steel pipe elbows. Mesh dependency effects are quantified using different meshed models, indicating minor impact in the quality of the numerical results. Particularly for the 3D formulation where hybrid finite elements are employed, the solution is found to be free from spurious mesh dependency and abrupt pressure oscillations. Overall, the numerical results indicate that the simulation methodology employed in each case can be efficiently applied in large-scale structural computations of metal components subjected to low-cycle fatigue.

Chapter 4

Ultra low-cycle fatigue of S420 and S700 steel welded tubular X-joints

4.1 Introduction

The offshore renewable industry is growing rapidly and its industrial targets hit new records every decade [Jeffrey and Sedgwick (2011); Moccia et al. (2011)]. According to the European Wind Energy Association (EWEA) [Selot et al. (2019)], currently, 87.7% of the offshore wind turbines are supported by monopile systems and are located in depths shallower than 25 m, while the resulting capacity is less than 4 MW. The exploitation of deeper waters and the use of higher output wind turbines require the employment of stiffer and more resilient support systems. Bottom-founded jacket substructures, assembled from tubular welded connections, constitute an attractive solution and characteristic examples of successful installation in depths of 30-45 m are, among several others the Beatrice (2018) and Alpha Ventus (2013) windfarm parks. The use of offshore wind jackets in depths up to 80 m is also under consideration in ongoing research projects [JABACO (2019)]. The supporting units are exposed to repeated loading due to ocean waves and the operational loads of the turbine, and may

fail due to fatigue at critical locations. The accurate assessment of the fatigue life of jacket substructures is crucial for the sustainability of the project over its design life and it has been the subject of investigation in numerous recent research articles [Dong et al. (2011, 2012); Mohammadi et al. (2016)].

In the last Chapter of the Thesis, the ultra low-cycle fatigue performance of high-strength steel tubular welded X-joints is examined through a large experimental program, supported with corresponding numerical analyses. The research work is motivated by the needs to provide cost-efficient structural solutions for the oil and gas sector and particularly offshore renewables. The specimens represent the X-brace joints of an offshore wind turbine jacket substructure considered for installation at a depth of 55 m with a scaling factor of 1:3 employed in JABACO (2019) project. The X-joint specimens have been manufactured using S420 and S700 steel grade tubes and are subjected to extreme cyclic in-plane bending, leading to ultra low-cycle fatigue failure within less than 100 cycles. Furthermore, rigorous numerical models are used to simulate the experimental response of the specimens and examine whether finite element models can provide accurate predictions for the bending moment-displacement global response and for local strains at critical locations. Comparison is also conducted between the present experimental data and relevant test results on mild or high-strength steel welded tubular components, as well as design predictions from existing codes and standards.

4.2 Experimental Program

The experimental program consisted of seven ultra low-cycle fatigue tests on high-strength steel tubular welded X-joints. The tubular members used for fabricating the connection have been provided by SSAB, Stockholm, Sweden. The specimens have been fabricated in Hollandia Systems, Rotterdam, Netherlands according to the American Welding Society (2004) (AWS D1.1) provisions for the tubular member

welds and in accordance with appropriate Welding Procedure Specifications (WPSs) developed by the authors, in cooperation with Hollandia Systems, so that the specimen welds are representative of those found in offshore steel platforms.

4.2.1 Description of specimens

The seven X-joint specimens are denoted as $X_1 - X_7$. The first set of X-joints ($X_1 - X_4$) was fabricated using tubular components made of S420 steel grade with external diameter and thickness equal to 219.1 mm and 10 mm corresponding to a diameter-to-thickness ratio (D/t) of about 22. In addition, S700 tubes with external diameter and thickness of 273 mm and 10 mm and D/t equal to 27 were used for manufacturing specimens $X_5 - X_7$. For convenience, connections $X_1 - X_4$ and $X_5 - X_7$ were grouped to "Joint-1" and "Joint-2" assemblies. The three-dimensional configuration of the specimens is depicted in Fig. 4.1, while the geometric properties of each joint are summarised in Table 4.1. As shown in Fig. 4.1, the free ends of the tubular components are capped with welded plates for the requirements of testing. For clarity, the four chord crown locations where strain gauges are attached, are labelled as (1), (2), (3), (4), starting from the upper left corner and proceeding clockwise; the two crown locations located above the braces are labelled as (1), (2) and the other two crown points are represented by numbers (3) and (4). Strain measurements were also recorded at the point where the maximum principal strains/stress were observed during the linear elastic analysis of Joint-1 and Joint-2 connections, subjected to monotonic/cyclic in-plane bending. This additional location is labelled in Fig. 4.1 as "in-between" point.

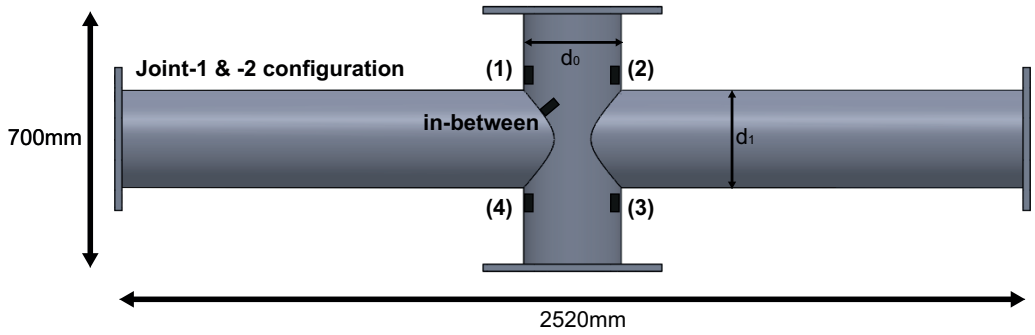

Figure 4.1: Three-dimensional configuration of Joint-1 and Joint-2.

Table 4.1: Geometric properties of specimens $X_1 - X_7$.

Joint:	Joint-1				Joint-2		
Specimen:	X_1	X_2	X_3	X_4	X_5	X_6	X_7
d_0=d_1 (mm)	219.1				273		
t_0=t_1 (mm)	10				10		
β=d_1/d_0	1.0				1.0		
τ=t_1/t_0	1.0				1.0		
γ=$d_0/2t_0$	10.96				13.65		

4.2.2 Material characterisation

A series of laboratory tests on strip specimens (coupons) extracted from the tubes of the same heat as those used for the fabrication of the specimens were performed to determine the monotonic and cyclic properties of the steel material in the inelastic range. The material tests have been performed using an Instron servo-hydraulic actuator of 250kN capacity. An anti-buckling device, shown in Fig. 4.2, was used in the fully-reversed cyclic tests to restrict buckling of the specimens under compressive loading. The resulting stress-strain curves obtained from those coupons are presented in Fig. 4.3. Monotonic tests showed a 0.2% proof stress/ultimate strength of 519/585 MPa and 745/840 MPa for the S420 and S700 steel grades respectively. Furthermore, cyclic tests at 2% strain amplitude indicated a minor cyclic hardening in both metals during initial load cycles. The welding materials were selected according to the WPSs developed for each joint configuration and their nominal grades overmatch the nominal

yield strength of S420 and S700 steel grades by 29% and 6% respectively, which complies with the design provisions of DNVGL-RP-C203 (2016); DNVGL-RP-C208 (2016) and is in accordance to common practice in offshore steel construction.

Figure 4.2: Fully-reversed cyclic material tests and anti-buckling device.

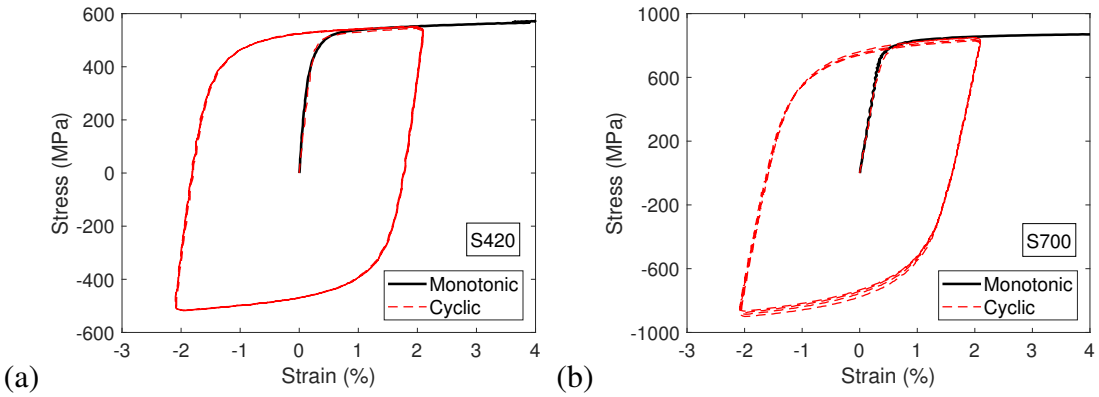

Figure 4.3: Monotonic and cyclic stress strain response obtained from testing coupon specimens extracted from tubes (a) S420 steel grade and (b) S700 steel grade.

4.2.3 Instrumentation

The specimens were properly instrumented during testing to record the force-displacement response and the induced strains at the locations of interest and to identify through-thickness cracking. The applied load was measured directly from the load cell

of the actuator system and was recorded with the use of an external data logger. Displacement measurements were obtained with the use of string potentiometers, placed as shown in Fig. 4.4(a) in order to measure accurately the actual vertical displacement of the brace end. Local longitudinal strains were measured at crown locations of the chord with the use of uni-directional five-element-strip strain gauges (FXV-1), oriented perpendicular to the weld toe. Two FXV-1 series were used in every experiment, placed on chord crown points as shown in Fig. 4.4(b), at distance 5-9 mm from the weld toe. In the majority of the tests, two additional strain gauges were attached at the "in-between" location of the chord side (Fig. 4.1), at distance of 5-25 mm from the weld toe.

(a) 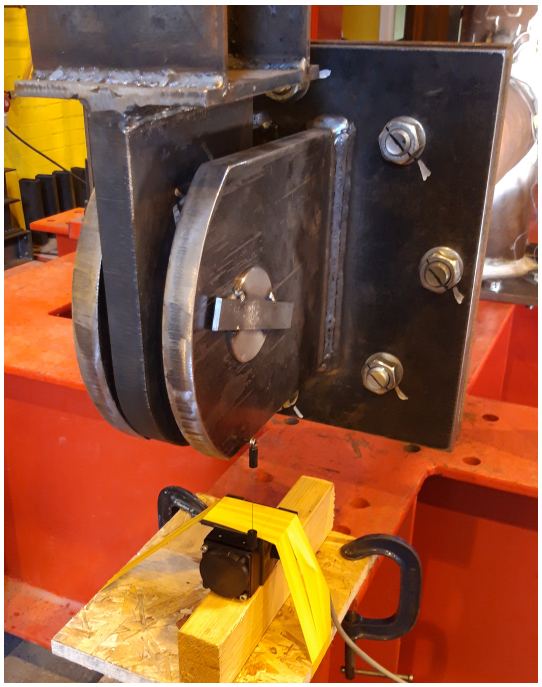 (b) 

Figure 4.4: (a) End brace displacement measurement and (b), local strain measurements in specimens X_1-X_7.

In the present test, initiation and propagation of surface cracks was monitored with a camera, shown in Fig. 4.5, while failure was defined as through-thickness cracking. To detect the stage at which the crack developed through the thickness of the tube wall, a small hole was drilled on the capping plate of each specimen, prior to testing, and two

smoke flares were inserted into the chord; subsequently the hole was sealed with a re-usable envelope. As shown in Fig. 4.5, when the through-thickness crack occurred, the trapped smoke escaped through the crack so that it was visible, and the corresponding number of cycles to failure was recorded.

Figure 4.5: Trapped smoke escaping through the crack which allows the measuring of the number of cycles to failure.

4.2.4 Experimental set-up

The experiments were conducted at the Structures Laboratory of The University of Edinburgh (School of Engineering) using an Instron 8800 servo-hydraulic actuator system of 1 MN capacity. The three-dimensional configuration of the experimental set-up is presented in the sketch of Fig. 4.6 and the main parts of the set-up are denoted in that figure. For clarity, a close-up sketch of the connection between the specimen and the experimental set-up is illustrated in Fig. 4.7, while a photo of the constructed set-up is depicted in Fig. 4.8 for the sake of completeness.

The hydraulic actuator was mounted on the test-ring to assemble a self-reacting structural system. The actuator was placed vertically, hanged from the horizontal

crossbeam. The other end of the actuator was pin-connected at the centre of the 3.3 m-long spreader beam, as shown in Figs. 4.6 and 4.7 initially located at a distance of 200 mm from the top of the specimen. A pin-ended column, highlighted in Fig. 4.6, was used to connect the spreader beam with the specimen, allowing for axial deformations to take place while preventing the development of axial tensile forces on the bracings (stretching). The X-joint specimen, shown more clearly in Fig. 4.7, was rigidly supported at the base of the chord member, while the top edge of the chord was capped with a welded plate to preserve symmetry. Two lateral support systems were fixed on the test-rig to ensure the safe operation of the actuator by restricting sideways movements of the crossbeam, which was free to move in the vertical direction. During testing, the actuator was moving vertically together with the spreader beam, which was imposing a repeated displacement of alternating sign at the ends of the braces, introducing in-plane cyclic bending loading at the welded connection. The experimental arrangement was symmetric and the lateral distance between the centroid of the chord and the load application points was equal to 1.5 m. The experiments were conducted under a displacement-control scheme with ratio $R =$ -1 (fully-reversed displacement) and the movement of the hydraulic actuator was controlled via the Instron WaveMatrix software.

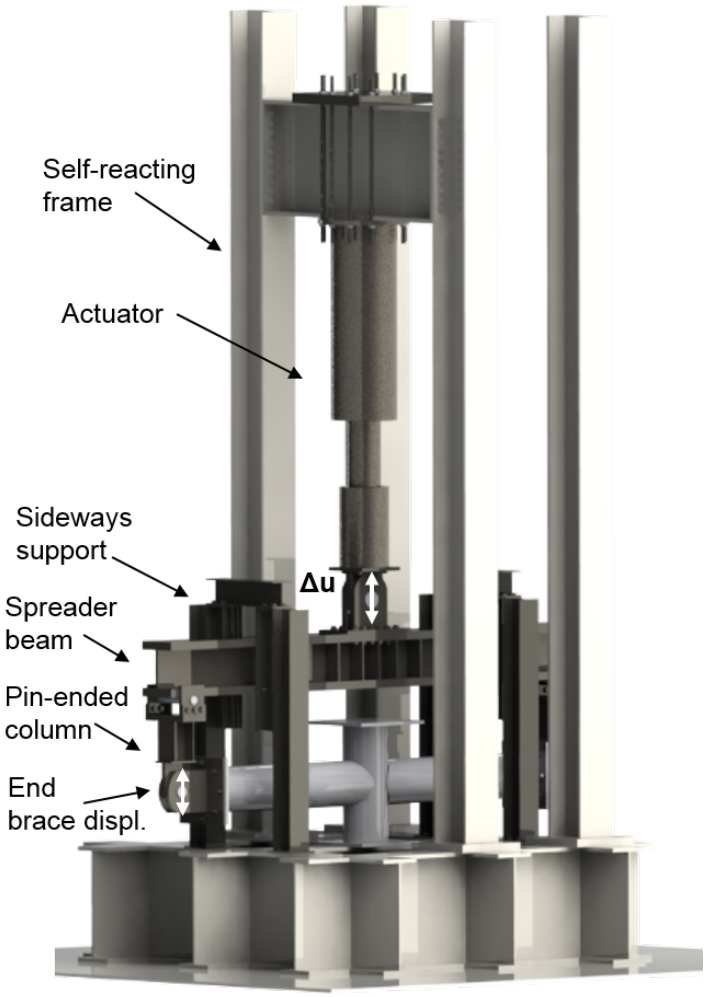

Figure 4.6: Three-dimensional computer visualisation of experimental set-up.

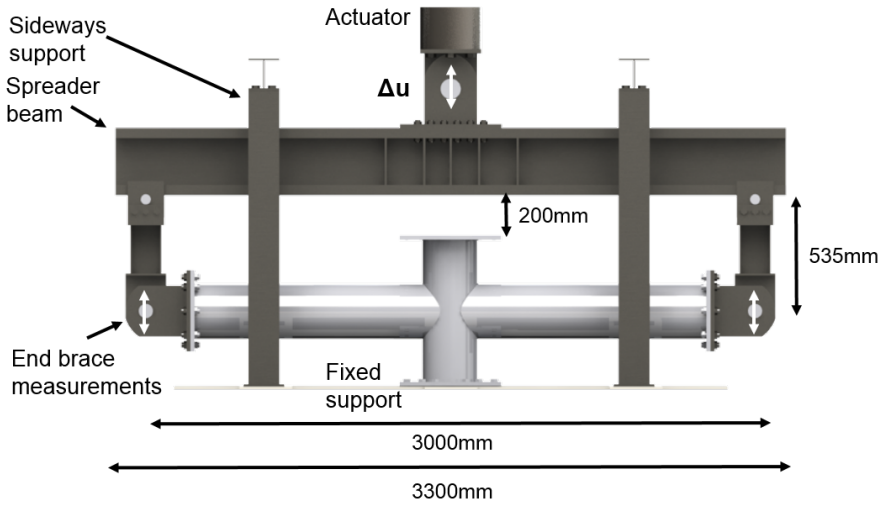

Figure 4.7: Schematic representation of in-plane cyclic bending testing arrangement.

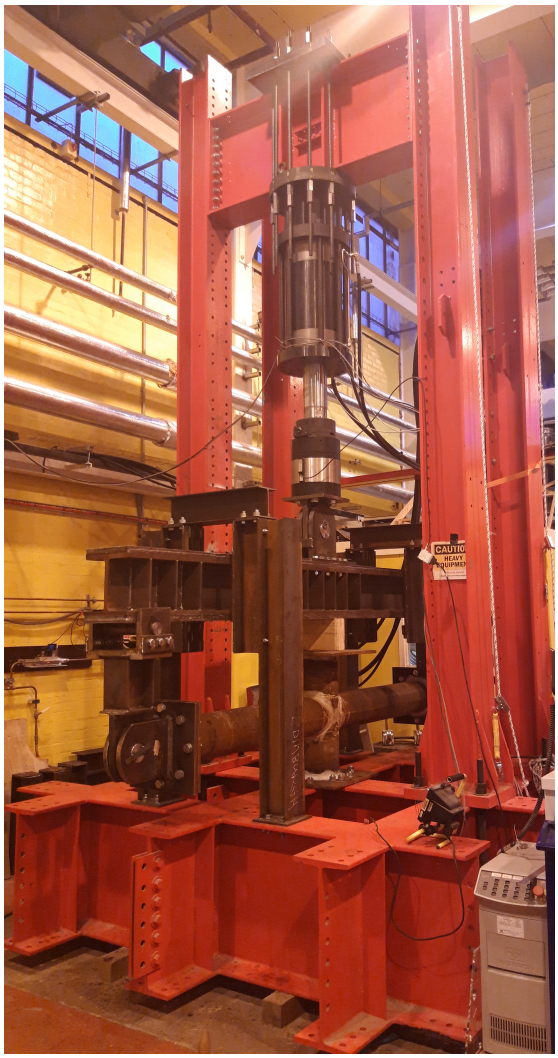

Figure 4.8: Photo of the experimental set-up.

Each tubular X-joint specimen was subjected to a specific displacement amplitude, in order to explore the ultra low-cycle fatigue performance of the welded tubular steel joints at a wider range of fatigue life. A preliminary finite element analysis was conducted prior to the experiments to support the selection of the testing displacement amplitudes, shown in Table 4.2 together with the value of the maximum applied moment normalised with respect to the "yield bending moment" M_y. The value of M_y was defined as the bending moment that corresponds to first yielding of the joint, computed numerically through the finite element model under monotonic loading conditions. The M_y values are equal to 109 kNm and 239 kNm for Joint-1 and Joint-2, respectively. The

resisting bending moment was decreasing gradually over the loading cycles due to material degradation.

Table 4.2: Testing conditions of specimens $X_1 - X_7$.

Joint:	Joint-1				Joint-2		
Specimen:	X_1	X_2	X_3	X_4	X_5	X_6	X_7
Edge brace displ. (mm)	± 29	± 35	± 41	± 47.5	± 31.6	± 38	± 48
$\lvert M_{max}/M_y \rvert$	1.19	1.34	1.40	1.49	1.16	1.32	1.51

4.2.5 Experimental results

The bending moment-displacement response recorded at various load cycles during testing of specimens X_1-X_4 and X_5-X_7 is presented in Fig. 4.9 (a-d) and Fig. 4.10 (a-c), respectively. Figs. 4.9 and 4.10 show that all specimens experienced a small amount of cyclic hardening during the first load cycle, while the hysteresis response changed slightly prior to damage initiation, in which case, the resisting moment capacity started decreasing noticeably. The sudden decrease observed in the bending moment-displacement diagram of specimen X_6 during the initial load cycles (Fig. 4.10(b)) was attributed on a loose bolted connection and not to any material damage. In this case, the test was interrupted to tighten the bolts in this joint, and the slippage effects have been eliminated.

In Joint-1 specimens and in particular specimen X_2, which was subjected to brace edge displacements of ± 35 mm, strength reduction due to material degradation initiated at about the 10^{th} load cycle, whereas damage effects become more pronounced after 30 load cycles. Through-thickness cracking occurred at the 47^{th} load cycle and the test was interrupted after 49 cycles, where the maximum resisting bending moment was reduced by 42% with respect to the corresponding maximum bending moment of the first cycle. In specimen X_5 of the Joint-2 group, through-thickness cracking occurred

at the 58^{th} load cycle. In this case, material degradation initiated after 15 load cycles and became noticeable after 40 load cycles. The experiment was interrupted after 65 cycles, where the structural capacity has been reduced by almost 30%.

The experimental results show that in both joint configurations, strength degradation manifested initially at low rate, while rapid reduction of resisting bending moment was observed as the specimen approached failure, indicating two distinct stages of damage evolution.

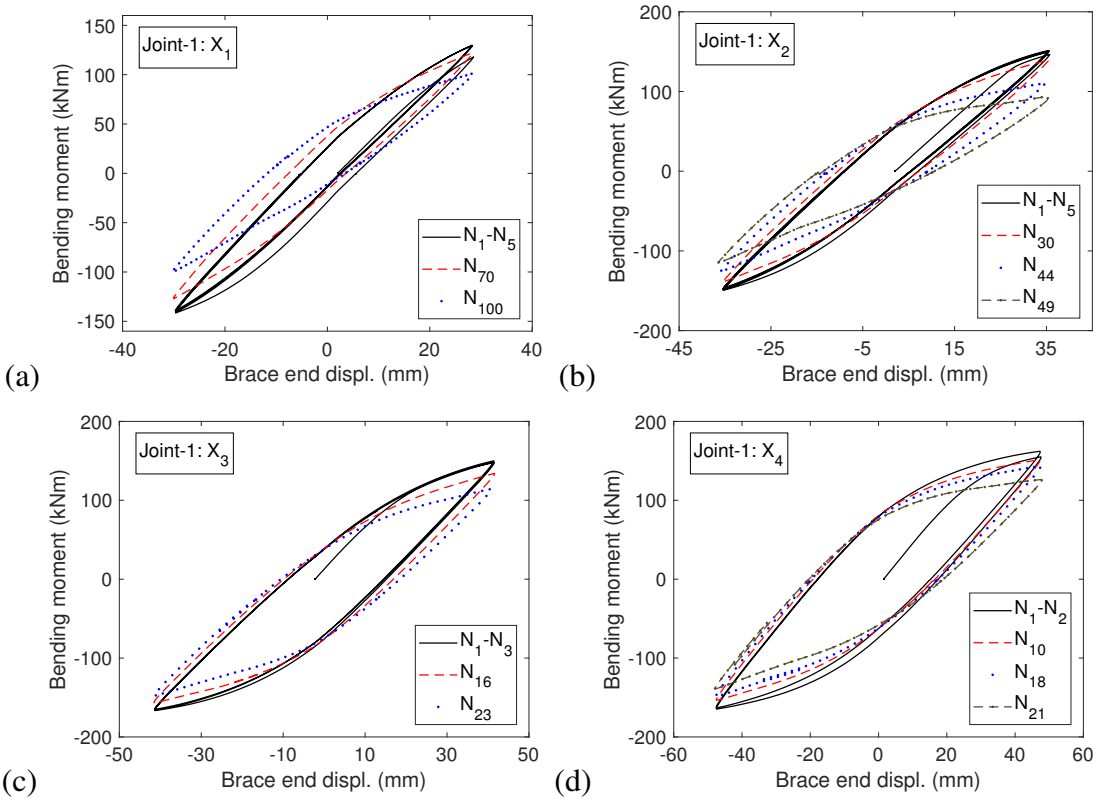

Figure 4.9: Bending moment-displacement response obtained from specimens X_1-X_4.

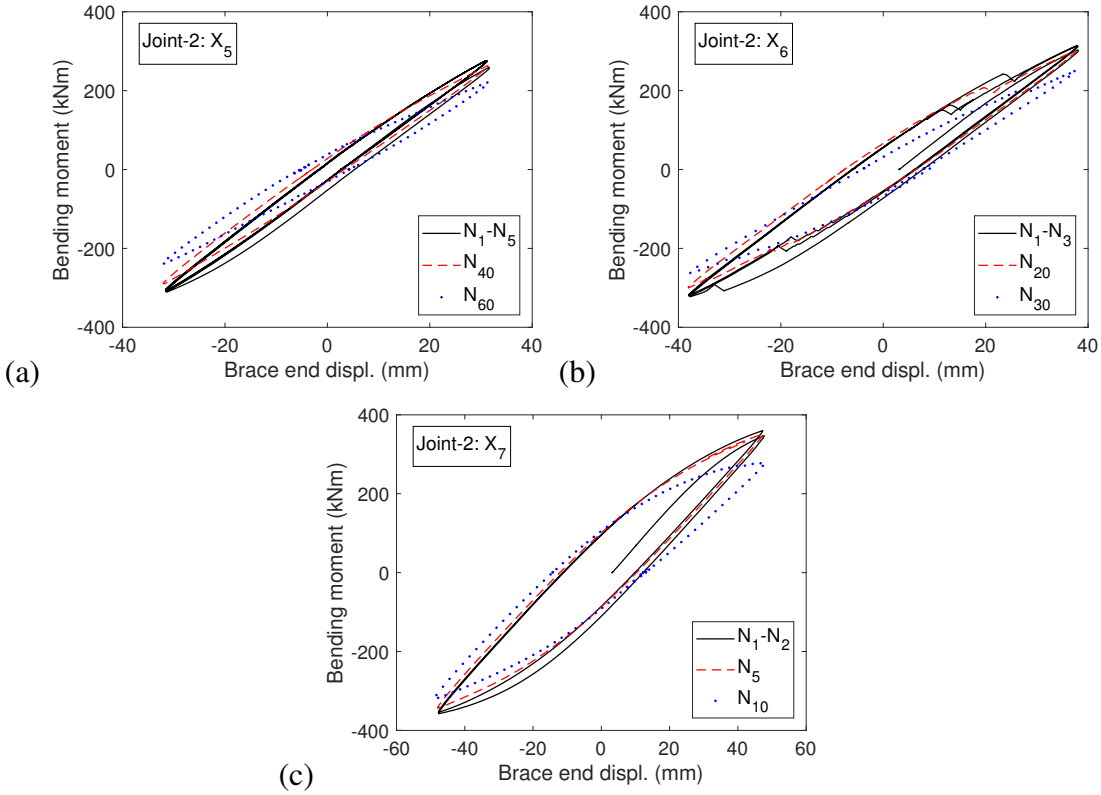

Figure 4.10: Bending moment-displacement response obtained from specimens X_5-X_7.

Local strains were measured at the chord member at the two crown locations and results are presented in Fig. 4.11 for Joint-1 and Joint-2 specimens. The distance of each strain gauge from the weld toe is denoted at the legend of each figure, while the chord crown location where measurement was obtained, is defined using the number in parenthesis. Strain gauges have also been attached at the "in-between" location, shown in Fig. 4.1, and strain measurements have been obtained, but the recordings are significantly lower than the strains obtained at the chord crown locations.

Strain measurements are analysed in terms of strain-range evolution with respect to loading cycles. Fig. 4.11, shows that the induced strain-range due to cyclic loading increased slightly during initial load cycles, reached a constant value and subsequently, it started decreasing when cracks were formed at the weld toe. Clearly, after a substantial number of load cycles, significant surface cracks developed and became quite visible, and the corresponding strain recordings started decreasing rapidly.

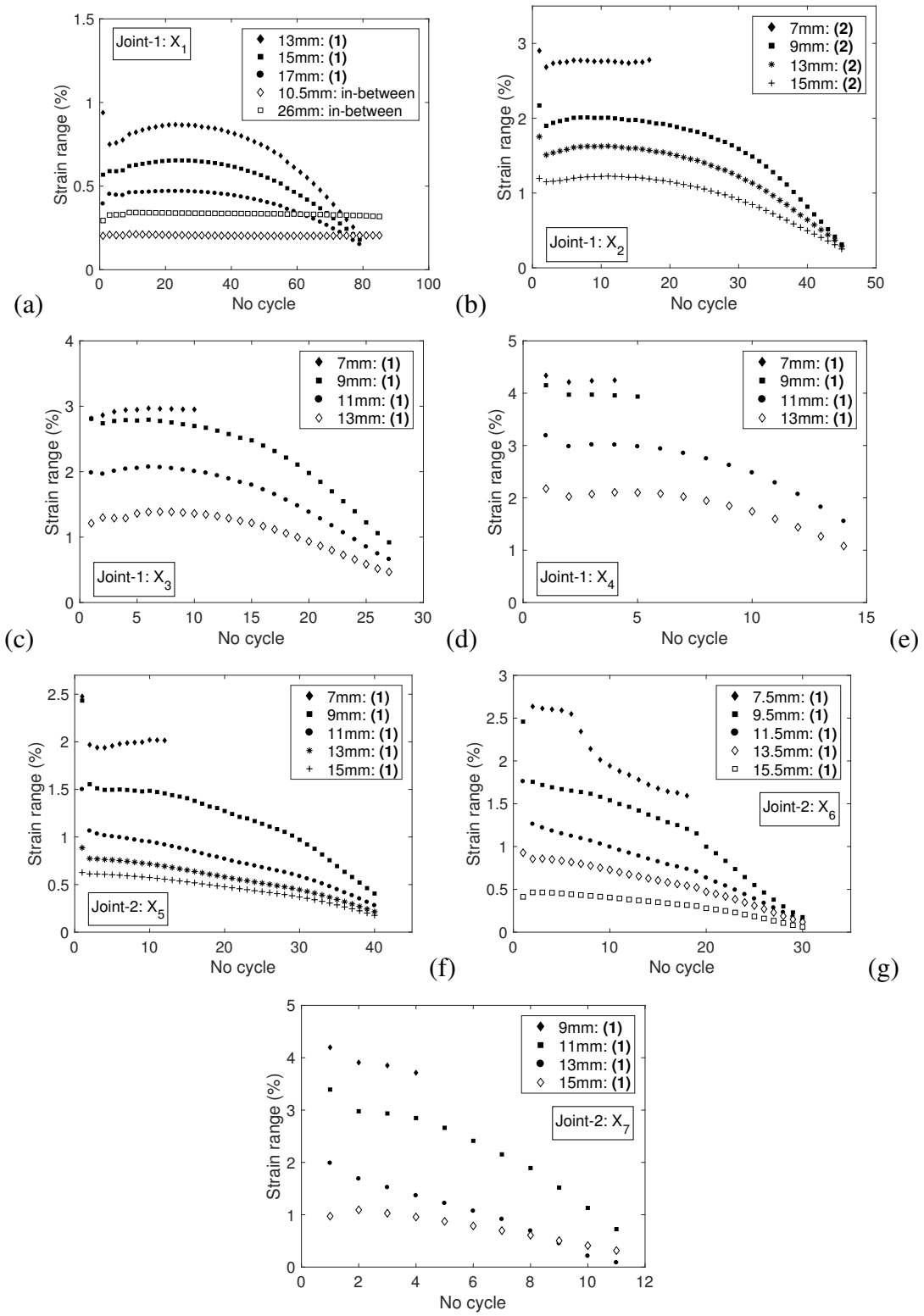

Figure 4.11: Strain range evolution over the loading cycles obtained from testing specimens X_1-X_7.

The final fractured shapes of specimens X_1-X_7 are illustrated in Fig. 4.12, while the fatigue crack initiation stage of an example case (specimen X_6) is presented in Fig. 4.13. In all cases, through-thickness crack initiated at one of the four chord crown locations. Continuation of cyclic loading resulted in propagation of initial cracks along the weld toe in a pattern which is symmetric with respect to the crown location.

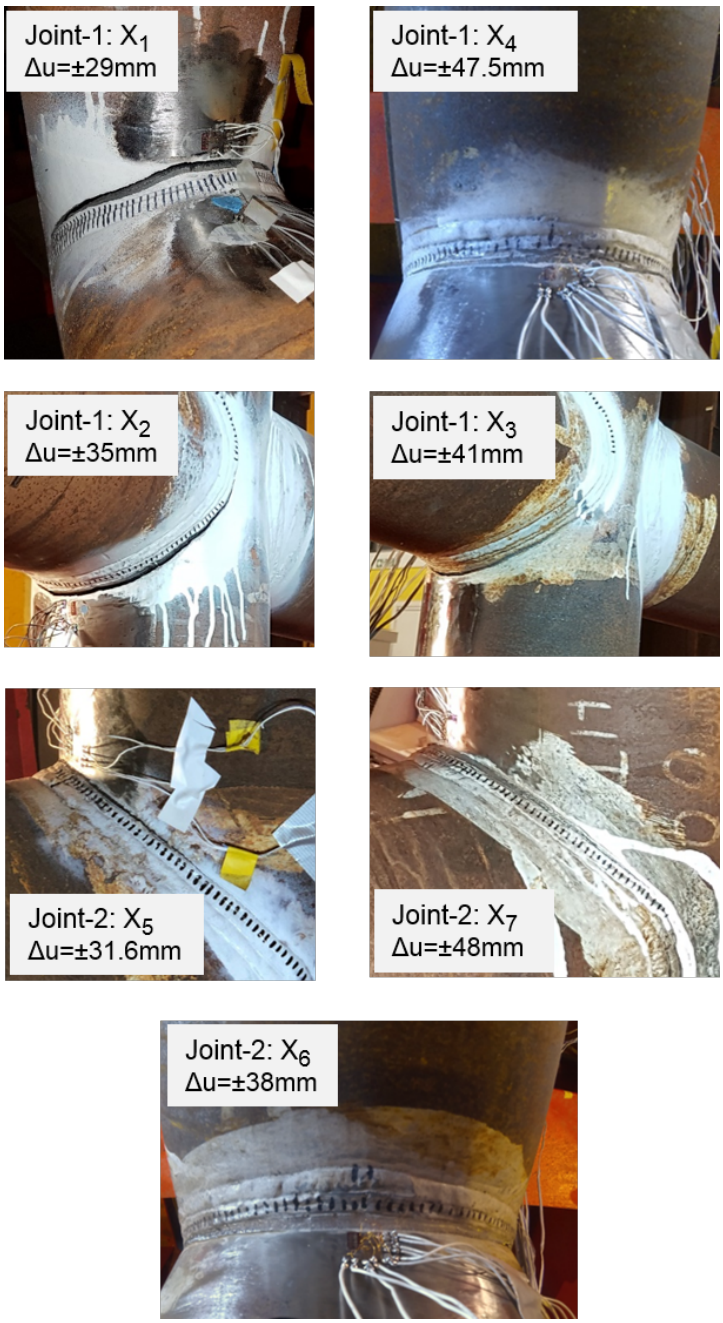

Figure 4.12: Failed specimens X_1-X_7

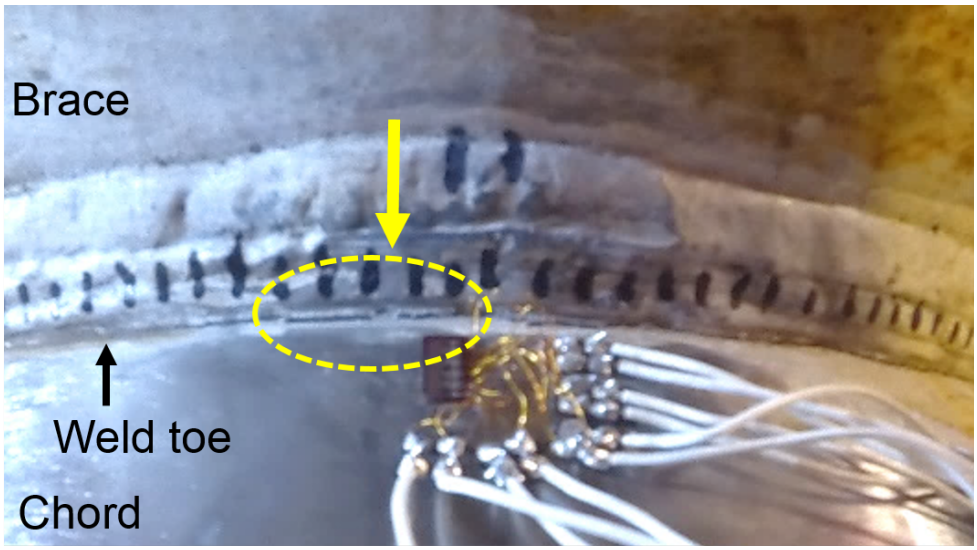

Figure 4.13: Fatigue crack at early stage of test X_6.

4.3 Numerical simulation and comparison with test data

4.3.1 Finite element model

The experimental results of the present study are numerically simulated with advanced finite element models. Both Joint-1 and Joint-2 are modelled with the use of commercial finite element package ABAQUS (2016). The main features of the finite element model, used to simulate the mechanical response of Joint-1 and Joint-2 specimens, are presented in Fig. 4.14. The finite element mesh at chord-brace intersecting area of the models of Joint-1 and Joint-2 is shown in Fig. 4.15. Double symmetry is considered for computational efficiency with the appropriate boundary conditions and therefore, only 1/4 of the X-joint specimen is modelled. Two reference points are also imposed to simulate the boundary conditions applied during testing. Reference point RP-1 is kinematically coupled with the end of the brace, to simulate the hinge in the experimental set-up shown clearly in Fig. 4.7, given the fact that the end of the brace is capped.

Point RP-1 is unrestrained in the axial direction of the brace, while the vertical displacement is prescribed in the analysis and corresponds to the brace edge displacement recorded during testing. Additionally, reference point RP-2 is kinematically coupled with the end nodes at the top section of the chord, simulating the cap welded plate. Furthermore, the nodes at the bottom edge of the chord member are fully fixed, as in the experiment.

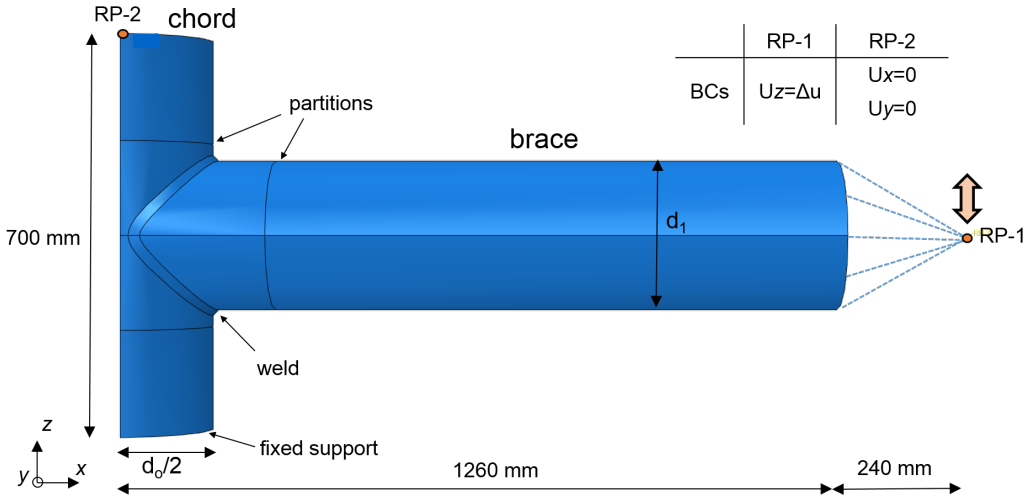

Figure 4.14: Numerical model of the test specimen.

The finite element models of Joint-1 and Joint-2 are meshed with linear solid finite elements (C3D8) and include the accurate modelling of the weld geometry based on the provisions of the American Welding Society (2004) (AWS D1.1). A sensitivity analysis has been conducted, showing that 43000 and 48000 linear solid finite elements are adequate for discretising Joint-1 and Joint-2 configurations. Joint-1 model uses 60 elements along the circumference of the brace and 28 elements around the circumference of the chord, while 5 elements are considered through the thickness of the brace and the chord to provide a well-posed mesh at the welding area. Similarly, in Joint-2 model 64 elements are adequate for discretising the circumference of the brace and 32 for the chord, while 5 elements are used through the thickness of each part. In the longitudinal direction the "single bias meshing" technique is used, leading to finer discretisation

close to the brace-chord intersection and coarser mesh away from the weld, where the stresses and the strains are significantly lower.

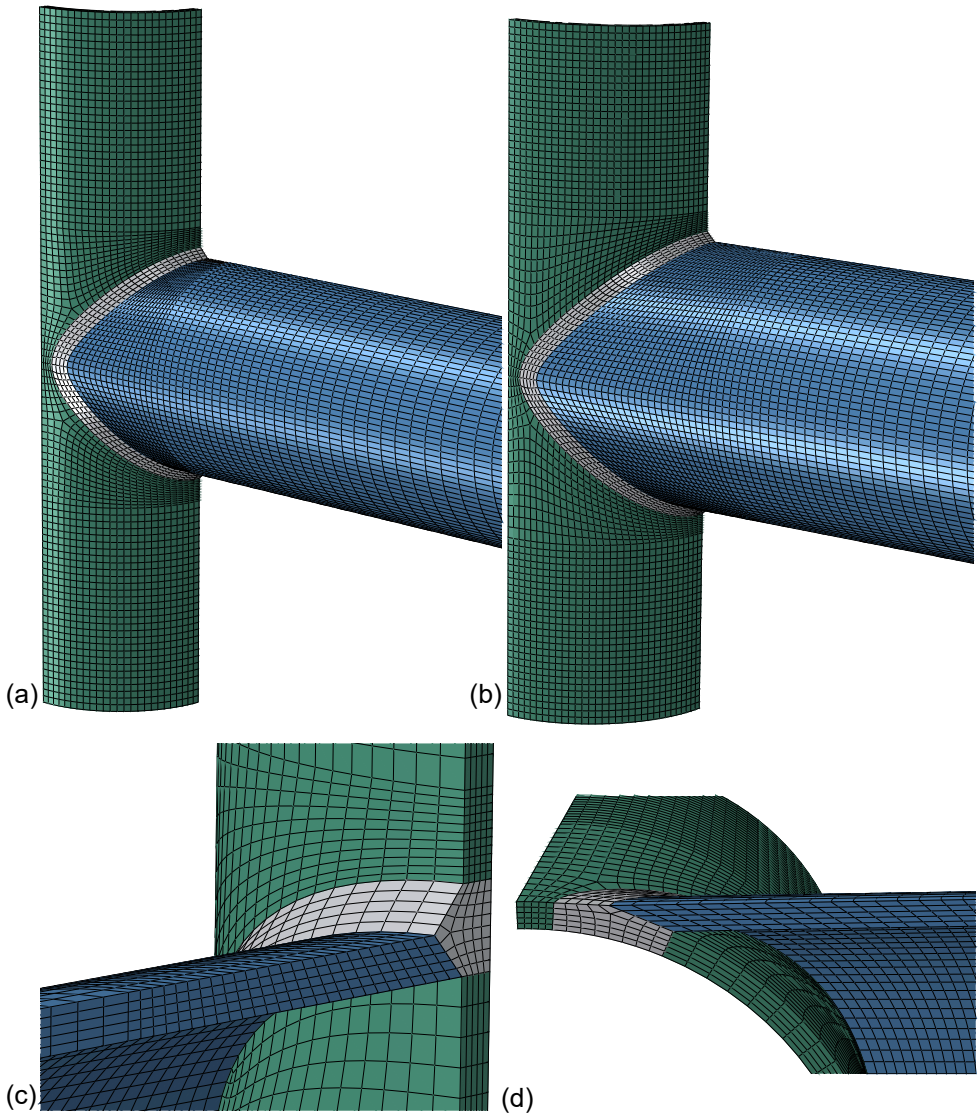

Figure 4.15: Discretised finite element model of (a) Joint-1 and (b) Joint-2. Detail representation of the welded area of Joint-2 at (c) the crown point and (d), the saddle point.

4.3.2 Constitutive model

The use of an appropriate cyclic-plasticity model is of great importance for simulating accurately the inelastic response of the specimen. The constitutive model employed herein is based on a J_2 (von Mises) cyclic elastoplasticity model with mixed hardening. The numerical implementation of the material model is utilised through the use of an external material user subroutine (UMAT) presented in Section 3.2 [Chatziioannou et al. (2019c)]. The governing equations of kinematic and isotropic hardening rules employed are presented in Eqs. (4.1-4.2) below. Kinematic hardening obeys the Chaboche (1986) model, with four nonlinear backstress tensors, as proposed by Chaboche (1991); Bari and Hassan (2002)

$$\dot{\boldsymbol{\alpha}} = \sum_{i=1}^{4} (C_i)\, \dot{\boldsymbol{\varepsilon}}^p - \sum_{i=1}^{4} \left(\gamma_i \boldsymbol{\alpha}^i\right) q \tag{4.1}$$

whereas isotropic hardening is represented with the use of an exponential function with saturation.

$$k(q) = \sigma_y + Q_\infty \left(1 - e^{-bq}\right) \tag{4.2}$$

All material parameters of the constitutive model are calibrated for each steel grade separately, so that the small-scale tests on strip specimens, shown in Fig. 4.3, are accurately represented. The material parameter sets adopted in the present analysis for S420 and S700 steel grades are listed in Table 4.3. Furthermore, it is clarified that for the purposes of the present work, whilst damage phenomena exist, they are not accounted for. An additional experimental program, which is not discussed within the Thesis has been recently undertaken to calibrate a new CDM model, specifically developed to simulate damage evolution under strong cyclic loading.

Table 4.3: Material properties of constitutive model.

Mat.	E (MPa)	v	σ_y (MPa)	Q_∞ (MPa)	b	C_{1-4} (MPa)	γ_{1-4}
S420	$1.9 \cdot 10^5$	0.3	425	-50	100	20,000	610
						8,000	420
						3330	220
						1,667	30
S700	$1.9 \cdot 10^5$	0.3	650	-60	100	23,330	500
						11,330	240
						8,000	180
						550	20

The finite element models shown in Figs. (4.14-4.15) are employed for the numerical simulation of the experimental procedure for specimens X_1 to X_7. The numerical analyses are conducted considering the actual displacement amplitudes recorded at the brace end during testing and listed in Table 4.2. Comparisons between numerical and experimental results are provided in detail for the two most extreme cases, involving specimens X_4 and X_7, and more briefly for the other experiments. It should be underlined that the numerical simulation refers to the first 5-10 load cycles, corresponding to the first stage of the welded joint response. In the subsequent stages, the joint material undergoes degradation and a cyclic plasticity model may not be adequate to describe the actual material behaviour. In such a case, coupled plasticity-damage models are required to simulate the mechanical response of the steel material, but such a modelling effort lies outside the scope of the present study.

Fig. 4.16 presents the bending moment-displacement diagram obtained from the numerical analysis and experimental testing of specimens X_4 and X_7. The comparison shows the ability of the finite element model to simulate accurately the inelastic bending moment-displacement response of the X-joint specimens under consideration. Comparisons are also provided in terms of strain-range predictions ($\Delta\varepsilon$) obtained at location (1) and the corresponding results are presented in Fig. 4.17. The results obtained from the finite element model are presented with a dashed line. The strain gauges located very close to the weld toe failed during the initial load cycle in

both tests, probably because of the high value of strain developed at that location and, therefore, measurements are provided for the other four strain gauges located at distances ranging from 7 mm to 15 mm away from the weld toe. Fig. 4.17 shows that the numerical model predicts the experimental values of strain range satisfactorily for both joints. Furthermore, the distribution of von Mises stress obtained from the numerical simulation of specimens X_4 and X_7 is depicted in Fig. 4.18, corresponding to the maximum bending moment, and shows the most highly stressed areas in each specimen.

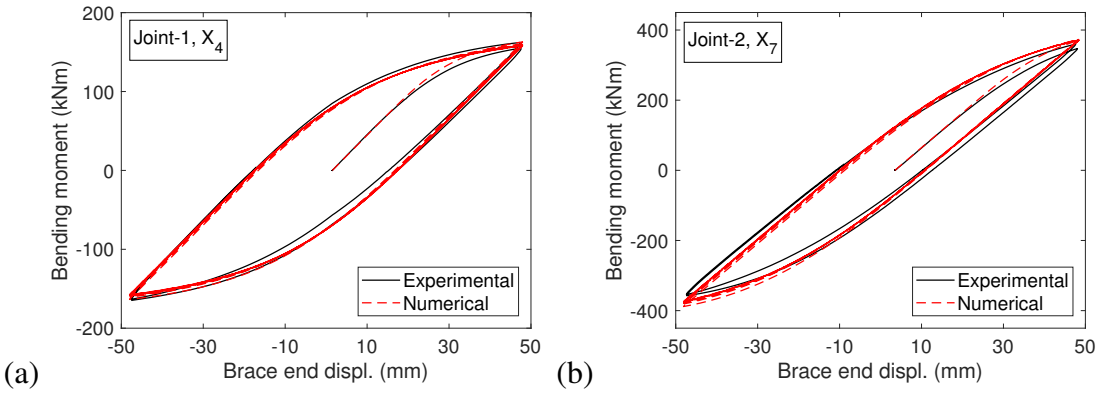

Figure 4.16: Bending moment-displacement relation obtained through numerical simulations and experimental testing of specimens (a) X_4 and (b) X_7.

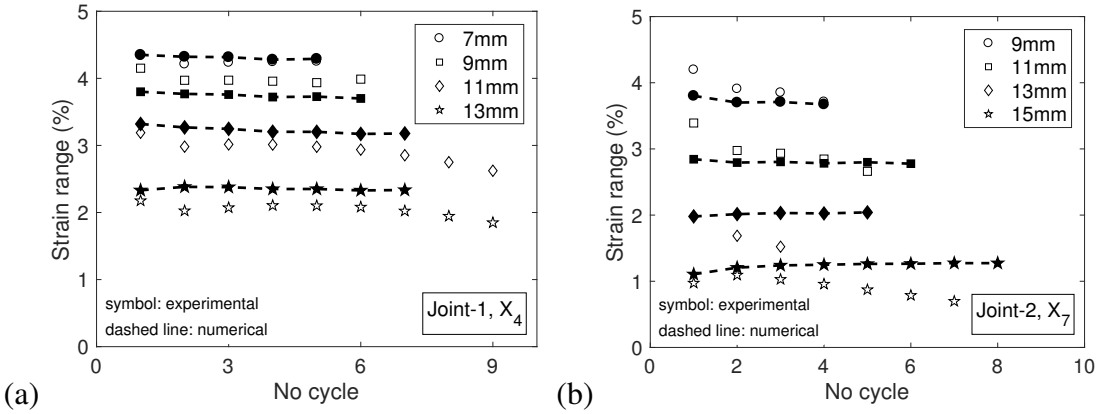

Figure 4.17: Strain range evolution obtained at location (1) through numerical analysis and experimental testing of specimens (a) X_4 and (b) X_7.

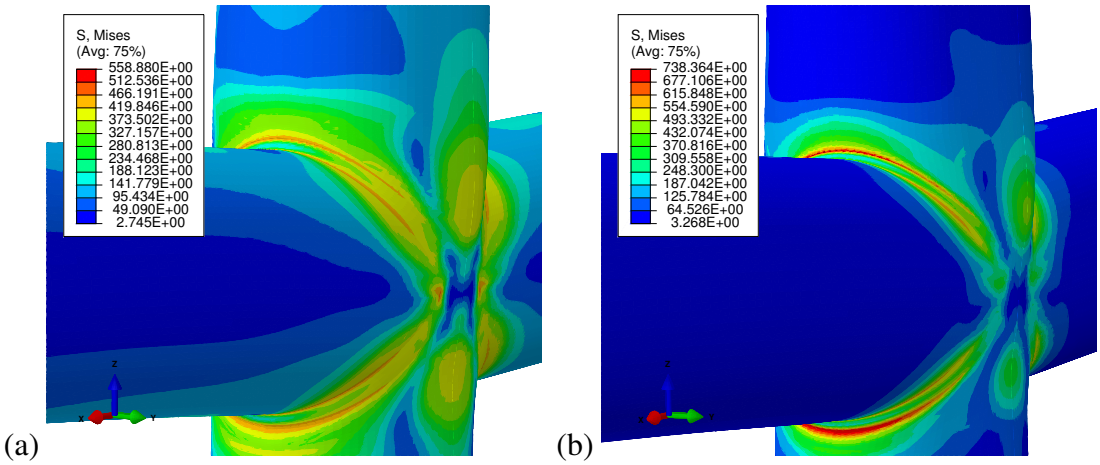

(a) (b)

Figure 4.18: Von Mises stress distribution obtained from the simulation of specimens (a) X_4 and (b) X_7 at the moment of maximum bending moment.

4.4 Comparison with design provisions and relevant available data

4.4.1 Evaluation of hot-spot stress/strain range

Experimental and numerical results are further analysed by correlating the so-called "hot-spot strain" range ($\Delta\varepsilon_{hs}$) and "hot-spot stress" range ($\Delta\sigma_{hs}$) with the number of cycles to failure (N_f). Herein, $\Delta\varepsilon_{hs}$ is computed by extrapolating linearly the local strain range values obtained from either numerical results or experimental data at the location of the weld toe. It is noted that the extrapolated value $\Delta\varepsilon_{exp,hs}$, obtained from the experimental results, is calculated using the measurements recorded after the first two load cycles to ensure that the induced strain range has reached a constant value (see Fig. 4.11).

The hot-spot strain range values of specimens $X_1 - X_7$ obtained using test data ($\Delta\varepsilon_{exp,hs}$) and the numerical results ($\Delta\varepsilon_{FEM,hs}$) are presented in Table 4.4 along with the number of cycles to through-thickness cracking (N_f) as measured in the experiments. In specimen X_1, a single value is presented as the second FXV-1 series has been attached on

the brace crown location and the recordings are significantly low ($\Delta\varepsilon_{exp,hs} = 0.5\%$). Two hot-spot strain range values are computed in each experiment and in the majority of cases differ slightly with respect to each other. A significant difference of measurement at each side of the specimen is observed only in test X_5. Post-processing of the experimental data showed that, in this test, the induced displacement range has been slightly unsymmetrical, and this is attributed to geometric imperfections in the specimen, leading to higher strain values on the weld of one side of the chord with respect to the other weld. Furthermore, comparison of the experimental data with the numerical results shows that the finite element model predicts very accurately the measured hot-spot strain range.

Hot-spot stress range values ($\Delta\sigma_{hs}$) are also evaluated for each experiment following the provisions of CIDECT (2001) (Committee for International Development and Education on Construction of Tubular Structures). The nominal stress range ($\Delta\sigma_{nom}$) at the braces due to bending is calculated considering the applied bending moment and the elastic modulus of the pipe, while the stress concentration factors (SCFs) of Joint-1 and Joint-2 connections are obtained: (a) using the parametric equations proposed in CIDECT (2001), and (b) using the finite element models described in Section 3. In the latter case, a small load has been applied so that plastic deformation is eliminated in the calculation of the SCF value. The resulting SCFs values are presented in Table 4.4, highlighting that the numerically computed SCFs are very similar with those calculated using the parametric formulas in CIDECT (2001). The hot-spot stress range values ($\Delta\sigma_{hs}$) presented in Table 4.4 is calculated by multiplying the SCF value with the nominal stress range value $\Delta\sigma_{nom}$. In this calculation, the highest of the two SCF values obtained for each type of connection is used. It should be noted that the $\Delta\sigma_{hs}$ are very high, much higher than the yield stress of the material, therefore these stress values should be considered as "pseudo-elastic" stresses.

Table 4.4: Main testing results of specimens $X_1 - X_7$.

Specimen	N_f	$\Delta\varepsilon_{exp,hs}$ (%)		$\Delta\varepsilon_{FEM,hs}$ (%)	SCF		$\Delta\sigma_{hs}$ (MPa)
					CIDECT	FEM	
X_1	88 **(1)**	1.72 **(1)**	**(-)**	1.71 **(1 & 2)**			2797
X_2	47 **(3)**	3.65 **(2)**	3.82 **(3)**	3.82 **(1 & 2)**	3.119	3.386	3052
X_3	21 **(4)**	5.97 **(1)**	5.83 **(2)**	5.63 **(1 & 2)**			3240
X_4	15 **(1)**	7.07 **(1)**	7.09 **(2)**	6.66 **(1 & 2)**			3371
X_5	58 **(1)**	3.63 **(1)**	3.04 **(2)**	3.06 **(1 & 2)**			3750
X_6	34 **(1)**	4.43 **(1)**	4.28 **(2)**	4.17 **(1 & 2)**	3.347	3.223	4067
X_7	10 **(2)**	8.05 **(1)**	8.28 **(2)**	6.92 **(1 & 2)**			4583

Note: The number within (·) indicates the reference location.

4.4.2 Comparison with relevant test data and stress-based provisions

The design of tubular welded joints under ultra low-cycle fatigue remains a challenging task, as limited guidance is available in relevant design codes and standards, especially for high-strength steel material. The methodologies proposed in DNVGL-RP-C203 (2016), CIDECT (2001), API RP2 (2000) and EN 1993-1-9 (2002) for the fatigue design of welded tubular connections have been developed for regular steel material and are valid for cases mainly associated with high-cycle fatigue; i.e. with fatigue failure at a number of cycles that exceeds $N_f \geq 10^4$. Nevertheless, in the absence of design guidance for low-cycle fatigue, it has been proposed in Appendix F.1 of DNVGL-RP-C203 (2016) to extrapolate the proposed $S-N$ curves into the low-cycle fatigue regime. In the present study this extrapolation is performed and those design provisions are compared with respect to experimental results obtained from low-cycle fatigue tests. In addition to the present experimental results, experimental data reported in the literature are also plotted together with the design $S-N$ curves provided in DNVGL-RP-C203 (2016); API RP2 (2000) as well as the $S-N$ curve proposed by

Hochman et al. (2010), for predicting the fatigue life in the range of $1 \leq N_f \leq 10^3$. The $S-N$ curves proposed in CIDECT (2001) and EN 1993-1-9 (2002) are not included in the plot, because, for the range under examination, they are almost identical with the curve proposed in DNVGL-RP-C203 (2016).

The experimental results obtained from specimens $X_1 - X_7$ and those reported in previous works [Scavuzzo et al. (1998); Waalen and Berge (2005); Boge et al. (2007); Hochman et al. (2010); Varelis et al. (2020)] are plotted in Fig. 4.19 in terms of the hot-spot stress range ($\Delta\sigma_{hs}$) and number of cycles to failure (N_f). The examined data are collected from large-scale tests on tubular welded components fabricated from mild steel or high-strength steel metal alloys. Fig. 4.19 shows that the results of the present investigation fall well beneath the $S-N$ curve proposed in DNVGL-RP-C203 (2016) while the predictions of this code in particular are satisfactory for tests with $N_f \geq 10^2$. On the other hand, the $S-N$ curve proposed in API RP2 (2000) is quite conservative and will not be discussed further.

In the $\log\Delta\sigma_{hs} - \log N_f$ plot, the results obtained from specimens $X_1 - X_7$ show very small slope of the corresponding fatigue curve, indicating that the hot-spot stress methodology employed in the present work may not be a reliable measure of fatigue resistance in the ultra low-cycle fatigue regime. It should be considered that under intense cyclic loading, the structural components are loaded far beyond their elastic limit and the bending moment-displacement relation is highly nonlinear. Hence, the hot-spot stress concept, which is mainly based on the concept of elastic stress concentration, might not be reliable for describing the behaviour of tubular welded structural components in the range of ultra low-cycle fatigue ($1 \leq N_f \leq 10^2$) and predicting the fatigue life.

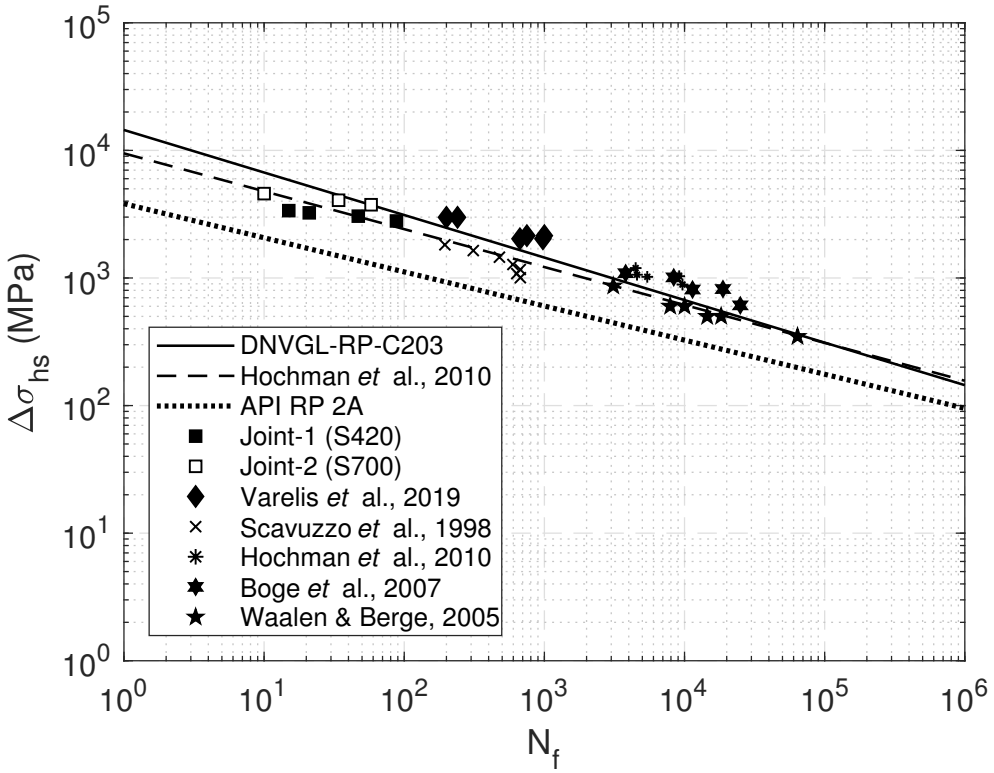

Figure 4.19: Hot-spot stress method, extended to the low-cycle fatigue regime.

4.4.3 Comparison with relevant data and codes using a strain-based framework

A different approach is adopted in DNVGL-RP-C208 (2016) standard provisions. DNVGL-RP-C208 (2016) proposes a design methodology against ultra low-cycle fatigue using the hot-spot strain range ($\Delta\varepsilon_{hs}$) and a modified Coffin-Manson equation [Coffin (1954); Manson (1954)]. For tubular welded connections, a mean and a design $\Delta\varepsilon_{hs} - N_f$ curve are presented in Section 7.12 of DNVGL-RP-C208 (2016). The mean curve is derived based on the limited available experimental data reported in the literature. The design $\Delta\varepsilon_{hs} - N_f$ curve is constructed by subtracting three standard deviations of 0.2 in the logN scale.

The experimental findings of the present study as well as those reported in Skallerud

et al. (1995); Scavuzzo et al. (1998); Varelis et al. (2020) are analysed in terms of hot-spot strain range ($\Delta\varepsilon_{hs}$) against number of cycles to failure (N_f) and the results are presented in Fig. 4.20. Comparing the present experimental data with those reported by Skallerud et al. (1995) concerning steel T-joints with yield strength of 360 MPa, it is deduced that high-strength steel tubular joints perform equally well with mild steel connections under intense cyclic loading.

The experimental data ($\Delta\varepsilon_{exp,hs} - N_f$) are also compared with respect to the mean $\Delta\varepsilon_{hs} - N_f$ curve and the design $\Delta\varepsilon_{hs} - N_f$ curve provided in DNVGL-RP-C208 (2016). The mean curve proposed in DNVGL-RP-C208 (2016) is in very good agreement with the experimental results reported in the present study and those of Skallerud et al. (1995). The results of Varelis et al. (2020) fall between the mean curve and the design curve. A possible explanation could be that the tests in [Varelis et al. (2020)] were conducted under a load-controlled pattern with a load ratio of $R = 0.1$, whereas the present experimental data and those reported by Skallerud et al. (1995) are obtained using a displacement-control testing protocol with ratio of $R = -1$ (fully-reversed). The design $\Delta\varepsilon_{hs} - N_f$ curve may underestimate the fatigue life of the tests with a number of cycles to failure less than 100, but provides satisfactory predictions with respect to the findings of Scavuzzo et al. (1998) and Varelis et al. (2020). Comparing Fig. 4.19 with Fig. 4.20, it is concluded that the design of welded joints against ultra low-cycle fatigue should be preferably conducted in a strain-based framework, using an appropriate $\Delta\varepsilon_{hs} - N_f$ curve. The methodology provided in DNVGL-RP-C208 (2016) constitutes a basis for such an approach but additional experimental data are required for validating the methodology and predict the ULCF life with good accuracy.

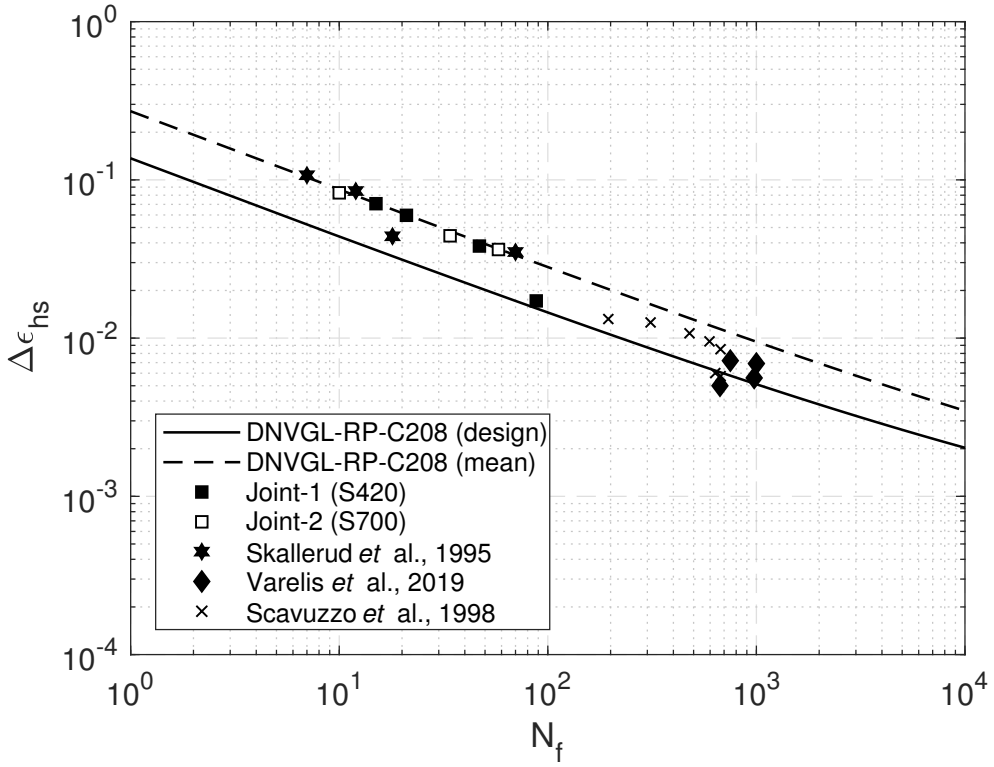

Figure 4.20: Hot-spot strain method for the low-cycle fatigue regime.

4.5 Summary

The ultra low-cycle fatigue performance of tubular welded X-joints, made of S420 and S700 steel material was investigated, using large-scale experiments and numerical simulations. The work refers to extreme loading exerted on representative tubular X-joints of an offshore wind structural system designed for installation in water depth of 55 m. Seven large-scale specimens were tested under intense cyclic in-plane bending, leading to failure with a number of cycles less than 100, which is referred to as "ultra low-cycle fatigue". Experimental results were provided in terms of bending moment-displacement relation, local strain measurements and the number of cycles to failure, which is defined as the stage where through-thickness crack occurs. The experimental program is simulated numerically using rigorous finite element models, which employ advanced cyclic-plasticity models through an in-house material subroutine. Very good comparisons are obtained in terms of bending moment-displacement relation and local

strain predictions. The experimental data of the present study are compared with similar studies reported in the literature concerning regular or high strength steel welded components. It is demonstrated that both metal alloys perform equally well against strong cyclic loading. In addition, state of art design standard are validated in predicting the number of the cycles to failure, obtained by testing large-scale specimens. The results of the analysis indicate that a strain-based design approach such as the one proposed in DNVGL-RP-C208 (2016) may be more appropriate for designing against ultra low-cycle fatigue.

Chapter 5

Conclusions

The present study investigates, through advanced numerical simulations and large-scale experiments, the mechanical behaviour of steel metal components, and particularly steel circular tubular components and tubular joints subjected to extreme cyclic loading. Computational frameworks are developed with the purpose of simulating with the best accuracy multi-axial material ratcheting and cyclic plasticity-damage response in metallic alloys. The research work addresses issues related to the numerical analysis and design of steel components under extreme loading conditions, contributing to the current state of the art.

The multi-axial ratcheting response of steel circular tubular components is elaborated in Chapter 2. An implicit numerical scheme is developed in Section 2.2, capable of integrating a wide range of metal cyclic plasticity models, which are not available even in leading commercial finite element packages. Constitutive relations are formulated explicitly for plane stress conditions using a J_2 *plane-stress projection* cyclic-plasticity model, which considers nonlinear isotropic hardening and a generalised version of the nonlinear multi-backstress kinematic hardening rule proposed by Bari and Hassan (2002), towards accurate simulation of multi-axial material ratcheting. An implicit

numerical integration scheme of the constitutive equations is developed, where incremental update of the internal variables is achieved through the solution of a single scalar equation. After proper mathematical treatment, the scalar equation obtains a rather simple form and is solved using a robust solution method. This constitutes a key novel feature of the proposed algorithm (scheme). The accuracy of the numerical integration is assessed by means of iso-error maps, showing excellent performance. Furthermore, the integration algorithm is consistently linearised, and the corresponding Jacobian is provided in explicit form, therefore ensuring the numerical robustness of the finite element solution.

The numerical scheme is implemented in a finite element environment as a user material subroutine and three advanced hardening models are selected for simulating cyclic bending experiments on pipe elbows. Comparisons between experimental data and numerical results are performed in terms of force-displacement response, cross-sectional ovalization and in particular local strains, with emphasis on ratcheting. The results show that the finite element model equipped with the material user subroutine could simulate accurately the inelastic force-displacement response obtained from the elbow experiments and reproduce the corresponding ovality values. In terms of strain measurements obtained at the elbow flank, the extrados and the intrados, the hardening model of Chaboche (1986) tends to over-predict ratcheting, whereas the results obtained with the models of Chaboche (1991) and Bari and Hassan (2002) provide more accurate predictions. Considering both axial and hoop strain measurements, the model of Bari and Hassan (2002) provides the best accuracy in terms of ratcheting prediction. It is expected that upon proper calibration, the kinematic hardening model in its generic form, as proposed herein, would lead to more accurate prediction of ratcheting. As a general conclusion, accurate prediction of elastoplastic response of steel piping components constitutes a challenging task, mainly due to the presence of ratcheting. The consideration of less elaborate and more conventional hardening models, such as the model of Chaboche (1986), may result in overestimating the strain evolution rate, possibly leading to conservative design.

The mechanical behaviour of smoothly-dented externally pressurised pipes is numerically simulated, aiming at quantifying the effect of dent magnitude and external pressure on the structural performance of the pipe under monotonic and cyclic loading. The numerical scheme presented in Section 2.2 is employed to simulate the material response of the high-strength stainless steel under cyclic inelastic loading. The pipe analysis is divided into three steps in order to examine the denting procedure, the pressure-axial loading interaction and the response of dented pipes under cyclic axial loading. With respect to the denting phase, it is identified that dents of considerable magnitude can be formed in piping components without the requirement of excessive loading. In addition, analysis results showed that the presence of external pressure higher than 50% of the collapse pressure may lead up to 25% amplification of the initial dent. The numerical results of two dented pipes, subjected to different pressure levels and loading amplitudes demonstrated the following:

- Dent depth may not have a severe effect on the monotonic axial load capacity of pipes under relatively low external pressure. However, the effect of dent depth is more pronounced in higher pressure levels.
- Dent depth influences the structural performance of the pipe under cyclic conditions by reducing the number of cycles to collapse.
- High pressure levels have a significant effect on the behaviour of dented pipes and lead to collapse within a very small number of cycles, even for relatively low axial tensile loading amplitude.
- Ovalization measurements showed that for relatively low pressure levels the pipe ratchets significantly, leading to normalized ovalization values of up to 50% prior to collapse.
- Collapse under cyclic and monotonic axial loading can be correlated through the averaged accumulated plastic strain at the dent location.

The numerical implementation of cyclic plasticity-damage constitutive models is elaborated in Chapter 3. A computational framework is developed for 3D formulation and another for plane stress condition, with the purpose of simulating the mechanical behaviour of metal structural components under severe cyclic loading that leads to low-cycle fatigue. The constitutive relations are formulated based on J_2 plasticity with combined nonlinear kinematic and isotropic hardening, coupled with isotropic damage mechanics. Constitutive equations are integrated implicitly using the Euler-backward integration scheme. For both 3D and plane stress formulation, incremental update of the internal variables is achieved through the solution of a single scalar equation and this constitutes a main feature of the presented schemes. Furthermore, the integration algorithms are consistently linearised and the corresponding consistent tangent moduli are provided in explicit form, ensuring numerical robustness of the finite element solution.

The efficiency and robustness of the proposed algorithms are demonstrated by comparing very successfully numerical results with experimental measurements obtained from two large-scale laboratory (physical) tests on steel pipe elbows. In the 3D model, finite element analyses are conducted using mixed pressure/displacement finite elements, while the damage function is properly regularised within the proposed numerical scheme according to the element's characteristic length to account for size effects. Using this formulation, mesh dependency effects are alleviated and consistent numerical results are obtained using four meshes of different density. In the shell model (plane stress), the damage function is regularised with respect to the element's length, but numerical simulations are conducted using standard finite elements. Mesh dependency effects are not observed in the force-amplitude diagram obtained with the four finite elements. However, strain predictions at the flank and the number of cycles to through-thickness cracking computed with the four finite element models indicate some small differences with each other which are related to some extent with pressure localisation at the shear band. Overall, the numerical results are in very good agreement with the experimental data in terms of force-displacement, strength degradation, local strains,

and most importantly in terms of number of cycles to through-thickness crack formation.

The numerical results indicate that the simulation methodology employed can be efficiently applied in large-scale structural computations in metal components. From a computational standpoint, the proposed numerical implementation schemes offer optimised and efficient numerical tools, which allow for the implementation of various isotropic damage models in an straightforward manner under 3D and plane stress formulation. Therefore, they can be employed as "computational platforms" for simulating and assessing low-cycle fatigue performance of metal structural components subjected to severe cycling loading.

In Chapter 4, the fatigue performance of tubular welded X-joints made of S420 and S700 steel material is examined under severe cyclic loading conditions, using large-scale experiments and numerical simulations. The work refers to extreme loading exerted on representative tubular X-joints of an offshore wind structural system designed for installation in water depth of 55 m, which may lead to low-cycle fatigue. Seven large-scale specimens were tested under intense cyclic in-plane bending, leading to failure with a number of cycles less than 100, which is referred to as "ultra low-cycle fatigue". Experimental results were provided in terms of bending moment-displacement relation, local strain measurements and the number of cycles to failure, which was defined as the stage where through-thickness crack occurs. The experimental program is simulated using rigorous finite element models, which employ an advanced cyclic-plasticity model through an in-house material subroutine. Very good comparisons are obtained in terms of bending moment-displacement relation and local strain predictions.

The main purpose of the current experimental program is to provide additional information regarding the ultra low-cycle fatigue performance of steel tubular welded connections made of S420 and S700 steel, as very limited guidance is available in relevant codes and standards, especially for high-strength steel. The specimens from both steel

grades provided similar structural fatigue behaviour whereas comparison with relevant data reported in the literature showed that under severe cyclic loading, high-strength steel welded connections perform equally well with mild steel welded connections. Therefore, the present results are quite promising for the use of high-strength steel in offshore applications.

Existing design provisions are validated against a large set of experimental data collected from the literature including also the present experimental results. The analysis results showed that the "hot-spot stress" method, extrapolated in the low-cycle fatigue regime, could be used for cases where failure is expected in more than 100 load cycles, but it might not provide accurate fatigue life predictions in the range of ultra low cycle fatigue, corresponding to less than 100 cycles. On the other hand, the strain-based method proposed in DNVGL-RP-C208 (2016) provided fatigue life predictions of reasonable accuracy with respect to the experimental data. The present results can be employed for establishing a unified design methodology suitable for low-cycle fatigue of welded tubular connections ($1 \leq N_f \leq 10^4$), including the use of high-strength steel material, towards reducing the construction cost of offshore platforms and increasing their life-cycle performance.

Future work

The Thesis provides advancements in the simulation of multi-axial material ratcheting and cyclic-plasticity damage response on metal alloys, combined with large-scale ultra low-cycle fatigue tests on welded tubular components.

The examined research topics are still open for investigation and future endeavours could be focused on:

- Increasing further the accuracy of multi-axial ratcheting simulation by modifying appropriately advanced kinematic hardening rules.

- Developing and calibrating Continuum Damage Mechanics models for low-cycle and ultra low-cycle fatigue.
- Conducting additional experiments on high-strength steel tubular welded joints with the purpose of developing a low-cycle fatigue design methodology for high-strength steel.

Bibliography

ABAQUS. Standards user's manual, Version 2016. Hibbitt, SImulia and Sorensen, Inc., 1997, Dassault Systems, 2016.

M Abdel-Karim and N Ohno. Kinematic hardening model suitable for ratchetting with steady-state. *International Journal of Plasticity*, 16(3-4):225–240, 2000.

G R Ahmadzadeh and A Varvani-Farahani. Ratcheting assessment of materials based on the modified Armstrong–Frederick hardening rule at various uniaxial stress levels. *Fatigue & Fracture of Engineering Materials & Structures*, 36(12):1232–1245, dec 2013.

E. C. Aifantis. On the microstructural origin of certain inelastic models. *Trans ASME J. Engrg. Mater. Technol.*, 106:326–330, 1984.

Alpha Ventus. Alpha ventus windfarm park. https://www.alpha-ventus.de/ueberblick/, 2013.

American Welding Society. Structural welding code-Steel AWS D.1.1/D1.1M, 2004.

ANSYS. Swanson Analysis System, Inc., Houston, PA 15342, 1995.

API RP2. API 2000, Recommended Practice 2A-WSD, Recommended practice for planning, designing and constructing fixed offshore platforms, working stress design (RP 2A-WSD), 2000.

N. Aravas. On the numerical integration of a class of pressure-dependent plasticity models. *International Journal for Numerical Methods in Engineering*, 24:1395–1416, 1987.

P J Armstrong and C O Frederick. A mathematical representation of the multiaxial Bauschinger effect. *Materials at High Temperatures*, 24(1):1–26, 1966.

ASME B31.3. American Society of mechanical engineers, ASME code for pressure piping. Technical report, New York, NY., 2006.

AWS D.1.1-83. Structural welding code-Steel ANSI/AWS D.1.1-83, 1983.

M. Azadeh and F. Taheri. Ratcheting response of dented pipes under monotonic and cyclic axial loadings. *The Journal of Strain Analysis for Engineering Design*, 49(2): 122–132, 2014.

Shunsuke Baba, Masao Naruoka, and Yasunori Arizumi. Low-cycle fatigue test of welded tubular joints. *Journal of the Structural Division*, 107(3):487–505, 1981.

Yong Bai and Wei-Liang Jin. Fatigue Reliability. *Marine Structural Design*, pages 671–687, jan 2016.

Yuanli Bai and Tomasz Wierzbicki. A new model of metal plasticity and fracture with pressure and Lode dependence. *International Journal of Plasticity*, 24(6):1071–1096, 2008.

C. Balan and D. Redektop. The effect of bidirectional loading on fatigue assessment of pressurized piping elbows with local thinned areas. *Int. J. Pressure Vessels Piping*, 81:235–242, 2004.

Shafiqul Bari and Tasnim Hassan. Anatomy of coupled constitutive models for ratcheting simulation. *International Journal of Plasticity*, 16(3-4):381–409, jan 2000.

Shafiqul Bari and Tasnim Hassan. Kinematic hardening rules in uncoupled modeling for multiaxial ratcheting simulation. *International Journal of Plasticity*, 17(7):885–905, jul 2001.

Shafiqul Bari and Tasnim Hassan. An advancement in cyclic plasticity modeling for multiaxial ratcheting simulation. *International Journal of Plasticity*, 18(7):873–894, jul 2002.

K.J. Bathe. *Finite element procedures*. Prentice-Hall: Englewood Cli s, NJ, 1996.

Z. Bazant and M. Jirasek. One dimensional softening with localization. *J. Engrg. Mech.*, 128:1119–1149, 2002.

Z. P. Bazant and B. H. Oh. Crack band theory for fracture of concrete. *Materials and Structures*, 16:155–177, 1983.

Beatrice. Beatrice windfarm Ltd. https://www.beatricewind.com, 2018.

Ahmed Benallal, René Billardon, and Issam Doghri. An integration algorithm and the corresponding consistent tangent operator for fully coupled elastoplastic and damage equations. *Communications in Applied Numerical Methods*, 4(6):731–740, 1988.

J Besson. Continuum models of ductile fracture: A review. *International Journal of Damage Mechanics*, 19(1):3–52, 2009a.

J. Besson. Damage of ductile materials deforming under multiple plastic or viscoplastic mechanisms. *International Journal of Plasticity*, 25(11):2204–2221, nov 2009b.

Froydis Boge, Torgeir K Helland, and Stig Berge. Low cycle fatigue of T-tubular joints with out-of-plane bending loading. In *26th International Conference on Offshore Mechanics and Arctic Engineering*, pages 107–115, 2007.

N Bonora. A nonlinear CDM model for ductile failure. *Engineering Fracture Mechanics*, 58(1-2):11–28, 1997.

N. Bonora, D. Gentile, and Pirondi. A. Identification of the parameters of a non-linear continuum damage mechanics model for ductile failure in metals. *The Journal of Strain Analysis for Engineering Design*, 39(6):639–651, 2004.

N. Bonora, G.H. Majzoobi, and E. Khademi. Numerical implementation of a new coupled cyclic plasticity and continuum damage model. *Computational Materials Science*, 81:538–547, jan 2014.

BS EN 10216-1. Seamless steel tubes for pressure purposes. Technical delivery conditions. Non-alloy steel tubes with specified room temperature properties. Technical report, 2013.

H. Burlet and G. Cailletaud. Numerical techniques for cyclic plasticity at variable temperature. *Engineering Computations*, 3(2):143–153, 1986.

Diego J. Celentano and Jean-Louis Chaboche. Experimental and numerical characterization of damage evolution in steels. *International Journal of Plasticity*, 23(10-11): 1739–1762, oct 2007.

M. Cervera and M. Chiumenti. Mesh objective tensile cracking via a local continuum damage model and a crack tracking technique. *Computer Methods in Applied Mechanics and Engineering*, 196(1-3):304–320, dec 2006.

M. Cervera and M. Chiumenti. Size effect and localization in J2 plasticity. *International Journal of Solids and Structures*, 46(17):3301–3312, aug 2009.

M. Cervera, M. Chiumenti, Q. Valverde, and C. Agelet de Saracibar. Mixed linear/linear simplicial elements for incompressible elasticity and plasticity. *Computer Methods in Applied Mechanics and Engineering*, 192(49-50):5249–5263, dec 2003.

M. Cervera, M. Chiumenti, and C. Agelet de Saracibar. Shear band localization via local J2 continuum damage mechanics. *Computer Methods in Applied Mechanics and Engineering*, 193(9-11):849–880, mar 2004.

M. Cervera, M. Chiumenti, and R. Codina. Mixed stabilized finite element methods in nonlinear solid mechanics: Part II: Strain localization. *Computer Methods in Applied Mechanics and Engineering*, 199(37-40):2571–2589, aug 2010a.

M. Cervera, M. Chiumenti, and R. Codina. Mixed stabilized finite element methods in nonlinear solid mechanics: Part I: Formulation. *Computer Methods in Applied Mechanics and Engineering*, 199(37-40):2559–2570, aug 2010b.

M. Cervera, M. Chiumenti, L. Benedetti, and R. Codina. Mixed stabilized finite element methods in nonlinear solid mechanics. Part III: Compressible and incompressible plasticity. *Computer Methods in Applied Mechanics and Engineering*, 285: 752–775, mar 2015.

J. L. Chaboche. *Description thermodynamique et phenomenologique de la viscoplasticite cyclique avec endommagement*. PhD thesis, Universite Paris, 1978.

J. L. Chaboche. Time-independent constitutive theories for cyclic plasticity. *International Journal of Plasticity*, 2(2):149–188, 1986.

J. L. Chaboche. On some modifications of kinematic hardening to improve the description of ratchetting effects. *International Journal of Plasticity*, 7(7):661–678, jan 1991.

J.L. Chaboche and G. Cailletaud. Integration methods for complex plastic constitutive equations. *Computer Methods in Applied Mechanics and Engineering*, 133(1-2): 125–155, jun 1996.

K. Chatziioannou, Y. Huang, and Spyros A. Karamanos. Simulation of piping ratcheting experiments using advanced plane-stress cyclic elastoplasticity models. In *Proceedings of the ASME 2019 Pressure Vessels and Piping Conference*, pages PVP2019–93507, 2019a.

K. Chatziioannou, S. A. Karamanos, and Y. Huang. An implicit numerical scheme for

cyclic elastoplasticity and ratcheting under plane stress conditions. *Computers & Structures*, 2019b.

Konstantinos Chatziioannou. *Experimental and numerical investigation of ratcheting and low-cycle fatigue in metal components*. PhD thesis, The University of Edinburgh, 2020.

Konstantinos Chatziioannou, Spyros A. Karamanos, and Yuner Huang. Ultra Low-Cycle Fatigue Performance of S420 and S700 Steel Welded Tubular X-joints. *International Journal of Fatigue*, page 105221, aug 2019c.

X. Chen and R. Jiao. Modified kinematic hardening rule for multiaxial ratcheting prediction. *International Journal of Plasticity*, 20(4-5):871–898, apr 2004.

X. Chen, B. Gao, and G. Chen. Ratcheting study of pressurized elbows subjected to reversed in-plane bending. *ASME. J. Pressure Vessel Technol.*, 128(4):525–532, 2005.

Xiaohui Chen, Xu Chen, Dunji Yu, and Bingjun Gao. Recent progresses in experimental investigation and finite element analysis of ratcheting in pressurized piping. *International Journal of Pressure Vessels and Piping*, 101:113–142, jan 2013.

CIDECT. Design guide for circular and rectangular hollow section welded joints under fatigue loading, 2001.

Sanda Cleja-Ţigoiu and Nadia Elena Stoicuţa. Revisited Simo algorithm for the plane stress state. *Applied Mathematics and Computation*, 237:730–751, jun 2014.

Jr. LF Coffin. A study of the effects of cyclic thermal stresses on a ductile metal. *Transactions of ASME*, 76:931–950, 1954.

E. Corona and S. Kyriakides. On the collapse of inelastic tubes under combined bending and pressure. *International Journal of Solids and Structures*, 24(5):505–535, jan 1988.

Edmundo Corona and Stelios Kyriakides. An experimental investigation of the degradation and buckling of circular tubes under cyclic bending and external pressure. *Thin-Walled Structures*, 12(3):229–263, jan 1991.

A.M. Cruz and E. Krausmann. Damage to offshore oil and gas facilities following hurricanes Katrina and Rita: An overview. *Journal of Loss Prevention in the Process Industries*, 21(6):620–626, nov 2008.

Lianshuang Dai, Dongpo Wang, Ting Wang, Qingshan Feng, and Xinqi Yang. Analysis and comparison of long-distance pipeline failures. *Journal of Petroleum Engineering*, 2017:7, 2017.

S. De and K.-J. Bathe. Displacement/pressure mixed interpolation in the method of finite spheres. *Int. J. Numer. Meth. Engng.,*, 51:275–292, 2001.

R. de Borst. Some recent issues in computational failure mechanics. *Int. J. Numer. Methods Engrg*, 52:63–95, 2001.

R. de Borst, L. Sluys, H. Muhlhaus, and J. Pamin. Fundamental issues in finite element analyses of localization of deformation. *Engineering Computations*, 10(2):99–121, 1993.

E. A. de Souza Neto. A fast, one-equation integration algorithm for the Lemaitre ductile damage model. *Communications in Numerical Methods in Engineering*, 18: 541–554, 2002.

E. A. de Souza Neto, D. Perić, and D. R. J. Owen. *Computational methods for plasticity: Theory and applications*. John Wiley & Sons, Ltd, 2008.

R. Desmorat and S. Otin. Cross-identification isotropic/anisotropic damage and application to anisothermal structural failure. *Engineering Fracture Mechanics*, 75 (11):3446–3463, jul 2008.

L. Di Vito. Ultra heavy-wall linepipe X65: Ratcheting in severe cyclic straining. In *29th International Conference on Ocean, Offshore and Arctic Engineering*, pages OMAE2010–20897, 2010.

DNV-RP-F111. DNV-RP-F111. Intereference between trawl gear and pipelines. DNV, Oslo, 2010.

DNVGL-RP-C203. Fatigue design for offshore steel structures. Recommended Practice, DNV GL AS, 2016.

DNVGL-RP-C208. Determination of structural capacity by non-linear finite element analysis methods. Recommended Practice, DNV GL AS, 2016.

Robert H. Dodds. Numerical techniques for plasticity computations in finite element analysis. *Computers & Structures*, 26(5):767–779, jan 1987.

I. Doghri. Numerical implementation and analysis of a class of metal plasticity models coupled with ductile damage. *International Journal for Numerical Methods in Engineering*, 38(20):3403–3431, 1995.

Issam Doghri. Fully implicit integration and consistent tangent modulus in elasto-plasticity. *International Journal for Numerical Methods in Engineering*, 36:3915–3932, 1993.

P. Dong, X. Pei, S. Xing, and M.H. Kim. A structural strain method for low-cycle fatigue evaluation of welded components. *International Journal of Pressure Vessels and Piping*, 119:39–51, jul 2014.

Wenbin Dong, Torgeir Moan, and Zhen Gao. Long-term fatigue analysis of multi-planar tubular joints for jacket-type offshore wind turbine in time domain. *Engineering Structures*, 33(6):2002–2014, jun 2011.

Wenbin Dong, Torgeir Moan, and Zhen Gao. Fatigue reliability analysis of the jacket support structure for offshore wind turbine considering the effect of corrosion and inspection. *Reliability Engineering & System Safety*, 106:11–27, oct 2012.

Matthieu Dunand, Audrey P. Maertens, Meng Luo, and Dirk Mohr. Experiments and modeling of anisotropic aluminium extrusions under multi-axial loading-part I: Plasticity. *International Journal of Plasticity*, 36:34–49, sep 2012.

EN 13480-3. Comite Europe en de Normalisation, metallic industrial piping—part 3: Design and Calculation. Technical report, Brussels, 2002.

EN 1993-1-9. European Committee for Standardization, Eurocode 3: Design of steel structures - Part 1-9: Fatigue strength of steel structures. EN 1993-1-9 standard, Brussels, Belgium., 2002.

EPRI. Piping and fitting dynamic reliability program, Vol. 2-Component Test Report, EPRI Contract No. RP 1543-15, 1992.

EPRI. Fatigue management handbook, Vol. 2-fatigue screening criteria, EPRI contract No. TR-104534-V2, 1994.

European Convention for Constructional Steelwork. Recommended testing procedure for assessing the behavior of structural steel elements under cyclic loads. Technical report, ECCS Publication No. 45, Brussels, 1968.

Balazs Fekete. New energy-based low cycle fatigue model for reactor steels. *Materials & Design*, 79:42–52, aug 2015.

R. Fincato and S. Tsutsumi. Numerical modeling of the evolution of ductile damage under proportional and non-proportional loading. *International Journal of Solids and Structures*, 160:247–264, mar 2019.

M. Foroutan, G.R. Ahmadzadeh, and A. Varvani-Farahani. Axial and hoop ratcheting assessment in pressurized steel elbow pipes subjected to bending cycles. *Thin-Walled Structures*, 123:317–323, feb 2018.

Abhinav Gautam, K Priya AAjit, and Prabir Kumar Sarkar. A nonlinear CDM based damage growth law for ductile materials. *Materials Research Express*, 2(5):026518, 2018.

C. Guionnet. Modeling of ratcheting in biaxial experiments. *Journal of Engineering Materials and Technology*, 114:56–62, 1992.

S. Hartmann, M. Kamlah, and A. Koch. Numerical aspects of a non-proportional cyclic plasticity model under plane stress conditions. *Int. J. Numer. Meth. Engng.*, 42(1477-1498), 1998.

Stefan Hartmann and Peter Haupt. Stress computation and consistent tangent operator using non-linear kinematic hardening models. *International Journal for Numerical Methods in Engineering*, 36(22):3801–3814, 1993.

T. Hassan and M. Rahman. Constitutive models in simulating Low-Cycle fatigue and ratcheting responses of elbow. *ASME. J. Pressure Vessel Technol.*, 137(3):031002, 2015.

T. Hassan and S. M. Rahman. Simulation of ratcheting responses of elbow piping components. In *ASME. Pressure Vessels and Piping Conference, Volume 1: Codes and Standards*, pages 103–108, 2008.

T. Hassan, M. Rahman, and S. Bari. Low-cycle fatigue and ratcheting responses of elbow piping components. *ASME. Journal of Pressure Vessel Technology*, 137(3): 031010–031010–12, 2015.

Tasnim Hassan and Stelios Kyriakides. Ratcheting of cyclically hardening and softening materials: II. Multiaxial behavior. *International Journal of Plasticity*, 10(2): 185–212, jan 1994a.

Tasnim Hassan and Stelios Kyriakides. Ratcheting of cyclically hardening and softening materials: I. Uniaxial behavior. *International Journal of Plasticity*, 10(2): 149–184, jan 1994b.

Tasnim Hassan, Edmundo Corona, and Stelios Kyriakides. Ratcheting in cyclic plasticity, part II: Multiaxial behavior. *International Journal of Plasticity*, 8(2):117–146, 1992.

P. Haupt, M. Kamlah, and Ch. Tsakmakis. Continuous representation of hardening properties in cyclic plasticity. *International Journal of Plasticity*, 8(7):803–817, jan 1992.

Health and Safety Executive. Review of low cycle fatigue resistance. Research report 207. Technical report, BOMEL, Limited, Norwich, UK, 2004.

A Hillerborg, M Modéer, and P E Petersson. Analysis of crack formation and crack growth in concrete by means of fracture mechanics and finite elements. *Cement and Concrete Research*, 6(6):773–781, 1976.

Marie Hochman, Marte Madshus, and Stig Berge. Low cycle fatigue of T-tubular joints under axial loading. In *20th International Offshore and Polar Engineering Conference*, pages ISOPE–I–10–479. International Society of Offshore and Polar Engineers, 2010.

P. Hopkins. Transmission pipelines: how to improve their integrity and prevent failures. In *2nd International Pipeline Technology Conference*, pages 683–706, 1995.

H. Itoga, K. Tokaji, M. Nakajima, and H.-N. Ko. Effect of surface roughness on step-wise S-N characteristics in high strength steel. *International Journal of Fatigue*, 25 (5):379–385, may 2003.

JABACO. Development of modular steel jacket for offshore windfarms (JABACO). Technical report, 2019.

H. Jeffrey and J. Sedgwick. ORECCA. European offshore renewable energy road-map. Technical report, The University of Edinburgh, 2011.

Bub-Gyu Jeon, Sung-Wan Kim, Hyoung-Suk Choi, Dong-Uk Park, and Nam-Sik Kim. A failure estimation method of steel pipe elbows under in-plane cyclic loading. *Nuclear Engineering and Technology*, 49(1):245–253, feb 2017.

Philippe Jetteur. Implicit integration algorithm for elastoplasticity in plane stress analysis. *Engineering Computations*, 3(3):251–253, 1986.

Rui Jiang, Suranji Rathnayaka, Benjamin Shannon, Xiao-Ling Zhao, Jian Ji, and Jayantha Kodikara. Analysis of failure initiation in corroded cast iron pipes under cyclic loading due to formation of through-wall cracks. *Engineering Failure Analysis*, 103:238–248, sep 2019.

Rong Jiao and Stelios Kyriakides. Ratcheting, wrinkling and collapse of tubes under axial cycling. *International Journal of Solids and Structures*, 46(14-15):2856–2870, jul 2009.

Rong Jiao and Stelios Kyriakides. Ratcheting and wrinkling of tubes due to axial cycling under internal pressure: Part I experiments. *International Journal of Solids and Structures*, 48(20):2814–2826, oct 2011a.

Rong Jiao and Stelios Kyriakides. Ratcheting and wrinkling of tubes due to axial cycling under internal pressure: Part II analysis. *International Journal of Solids and Structures*, 48(20):2827–2836, oct 2011b.

L. M. Kachanov. Time of the rupture process under creep conditions, Izy Akad. *Nank S. S. R. Otd Tech Nauk*, 8:26–31, 1958.

Spyros A. Karamanos and Charis Eleftheriadis. Collapse of pressurized elastoplastic tubular members under lateral loads. *International Journal of Mechanical Sciences*, 46(1):35–56, jan 2004.

Spyros A. Karamanos and John L. Tassoulas. Tension effects on pressure capacity of tubular members. *Journal of Structural Engineering*, 121(6):955–963, 1995.

Peter I. Kattan and George Z. Voyiadjis. Decomposition of damage tensor in continuum damage mechanics. *Journal of Engineering Mechanics*, 127(9):940–944, 2001.

N. Khutia, P.P. Dey, and T. Hassan. An improved nonproportional cyclic plasticity model for multiaxial low-cycle fatigue and ratcheting responses of 304 stainless steel. *Mechanics of Materials*, 91:12–25, dec 2015.

D. Krajcinovic. Continuous damage mechanics revisited: Basic concepts and definitions. *Journal of Applied Mechanics*, 52(4):829–834, 1985.

R. D. Krieg and D. B. Krieg. Accuracies of numerical solution methods for the elastic-perfectly plastic model. *Journal of Pressure Vessel Technology*, pages 510–515, 1977.

S. Kyriakides and Y.C. Chang. On the effect of axial tension on the propagation pressure of long cylindrical shells. *International Journal of Mechanical Sciences*, 34(1):3–15, jan 1992.

S. Kyriakides and P. K. Shaw. Inelastic buckling of tubes under cyclic bending. *Journal of Pressure Vessel Technology*, 109(2):169–178, 1987.

Pierre B. Labbé, G. R. Reddy, C. Mathon, F. Moreau, and S. A Karamanos. The OECD-NEA programme on metallic component margins under high seismic loads (MECOS). In *Proceedings of the ASME 2016 Pressure Vessels and Piping Conference*, pages PVP2016–63119, 2016.

F. A. Leckie and E. T. Onat. *Tensorial nature of Damage measuring internal variables*. 1981.

J Lemaitre. Evaluation of dissipation and damage in metals submitted to dynamic loading. In *Proc. I. C. M. Kyoto*, pages 1–10, Kyoto, Japan, 1971.

J. Lemaitre and J. L. Chaboche. Aspects phenomenologiques de la pupture par endommagement. *Journal de Mecanique Appliquee*, 2, 1978.

J. Lemaitre and R. Desmorat. Engineering damage mechanics, 2005.

Jean Lemaitre. Coupled elasto-plasticity and damage constitutive equations. *Computer Methods in Applied Mechanics and Engineering*, 51(1-3):31–49, 1984.

Jean Lemaitre. A continuous damage mechanics model for ductile fracture. *Journal of Engineering Materials and Technology*, 107(1):83–89, 1985.

H Li, M W Fu, J Lu, and H Yang. Ductile fracture: Experiments and computations. *International Journal of Plasticity*, 27(2):147–180, 2011.

Jinghui Li, Fuguo Li, Xinkai Ma, Qianru Wang, Junzhe Dong, and Zhanwei Yuan. A strain-dependent ductile damage model and its application in the derivation of fracture toughness by micro-indentation. *Materials & Design*, 67:623–630, feb 2015.

Wei Li, Lin-Hai Han, and Tak-Ming Chan. Tensile behaviour of concrete-filled double-skin steel tubular members. *Journal of Constructional Steel Research*, 99:35–46, 2014.

J Lian, J Wu, and S Münstermann. Evaluation of the cold formability of high-strength low-alloy steel plates with the modified Bai–Wierzbicki damage model. *International Journal of Damage Mechanics*, 24(3):383–417, jun 2014.

J Lin, Y Liu, and T A Dean. A review on damage mechanisms, models and calibration methods under various deformation conditions. *International Journal of Damage Mechanics*, 14(4):299–319, 2005.

Caiming Liu, Dunji Yu, Waseem Akram, Yebin Cai, and Xu Chen. Ratcheting behavior of pressurized elbow pipe at intrados under different loading paths. *Thin-Walled Structures*, 138:293–301, may 2019.

Xiangyang Lu. *Influence of residual stress on fatigue failure of welded joints*. PhD thesis, North Carolina State University, 2003.

Songyun Ma and Huang Yuan. Damage evolution and modeling of sintered metals under multi-axial loading conditions. *Computational Materials Science*, 80:123–133, dec 2013.

R. Madhaven and C. D. Babcock. Pipe collapse under combined axial tension and external pressure. *ASME J. Press. Ves. Technol.*, 115:15–26, 1987.

G.H. Majzoobi, M. Kashfi, N. Bonora, G. Iannitti, A. Ruggiero, and E. Khademi. Damage characterization of aluminum 2024 thin sheet for different stress triaxialities. *Archives of Civil and Mechanical Engineering*, 18(3):702–712, jul 2018.

SS. Manson. Behaviour of materials under conditions of thermal stress. Technical report, National Advisory Commission on Aeronautics: Report 1170. Cleveland: Lewis Flight Propulsion Laboratory, 1954.

Saeed Masih, Mohammad Mashayekhi, and Noushin Torabian. Identification and validation of a low cycle fatigue damage model for Al 7075-T6 alloy. *Journal of Engineering Materials and Technology*, 137(1):Paper No: MATS–13–1089, 2015.

A. Millard. Numerical algorithms for plane stress elastoplasticity: review and recommendation. In *Computational Plasticity: Fundamentals and Applications*, pages 237–247, 1995.

J. Moccia, A. Arapogianni, J. Wilkes, C. Kjaer, and R. Gruet. PurePower. Wind energy targets for 2020 and 2030. Technical report, European Wind Energy Association (EWEA), 2011.

Said Fawad Mohammadi, Nelson Szilard Galgoul, Uwe Starossek, and Paulo Mauricio Videiro. An efficient time domain fatigue analysis and its comparison to spectral fatigue assessment for an offshore jacket structure. *Marine Structures*, 49:97–115, sep 2016.

D.N. Moreton, K. Yahiaoui, and D.G. Moffat. Onset of ratchetting in pressurised piping elbows subjected to in-plane bending moments. *International Journal of Pressure Vessels and Piping*, 68(1):73–79, aug 1996.

Z. Mróz. On the description of anisotropic workhardening. *Journal of the Mechanics and Physics of Solids*, 15(3):163–175, may 1967.

S. Murakami. Effects of cavity distribution in constitutive equations of creep and

creep damage. In *EUROMECH Colloquium on Damage Mechanics*, Cachan, France, 1981.

M. Naghipour, M. Ezzati, and M. Elyasi. Analysis of high-strength pressurized pipes (API-5L-X80) with local gouge and dent defect. *Applied Ocean Research*, 78:33–49, sep 2018.

Hyun-Suk Nam, Jong-Min Lee, Gyo-Geun Youn, Yun-Jae Kim, and Jin-Weon Kim. Simulation of ductile fracture toughness test under monotonic and reverse cyclic loading. *International Journal of Mechanical Sciences*, 135:609–620, jan 2018.

Giang D. Nguyen, Alexander M. Korsunsky, and Jonathan P.-H. Belnoue. A nonlocal coupled damage-plasticity model for the analysis of ductile failure. *International Journal of Plasticity*, 64:56–75, jan 2015.

K.H. Nip, L. Gardner, C.M. Davies, and A.Y. Elghazouli. Extremely low cycle fatigue tests on structural carbon steel and stainless steel. *Journal of Constructional Steel Research*, 66(1):96–110, jan 2010.

Norsok. Design of steel structures, 2004.

Denis Novokshanov, Benedikt Döbereiner, Mohamed Sharaf, Sebastian Münstermann, and Junhe Lian. A new model for upper shelf impact toughness assessment with a computationally efficient parameter identification algorithm. *Engineering Fracture Mechanics*, 148:281–303, nov 2015.

Chang-Sik Oh, Yun-Jae Kim, and Chi-Yong Park. Shakedown limit loads for elbows under internal pressure and cyclic in-plane bending. *International Journal of Pressure Vessels and Piping*, 85(6):394–405, jun 2008.

N Ohno and J D Wang. Kinematic hardening rules with critical state of dynamic recovery, part I and II. *International Journal of Plasticity*, 9(3):375–390, 1993.

N Ohno and J D Wang. Kinematic hardening rules with critical state of dynamic recovery. II: Application to experiments of ratchetting behavior. *International Journal of Plasticity*, 13:519–531, 1994.

Nobutada Ohno, Masatoshi Tsuda, and Takafumi Kamei. Elastoplastic implicit integration algorithm applicable to both plane stress and three-dimensional stress states. *Finite Elements in Analysis and Design*, 66:1–11, apr 2013.

J. Oliver. A consistent characteristic length for smeared cracking models. *International Journal for Numerical Methods in Engineering*, 28(2):461–474, 1989.

M. Ortiz and E. M. Popov. Accuracy and stability of integration algorithms for elastoplastic constitutive relations. *International Journal for Numerical Methods in Engineering*, 21(9):1561–1576, 1985.

I. Papadioti, N. Aravas, J. Lian, and S. Münstermann. A strain-gradient isotropic elastoplastic damage model with J3 dependence. *International Journal of Solids and Structures*, 174-175:98–127, nov 2019.

P. Pappa, G. E. Varelis, M. Vathi, P. C. Perdikaris, S. A. Karamanos, J. Ferino, A. Lucci, E. Mecozzi, and G. Demofonti. Structural safety of industrial steel tanks, pressure vessels and piping systems under seismic loading, Final report, INDUSE RFCS project. Technical report, University of Thesssaly, Greece, 2012.

J.A. Paquette and S. Kyriakides. Plastic buckling of tubes under axial compression and internal pressure. *International Journal of Mechanical Sciences*, 48(8):855–867, aug 2006.

Xianjun Pei and Pingsha Dong. An analytically formulated structural strain method for fatigue evaluation of welded components incorporating nonlinear hardening effects. *Fatigue & Fracture of Engineering Materials & Structures*, 42(239-255), 2019.

Xianjun Pei, Pingsha Dong, and Shizhu Xing. A structural strain parameter for a

unified treatment of fatigue behaviors of welded components. *International Journal of Fatigue*, 124:444–460, jul 2019.

J.C.R. Pereira, A.M.P. de Jesus, J. Xavier, and A.A. Fernandes. ULCF assessment of X52 piping steel by means of cyclic bending tests. *Journal of Constructional Steel Research*, 138:663–674, nov 2017.

A. Pirondi, N. Bonora, D. Steglich, W. Brocks, and D. Hellmann. Simulation of failure under cyclic plastic loading by damage models. *International Journal of Plasticity*, 22(11):2146–2170, nov 2006.

Aglaia Pournara, Theocharis. Papatheocharis, S. A. Karamanos, and Philip C. Perdikaris. Mechanical behavior of dented steel pipes subjected to bending and pressure loading. *Journal of Offshore Mechanics and Arctic Engineering*, 141(1): 011702, 2018.

W Prager. A new methods of analyzing stresses and strains in work hardening plastic solids. *J. Appl. Mech. (ASME)*, 23:493–496, 1956.

Syed M Rahman and Tasnim Hassan. Advanced cyclic plasticity models in simulating ratcheting responses of straight and elbow piping components, and notched plates. In *ASME Pressure Vessels and Piping Division Conference*, pages PVP2005–71635, Denver, Colorado, USA, 2005.

Syed M. Rahman, Tasnim Hassan, and Edmundo Corona. Evaluation of cyclic plasticity models in ratcheting simulation of straight pipes under cyclic bending and steady internal pressure. *International Journal of Plasticity*, 24(10):1756–1791, 2008.

Syed Mizanur Rahman. *Finite element analysis and related numerical schemes for ratcheting simulation*. PhD thesis, North Carolina State University, 2006.

Armin Rahmatfam, Mohammad Zehsaz, and T.N. Chakherlou. Ratcheting assessment of pressurized pipelines under cyclic axial loading: Experimental and numerical

investigations. *International Journal of Pressure Vessels and Piping*, 176:103970, sep 2019.

S.R. Reid and W.W. Bell. Influence of strain hardening on the deformation of thin rings subjected to opposed concentrated loads. *International Journal of Solids and Structures*, 18(8):643–658, jan 1982.

J. R. Rice and D. M. Tracey. On the ductile enlargement of voids in triaxial stress fields. *Journal of the Mechanics and Physics of Solids*, 17(3):201–217, jun 1969.

R.J. Rider, S.J. Harvey, and H.D. Chandler. Fatigue and ratcheting interactions. *International Journal of Fatigue*, 17(7):507–511, oct 1995.

G. Rousselier. Ductile fracture models and their potential in local approach of fracture. *Nuclear Engineering and Design*, 105(1):97–111, dec 1987.

Khémais Saanouni, Abdelhakim Cherouat, and Youssef Hammi. Numerical aspects of finite elastoplasticity with isotropic ductile damage for metal forming. *Revue Européenne des Éléments Finis*, 10(2-4):327–351, 2001.

J. P. Sawyer, C. H. Wang, and R. Jones. An implicit algorithm using explicit correctors for the kinematic hardening model with multiple back stresses. *International Journal for Numerical Methods in Engineering*, 50:2093–2107, 2001.

R. J. Scavuzzo, T. S. Srivatsan, and P. C. Lam. Fatigue of butt-welded steel pipes. *ASME publications-PVP*, pages 113–144, 1998.

H. L Schreyer, R. F. Kulak, and J. M. Kramer. Accurate numerical solutions for elastic-plastic models. *Transactions of the ASME*, 101:226–234, 1979.

Florian Selot, Daniel Fraile, and Guy Brindley. Offshore wind in Europe - Key trends and statistics 2018. Technical report, European Wind Energy Association (EWEA), 2019.

P.K. Shaw and S. Kyriakides. Inelastic analysis of thin-walled tubes under cyclic bending. *International Journal of Solids and Structures*, 21(11):1073–1100, jan 1985.

Gang Shi, Yang Gao, Xun Wang, and Yao Cui. Energy-based low cycle fatigue analysis of low yield point steels. *Journal of Constructional Steel Research*, 150:346–353, nov 2018.

Hongrui Shi, Gang Chen, Yong Wang, and Xu Chen. Ratcheting behavior of pressurized elbow pipe with local wall thinning. *International Journal of Pressure Vessels and Piping*, 102-103:14–23, feb 2013.

J C Simo and J W Ju. On continuum damage-elastoplasticity at finite strains. *Computational Mechanics*, 5(5):375–400, 1989.

J C Simo and R L Taylor. Consistent tangent operators for rate-independent elastoplasticity. *Computer Methods in Applied Mechanics and Engineering*, 48(1):101–118, 1984.

J C Simo and R L Taylor. A return mapping algorithm for plane stress elastoplasticity. *International Journal For Numerical Methods In Engineering*, 22(3):649–670, 1986.

Arbind. Kr. Singh and P.C. Pandey. An implicit integration algorithm for plane stress damage coupled elastoplasticity. *Mechanics Research Communications*, 26(6):693–700, 1999.

B. H. Skallerud, O. I. Eide, A. Johansen, and J. Amdahl. On the capacity of tubular T-joints subjected to severe cyclic loading. In *15th International conference on offshore mechanics and arctic engineering (ASME)*, pages 133–142, 1995.

Bjørn Skallerud. On the relationship between low cycle fatigue and crack growth rate properties in welded steel components. *Fatigue & Fracture of Engineering Materials & Structures*, 15:43–56, 1992.

G. C. Slagis. Experimental data on seismic response of piping components. *J. Pressure Vessel Technol.*, 120(4):449–455, 1998.

P. Sollogoub. The OECD-NEA Programme on metallic component margins under high seismic loads (MECOS): Towards new criteria. In *Proceedings of the ASME 2017 Pressure Vessels and Piping Conference*, pages PVP2017–65516, 2017.

C. Soyarslan and A.E. Tekkaya. Finite deformation plasticity coupled with isotropic damage: Formulation in principal axes and applications. *Finite Elements in Analysis and Design*, 46(8):668–683, aug 2010.

C. Soyarslan, M. Malekipour Gharbi, and A.E. Tekkaya. A combined experimental–numerical investigation of ductile fracture in bending of a class of ferritic–martensitic steel. *International Journal of Solids and Structures*, 49(13):1608–1626, jun 2012.

K. Suzuki, Y. Y. Namita, and H. H. Abe. Seismic proving test of ultimate piping strength: Current status of preliminary tests- II. *ASME. International Conference on Nuclear Engineering, 10th International Conference on Nuclear Engineering*, 1: 573–580, 2002.

Wei Hua Tai. Plastic damage and ductile fracture in mild steels. *Engineering Fracture Mechanics*, 37(4):853–880, jan 1990.

Wei Tai, Hua and Bing Xian Yang. A new microvoid-damage model for ductile fracture. *Engineering Fracture Mechanics*, 25(3):377–384, 1986.

R. Tremblay, M. H. Archambault, and A. Filiatrault. Seismic response of concentrically braced steel frames made with rectangular hollow bracing members. *Journal of Structural Engineering*, 129(12):1626–1636, 2003.

N. T. Tseng and G. C. Lee. Simple plasticity model of the two surface type. *Journal of Engineering Mechanics, ASCE*, 109:795–810, 1983.

George E Varelis and Spyros A Karamanos. Low-cycle fatigue of pressurized steel elbows under in-plane bending. *Journal of Pressure Vessel Technology*, 137(1): 11401–11410, 2015.

George E Varelis, Spyros A Karamanos, and Arnold M Gresnigt. Pipe elbows under strong cyclic loading. *Journal of Pressure Vessel Technology*, 135(1):11207–11209, 2013.

George E Varelis, Theocharis Papatheocharis, Philip C Perdikaris, and Spyros A Karamanos. High-strength steel tubular welded joints under extreme loading conditions. In *26th International Ocean and Polar Engineering Conference*, pages ISOPE–I–16–425, Rhodes, 2016. ISBN 978-1-880653-88-3.

George E Varelis, Theocharis Papatheocharis, Spyros A Karamanos, and Philip C Perdikaris. Structural behavior and design of high-strength steel welded tubular connections under extreme loading. *Marine Structures*, 71:102701, 2020.

Suhas P. Vaze and Edmundo Corona. Degradation and collapse of square tubes under cyclic bending. *Thin-Walled Structures*, 31(4):325–341, aug 1998.

G. J. Vegte, J. Back, and J. Wardenier. Low-cycle fatigue of welded structures. Analysis of low-cycle fatigue on tubular T- and X-joints. Technical report, 1989.

S. Vishnuvardhan, G. Raghava, P. Gandhi, M. Saravanan, Sumit Goyal, Punit Arora, Suneel K. Gupta, and Vivek Bhasin. Ratcheting failure of pressurised straight pipes and elbows under reversed bending. *International Journal of Pressure Vessels and Piping*, 105-106:79–89, may 2013.

George Z. Voyiadjis. Degradation of elastic modulus in elastoplastic coupling with finite strains. *International Journal of Plasticity*, 4(4):335–353, jan 1988.

George Z. Voyiadjis, Ziad N. Taqieddin, and Peter I. Kattan. Anisotropic damage-plasticity model for concrete. *International Journal of Plasticity*, 24(10):1946–1965, oct 2008.

George Z. Voyiadjis, S.H. Hoseini, and G.H. Farrahi. Effects of stress invariants and reverse loading on ductile fracture initiation. *International Journal of Solids and Structures*, 49(13):1541–1556, jun 2012.

George Z. Voyiadjis, S. H. Farrahi, and G. H. Hoseini. A plasticity model for metals with dependency on all the stress invariants. *Journal of Engineering Materials and Technology*, 135(1):Paper No: MATS–12–1059, 2013.

Jorn Waalen and Stig Berge. Low cycle fatigue of T-tubular joints with in-plane bending loading. In *24th International Conference on Offshore Mechanics and Arctic Engineering*, pages 211–219, Halkidiki, Greece, 2005.

K. C. Wang and E. D. Smith. The effect of mechanical damage on fracture initiation in line pipe, part I: Dents. Technical report, Canada Centre for Mineral and Energy Technology, 1982.

Ting Wang, Wenbo Xuan, Xueli Wang, and Kai Ren. Overview of oil and gas pipeline failure database. In *ICPTT 2013, International Conference on Pipelines and Trenchless Technology*, pages 1161–1167, 2013.

E Wei, B Postberg, T Nicak, and J Rudolph. Simulation of ratcheting and low cycle fatigue. *International Journal of Pressure Vessels and Piping*, 81(3):235–242, mar 2004.

J.M. Weigand and J.W. Berman. Behavior of butt-welds and treatments using low-carbon steel under cyclic inelastic strains. *Journal of Constructional Steel Research*, 75:45–54, aug 2012.

K. Yahiaoui, D. G. Moffat, and D. N. Moreton. Response and cyclic strain accumulation of pressurized piping elbows under dynamic in-plane bending. *The Journal of Strain Analysis for Engineering Design*, 31(2):135–151, 1996a.

K. Yahiaoui, D. N. Moreton, and D. G. Moffat. Response and cyclic strain accumulation of pressurized piping elbows under dynamic out-of-plane bending. *The Journal of Strain Analysis for Engineering Design*, 31(2):153–166, 1996b.

Halid Can Yildirim and Gary B. Marquis. Fatigue strength improvement factors for high strength steel welded joints treated by high frequency mechanical impact. *International Journal of Fatigue*, 44:168–176, nov 2012.

M. Zeinoddini, M. Ezzati, and G.A.R. Parke. Plastic buckling, wrinkling and collapse behaviour of dented X80 steel line pipes under axial compression. *Journal of Loss Prevention in the Process Industries*, 38:67–78, nov 2015a.

M. Zeinoddini, M. Peykanu, M. Varshosaz, M. Ezzati, and S.J. Zakavi. Ratcheting behaviour of corroded steel tubes under uniaxial cycling: An experimental investigation. *Journal of Constructional Steel Research*, 113:234–246, oct 2015b.

Zhixin Zhan, Weiping Hu, Binkai Li, Yanjun Zhang, Qingchun Meng, and Zhidong Guan. Continuum damage mechanics combined with the extended finite element method for the total life prediction of a metallic component. *International Journal of Mechanical Sciences*, 124-125:48–58, may 2017.

Kai Zhang, Houssem Badreddine, and Khemais Saanouni. Ductile fracture prediction using enhanced CDM model with Lode angle-dependency for titanium alloy Ti-6Al-4V at room temperature. *Journal of Materials Processing Technology*, 277:116462, mar 2020.